The University Of Sheffield.

Nuclear Fuel Route Thermal Hydraulics Analysis for Advanced Gas-cooled Reactors (AGRs)

Cosimo Trinca

A thesis submitted in partial fulfilment of the requirements for the degree of
Doctor of Philosophy

The University of Sheffield
Faculty of Engineering
Department of Mechanical Engineering

January 2019

Acknowledgements

'No man is an island', and if after four years this piece of work has finally come to existence it is because of the support I had from a bunch of incredible people. My biggest debt of gratitude is probably to my supervisors, Prof. Shuisheng He and Dr. Jiankang Li, for their invaluable guidance and endless patience. Without their help this thesis would not have gone farther than page one.

Many thanks also to my friends and colleagues at the Heat, Flow, and Turbulence Research Group who have walked with me along the road. They have made my toil easier with their help, their advice and, most importantly, their affection.

A big thank you also to Miss Maria Grazia (Grace) Taibi, for her material and emotional support over the years, and to all my family, whose infinite love has reached me across the distance.

I would also like to thank the staff of EDF Energy Research and Development team in Manchester, especially Dr. Juan Uribe and Mr. Jacopo De Amicis, as well as the development team of Code_Saturne. I owe the solution of many a seemingly insurmountable problem in the development of my model to their technical expertise.

I will always be grateful to the congregation of Carterknowle Methodist Church and all the special people I met in Sheffield, for the love and care they have shown to me. My special gratitude goes to Simon and Helen Etty, for the loving support they offered me in time of need.

Finally, I wish to thank Miss Catherine Hartley, whose support and faith have pushed me forward in the weeks before my viva, and during my work on the corrections to this Thesis. This is a late addition to this list, but well deserved.

Above all I thank my Lord for leading me here. To Him and to the memory of my Dad I dedicate this thesis.

Abstract

The nuclear industry has a long history of usage of reliable and well-validated software for design and safety analysis of nuclear power generation systems. However, the majority of codes employed are based on the assumption that the flow is essentially one-dimensional, and they often provide excessively conservative predictions when three-dimensional phenomena have a significant influence.

The aims of this study are twofold:

- Furthering the understanding of three-dimensional flow patterns that may occur within the AGR fuel stringer during refuelling operations.
- Developing a numerical tool for refuelling cooling analysis capable of supporting the existing methodology in scenarios where neglecting three-dimensional phenomena would affect significantly the accuracy of the calculations.

The software used in the calculations comprised of Code_Saturne, a finite volume CFD solver, and SYRTHES, a finite element solver for thermal conduction and radiation. Both solvers are open source and are developed by EDF.

To pursue the first objective, a Large Eddy Simulation of natural convection in an enclosed fuel pin bundle was carried out using the WALE model. The computational domain represented a 60° sector of a $250\,\mathrm{mm}$ long pin bundle. The roughness of the pins was neglected. The results of the calculation showed a pattern in which fluid motion takes place in thin boundary layers adjoining the active walls, separated by a stagnant core region. It has been found that the flow between the various pins resembles natural convection in a rectangular enclosure and that the local Nusselt number correlation takes the same form as that of the cavity flow.

The second line of work resulted in the development of POSTR, a numerical three-dimensional tool designed for routine usage in refuelling cooling calculations. The tool is based on the approximation of the fuel pin bundle as a porous medium to reduce the computational cost. A two-scale approach has been followed, with a coarse grid used for the calculation of the modelled quantities and a finer mesh used for the solution of the governing equations. A solver for conduction and thermal radiation in the solid compo-

nents of the stringer is coupled with the CFD model for the gas, and a simple turbulence model is adopted.

A demonstration of the capabilities of the code has been performed. The predictions of the code have also been validated against experimental data experiment for scenarios encompassing forced, natural, and mixed convection conditions. The solid temperatures predicted by POSTR are found to be in good agreement with those calculated by detailed CFD calculations and by legacy software formerly used in the industry, as well as with the measurements taken in a large scale experiment. Recommendation for the usage of the tool are provided and directions for future work are suggested.

Two main original contributions of this study can be highlighted:

- To the knowledge of the author, the Large Eddy Simulation presented in this thesis is the first numerical investigation of turbulent natural convection in an enclosed bundle of concentrically arranged pins. The observations described in Chapter 4 could provide useful guidance for further investigation on the topic.

- The hybrid approach between CFD and sub-channel analysis introduced in Chapter 5, based on the use in the calculation of two meshes at two different scales has been adopted in subsequent research projects on coarse-grid CFD, carried out at the Heat, Flow and Turbulence Research Group of the University of Sheffield.

Contents

List of Figures

List of Tables

List of acronyms

ABWR	Advanced Boiling Water Reactor
AGR	Advanced Gas-cooled Reactor
API	Application Programming Interface
BPG	Best Practise Guidelines
CANDU	Canadian Deuterium-Uranium
CDS	Central Differencing Scheme
CFD	Computational Fluid Dynamics
CEA	Commissariat à l'Energie Atomique
COP 21	21st Conference of the Parties
DES	Detached Eddy Simulation
DNS	Direct Numerical Simulation
ECORA	Evaluation of Computational fluid dynamics methods for Reactor safety Analysis
EDF	Electricité De France
EPR	European Pressurized Reactor
EVM	Eddy Viscosity Model
FM	Fuelling Machine
FMCS	Fuelling Machine Cooling System
FPU	Fuel Plug Unit
GNU GPL	GNU General Public Licence

GNU LGPL GNU Lesser General Public Licence

GUI Graphical User Interface

HRN High Reynolds Number

IAEA International Atomic Energy Agency

IEA International Energy Agency

IFD Irradiated Fuel Disposal

LES Large Eddy Simulation

LRN Low Reynolds Number

MEL Marchwood Engineering Laboratories

NPP Nuclear Power Plant

NRS Nuclear Reactor Safety

PHWR Pressurized Heavy Water Reactor

POSTR Porous Stringer

PWR Pressurized Water Reactor

RANS Reynolds Averaged Navier-Stokes

RSM Reynolds Stress Model

RST Reynolds Stress Tensor

SOLU Second Order Linear Upwind

UNFCCC United Nations Framework Convention on Climate Change

URANS Unsteady RANS

U.S.NRC United States Nuclear Regulatory Commission

WALE Wall-Adapting Local Eddy-Viscosity

Nomenclature

α	Thermal diffusivity: $\lambda/\rho c_p$ [$\mathrm{m^2\,s^{-1}}$]
β	Volumetric expansion coefficient: $(1/\rho)(\partial\rho/\partial T)$ [$\mathrm{^\circ C^{-1}}$]
ε	Rate of dissipation of turbulent kinetic energy [$\mathrm{m^2\,s^{-3}}$]
η	Kolmogorov length [m]
γ	Porosity
λ	Thermal conductivity [$\mathrm{W\,m^{-1}\,K^{-1}}$]
μ	Dynamic viscosity [$\mathrm{Pa\,s}$]
μ_t	Turbulent dynamic viscosity [$\mathrm{Pa\,s}$]
ν	Kinematic viscosity: μ/ρ [$\mathrm{m^2\,s^{-1}}$]
ω	Turbulent frequency [$\mathrm{s^{-1}}$]
ρ	Density [$\mathrm{kg\,m^{-3}}$]
Gr	Grashof number: $g\beta(T_w - T)L^3/\nu^2$
Pr	Prandtl number: ν/α
Ra	Rayleigh number: GrPr
Re	Reynolds number: UL/ν
Δt_η	Kolmogorov time scale [s]
${}^i\langle\phi\rangle$	Intrinsic average of the variable ϕ: $(1/V_f)\iiint_{V_f}\phi dV$
$\mathrm{LES_{iq}}$	LES Quality criterion
c_p	Specific heat (at constant pressure) [$\mathrm{J\,kg^{-1}\,K^{-1}}$]

C_s Smagorinsky coefficient

D_h Hydraulic diameter: $4A_{\text{cross section}}/P_{wet}$ [m]

D_p Diameter of the pin [m]

J Radiosity [$\mathrm{W\,m^{-2}}$]

k Turbulent kinetic energy [$\mathrm{m^2\,s^{-2}}$]

q'' Heat flux [$\mathrm{W\,m^{-2}}$]

R_p Radius of the pin [m]

s^* LES Quality criterion

S_{ij} Rate of strain tensor [$\mathrm{s^{-1}}$]

T Temperature [$^\circ\mathrm{C}$]

T_w Temperature of the wall [$^\circ\mathrm{C}$]

v^+ Non-dimensional mean velocity

v_η Kolmogorov velocity scale[$\mathrm{m\,s^{-1}}$]

v_x, v_y, v_z Velocity in the x, y and z direction [$\mathrm{m\,s^{-1}}$]

y^+ Non-dimensional distance from the wall

$\dot{m}$ Mass flow rate [$\mathrm{kg\,s^{-1}}$]

$\dot{Q}$ Heat generation rate [W]

Introduction

The global increase in the energy demand is due to continue in the next decades according to the latest World Energy Outlook issued by the International Energy Agency (IEA).[1] The world energy usage in 2040 is expected to be $25\,\%$ higher than its present value, whilst electricity consumption is expected to be at least $60\,\%$ higher. Despite all the countermeasures employed, this trend will most likely translate into increased $\mathrm{CO_2}$ emissions.[1]

The link between the concentration of Carbon Dioxide and other greenhouse gases in the atmosphere and global warming is being recognized more and more widely among the international community, so much so that the 21st Conference of the Parties (COP 21) of the United Nations Framework Convention on Climate Change (UNFCCC), held in Paris, France, in late 2015, saw China, India and the United States, countries that in the past had opposed calls to reduce their emissions, take a leading role in the negotiations.[2] The pledges of the parties involved were embodied into the *Paris Agreement*, which obliged the ratifying powers to take the necessary measures to control emissions in order to keep the global average temperature increase to less than $2\,^{\circ}\mathrm{C}$. Although the treaty was somewhat undermined by the withdrawal of the United States in 2017, the remaining signatories remain committed to the reduction of Carbon Dioxide emissions. However, the policies which have been enacted or announced to this date are unlikely to succeed in bringing about a peak in the emissions by 2040, according to the forecasts of the IEA.[1]

Among the positive signals reported by the IEA, there is a global growth in the relative importance of low-carbon technologies for electricity generation, i.e. renewable sources and nuclear power. For the latter, however, the main contribution comes from new builds in China, India and Russia, while in the West there is a continuing trend towards the reduction of the share of electricity produced by Nuclear Power Plants (NPPs). The United Kingdom represents an exception to this trend, with a new European Pressurized Reactor (EPR) unit wich is being built at the Somerset site of Hinkley Point by EDF Energy (Hinkley Point C), and a number of other plants waiting for regulatory approval, such as Horizon's new Advanced Boiling Water Reactor (ABWR) at the old Magnox site of Wylfa, in Wales.

Investments in nuclear energy represent an important part of the UK Government's *Clean Growth Strategy*,[3] which summarises the Government's ambitions for an eco-

nomic growth driven by low-carbon technologies, one of the Grand Challenges set in the Government's Industrial Strategy.[4] The Clean Growth Strategy encompasses all sources of Carbon Dioxide emissions, from transportation, to domestic heating, to agriculture. Electricity generation represents a large share of the UK's emissions ($21\,\%$ in 2016), and $25\,\%$ of the total investments in clean growth will be allocated to fund innovation aimed at cutting the emissions from the sector.[3]

As a low-carbon baseload power generation technology, nuclear power plays a major role in the strategy. The Nuclear Sector Deal[5] acknowledges the need for closer cooperation between the Government and the nuclear industry to drive innovation. Among the ambitions set out in the plan is the reduction in the cost of new builds and in decommissioning, respectively by $30\,\%$ and $20\,\%$. The development of new computational tools to assist design and safety analysis will certainly assume an important role in the reduction of these costs.

Currently, all but one of the nuclear reactors operating in the country are Advanced Gas-cooled Reactors (AGRs, see Section 1.1). With the whole fleet due to be shut down by 2030, decommissioning is on the verge of becoming one of the most pressing issues faced by the industry. Among the challenges, the safe and efficient removal and handling of nuclear fuel is of paramount importance for the safety of the workforce and the public

In this study, sponsored by EDF Energy, a three-dimensional model for the fuel stringer of an AGR is being developed. This is meant to support the current, well established analysis methodology for the cooling of the fuel during refuelling operations. The safe handling and storage of irradiated nuclear fuel depends on the integrity of the components of the fuel assembly, in particular of the fuel pins and of the tie bar. Their integrity, in turn, depends amongst other conditions on the temperature distributions within them. Should the highest temperature or gradient rise above the safe level, the resulting strain may lead to component failure, with potentially very serious consequences. Another objective of the study was to investigate the cooling of AGR fuel by natural convection, one of the main mechanisms of heat removal during refuelling operations.

To determine the temperatures of these critical components, the current analysis relies on software tools based on one-dimensional network analysis. These tools have a long history of validation and confidence in their results is therefore very high. However, in some situations, three-dimensional effects may have such an influence that neglecting them brings to solutions which are either too conservative or too optimistic. The model under development is aimed at using the techniques of Computational Fluid Dynamics (CFD), whose importance in the investigations of flows in nuclear plants has been growing in the last two decades, to provide an instrument to evaluate the three dimensional effect and produce more accurate predictions in these scenarios. The work is divided into two parts:

- One line of the work is concerned with the natural convection in an enclosed fuel pin bundle, in a simplified and reduced model of the AGR fuel element. The work was carried out with LES techniques, using a body-fitted mesh, to represent the geometry, and was aimed at furthering the understanding of a fundamental phenomenon of crucial importance in refuelling cooling.

- The second part of the project is directed at the development of a simplified model of the stringer and its surroundings, where the complex geometries are represented by a porous medium having an equivalent effect on the flow. The purpose of this work is to provide fast predictions about the flow and heat exchange, in particular for the analysis of faults and deviations that may occur during refuelling.

Outline of the dissertation

- In Chapter1, the Advanced Gas-cooled Reactor (AGR) and its fuel route are introduced, and an outline of the current methodology followed in the analysis of refuelling cooling is presented.

- In Chapter 2, a review of the publicly available literature relevant to this study is provided. In Sections 2.1 and 2.2 the use of CFD in the study of nuclear system is discussed. Section 2.3 focuses on the CFD modelling of porous media and their use to approximate complex geometries. Finally, in Section 2.4 a review of studies on natural convection in enclosures is presented, with particular attention to the study of natural convection in bundles of cylinders.

- Chapter 3 contains a summary of the CFD methodologies used in this study, together with a description of the software tools employed in the analysis.

- Chapter 4 presents the results of the 'detailed' simulation of natural convection in an enclosed pin bundle.

- Chapter 5 describes the development of POSTR, a numerical tool for refuelling cooling calculations based on the porous medium approximation applied to the AGR fuel stringer.

- Chapter 6 presents the validation of POSTR and the demonstration of its capabilities for refuelling cooling calculations.

Chapter 1

The AGR and its fuel route

In this chapter, an introduction to the background of this study is given. Section 1.1 contains a short description of the AGR core and of the design of its fuel assembly. In Section 1.2 the operations that take place during the refuelling of the reactor, the so-called fuel route, are outlined, with special attention to the steps where decay heat removal is crucial. Finally, in Section 1.3, the existing software in use for safety analysis of the fuel route is presented.

1.1 Overview of the AGR core

The Advanced Gas-cooled Reactor (AGR) is a CO_2 -cooled, graphite-moderated nuclear reactor design developed in the United Kingdom in the 1960s as a substitute design for the Magnox reactor, which had represented the first generation of European commercial reactors. Whilst in most countries the nuclear industry oriented its investments towards water-cooled reactors, the UK decided to continue on the path of the gas-graphite technology. The reasons were twofold: on the one hand, there was the political desire to develop a national technology; on the other hand, the high maximum temperatures of the primary (around $650\,^{\circ}\mathrm{C}$) and secondary (around $550\,^{\circ}\mathrm{C}$) coolants allow to achieve a thermodynamic efficiency of around 42%, higher than that reached by water cooled reactors.[6] The UK remains the only country to have ever built AGRs.[7]

The core of an AGR comprises of a 16 sided prism moderator, made of cylindrical bored graphite bricks connected by graphite keys. The interiors of the bricks form the fuel channels, which house the fuel assemblies.[6,7] The number of channels varies from station to station.[6] Surrounding the core, as well as on its top and at its bottom, are the graphite reflector and the steel neutron shields. The core is held together by a steel tank and its weight rests on a steel grid, called the *diagrid*. Around the core lies the gas baffle, which separates the hot gas which has flowed through the core from the cooler gas which

has yet to enter into it (see below). On the dome of the gas baffle are several penetrations for the fuel and the control rod assemblies. The latter are inserted from above at a number of positions between the moderator bricks. For fast shut-down, Nitrogen injectors are provided.[7]

A pre-compressed concrete pressure vessel contains the core, the gas circulators and, in most plants, the steam generators.[6,7] Above each of the fuel channels, the vessel is penetrated by an opening called *standpipe*, through which the fuel assembly is inserted. This is a $23\,\mathrm{m}$ long unit which comprises of a lower part, the *stringer*, where the fuel is housed, and an upper part, referred to as *Fuel Plug Unit (FPU)*.[7] The latter comprises of a number of sections, each serving a different purpose (Figure 1.1): beside the neutron reflector and the gamma ray and heat shields, it includes the gag unit, which controls the gas flow through the channel,[6] its actuators, and the $\mathrm{CO_2}$ outlet ports. The *stringer* consists, in most stations, of 8 fuel elements, piled one on another and held together by a $13\,\mathrm{m}$ long, $10\,\mathrm{mm}$ diameter *tie bar*. This carries the weight of all the stringer during the lifting and transportation operations, and it is not redundant: its failure would cause the whole stringer to be dropped, with very serious consequences, which makes its integrity a crucial concern. The fuel element, depicted in Figure 1.2, comprises of 36 fuel pins, clad in stainless steel and arranged in three concentric circular ranks of 6, 12 and 18 pins each. The pins are supported at the bottom by a grid and held by steel braces in the middle and at the top to prevent their bowing.[7] The fuel pellets are made of $\mathrm{UO_2}$ with an enrichment of $2.8\,\%$ to $3.8\,\%$. The burn-up of the fuel is normally between $27\,000\,\mathrm{MWd/t_U}$ and $32\,500\,\mathrm{MWd/t_U}$. The cladding is ribbed on the outer surface to promote heat transfer, and filled with helium to prevent oxidation of the fuel. The bundle is enclosed in a graphite sleeve, whose main function is to separate the flow around the pins from the re-entrant flow (see below). It also slows down the neutron, thus reducing the energy deposited into the moderator.[6]

A schematic representation of the coolant path is given in Figure 1.3. As shown in the Figure, the $\mathrm{CO_2}$ is blown by the gas circulators from the steam generators outlet into the space beneath the core. Around half of it passes through the fuel assembly, cooling the pins and the tie bar, and emerges into the hotbox, the space above the gas baffle, to be conveyed downward again, through the steam generators. The rest of the gas takes the way of the annular space between the core and the gas baffle, flowing into the space under the dome.[7] Flow into the hotbox is prevented by the fuel assembly piston seals, which block the penetrations in the dome. The gas then must return downward through the fuel channel, along the annular gap between the fuel element sleeves and the moderator (*re-entrant flow*); it emerges under the core where it is mixed with the rest of the gas to flow through the assembly. The function of this flow is to keep the temperature of the moderator lower than $450\,^{\circ}\mathrm{C}$ and to limit internal temperature gradients within the

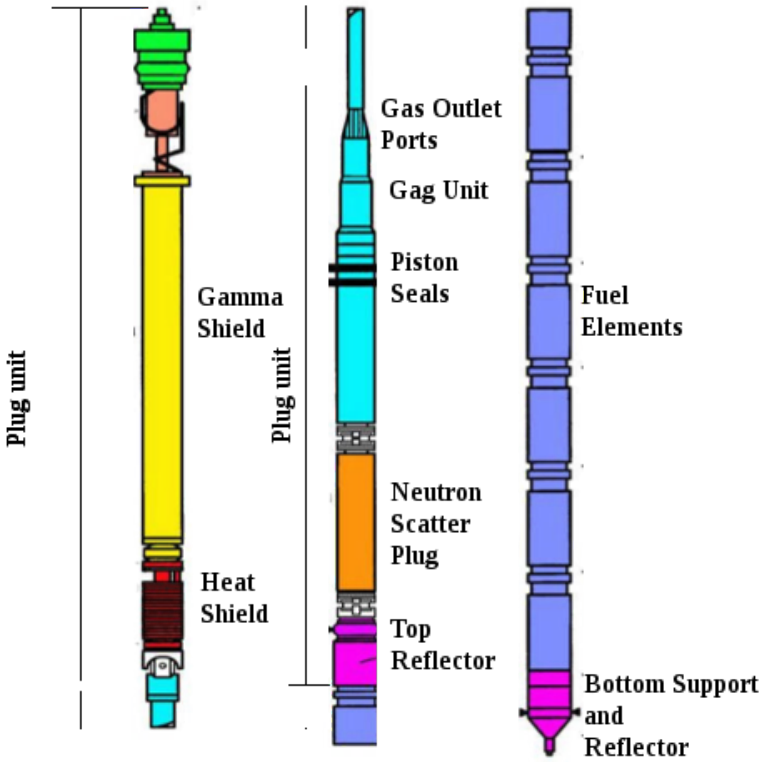

Figure 1.1: Schematics of the AGR fuel assembly. Adapted from ref. [8].

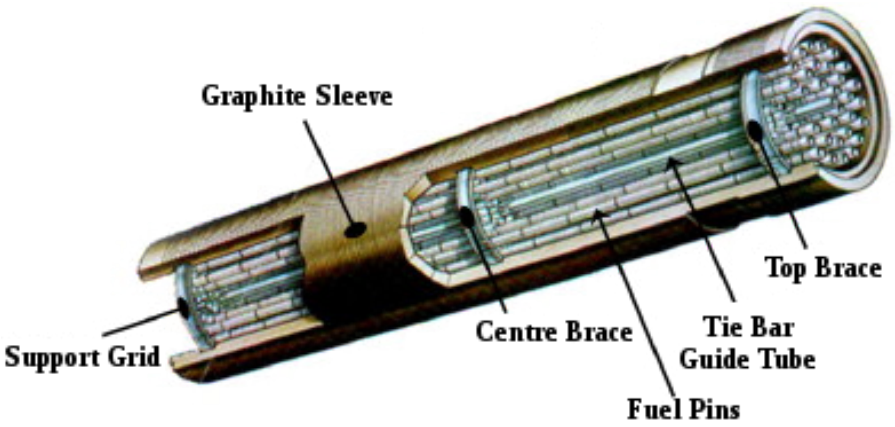

Figure 1.2: Schematics of the AGR fuel element. Adapted from ref. [9].

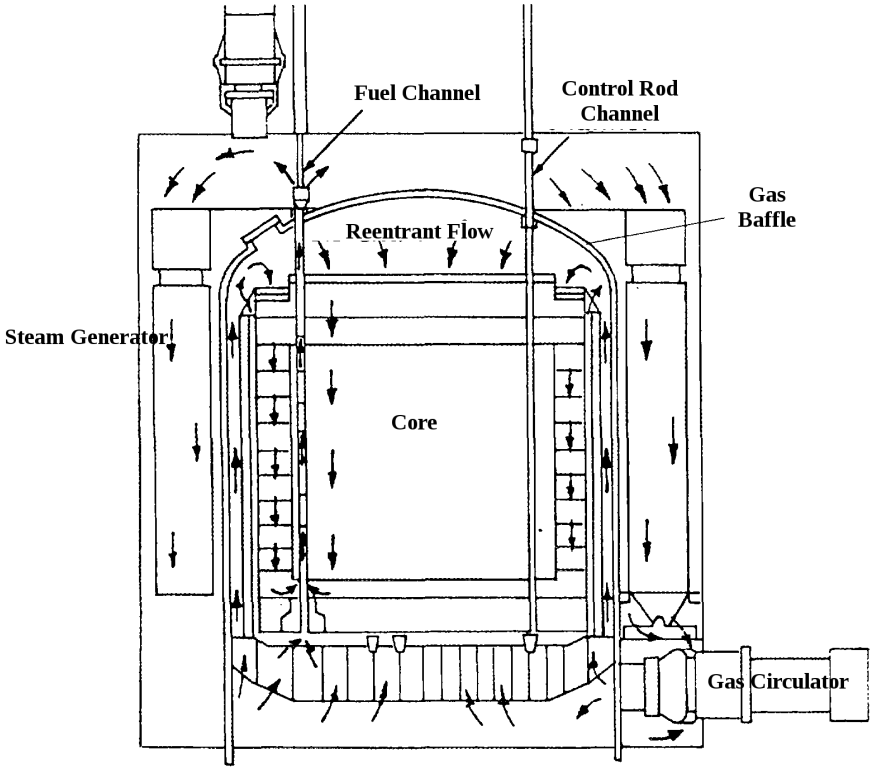

Figure 1.3: Path of the coolant in the core of an AGR. Adapted from ref. [7]

graphite.[7]

1.2 The fuel route in AGRs

To maintain the criticality of the reactor during its operational life, irradiated fuel must at some point be replaced by new assemblies. The operations involved in this vital process form the "*fuel route*". A comprehensive definition of the fuel route states that it is the "path the fuel takes from coming on site, through the build process, into the reactor, out through the Irradiated Fuel Disposal (IFD) cell and the irradiated fuel storage ponds, then off-site for re-processing" in order to "safely maintain the reactivity inventory of the reactor from receipt of new fuel to despatch of spent fuel".[8]

The activity is extremely sensitive from a safety point of view, so much so that, according to some estimations, as much as $50\,\%$ of the risk associated with an AGR plant comes from the fuel route, for what concerns both the safety and economic aspects. This is due mainly to the amount of manipulation the fuel undergoes during the various phases, with the possibility for the fuel assembly to be dropped or otherwise damaged during the lifting. Like every operation that carries a risk of radioactive release, the activities must be covered by a safety case, a detailed and evidence supported document where the hazards are identified, the risks evaluated and the controlling measures are described.[8]

To minimise operational downtime, refuelling is normally carried out in batches.[6] During its life at the station, every fuel element goes through several steps which bring it across several locations within the station. These steps can be outlined as follows:[8]

1. The fuel arrives at the plant from the manufacturer and it is stored in the **new fuel store** until a new stringer needs to be assembled;
2. When required, the elements are brought to the **new fuel cell**, where the assembly is built;
3. The new assembly is moved to the **buffer store**, together with the others in the same batch;
4. The assembly is put in place in one of the **reactor** channels, according to its enrichment;
5. At the end of its in-core irradiation time, the spent fuel assembly is extracted from the core and stored again into the **buffer store**, until the decay heat drops to a level that allows safe handling;
6. The assembly is sent to the **IFD cell** and dismantled;
7. Due to its high cost, the Fuel Plug Unit is sent to the **FPU maintenance facility** to be inspected and refurbished;
8. Conversely, the irradiated fuel elements are discharged into the **irradiated fuel storage ponds**, where they reside, on average, for a period of 58 days, shielded and cooled by the pond water;
9. Finally, the fuel elements are bottled into shielded **flasks** and sent to Sellafield for reprocessing.

The scope of this project concerns the phases from the extraction from the reactor channel to the handling in the IFD cell. Some detail on the key stages will be given in the following.[8]

The Fuelling Machine (FM) is used in the handling and transportation of the fuel assembly along the fuel route. It also assists during the construction of the assembly construction and is used to transport other reactor components. When in the FM, the fuel assembly is housed in a shielded pressure vessel, which can be sealed during the transport. When connected to a facility or to the reactor standpipe, other seals ensure continuity in the pressure boundary. The machine is equipped with a Fuelling Machine Cooling System (FMCS), which provides a downward gas flow to cool the irradiated fuel during the charge and discharge of the fuel stringer at the reactor.[8]

Although the AGR was originally designed to allow refuelling with the plant operating at full power, this was never achieved. Today, the reactor is refuelled with the reactor either at reduced power (around 30% of the nominal power) or off-load, depending on the station design. During the extraction of the spent assembly, the connection between the FM and the standpipe is sealed to maintain the pressure boundary. The assembly is lifted until is completely contained within the FM pressure vessel; in the meantime, the cooling of the stringer is ensured by a combination of the reactor flow and the fuelling machine coolant flow.[8] Figure 1.4 shows three stages of the fuel discharge at the Hinkley Point B power station.[10]

In the first stage of the lift (Figure 1.4a), the gas flows as during normal operation, driven by the reactor circulators, through the fuel elements and to the hot box, while the sleeve is cooled by the re-entrant flow. The FMCS is turned on as soon as the flow path to the reactor is clear, to keep the pressure in the machine higher than in the reactor. This prevent reactor gas from entering the machine when the outlet gas ports of the stringer enter the standpipe. The flow through the fuel is reduced since the piston seals do not block the path from the reactor to the hotbox outside the stringer any more, therefore allowing part of the flow to take the direct path to the hotbox through the annular gap outside the sleeve.[10]

At $13.57\,\mathrm{m}$ of lift (Figure 1.4b) the stringer nose enter the hot box. From this moment the fuel is cooled by a mixture of gas from the jet coming out of the reactor channel and hotter gas from the hotbox entrained by the jet, which results in a higher temperature of the coolant. In this region the sleeve is cooled by the FMCS.[10]

As soon as the stringer nose brush enters the standpipe ($15.85\,\mathrm{m}$, Figure 1.4c) the flow through the stringer becomes dominated by the FMCS, which cools both the fuel and the sleeve. Eventually, the stringer enters the Fuelling Machine, which is then isolated ($28.35\,\mathrm{m}$, Figure 1.4d). The stringer is cooled by natural convection, with the heat sink provided by the air outside the vessel.[10]

As mentioned above, the discharged fuel is moved from the channel to the buffer storage (Figure 1.5). This is a shielded concrete vault, accessible by the FM from the top, which contains a number of water-cooled, shielded vertical pressure vessel, named *decay tubes*. Here the irradiated fuel is stored in a pressurized $\mathrm{CO_2}$ atmosphere. Some of the decay tubes are provided with valves in order to house leaking fuel assemblies. Others are not pressurised and do not have a water jacket: they are used to store non-fuel reactor components.[8] The residence in the buffer store allows for the decay heat to drop to a safe level for handling in the IFD cell.[8] It also allows for the IFD cell itself to be "smaller" than it would need to be if it had to treat all the assemblies removed in a batch at the same time.[6]

The FM lowers the spent fuel assembly into one of the decay tubes. The fuel is cooled

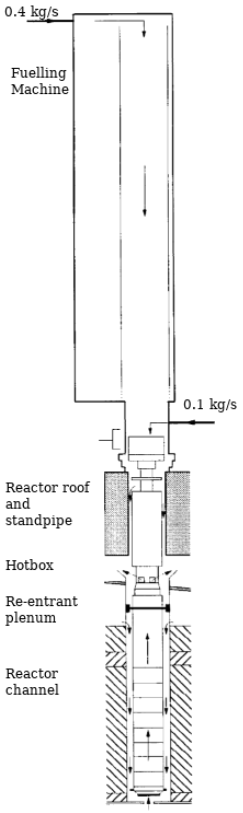

(a) Stringer in the reactor channel.

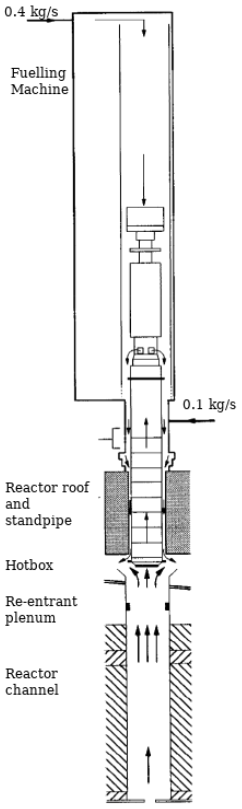

(b) Stringer nose in the hot box.

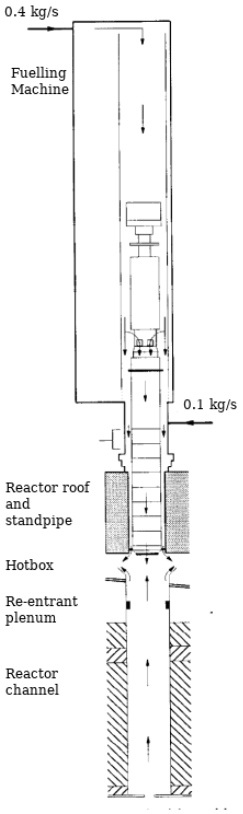

(c) Stringer nose brush in the stand-pipe.

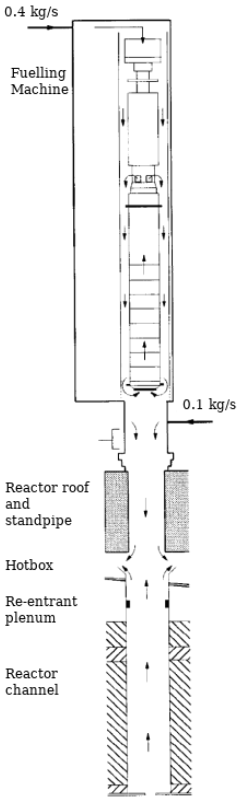

(d) Stringer in the Fuelling Machine.

Figure 1.4: Positions of the fuel stringer at various stages of the discharge. Adapted from ref. [10].

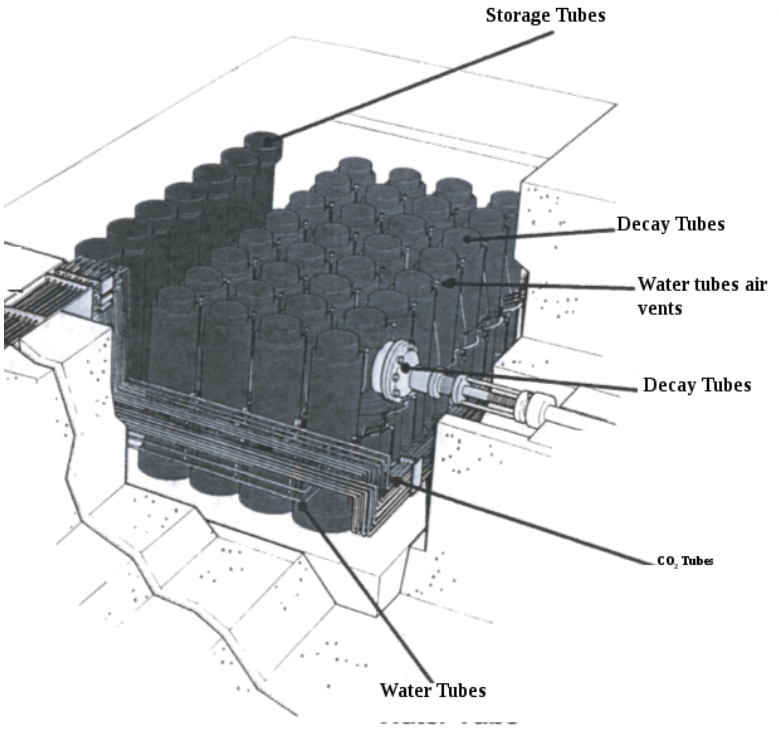

Figure 1.5: Schematics of the buffer store. Adapted from ref. [8].

by natural circulation of the CO_2, with the water jacket providing the heat sink. The effectiveness of the cooling depends on gas density: de-pressurisation is a major fault, which may lead to overheating of the fuel and eventually to the release of fission products through the leak into the vault. Loss of coolant could also potentially lead to overheating of the fuel. The most serious event is the drop of a fuel assembly, which beside damaging the fuel, in a potentially severe way, may also cause a breach in the tube, which in turn would cause de-pressurisation exacerbating the consequences.[8]

After its residence in the buffer store the assembly is transferred to the IFD cell (Figure 1.6), a shielded vault that houses sealed tubes which can be either pressurised or at a pressure lower than the cell, depending on the plant design. In these tubes the assembly is dismantled: the tie bar is cut, thus separating the FPU from the fuel elements. The former is sent to the FPU maintenance facility before being re-used, while the fuel elements are sent to the irradiated fuel storage ponds. Other components below the FPU are dumped in the debris vault, together with the tie bar. The cooling here is provided by a ventilation system, which also keeps the room at a pressure lower than the atmosphere to safeguard the environment against accidental release. The airflow passes through a filtering facility before being discharged. In some stations the tubes are also individually cooled through water jackets.[8]

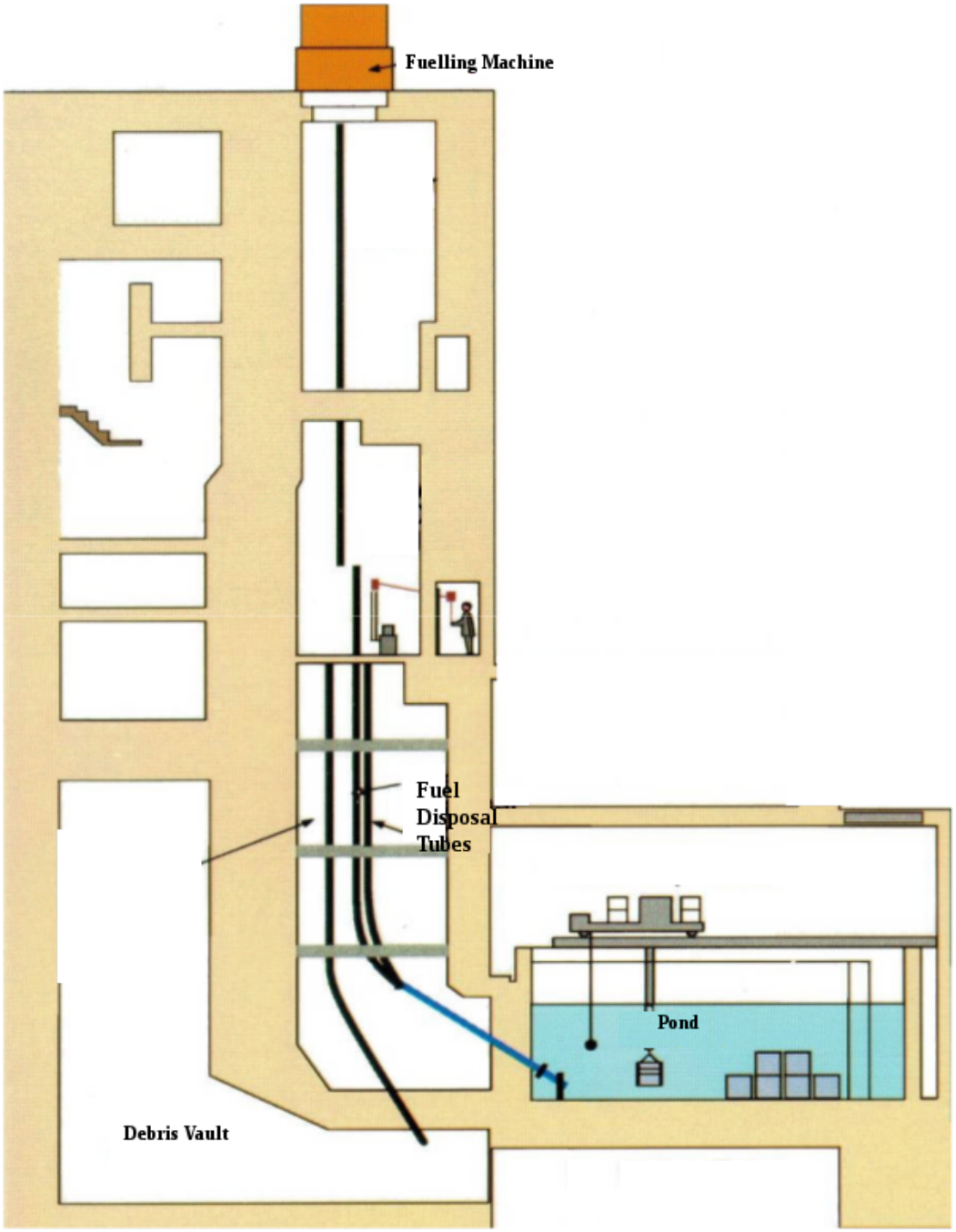

Figure 1.6: Schematic of the Irradiated Fuel Disposal cell. Adapted from [8].

1.3 Current tools of analysis for the fuel route in AGRs

In this section some of the existing software tools used for calculations concerning the fuel route will be presented. First, a brief overview of the workflow currently followed in refuelling cooling calculations will be given; then, a legacy code for three-dimensional analysis of dropped fuel cooling, COOLFUEL-3D, will be described. Although the latter is not routinely used in refuelling cooling studies, its approach to the CFD modelling of the fuel stringer will form the basis for one of the models that will be used in this project.

1.3.1 Refuelling cooling calculations

During refuelling operations, as during all the plant operations, it is crucial to ensure the integrity of safety-relevant components such as the pin cladding, the graphite sleeve, the pressure boundary seals and, specifically during this phase, the tie bar and the lifting equipment. It is therefore essential to determine the probability of failure of these components during normal operation and following deviations. Since the knowledge of the temperature of a component is one of the prerequisites of the evaluation of its probability of failure, thermal-hydraulic analysis of the fuel stringer during refuelling is a major part of the development of a safety case. A comprehensive procedure for this study is therefore in place at EDF Energy. The methodology relies on a series of computer codes for the required calculation. The output of each solver in the series provides the input of the next. An outline of the work flow is drawn here.[10]

In the first step of the analysis, a system code which models the thermal-hydraulic behaviour of the reactor, **MACE**, is run. In MACE all the reactor channels are lumped in a single channel with average properties. The whole reactor circuit, including the steam generators and the gas circulators, is modelled in the code, which is capable of modelling the presence of air, steam and particles from steam generation faults within the coolant. The system is modelled by a network of control volumes. Exchange of heat and mass between the volumes is modelled through lumped resistances. Equations of balance for mass, energy and momentum are defined and solved for each of the volumes.[10]

The goal of the calculation in MACE is to obtain the pressure and temperature in the hotbox, in the space under the gas baffle dome and in the headers of the reactor channel. These are then input as boundary conditions into **HOSTAGE**, which is used to model a single stringer during the discharge from the reactor, the residence in the FM and in the buffer store and during the handling in the IFD. Since it does not model the whole system, it relies on boundary conditions provided by external calculations carried out, for example, by MACE. HOSTAGE uses a solver, named **HOTWOLF**, to calculate the quantities of interest (temperature, pressure, flow rate) at the nodes and branches of two networks,

one for the flow and the other for the thermal aspect. HOSTAGE controls the boundary conditions passed to HOTWOLF to simulate the conditions encountered during the lift. Heat generation from fission and radioactive decay is calculated using the code **LIFTHT**, incorporated in HOSTAGE, which uses data about the irradiation history of the element and the neutron flux axial distribution.[10]

The computational domain of HOSTAGE covers, beside the stringer, all the fuel assembly and the refuelling channel up to the FM; this requires a coarse discretisation of the fuel elements. In order to achieve a more detailed treatment of the flow and heat exchange within the stringer, the next step in the chain is taken on by the code **STRINGER**, also based on HOTWOLF. It takes as input the values calculated by HOSTAGE for the heat generated in each element, the flow rate through the stringer, the temperature and pressure at the gas inlet and the outer temperature of the sleeve, to calculate the temperatures, pressures and flow rates distribution. Mass and heat exchange within different radial zones is taken into account: a single temperature is associated to each of the concentric ranks of pins. Both the guide tube and the tie bar are discretised with dedicated nodes.[10]

The temperatures obtained from HOSTAGE and STRINGER can then be used to estimate the likelihood of failures of the various components. For instance, the temperature distribution on the tie bar is passed to the **CASBAR** code, together with the irradiation history of the fuel assembly. CASBAR uses a Monte Carlo technique, selecting for a large number of test runs (usually 10^6) a random set of values for the mechanical properties of the tie bar, whose structural integrity is then verified. The number of failures observed, out of the total number of test runs, is used to estimate the probability of failure of the tie bar.[10]

1.3.2 COOLFUEL-3D

COOLFUEL-3D was code for the numerical simulation of the cooling of a damaged fuel stringer in the event of a dropped fuel incident during the refuelling, developed in the 1990s by NNC on behalf of Nuclear Electric.[11]. The software was introduced to provide three-dimensional capability to support the methodology described above. It was implemented as a set of input files and subroutines for the CFD code PHOENICS

Instead of using a body fitted mesh, which would have been extremely resource consuming, it modelled the domain as a porous medium, with an approach similar to those described in section 3.2. It discretised the fluid domain, which covered the stringer and its surroundings, using a coarse mesh, and modelled the effect of the solid bodies, including the fuel pin bundle, the graphite sleeve and the tie bar, by means of experimental correlations for the flow resistance and the heat exchange. Diffusion within the solid was treated separately, and coupling between the solutions was achieved through successive

iterations between the two stages.[11]

Since the main purpose of COOLFUEL-3D was the analysis of cooling of fuel debris, it was capable of simulating several configurations of the damaged fuel, with the centrelines of the fuel pins approximated by piecewise straight segments. The porosity distribution was also modified accordingly. Cracks in the sleeve or misalignments between the fuel elements were modelled through finite radial flow resistances.[11]

The calculation of the flow field was carried out by the finite volume method to solve the Navier-Stokes equations. Buoyancy was treated without recurring to Boussinesq approximation, due to the potentially large temperature variations involved. Turbulence was treated with a simple 0-equation eddy viscosity model, presented in Section 5.2. Friction due to solid components was introduced into the momentum equations as additional source terms, computed by means of empirical correlations (see Appendix B). Heat exchange with the solid surfaces was also modelled through correlations: the methodology had points in common with that presented in more detail in Section 5.2. The solid domain consisted of the discretisation of the fuel pins, the tie bar guide tube and the graphite sleeve. Conduction was simulated using the finite volume method, on a rather coarse mesh, whilst thermal radiation was treated similarly to the method described in Section 3.3.2, but assuming a two-dimensional heat exchange model, where every point irradiates only to points located at the same height.[11]

To conclude this section, it is worth mentioning COOLFUEL-1D, a computational code developed for similar purposes to COOLFUEL-3D, but based on the solution of networks of thermal and flow resistances to model the cooling of intact and damaged fuel. Most correlations used in COOLFUEL-3D were also included in COOLFUEL-1D. A detailed description of COOLFUEL-1D is beyond the scope of this document, although results obtained with the code are compared with the output of POSTR in 6.2.

Chapter 2

Literature review

In this chapter, the current knowledge and practice relevant to the present study and available in literature are reviewed. Section 2.1 reviews the debates on the validity of CFD studies in nuclear safety assessment. In Section 2.2, examples of applications of CFD to flows in nuclear reactor cores are presented. In Section 2.3, CFD methods applied to porous media are reviewed, with special attention to techniques that allow the modelling of complex geometries without the use of body-fitted meshes. Section 2.4 reviews some of the work aimed at investigating buoyancy driven flows established in vertical enclosures, with particular attention to studies concerning flow along fuel bundles. Finally, Section 2.5 provides a summary of the findings of the review, with highlights on how the information extracted has been used in this study and how it can guide future research, as well as identify the gap in knowledge that this Thesis aims to address with its contributions.

2.1 The role of CFD in nuclear safety analyses

The use of CFD for the assessment of safety related flow scenarios in NPPs is not a novelty anymore. Beside the traditional one-dimensional calculations performed using system codes with a long history of validation and regulatory acceptance, CFD calculations are increasingly being submitted to nuclear regulators to support safety assessments concerning both existing and innovative plants.[12]

The application of CFD to industrial problems can follow several different strategies, each with its own specific strengths and weaknesses. One possible approach is based on problem-specific models, which make heavy use of empirical correlations and aim to describe the behaviour of a particular system with limited computational cost. Examples of this philosophy are the so-called coarse-mesh CFD techniques, or models based on the porous medium approximation (see Section 2.3). At the other side of the spectrum are

high fidelity simulations, such as Direct Numerical Simulations (DNSs) and Large Eddy Simulations (LESs) of industrial turbulent flows, which have attracted increasing interest in recent years due to the increase in the computational power available. A third approach, more general than the former but less computationally expensive than the latter, is the use of general-purpose Reynolds Averaged Navier-Stokes (RANS) turbulence models. Examples of studies carried out using these methodologies are presented in Section 2.2.

The fascination with CFD arises from the importance of three-dimensional flow phenomena which cannot be predicted by one-dimensional analysis in some safety related transients.[13,14,15] CFD simulations can sometimes be faster than experiments in providing reliable answers to such problems.[14]

However, obstacles still exist to the widespread use of CFD studies in the regulatory process and for safety studies. For example, Boyd,[12] as late as 2015, describes the "application of CFD in regulatory activities" as "not common". Regulatory agencies bear a critical role in protecting the public, by evaluating and reviewing the analyses submitted by nuclear operators before authorising any practice involving radioactive materials, including the construction of a new NPP. Although there are applications for which the regulatory use of CFD is well established, the non-universality of the models used makes it difficult to extend the techniques employed to other fields: the success is usually due to the availability of application-specific Best Practise Guidelines (BPG), whose development requires lengthy and costly campaigns of verification and validation. These BPG have proved themselves immensely valuable to tackle the specific problems for which they are conceived, but cannot be extended to other applications, which have to be evaluated on a case-by-case basis.[12] An example is given by the set of guidelines published by the United States Nuclear Regulatory Commission (U.S.NRC) for the simulation of the cooling of dry storage casks for spent nuclear fuel.[16]

Early successes in the application of CFD in the nuclear field came from design studies, where the output of simulations has proven valuable in building a qualitative understanding of the physical phenomena occurring in new components. Quantitative information was also used as a guidance for design, although always subject to verification *a posteriori*.[17] This combination of three-dimensional numerical studies and experimental tests has been used in the development of new NPP designs, including the EPR.[14] Safety analyses, on the other hand, especially for licensing purposes, require reliable quantitative data on scenarios which are hypothetical by their nature, since they must predict the response of a system to a potential incident.[17]

In the light of the results obtained by the nuclear and non-nuclear industries in the use of CFD for design purposes, in the early 2000s there was a growing interest from the international community towards the application of three-dimensional analysis to

Nuclear Reactor Safety (NRS) assessment. It was believed that more reliable CFD predictions would help improve the design of safety measures in NPPs, resulting in better protection and lower costs.[14] However, while traditional one-dimensional system codes had a long history of verification and validation, and were considered mature by both the analysts and the regulators, the use of CFD in this field still lacked widespread acceptance. The shortage of experimental data suitable for comparison with CFD results and of shared guidelines for the estimation of errors and uncertainties were amongst the issues the community had to face. In 2002 an international meeting on the "*Use of computational fluid dynamics codes for safety analysis of nuclear reactor systems*" was held in Pisa, Italy, under the sponsorship of the International Atomic Energy Agency (IAEA), to discuss the progress made until then and to set up a strategy to increase confidence in CFD results to a point where they are more widely accepted in the licensing process.[18]

Despite being considered a reliable tool for physical investigation and for helping in the design process, at the time when the meeting took place safety studies were still predominantly based on the results of one-dimensional analyses carried out on thermal-hydraulic system codes. Use of CFD was limited to qualitative studies, but even so its results were deemed to be very useful, in particular to identify issues and flow behaviours which required further investigation. The potential of this methodology was then already recognised, and although it was clear that CFD could not replace experiments altogether, it was understood that it could reduce the number of experiments needed for studies concerning new designs. A recurring theme during the meeting was the potential use of CFD beside system codes, to cover situations where three-dimensional aspects cannot be neglected. In situations like these, the very assumption of conservativeness of the one-dimensional calculation can be questioned, since three-dimensional effects may well aggravate the predicted scenario. It was suggested that efforts be undertaken to integrate system code with CFD software, which could prove useful in complex situation.[18]

However, it was pointed out that, for their use to be accepted in regulatory activity, improvements were needed in physical modelling, as well as in reducing the influence of user's experience and in the evaluation of uncertainties, which needs to accompany every calculation submitted in support of a safety assessment. It was recognised that, having overcome these issues, CFD would prove invaluable in providing knowledge on safety related issues with a better estimation of safety margins than the traditional methodologies.[18] The participants to the meeting agreed that, to extend the success of CFD from fundamental research to safety assessment, a set of BPG needed to be established. These guidelines would minimise the influence of the user experience, contributing to the reproducibility of the results; they would also make it easier to maintain expertise in the field.[18]

It was recognized that the results of a calculation are only as reliable as the physical

model they are based upon. The common perception was that dedicated experimental campaigns, designed to provide data for code validation were needed to build confidence on these models. Beside providing accurate local measurements to make the data suitable for comparison with CFD results, the control of the initial and boundary condition was deemed crucial for these experiments.[18]

The optimism of the participants was, however, limited to the application of CFD to single-phase problems, whose models were considered sufficiently mature at that time. Two-phase models were deemed to be still in their childhood, and further research was considered necessary before their use for safety analyses could be accepted.

In his opening address to the meeting, Reocreux attempted to outline a classification of the available codes and the computational strategies, as well as to identify the requirements of CFD calculations for safety assessment. According to Reocreux, acceptance of the results of a calculation for safety assessment depends on three prerequisites, namely *reproducibility*, *assessment* and *traceability*.[17]

The results are *reproducible* if they can be obtained when the same simulation is carried out by different users, on different machines, even at years of distance. To guarantee reproducibility of its results, a CFD code must have a "frozen" released version and minimize user effects, which could imply keeping the number of available option to a minimum or providing guidance to constrain users' choice.[17].

During the *assessment* of the results it should be verified that the model is correctly implemented in the code, that it is capable of predicting the relevant phenomena and that the case under analysis falls into the domain of applicability of the code. The modelling assumptions and limitations should be discussed in detail. Comparison with experimental data should verify that the model is capable of predicting basic phenomena as well as the global behaviour of the flow. Moreover, numerical effects should be thoroughly quantified to ensure that convergence of the results has been achieved and that numerical artefacts are negligible.[17]

Traceability of the results is ensured by the presence of a documentation covering all the aspects that have an influence on the results, including the description of the code, the assessment procedure and its conclusions, and the guidelines followed while performing the analysis.[17]

In reviewing the calculation strategies used at the time in the practise of CFD, Reocreux concluded that to conduct a computational study which can be accepted in a safety assessment, it is not sufficient to introduce conservative assumptions in the model or in the boundary condition if the actual margin of conservatism cannot be estimated. The suggested approach, called *Best Estimate calculation*, consisted minimizing the uncertainties from the beginning, wherever possible, by using the most accurate model available, then conducting an uncertainties evaluation analysis to quantify the accuracy of the

result.[17]

However, the desired accuracy of the models requires thorough validation, which in turn relies on the availability of experimental data which consist of a set of accurately measured local data distributed on a sufficiently fine grid. The necessity to invest in experimental programs of this nature, and in campaigns of verification and validation to select the most promising models and improve confidence in them was frequently stressed during the 2002 meeting.[18] The outcome of the ECORA project,[14,15] started in 2001 with the participation of several European industries and research institutions under the sponsorship of the European Community, represented a first step in the path drawn during the meeting. The goal was to provide a solid base for the use of CFD in safety assessment, particularly in the simulation of flows in the primary coolant system and in the containment of nuclear reactors, both existing and under development. A major achievement was the development of a set of BPG for the validation of CFD results.[14,15]

The purpose of the BPG was to provide guidance for the verification and validation of CFD results, providing a common ground at European level for the evaluation of the quality of submitted calculations. *Verification* was defined as the process of checking whether the model is implemented correctly, while *validation* was defined as the process of comparing the prediction of the model against experimental data. The existence of a set of criteria shared at a European level was believed to lead to an increase in confidence in the results, and arguably in economic savings. A secondary scope of the BPG was to provide tools for the estimation of computational resources and time needed for a simulation, to discriminate between applications which are within reach from those that are not.[14]

The first application of the BPG was in the course of the programme itself. The production of the guidelines was the first step of ECORA and all the subsequent work made in its frame employed them. Special sections were included in the BPG for exclusive use in ECORA, including templates for the project's internal reports. To allow for their use outside of the programme, the BPG were made available on the internet and kept open to external contributions, to keep them up-to-date with the results of the latest research.[14]

The BPG developed by the ECORA team were structured in the following way:

1. Sources of errors in CFD calculations, namely numerical errors, modelling uncertainties, software errors, application uncertainties.[14,19]

2. General guidance for the use of CFD, including geometry and mesh generation.[14,19]

3. Guidelines for the evaluation of existing CFD calculations.[14,19]

4. Guidelines for the choice of experimental data for verification and validation, the quality of which is essential for the correct evaluation of the results.[14,19]

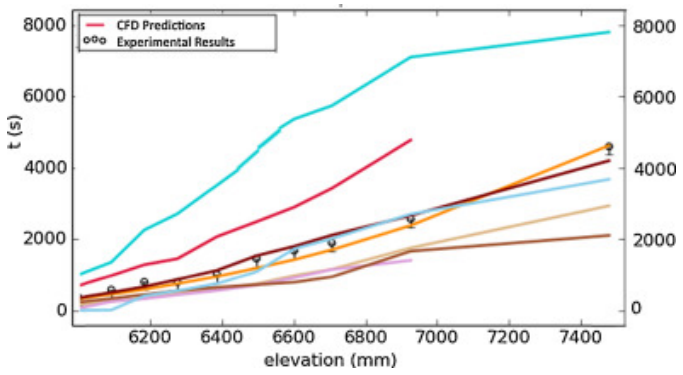

Figure 2.1: Findings of the 2014 benchmark presented by Boyd.[12] The solid lines show the predictions obtained by different participants to the benchmark, the circles represent experimental data. The plot presents erosion times of a gas layer (y-axis) at different vertical position in the test rig (x-axis).

5. Special guidelines for ECORA.[14,19]

The main concept was to minimise all the errors due to the factors other than the model, in order to verify its agreement with the physical phenomena.

The rigid application of the guidelines requires several calculations on grid which can be very large; for complex cases the available resources may not be sufficient to follow the procedure strictly. In some cases involving free surface flows, it was observed that the strict application of the guidelines for mesh refining could create convergence problems. Compromise is then necessary in most applications, following the guidelines in more or less detail according to the complexity of the problem in order to keep the computational time and resources within reasonable limits.

Despite the progress made in the ten years since the end of the ECORA programme, obtaining reliable, high quality, solution from CFD, suitable for use in safety assessment, is still a challenge. In his 2015 paper, Boyd presented the point of view of the nuclear regulator on the matter. As a striking example of the challenges still encountered by safety analysts, he presented the results of a blind benchmark campaign carried out one year before. The study concerned the prediction of the erosion time of a layer of stratified helium from a vertical jet, and its comparison against data from a large scale experiment. The computational results were spread in a range between $50\,\%$ and $200\,\%$ of the experimental data, despite the geometry and the boundary and initial conditions being very well documented. For real plant scenarios the variations can be expected to be even broader.[12]

Nevertheless, progress had been made in the preceding years, especially for what concerns the availability of data suitable for verification and validation. However, not all the potential applications benefit from these developments. Some scenarios still lack full benchmark data. Experimental programs are usually expensive and time consuming and

are often not compatible with the time and resources constrains that exist in industrial practice. Furthermore, when data is available, there are issues that can complicate the validation process. Good agreement with experimental data does not eliminate all the doubts when the real component is modelled: the size is different, and the boundary and initial conditions are seldom completely known. Sometimes good agreement with the experiment is due to the combined effect of two or more errors that cancel each other: when the conditions change their relative weight may vary, causing the model to fail.[12]

The size and complexity of nuclear components make it necessary to make assumptions and simplifications. If common guidelines for the specific problem are not available, the success of the approach relies on the analyst's experience. Moreover, all the assumptions must be carefully reviewed by the regulator before the assessment is accepted. Without recognised guidelines, this review must be performed on a case-by-case basis. Instead, where BPG are available, they provide an accepted methodology which facilitate both the production and revision of the results. However, their development takes years, requiring large amounts of experience and dedicated programmes.[12]

Moreover, even when they are available, their strict application can still be impractical due to resources constrains. Traditional methods for uncertainty evaluation, in particular, may require a large number of calculations. Experience and common sense are still required in order to make compromises.[12]

2.2 CFD modelling of flows in nuclear reactors

In Section 2.1 the problem of the trustworthy application of CFD techniques to Nuclear Reactor Safety studies, especially for their acceptance in regulatory environments was presented. We have seen how the recommendations of the ECORA project, as well as those of professionals of the regulatory agencies like Boyd, focus on the importance of verification and validation of numerical results for them to be trusted as part of a safety assessment. This may be somewhat difficult, especially for large scale problems, but it is essential to chose the "right" approach, the one which allows reliable predictions to be achieved at an affordable computational cost.

As an example, Rohde et al.[20] applied the BPG established by ECORA to validate a number of studies concerning mixing phenomena in the primary circuit of Pressurized Water Reactors (PWRs), comparing their results with experimental data obtained in test facilities. The calculations involved a range of RANS models in coarse meshes, with some of the simulations including porous region to model the effects of complex component such as grids. The authors reported problems in achieving the requisites of the BPG: in particular, they never managed to achieve mesh independence with the resources they

could employ. This made some of their results difficult to interpret. They were nonetheless able to identify the limits of some of the simplifications adopted, for instance neglecting diffusion in cold slug transport problems. They also pointed out the inadequacy of the porous approximation used, although they suggested this could be due to the choice of an isotropic equivalent porosity. In the following a selection of work that is aimed at investigating the validity of certain CFD approaches for specific problems is discussed. A vast literature exists on the topic, which presents approaches ranging from relatively simple RANS models to LESs and even some attempts at DNS.

Turbulence modelling for arrays of rod bundles There are not many computational works on AGRs in the open literature, especially for what concerns the flow in the fuel elements. The attention will then be oriented mostly to general studies on flows over rod bundles and to application to water cooled reactor, with wide space given to studies on Pressurized Heavy Water Reactors (PHWRs) of the CANDU type, whose geometry is the closest to that of interest here.[a]

In most existing reactor designs the fuel is found in form of rod bundles, with various arrangements, where the coolant flows parallel to the pins. Therefore the flow along an infinite regularly spaced array of pins can be used as an abstraction for the flow in reactor cores, a scenario where fundamental phenomena found in reactor flows can be investigated. One of these features, which is typical of non-circular channels, is the occurrence of secondary flow patterns perpendicular to the main flow, driven by the anisotropy of normal Reynolds stresses(Figure 2.2). The intensity of these flows can vary broadly (velocities as high as $2\,\%$ of the main flow velocity have been observed)[22] but their effect on the flow, concerning for instance the distributions of the wall shear stress and axial mean velocity, is non-negligible. Simple Eddy Viscosity Models (EVMs) fail to model the anisotropy of the Reynolds stresses, and are therefore unable to predict the secondary flows, which results in distorted predictions of the flow field. The work of many authors has been directed towards the identification of an accurate and efficient turbulence treatment which correctly predict this behaviour.

Rapley and Gosman[22] presented a set of simulations of an infinite triangular array of rods, with various pitch-to-diameter ratios. They performed a steady state calculation of fully developed flow in one sixth of a sub-channel, at Reynolds numbers between 27000 and 49000, comparing their results with previous experimental data. They chose an approach based on the $k-\varepsilon$ model as turbulence treatment, but in order to account

[a] In particular, in the 37-pins version of the fuel element of a CANDU the arrangement of the pins is the same as in AGRs. The dimensions, however, are different, the CANDU pins being shorter and more closely packed.[21] Moreover, the fuel element does not have a sleeve, the flow boundary being the inner wall of the pressure channel, the central position is occupied by an active pin, and its orientation in the reactor is horizontal instead of vertical.

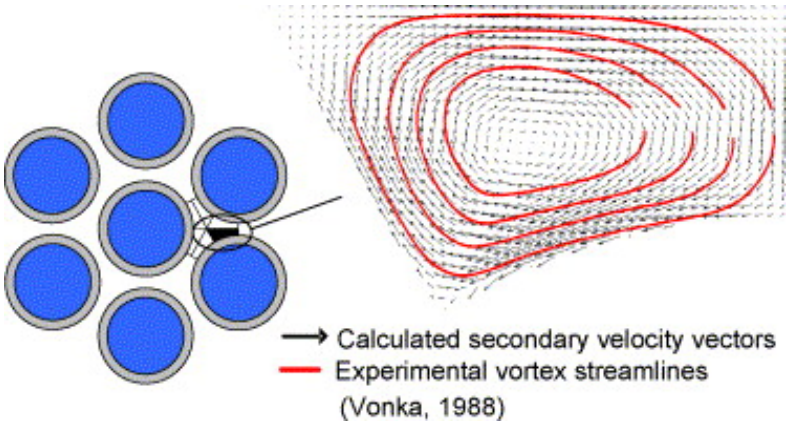

Figure 2.2: Secondary flow in a sub-channel of a triangular array of cylinders. Image from ref. [23]

for the anisotropy of the turbulent stresses, they modelled them by a set of algebraic expressions, based on simplifying assumptions made for square ducts. They obtained good qualitative agreement with the experiment, with variable success on quantitative predictions. The comparison between the model results and those obtained by suppressing secondary flows, in particular, showed well how strongly they contribute to the wall shear stress and the mean velocity profiles. Lee and Jang[24] studied a similar problem, at a Reynolds number of 27000, assuming, for the Reynolds stresses, a non-linear dependence from the strain rate tensor. This *non-linear* $k-\varepsilon$ model, which was paired with a Low Reynolds Number (LRN) approach to wall treatment, also provided results in rather good agreement with experimental data. However, turbulence in the gap between the rods was under-predicted, which was put in relation with unsteady phenomena out of the reach of the steady-state approach used.

Baglietto and Ninokata[25] chose a different formulation of the *non-linear* $k-\varepsilon$ model to tackle an analogous problem, comparing the results with those of linear EVMs such as the linear $k-\varepsilon$, $k-\omega$ and $k-\omega$ SST. Although the predictions of the non-linear model were slightly closer to the experimental data used for the validation, at first it underestimated the intensity of the tangential velocities. Thus, the model did not predict significant differences in the distributions of the wall-shear stresses and the mean velocity until they increased one of the coefficient in the expression for the Reynolds stresses, the one responsible for the secondary motion. After this modification the model results were in good agreement with the experimental data, except at low Reynolds number, where only the qualitative trend was caught. The model was later applied to cases at different Reynolds numbers (between 39000 and 181000) in a subsequent paper,[23] where good agreement was found with experimental data, again except at the lowest Reynolds number. Again the discrepancy occurred close to the gap,which was associated with unsteady phenomena (periodic structures transported streamwise). To verify this hy-

pothesis a "DNS" simulation was performed, whose mesh, however, did not resolve the Kolmogorov length scale. Despite the coarseness of the mesh, the agreement between the results and the experiment was considered satisfactory, although the simulation did not give the expected information on the nature of the unsteady phenomena in the gap between the pins.

Chang and Tavoularis[26] performed a computational study on a more realistic geometry, modelling a 60° sector of a scaled model representing a 37-pins CANDU fuel element. They distanced themselves from the studies cited above by choosing to abandon two-equation turbulence models to employ a Reynolds Stress Model (RSM). The rationale of the decision laid in the propriety of the RSM to account for the Reynolds stresses anisotropy without the need for geometry dependent assumptions, since a transport equation is solved for each of them. Moreover, having in mind the limitations of steady-state simulations pointed out by Lee and Jang[24] and Baglietto, Ninokata, and Misawa,[23] they chose to perform an unsteady calculation. The results were compared with experimental data from an in-house test facility, which differed from the computational model in that it only represented a single sub-channel of the fuel element, and they were found in good agreement with them. The boundary conditions were chosen in order to match the Reynolds number in that sub-channel, which was around 40000. Also, the solution of the time-dependent equations allowed to observe the periodic turbulent structures occurring in the gap region.

As the computer power becomes more affordable, the use of LES becomes practicable for the study of flows in relatively complex geometries. Abbasian, Yu, and Cao[27] presented a comparison between the performances of LES, RSM and Detached Eddy Simulation (DES) applied to the flow through a 43-pins fuel element of a CANDU. The DES simulation employed a $k - \varepsilon$ model in the near wall region while modelling the bulk of the flow using a LES. The computational domain included an inlet and an outlet region, in the form of a straight circular pipe. The solutions were validated with high frequency pressure measurements at the wall taken at a test rig built for the purpose. It was found that all the models performed well in the prediction of the mean value. However, the LES performed clearly better than the other methods in the prediction of the root mean square and of the power spectrum of the pressure fluctuations, while the DES proved superior to the RSM. On the other hand, the latter ran at twice the speed of the LES, whilst the DES placed itself in between thanks to the use of a relatively fast RANS model along the wall.

The studies reviewed above point out the necessity of accounting for the anisotropic and transient behaviour of turbulence in order to provide reliable predictions for the flow along rod bundles. However, this fact is still not universally acknowledged by the nuclear thermal-hydraulics community: Benhamadouche[28] considered the current (2017) use of CFD in Nuclear Engineering with particular focus on Unsteady RANS (URANS) and

LES applications, and pointed out that, alongside many good practices now consolidated, there are still numerous studies based on techniques which are inadequate to the problems studied. While recognising the validity of EVMs in several applications, especially for the determination of global quantities, the contribution criticised their use in scenarios where the anisotropy of the Reynolds Stress Tensor (RST) is significant enough to alter the main flow features. On the other hand, the inferior performances of the advocated RSMs compared to EVMs, which had been reported by some workers, were linked to their sensitivity to weaknesses in the numerical methods employed. It was suggested that increased usage of the model is necessary to develop a collective base of expertise, which in turn would contribute to the establishment of RSM as a mature tool for engineering use.[28] The study also highlighted the superiority of wall resolved RANS over the use of wall-functions and stressed that unsteady features predicted by URANS approaches should be critically examined, as in many cases they were found to be spurious numerical effects.[28]

Benhamadouche[28] also pointed out the need for an increased use of LESs and DNSs in nuclear application. However, Merzari et al.[29] highlighted the fact that time resolved LES of large systems will continue to require lengthy calculations, due to the separation between the smallest and largest time scales, which can amount to several orders of magnitude. According to the authors, the sheer number of time steps required to simulate a slow transient can make the simulation impractical even with the increase in computational power expected in the future, unless specific numerical techniques are used to accelerate the simulations. These techniques would, however, require significant validation effort to ensure the accuracy.[29]

The studies reviewed above highlight the challenges posed by the peculiar geometry of arrays of pins to the numerical simulation of flow along them. It is clear that simple EVM do not tend to give accurate predictions, due to their incapability to take into account the anisotropy of the Reynolds Stresses in the sub-channels of a fuel bundle and consequently to predict the secondary flows that anisotropy induces. It was noted how relatively good results have been obtained by using algebraic corrections to the $k - \varepsilon$ model to include this effect. However, such an approach rather lacks in generality, as pointed out by the worsening of its performance at low Reynolds numbers in the studies by Baglietto and Ninokata.[25,23] The necessity of time-resolved simulations to take into account the unsteady flow phenomena that can occur in these domains was also noted. The study presented in Chapter 4 was carried out using a Large Eddy Simulation, a technique that fulfils both of the requirements identified in this review.

Effects of spacers and braces on the flow A number of studies addressed the effect on the coolant flow of the presence of spacing grids and braces, structural components

found in all designs of nuclear fuel assemblies. As described in Section 1.1, three such grids are found in each of the eight fuel elements of an AGR fuel stringer. Although in the studies presented in this work the modelling of these structures has not been attempted, a short exploratory review of the literature on the subject has been undertaken, and could form a starting point for future investigation.

The test facility used by Abbasian, Yu, and Cao[27] provided the validation data to the simulation of the flow through two 43-pins CANDU fuel elements by Zhang and Yu[30]. The study's objective was to obtain data about the causes of vibration in the fuel. Their computational domain included the end-plates holding the fuel rods at the ends. The vortex shedding caused by the inlet end-plate was found to be the main contribution to the pressure power spectrum, thus proving itself the main concern for mechanical vibrations. The effect of the end-plate in a 37-pin fuel element was later investigated by Bhattacharya, Yu, and Kawall[31], who made analogous observations. They also observed the lack of tangential periodicity in the flow field, which was put in relation with the geometrical peculiarity of the domain.

The studies cited above warn about the flow complications introduced by the presence of a spacer. Its obstructing effect causes vortex shedding, which requires the use of a time-resolved simulation to capture its influence on the flow. Moreover, the geometry of the spacer can alter the flow pattern far downstream of the spacer itself, and can introduce non-periodicity in a domain that would otherwise be periodic, thus preventing the use of geometric simplifications.

More recently (2015), LES was employed by Chang and Tavoularis[32] to model the flow across a spacer grid provided with mixing vanes in a square-lattice rod bundle. The study was submitted as part of an international blind benchmark exercise against laser-Doppler velocimetry data from an experimental facility operating at the Korea Atomic Energy Research Institute (KAERI). LES itself was used to model the flow in the vane region, while, to save memory, in the rest of the domain a relatively new approach named Scale Adaptive Simulation (SAS) was employed, which behaves as the LES in the regions of flow detachment and as an unsteady RANS everywhere else. The final mesh comprised of more than 40 millions elements. This approach was able to provide a detailed description of the flow structures downstream the spacer (Figure 2.3), and allowed the predictions of this study to be judged the best overall amongst the participants to the benchmark, with high ranking in all the parameters considered. The study points out to the complexity of the flow patterns that can be observed in real nuclear reactor cores and the challenges they pose to the analyst. Novel computational techniques, as that employed by Chang and Tavoularis[32] have the potential to reduce the numerical burden of performing detailed simulations of these flows while still retaining the high level of accuracy required to gain an insight on the phenomena that characterise them.

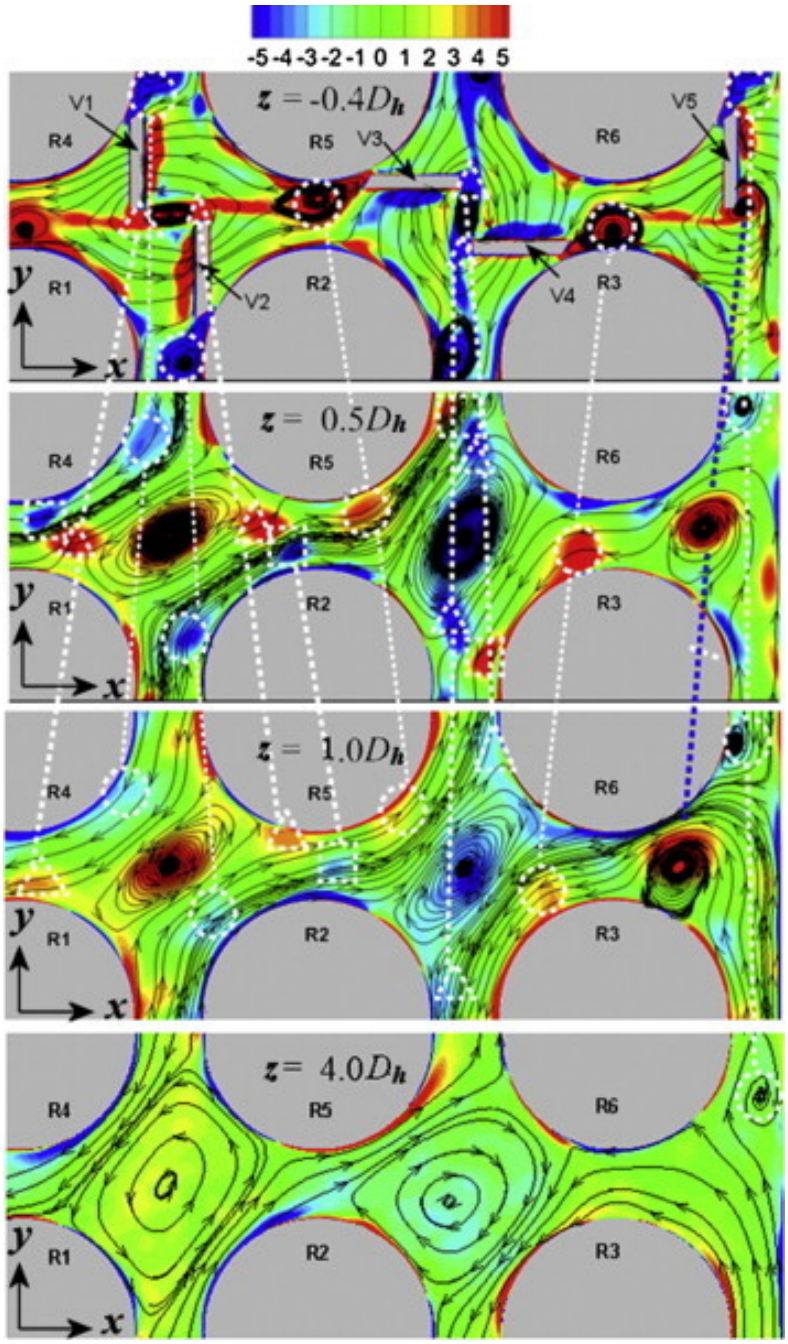

Figure 2.3: Stream-lines of the cross-sectional flow calculated by Chang and Tavoularis,[32] highlighting the complexity of the flow structures induced by the mixing vanes. The colours represent the time-averaged stream-wise vorticity $\overline{\omega}_z$.

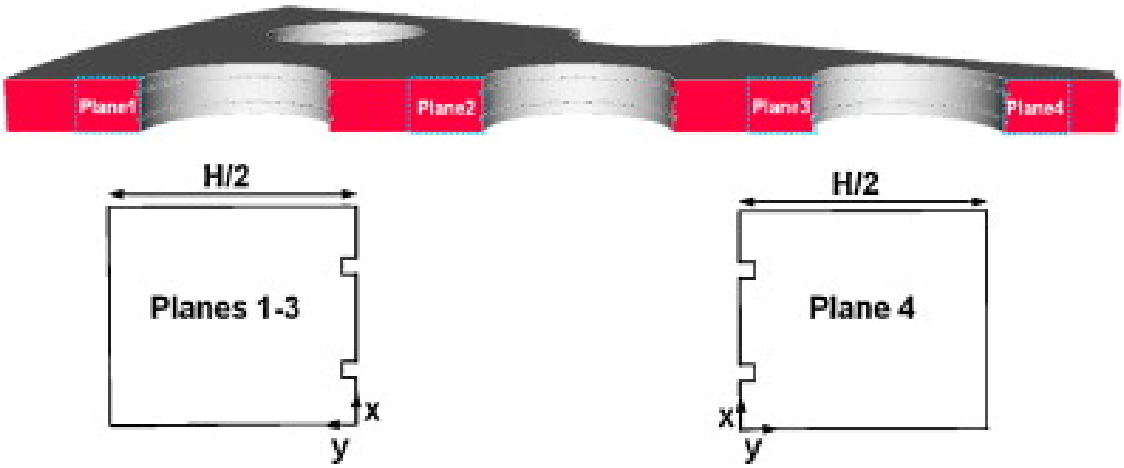

Figure 2.4: Geometry considered by Keshmiri,[9] with details of the simplified ribs.

CFD studies on AGRs It is now worth looking at two works regarding the object of this project, the AGR fuel stringer. The first one, by Keshmiri,[9] describes a numerical simulation of the flow through the fuel pin bundle of an AGR, whilst the second, by He and Gotts,[33] concerns the flow in the annular gap between the moderator and the graphite sleeve of a fuel stringer. Keshmiri,[9] performed a three-dimensional simulation in a 30° sector of an AGR fuel element. Contrary to the geometry simulated by Chang and Tavoularis,[26] the span of the sector required the use of symmetry,instead of rotational periodicity, boundary conditions, while translational periodicity was imposed on the streamwise direction. A steady-state Low Reynolds Number RANS model was chosen, namely the $k - \varepsilon - v^2 - f$ model, after it proved the best performing of a set of EVM in a series of preliminary two-dimensional calculations.[34] The main feature of the study was the inclusion, in the model of the pin walls, of a pair of parallel ribs to take into account, in a simplified manner,[b] of the roughness of the AGR pins mentioned in Section 1.1. The unavailability of suitable experimental data prevented a proper validation of the results, although a comparison between the computed value of the friction factor was found to be in good agreement with an experimental correlation. Contour maps for the stream-wise velocity and the temperature are shown for the channel cross section and for the near wall area, with particular attention to the recirculation area downstream of the ribs. The highest velocities are found, unsurprisingly, in the sub-channels centres, while the velocities are higher along the pins and lower along the sleeve and the guide tube. It is worth noting, nonetheless, that the use of an EVM may have missed the dumping effect of the secondary motion described in the works reviewed above.

He and Gotts[33] performed a conjugate heat transfer analysis of a moderator brick, the graphite sleeve of a fuel stringer and the flow through the annular gap between them

[b]The actual roughness, in real plant pins, currently consists in 12 helicoidal ribs winding around the pins, at an angle above the horizontal of about 50°.

to study the occurrence of hot spots in scenarios where the gap becomes eccentric due to deformation of the stringer. A standard $k - \varepsilon$ model was used for turbulence. The coolant flow in the stringer and in the spaces between the bricks were represented as boundary conditions, which required an iterative approach due to the dependence of the gas temperature along the fuel from the heat flux through the sleeve. The cases studied varied for the degree of deformation and included scenarios where the sleeve and the moderator entered into contact for a certain length. The short distance between the walls in most scenarios required modifications to the turbulence model in order to account for the fact that, even in the smallest gaps, laminarisation was prevented by the roughness of the wall. The results were validated against data available for simpler geometries and for the concentric case, and reasonable agreement was found overall, with few exceptions. The analysis of the eccentric cases showed that, even in the extreme scenario, where the stringer bending is the maximum allowed by the physical constrains, the deviation of the graphite temperature from the design case, albeit significant (up to $70\,^{\circ}\mathrm{C}$), does not cause concerns for the integrity of the moderator. The problems faced by the authors are likely to be found in studies concerning the cooling of damaged fuel, where deformation and dislocation of pins can bring their roughened walls close to each other, forming narrow passages where residual turbulence could still be observed.

In the studies presented in this Thesis, High Reynolds Number (HRN) RANS methods are employed to simulate forced flow through a pin bundle (see Section 6.1) and compared to the prediction of the coarse-mesh model presented in Chapter 5. Simulations of natural convection along an enclosed bundles were performed using wall refined meshes, with an LES model employed for turbulence treatments.

In the next section, the treatment of porous media in CFD simulations will be reviewed, with particular attention to their use to approximate complex geometries in nuclear systems.

2.3 CFD modelling of porous media

In Section 3.2 the spatially filtered equations that govern the flow in porous media and the procedure followed to obtain them, are presented. In this section, a number of computational studies based on that methodology is reviewed.

Many studies were directed towards the development of turbulence models suitable for simulating turbulent flows in porous media. Masuoka and Takatsu[35] developed a zero-equations model for porous medium which consists of a packed bed of spheres. The model was based on the assumption that the dynamic turbulent viscosity μ_t can be decomposed into the sum of a component due to the blocking effect of the particles and one related to the vortices occurring in the inter-particle spaces. An algebraic formula was proposed for μ_t, which was considered to be proportional to the norm of the time-averaged velocity $|\bar{v}|$ and $\sqrt{K}$, where K is the permeability of the porous medium. The momentum equation used in that work was derived under some simplifying assumptions, among which was the hypothesis that the pressure loss in the porous medium can be represented by a term given by the Darcy's Law and one due to turbulence. This assumption was challenged by Nield,[36] who observed how the pressure drop deviates from Darcy's Law at Reynolds numbers much lower than those associated with turbulent flows.

Nakayama and Kuwahara[37] chose to adopt an EVM approach using a $k-\varepsilon$ model. The expression for the macroscopic turbulent kinematic viscosity $\nu_{t,\gamma}$ defined from the relation $\nu_{t,\gamma}\,{}^{i}\langle S_{ij}\rangle = {}^{i}\langle \nu_t S_{ij}\rangle$, mirrored the one used in the standard $k-\varepsilon$ at the microscopic scale, assuming thus:

$$\nu_{t,\gamma} = C_\mu \frac{{}^{i}\langle k\rangle^2}{{}^{i}\langle \varepsilon\rangle} \tag{2.1}$$

The expressions for the production and dissipations terms in the k and ε equations were tuned using the steady state results of a simulation in a body fitted mesh of transverse flow over an array of square rods. The capability of the model to predict the evolution of the turbulence level of the flow toward equilibrium was tested, with good agreement especially further from the inlet. Pedras and Lemos[38] proposed a very similar model, which differed only for the expressions for the production and dissipation terms. The model was tuned using the solution of a detailed calculation, in this case, of flow over an array of circular rods. The results, compared with the data by Nakayama and Kuwahara[37] were found in relatively good agreement, with the differences put in relation with the differences between the geometries.

Chandesris, Serre, and Sagaut[39] developed a $k-\varepsilon$ model closely inspired by those of Nakayama and Kuwahara[37] and Pedras and Lemos,[38]. They derived expressions for the source and sink terms in the equations for the turbulent quantities specifically for

longitudinal flow, adapted therefore to simulate arrays of channels or flows along rod bundles, as in nuclear reactors cores. The constants of the model were determined by comparison with DNS, RANS and experimental data, and the model itself was found to predict well the turbulence development in a plane channel, for which the reference values were the results of a RANS simulation, and in a fuel bundle, where it matched well with experimental data from a test facility.

A different approach was used by Drouin, Gregoire, and Simonin,[40], who developed a three-equation model, based on the balance of ${}^{i}\langle\bar{k}\rangle$, the macroscopic turbulent kinetic energy, E_m, the kinetic energy associated with the sub-filter deviatoric components, and ${}^{i}\langle\bar{\varepsilon}_w\rangle$, called the "wake dissipation", the sink term for E_m. An algebraic expression was instead proposed for ε. A general methodology for the calibration of the model constants was also presented. The predictions of the model were compared with the solutions of a LRN $k-\varepsilon$ model, and were found to be in better agreement with other models for what concern the development of the flow, especially for the cases where the inlet turbulence was more intense than the asymptotic value. The advantage of the model was identified in the calibration procedure which paid attention to the development of the flow beside the equilibrium values as in the works reviewed above.

Jin and Kuznetsov[41] proposed an alternative treatment for turbulence in porous media, based on the hypothesis that turbulent effect on scales larger than the pores size are negligible. In particular, they assumed that the Reynolds stresses do not contribute significantly to the macroscopic momentum transport, and that the production and dissipation of the turbulent kinetic energy k occurs mainly within the pores themselves, making an equation to model its transport unnecessary. They verified their assumption by carrying out a DNS of turbulent flow in a simple porous domain, which consisted of an array of equally spaced spheres, with the porosity in the range 0.69-0.8. Lower values of the porosity were reportedly investigated in previous studies. The simulation was carried out using a Lattice Boltzmann Method. The results obtained seemed to confirm the initial assumptions, and were employed to develop and validate a mixing length turbulence model which incorporate the turbulent effects in the drag term, rather than as an equivalent viscosity. Despite the encouraging findings, it was admitted that the proposed model would require further investigation before its applications to more complex scenarios.

To close this section, it may be worth mentioning a few works concerning the use of the porous medium approximation to model complex nuclear reactor components. Chantelot[42] used Code_Saturne and SYRTHES (see Section 3.3) to investigate the temperature distribution of a steam penetration in the core of an AGR. A porous medium was used to model the effect of the "bobbin", a complex component having the purpose of protecting the penetration from the hot gas in the core. The heat exchange in the porous region was simulated by defining an additional transport equation for the solid domain,

as opposite to the volumetric coupling with SYRTHES which was judged problematic. Thermal non-equilibrium between the solid matrix and the fluid was taken into account using the model proposed by Nield,[43] which accounts for the anisotropy of the matrix.

Fiorina et al.[44] discussed the development of a multi-physics code for nuclear reactors analysis based on OPENFOAM, in which the thermal-hydraulic solver makes use of the porous medium approximation for the core region. The CFD model used was based on the Darcy velocity $v_{Di} = \gamma v_i$ which, together with certain simplifying assumptions, avoided the numerical oscillations usually found at the interface between porous and clear regions. The turbulence model used was a standard $k-\varepsilon$, which was modified to converge to some pre-set values for the turbulent quantities to be estimated from experiments or other considerations. A finite difference solver for the fuel and cladding temperature was included, coupled with the fluid region in similar fashion to that described in Section 5.2.4. The solver was successfully compared with the output of a well-validated one-dimensional system code, although a number of weaknesses were identified and made the target of future work.

Capone, Benhamadouche, and Hassan[45] adapted a technique used previously to couple RANS and LES calculations to model the effect of a spacer grid equipped with mixing vanes. The method requires the availability of a detailed solution, which is then interpolated in a coarser mesh; the latter is then used in the following calculations, during which the local tangential velocity and the Reynolds stresses are forced to the values previously calculated by additional source terms.

2.4 Natural convection in vertical enclosures

Natural convection in enclosures, defined as fluid regions entirely surrounded by walls, is found in a large number of industrial contexts, such as ovens and furnaces, energy storage devices, thermal insulation in buildings, chemical reactors[46] or, in the nuclear industry, spent fuel storage pools and shipping casks,[47] as well as passive heat removal systems.[48] This broad range of applications has driven the interest of researchers for decades and an overwhelming number of studies have been produced. The scope of this review is mainly limited to work concerning natural convection along enclosed fuel bundles, complemented by studies regarding simpler geometries, such as vertical annular and rectangular cavities.

Natural convection in vertical enclosures, i.e. enclosures in which heat is provided and removed through vertical surfaces, can establish a number of flow regimes, depending on the values assumed by the relevant non-dimensional parameters. These parameters are identified by means of non-dimentional analysis, such as manipulation of the

governing equations under simplifying assumptions.[85] For rectangular and annular cavities, these parameters can be identified as:[49]

- The Prandtl number Pr:

$$\mathrm{Pr} = \frac{\nu}{\alpha} \tag{2.2}$$

  where ν is the kinematic viscosity and α is the thermal diffusivity of the fluid. It represents the ratio between the transport by diffusion of momentum and thermal energy, which translates in the relative thickness of the velocity and temperature boundary layers — the higher Pr, the thicker the velocity boundary layer compared to the temperature boundary layer.

- The Rayleigh number Ra, which in the case of imposed temperature at the wall can be defined as:

$$\mathrm{Ra} = \frac{g\beta\Delta T L^3}{\nu\alpha} = \mathrm{GrPr} \tag{2.3}$$

  where g is the acceleration due to gravity, β is the volumetric expansion coefficient, ΔT is the temperature difference between the walls and L is the width of the gap. Gr is the Grashof number, which represents the ratio between buoyancy and viscous forces. Criteria for transition to turbulent natural convection are given in terms of Ra.

- The aspect ratio $a = H/L$, where H is the height of the cavity.

- For annular cavities, the radius ratio $\eta = R_i/R_o$, where R_i and R_o are respectively the inner and outer diameters. The latter two parameters account for the influence of geometry on the flow regime.

The challenging nature of turbulent natural convection Countless researchers have investigated the features of the flow in vertical enclosures and their heat transfer performances. Many studies have been targeted at simple geometries such as rectangular or annular enclosures, where fundamental phenomena can be observed with relatively simple experimental facilities or numerical models. The approximate range of conditions explored is shown in Figure 2.5. Despite the interest attracted and the long history of the studies on the topic, however, the numerical simulation of turbulent buoyancy driven flows still poses challenges to the scholar, due to the peculiarities of the physical phenomena involved.

An extensive and somewhat dim exposition of the many challenges posed to the effective modelling of turbulent natural convection in enclosures was given by Hanjalić and Vasić.[50] Amongst the difficulties identified by those authors were: the presence of complex interactions between the near wall region and the core of the domain, which hinders

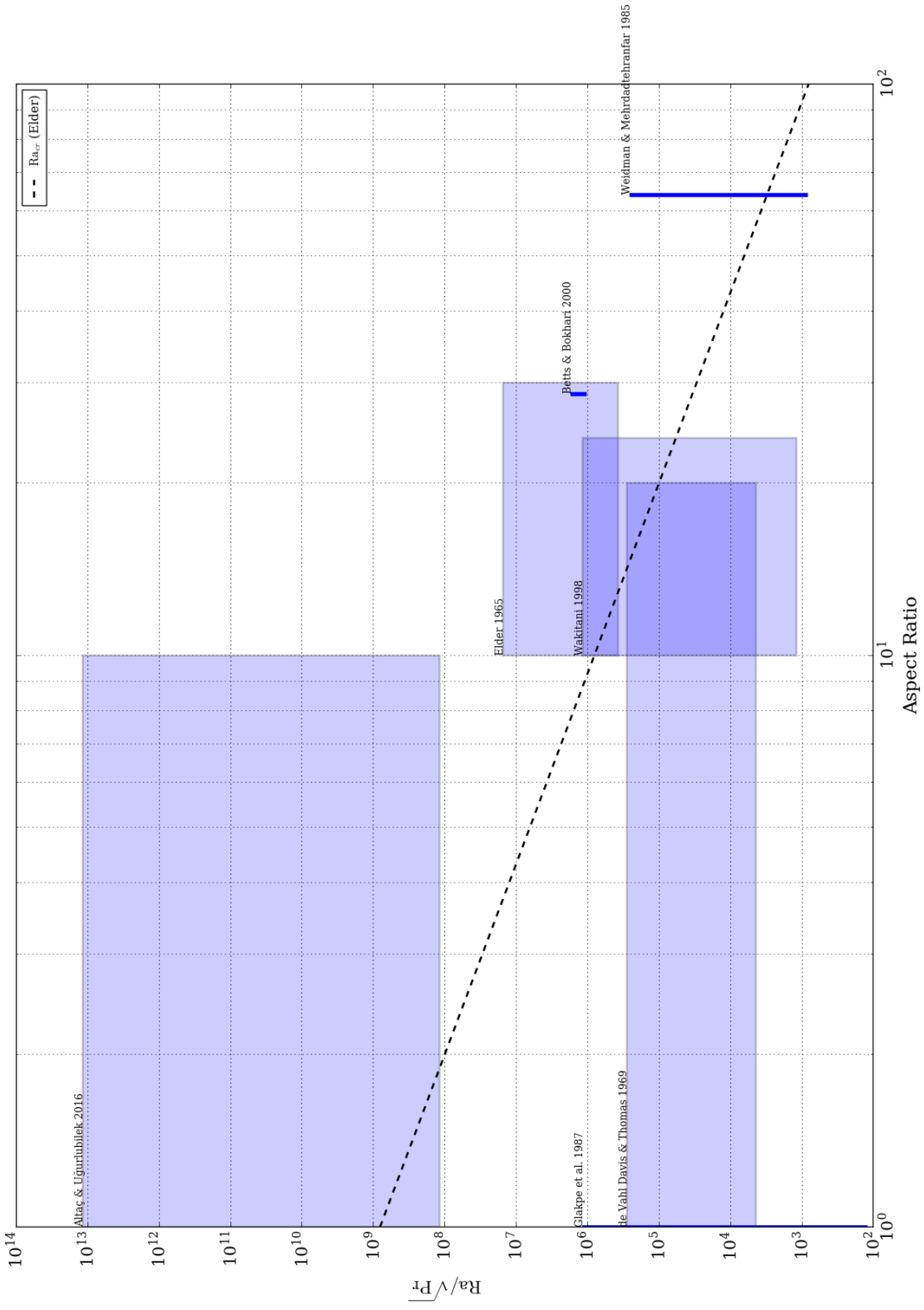

Figure 2.5: Approximate range of conditions explored in the studies reported in Section 2.4 concerning natural convection in rectangular or annular enclosures. The rectangles represent the boundaries of the conditions explored, while the actual studies spanned sub-sets of the range.

the development of a universally reliable wall treatment; the difficulty of conducting accurate and repeatable experiments to validate the models proposed, also due to the high sensitivity of the flow to the experimental conditions; the strong, bi-directional coupling between energy and momentum transport in buoyancy driven flows; the challenge of modelling flows where laminar and turbulent regions coexist. Although they recognised that a second-order turbulence model would seem more capable of predicting some of the complex features observed in these flows, Hanjalić and Vasić[50] recognised the increased complexity in the development of these models and their heavier computational burden, which was perhaps particularly true with the resources available at the time (1993), and opted for an algebraic model for the turbulent heat flux.[50]

Special attention must also be put in the choice of the simplifications used. For instance, while two-dimensional simulations can provide reasonably accurate results for moderate Rayleigh number flows, it has been noted that, at higher Ra, they tend to overestimate the Nusselt number, and three-dimensional calculations may be required.[51] In any case, experiments such as that carried out by Betts and Bokhari,[52] which provide detailed data for the validation of CFD simulations, are invaluable to assess the performances of the numerical methods and turbulence models employed.[53]

Instabilities and transition to turbulence It is well established that laminar flow fields in these geometries can be classified in three regimes:[54]

- At low Rayleigh numbers the temperature distribution is not influenced significantly by the flow field and the vertical temperature gradient is small. This is commonly labelled the *Conduction* or *Pseudo-conduction* regime.

- As Ra increases, the flow moves to the *Transition* regime: the effect of the velocity field begins to influence the temperature distribution, and thermal stratification starts to build up.

- Increasing Ra further, the *Convection* regime, or *Boundary Layer* flow, is established: significant velocities are found only near the walls, separated by a stagnant, thermally stratified core region. The thickness of these boundary layers decreases with increasing Ra and decreasing Pr.

As the Rayleigh number increases beyond certain critical values, flow instabilities are originated, studied extensively by Bergholz[54] under the simplifying assumption of infinite aspect ratio and uniform temperature gradient in the axial direction. The stability analysis performed in that influential study pointed out that instability can take the form of multiple stationary rolls or travelling waves, depending on the Prandtl number and the temperature gradient. Stability analysis for the annular geometries was carried out by

Prud'homme and Le Quéré[55] under the same hypotheses. In that case, instabilities are always of the unsteady kind. It was found that the curvature of the walls promotes instability, except at low Pr where its effect depends on the degree of thermal stratification.

A number of studies have been published which investigated the transition from these flow instabilities to fully developed turbulence.[49,56,57] An early experimental study was conducted by Elder[56] in 1965, using flow visualisation techniques and temperature measurements in rectangular cavities with constant temperature at two vertical walls and an annular cavity with heat uniformly supplied through the central rod. The study identified the formation of wall waves, which alter the established boundary layer, as the main phenomenon during transition to turbulence. A criterion was proposed for the onset of these waves, which identified the critical Rayleigh number at which transition begins. This can be expressed as a function of the Prandtl number Pr and the aspect ratio a, as:[56]

$$\mathrm{Ra}_c = 8 \times 10^8 \frac{\sqrt{\mathrm{Pr}}}{a^3} \tag{2.4}$$

At higher values of Ra, the wall waves become more and more irregular and start to break up, until a fully turbulent zone of intense mixing is formed in the core of the cavity, where the temperature is sensibly uniform. The experiments conducted on the annular cavity, where the uniform heated central rod caused a vertical temperature gradient, the fully turbulent region occurred at the top of the cavity.

Vahl Davis and Thomas[58] reported an early numerical investigation of laminar natural convection in a vertical annular enclosure. The axial symmetry of the domain was exploited to perform the calculation in a two-dimensional domain using the Vorticity-Stream Function formulation of the governing equations. The study explored a broad range of aspect ratios, radius ratios and Rayleigh number, using Equation 2.4 to ensure the cases studied fell into the region of laminar regime. It was found that for low values of Ra the flow field forms a single-cell pattern, with the centre of rotation moving upward with increasing radius ratio. At higher Rayleigh numbers, greater than $\sim 8 \times 10^4$, a two-cell circulation pattern appears, a phenomenon that was confirmed in previous experiments by other workers. An expression for the Nusselt number was derived from the simulations, which accounted for the observed decrease of Nu as the aspect ratio increases:[58]

$$\mathrm{Nu} = f \mathrm{Ra}^{0.3} a^{1/3} \tag{2.5}$$

Where f is a function of R_i/R_o and Pr. When compared with results of previous experiments, however, this correlation was found to over-predict Nu for certain aspect ratios.

Weidman and Mehrdadtehranfar[49] investigated the onset of the instabilities leading to turbulence for high Pr fluids (solutions of glycerol) in a tall annular cavity, using flow

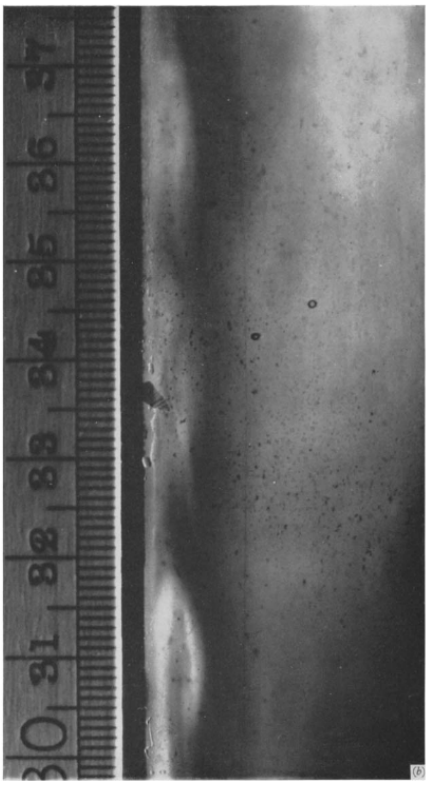

(a) Photograph of the wall waves observed by Elder[56] at Rayleigh numbers higher than the critical.

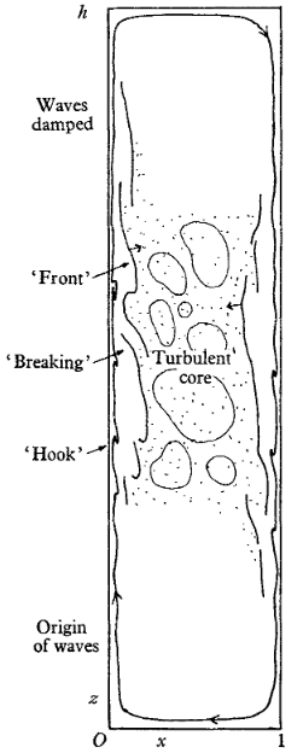

(b) Schematics of the flow regime observed by Elder[56] at high Rayleigh numbers.

Figure 2.6: Transition to turbulent natural convection in a rectangular enclosure according to Elder[56].

visualisation techniques. The study aimed at providing both qualitative and quantitative information on the flow, although admittedly the latter was affected by large uncertainties in the measurements, particularly in the wall temperatures. It was observed that the flow instabilities occur as travelling annular waves surrounding the 'hot' inner wall, followed by similar structures along the 'cold' outer walls, wich develop at Rayleigh numbers slightly higher. The position at which these waves are formed shifted upstream with increasing Ra. At higher values of Ra the structures begin to break up, and the instability extends further from the wall, until the whole core region is occupied by fully developed turbulence, which occurs at Rayleigh numbers about eigth times higher than that at the onset of the travelling waves.[49] A detailed experimental investigation of transition to turbulence was performed more recently by Lepiller et al.,[57] with water as the working fluid, in an annular cavity with aspect ratio $a = 114$.

Wakitani[59] investigated the flow patterns of a differentially heated rectangular enclosure of various Rayleigh numbers and aspect ratios by means of two-dimensional numerical simulations. They explored the transition from a flow regime of a single convective cell to a pattern made out of up to five rolls, which could be steady or unsteady. As the Rayleigh number increased further, a decrease in the number of rolls, progressively back to a single cell pattern, was observed. This behaviour, labelled 'reverse transition', occurred at all the aspect ratios tested, which disagreed with previous experiments where the phenomenon occurred only in a narrower range of aspect ratios.[59]

Natural convection along cylinders and arrays of cylinders Due to its technological relevance and the simplicity of the geometry, natural convection in annular cavities has been subject to several studies. A representative example is given by the study by Venkata Reddy and Narasimham,[60] who carried out a set of two-dimensional numerical simulations of conjugate heat transfer by laminar natural convection in an annular enclosure surrounding a heat generating rod. The simulations reported employed the Boussinesq approximation for the density variations in the fluid. The effect of Gr, a, η and the ratio between the conductivity of the solid and the fluid was explored to derive correlations for the Nusselt number and the average and maximum temperatures. Comparing the Nusselt number for this configuration with those for equivalent set-ups with uniform temperature or heat flux as boundary conditions, it was found that the Nusselt number for the conjugate heat transfer scenario lies between them two. The flow field showed one single convective cell, except for high aspect rations where recirculation in the upper region was observed.[60] The influence of the Boussinesq approximation was evaluated in a later study by Venkata Reddy et al..[61] The approximation was considered satisfactory except at the highest value of Gr tested. An increase in the average pressure with increasing Gr was observed, which could not be captured using the Boussinesq approximation.[61]

A number of studies have been oriented towards the effect of fins and ribs in promoting heat transfer in natural convection scenarios. An example is the work of Senapati, Dash, and Roy[62], which studied the effect of the size and spacing of annular fins on the heat transfer by natural convection from a vertical cylinder using the standard $k-\varepsilon$ model for turbulence treatment. The existence of an optimum spacing to maximize heat transfer was observed and correlations were obtained for this and for the Nusselt number as functions of the Rayleigh number.[62]

Fewer studies exist on the natural convection cooling of arrays of cylinders, despite the technological importance of the scenario. The interest in the passive cooling of nuclear reactor cores has guided the research on buoyancy driven flows in hydraulic loops, where the location of the heating elements is physically separated from the heat sink, often several metres apart in height. Flow patterns in enclosures containing heat generating rods and cooled from one walls have been relatively less explored. In the following the phrase 'natural convection' will be used to refer to the latter scenario, while the scenario with separated heat source and sink will be labelled 'natural loop circulation'. This distinction is, however, not universally adopted in the literature, and the expression 'natural convection' is often used to describe both configurations.

Hudina[63] reported on an experimental campaign carried out at the Swiss Federal Institute for Reactor Research to investigate the cooling of a fuel bundle by natural loop circulation in a hydraulic loop. The tests were performed at different loop pressure and blockage level, simulated by the opening of a valve. The temperature of the rods was recorded at several axial positions. It was found that up to $18\,\%$ of the nominal power of the test rig could be removed by natural loop circulation, and that this proportion decreased significantly with decreasing gas pressure and increasing inlet blockage. Significantly, it was observed a dependence of the heat removed and of the shape of the temperature distribution from the system pressure also with $100\,\%$ inlet blockage. This pointed to the presence of gas circulation within the test section which contributed to the heat removal by natural convection despite the net flow rate through the bundle had fallen to zero.

Keyhani, Kulacki, and Christensen[64] reported an experimental campaign aimed at studying natural convection in enclosed square rod bundles. Two arrangements were tested, a 3×3 bundle with pitch-to-diameter ratio equal to 3.08 and a 5×5 bundle with pitch-to-diameter ratio equal to 2.25. Correlations for the Nusselt number were obtained for each rod and for the whole bundle, for a range of Ra that spanned flow regimes from pseudo-conduction to boundary-layer flow. It was found that such regimes can coexist at certain values of Ra, with the pseudo-conduction regime ending for some rods before others. Data from flow visualisation experiments were also reported, which showed that, in the boundary-layer flow regime, low-speed downward flow can be observed. A

methodology was also proposed to construct an equivalent annulus, to adopt general correlations for the global Nusselt number and the identification of the critical Rayleigh number for the end of the pseudo-conduction regime.[64]

El-Genk, Su, and Guo[65] investigated the cooling of arrays of vertical rods by flows at low Reynolds numbers. The bundle was surroundad by a shroud and immersed in a water filled tank. Forced, mixed and natural loop circulation conditions were explored. Correlations for the Nusselt number were derived for all regimes. In the natural loop circulation case the upward flow along the bundle was physically separated from the returning flow in the tank. For this configuration, correlations of the form $\mathrm{Nu} = a\mathrm{Ra}^b$ where obtained, with non-negligible dependence from the pitch-to-diameter ratio only at high Rayleigh numbers. For the mixed convection case a blending between the correlations for natural and forced circulation was proposed as $\mathrm{Nu} = \sqrt[m]{\mathrm{Nu}_f^m + \mathrm{Nu}_n^m}$, with $m = 2$ or 3 for triangular arrangements and 4 for a square lattice.[65]

More recently, turbulent flow driven by natural loop circulation of water along a square rod bundle was investigated experimentally by Arshad, Inayat, and Chughtai[66]. The test rig used was centred on an array of electrically heated cylinders surrounded by a perspex shroud, with cold fluid entering the enclosure through inlet ports at the bottom and leaving at a higher temperature from outlet openings at the top. It was observed that, along the heated rods, the surface temperature first increased, reaching a maximum at a certain height, and then decreased afterwards. This was put in relation with increased turbulent mixing caused by the presence of cooler, and therefore denser fluid above the active part if the cylinders.[66] This trend was replicated by Shafiq et al.[67] in a CFD simulation of the experiment using the $k - \omega$ turbulence mode.[67] Flow visualization was also performed, with a single cylinder present in the test rig. An average ascending velocity of $1.25 \times 10^{-2}\,\mathrm{m\,s^{-1}}$ was measured, although the use of a low density tracer makes this result questionable.[66]

Literature on numerical studies of natural convection along fuel bundles is even scarcer than that on experimental studies. In some cases geometrical simplifications were adopted in the investigation. For instance, Glakpe, Watkins, and Kurien[47] performed a campaign of simulations of natural convection along a square rod enclosed in a cylinder, a simplified representation of the storage of a spent nuclear fuel element in a shipping cask. The solution algorithm was adapted to the geometry using a coordinate transformation. The range of Rayleigh numbers explored spanned from 0 to 10^6, encompassing the evolution of the flow regime between pseudo-conduction and fully developed boundary layer flow. No transition to a two-cells flow patterns such as that described by Vahl Davis and Thomas[58] was observed in the geometry under analysis. Temperature inversion, i.e. the presence of local maxima of temperature in the cold region and local minima in the hot region, were observed at the highest values of Ra.[47] Another example is provided by a

study by Abdul Basit et al.,[68] who adopted a numerical methodology based on geometrical simplification to study buoyancy driven flow along the pins of a pool-type research reactor. The fluid region surrounding a single pin was modelled as an annulus, with symmetry boundary conditions applied at the outer surface. The evolution of the boundary layer and of the heat transfer at the pin surface was studied along the axial direction.[68]

Rao and Glakpe[69,70] performed a numerical study of natural convection in an enclosed seven-rod bundle in a hexagonal arrangement in which the outer wall was kept at a constant 'low' temperature, while constant temperature[69] or heat flux[70] were imposed on the rod surface. The numerical methodology was based on transformed coordinates to tackle the complexity of the geometry. The ratio between the half width and the height of the cavity was equal to 1, as was the Prandtl number of the fluid. The range of Rayleigh numbers explored (which are in this case equal to Gr) went from 10^2 to 10^8, which range from the pseudo-conduction regime to a developed boundary layer regime. The articles did not report the use of any turbulence model. The flow patterns and temperature distributions were analysed, showing a clear shift in the flow patterns as the Rayleigh number was increased. At low Ra the flow field has little or no influence in the temperature distribution, whilst at higher values strong boundary layer flows caused thermal stratification within the domain. In this scenario, the surface temperature of the rods was only dependent on the axial coordinate, with different rods achieving similar temperatures.[70] The effect of the type of boundary conditions on the temperature distribution and the flow pattern was described. In particular, it was noted that in the gap between the outer rods and the cold wall, a circulation cell is always present when constant temperature is applied at the walls, whilst if uniform heat flux is imposed the flow in the region is dominated by the influence of the cold wall except at the highest values of Ra.

More recently, Hata, Fukuda, and Mizuuchi[71] simulated the cooling of a 5×5 array of rods by laminar natural convection in liquid sodium. The pins, arranged either in squares or equilateral triangles, were placed at the centre of a rectangular vessel. The local and average Nusselt number was analysed for a range of heat fluxes pitch-to-diameter ratios, and new correlations were established. Slightly higher values of Nu were found for the triangular arrangement than for the square array.

It is unfortunate that, despite the large amount of interest among researchers for the study of buoyancy driven flows, very little work has been addressed towards natural convection in enclosed pin bundles, with the overwhelming majority of studies concerning laminar flows. Moreover, to the best of the author's knowledge, the geometry considered in this dissertation, based on the fuel element of the AGR, has never been considered in natural convection studies. The investigation presented in Chapter 4 aims to provide a preliminary contribution to this field.

2.5 Concluding remarks

The review presented above has covered three main fields related to the subject of this thesis:

- The use of CFD in the study of the flows occurring in nuclear reactors (Sections 2.1 and 2.2).
- The simplification of complex geometries by the use of the porous medium approximation, with particular attention to the application of this technique to nuclear plant (Section 2.3).
- Natural convection in vertical enclosures, with particular attention to buoyancy driven flows along bundles of cylinders (Section 2.4).

An overview of the state of the use of Computational Fluid Dynamics for nuclear safety applications was presented in Section 2.1. CFD is becoming more and more valuable as a tool for nuclear safety analyses, alongside system codes and large scale experiments, for its ability to provide insight on the flow phenomena while reducing the cost of the investigation. However, it was noted how it is still reliant on validation with experimental data to be reliably used in industrial practice. This is especially true for models not based on first principles, such as the one presented in Chapter 5. Care was taken to demonstrate the capability of the model by comparing its prediction with reliable experimental data, as shown in Section 6.3.

Section 2.2 reviewed work carried out on the simulation of turbulent flows in nuclear reactors and related geometries. The studies reviewed highlight the necessity of taking into account flow features such as the secondary flows induced by the non-isotropy of the Reynolds Stresses found in non-circular ducts, due to the effect those features have on macroscopic quantities. Time-resolved simulations are also required to take into account unsteady phenomena that may occur in these flows. These requirements are even more crucial when the effect of additional features found in nuclear fuel, such as the presence of structural material such as grids and braces or of artificially roughened surfaces is to be investigated. Although such features were not considered in this study, they are a possible topic for follow-up investigations. Vortex shedding and the possible disruption of symmetry and periodicity caused by grids and spacers require accuracy in time and careful selection of the computational domain, while surface roughness poses requirement on the treatment of turbulence, as pointed out by the work of Keshmiri[9] and He and Gotts[33]. In this study, forced flow along a pin bundle was simulated to compare the performances of 'detailed' and 'porous' models. Even though a steady state High Reynolds Number Eddy Viscosity Model was deemed sufficient for this application, a

Reynolds Stress Model was employed in one of the calculations to confirm the validity of the assumption (see Section 6.1).

The studies presented in Section 2.3 show the successes obtained in simplifying complex geometries by approximating them as porous media. This approach was used in this study to develop a tool for the simulation of the cooling of the AGR stringer during the refuelling of the reactor (Chapter 5). The geometry considered differed from that of other studies in that the dimension of the pores is relatively large compared to the size of the domain. This consideration drove the development of a novel approach to the discretisation of the domain, which is presented in Section 5.2.1.

Section 2.4 was dedicated to a survey of literature on the study of natural convection in enclosures. The challenges posed by its simulation were highlighted, which supported the choice of a Large Eddy Simulation for the analysis discussed in Chapter 4, more suitable than other techniques in that it is less reliant on modelling hypotheses. Attention was given to studies concerning flow instability and transition to turbulent natural convection, and observations reported in some of those studies guided the interpretation of phenomena predicted in this work (compare Figures 2.6a and 4.12). Finally, research concerning natural convection along fuel bundles was reviewed, which also provided guidance in interpreting the results presented in Chapter 4. However, the review also highlighted the scarcity of computational studies concerning turbulent natural convection along enclosed fuel bundles. The simulation reported in Chapter 4 aims to be an early contribution to this seemingly neglected field.

Chapter 3

Methodology

In this chapter an outline of the fundamental concepts and tools used in this study is presented. The governing equations of thermal hydraulics and the numerical techniques for their solution are discussed. Due to the breadth of the discipline, the description will be, by necessity, brief and incomplete.

The Chapter consists of two parts. The first part (Sections 3.1 and 3.2) discusses the general theoretical formulation of the problems of interest for this research. The second part (Section 3.3) describes the software tools used in this study and their approaches to the numerical solutions of thermal-hydraulic problems.

3.1 Modelling of turbulent flows

3.1.1 The governing equations of thermal hydraulics

Most mathematical descriptions of the behaviour of the flow of a fluid are based on the assumption of continuum mechanics, and take the form of a set of equations for all the physical properties which are relevant to the problem studied. These equations are derived from conservation principles applied to an arbitrary control mass.[72]

The variables considered can vary significantly from one scenario to another, ranging from the mass and momentum of the fluid, to the concentration of a chemical, to mathematical constructions such as the Reynolds stresses in turbulent flows.

In the following, the governing equations for the quantities of interest in this study will be recalled, before a summary of the models available for the simulation of turbulent flows is presented.

Continuity Equation

The *Continuity Equation* formalises the balance of mass in an arbitrary volume of fluid. It states that the rate of increase of mass in a region of the domain, plus the rate at which mass leaves the region, must equal the rate at which mass is produced within the region. In a differential form, using tensor notation:[73]

$$\frac{\partial \rho}{\partial t} + \frac{\partial \rho v_i}{\partial x_i} = \Gamma \tag{3.1}$$

where ρ is the density of the fluid, v_i is the velocity vector and Γ is the rate of mass production, which is 0 in most applications.

Momentum Equations

The *Momentum Equations*, known as the *Navier-Stokes Equations*, are derived from Newton's second law and describe the balance between the rate of variation of the momentum of a fluid particle and the forces acting on it. In a differential form they can be written as:[72,73]

$$\begin{aligned} \rho \frac{\partial v_i}{\partial t} + \rho v_j \frac{\partial v_i}{\partial x_j} = &- \frac{\partial p}{\partial x_i} + \frac{\partial}{\partial x_j} \mu \left(\frac{\partial v_i}{\partial x_j} + \frac{\partial v_j}{\partial x_i} \right) - \frac{2}{3} \mu \frac{\partial^2 v_j}{\partial x_i \partial x_j} \\ &+ \rho g_i + ST_i - k_{ij} u_j + \Gamma (u_i^{in} - u_i) \end{aligned} \tag{3.2}$$

where p is the fluid pressure, μ is the dynamic viscosity of the fluid, g_i is the acceleration vector due to gravity, ST_i and $k_{ij}u_j$ are respectively an explicit and implicit source term and u_i^{in} is the velocity vector associated with the mass source. This form of the Navier-Stokes Equations takes the name of *non-conservative* form.

The source terms ST_i and $k_{ij}u_j$ can be used to model the pressure drop induced by other forces acting on the fluid. In the model described in Chapter 5, for instance, they are used to represent the forced exerted by the solid components immersed in the fluid, according to the porous medium approximation.

Energy Equation

The *Energy Equation* is derived from the First Law of Thermodynamics and represents the balance between the thermal energy associated with the fluid and the heat and work transferred to it. It can be written in terms of variables such as the internal energy, the enthalpy or the temperature of the fluid. In this study, the form based on temperature is

used:[73]

$$\rho c_p \frac{\partial T}{\partial t} + \rho c_p \frac{\partial T v_j}{\partial x_j} = \frac{\partial}{\partial x_j}\left(\lambda \frac{\partial T}{\partial x_j}\right) + \beta T \left(\frac{\partial p}{\partial t} + \frac{\partial p v_j}{\partial x_j}\right) + \mu\Phi^2 + q''' \tag{3.3}$$

where c_p is the specific heat, λ is the thermal conductivity of the fluid, T is the temperature, $\beta = \frac{1}{\rho}\frac{\partial \rho}{\partial T}$ is the volumetric expansion coefficient, $\mu\Phi^2$ is the volumetric rate of heat generation due to viscous dissipation, which is a function of the velocity field, and q''' is the volumetric rate of heat generation by any other mechanism.

For an incompressible or weakly compressible flow, Equation 3.3 can be simplified as follows:[73]

$$\rho c_p \frac{\partial T}{\partial t} + \rho c_p \frac{\partial T v_j}{\partial x_j} = \frac{\partial}{\partial x_j}\left(\lambda \frac{\partial T}{\partial x_j}\right) + q''' \tag{3.4}$$

a form that will be used in the following.

3.1.2 Direct Numerical Simulation of turbulent flows

The Navier - Stokes Equations describe exactly the behaviour of a Newtonian fluid in any situation: the principles of continuity and momentum conservation are obeyed by laminar and turbulent flows alike, with the chaotic evolution of the latter originated from the non linearity of the equations. A numerically accurate solution of Equations 3.1 and 3.2, or DNS, is now widely regarded as trustworthy as an experimental investigation, and there have been reports of cases when a disagreement between the results of a Direct Numerical Simulation (DNS) and the findings of an experiment demonstrated the weaknesses in the latter.[72]

However, the DNS approach to study of turbulent flows becomes impractical quickly when the Reynolds number of the flow increases, especially for complex geometries. The reason lies in the underlying physics of turbulence as described in the 1920s by L. F. Richardson and in the 1940s by A. N. Kolmogorov. They found that in a turbulent flow, coherent structures, or *eddies*, are formed at scales comparable with a characteristic length L of the geometric domain, which can be denominated integral scale.[74,75] Progressively smaller eddies are formed by the breaking up of these large eddies, with a process that transfers the mechanical energy from the large scales to the small scales.

Richardson postulated that energy dissipation due to viscosity only takes part to this process at the smallest scales.[74] Under this hypothesis, at steady state the rate at which energy is transferred from large eddies to smaller structures is equal to the rate of dissipation of the turbulent energy ε, which in turn is related to the dissipation function Φ of Equation 3.3.[75] Figure 3.1 shows the spectral distribution, under this hypothesis, of the turbulent energy at different scales, represented as their reciprocal, the wave number n. Note how the spectrum presents a peak at the wave number corresponding to the integral

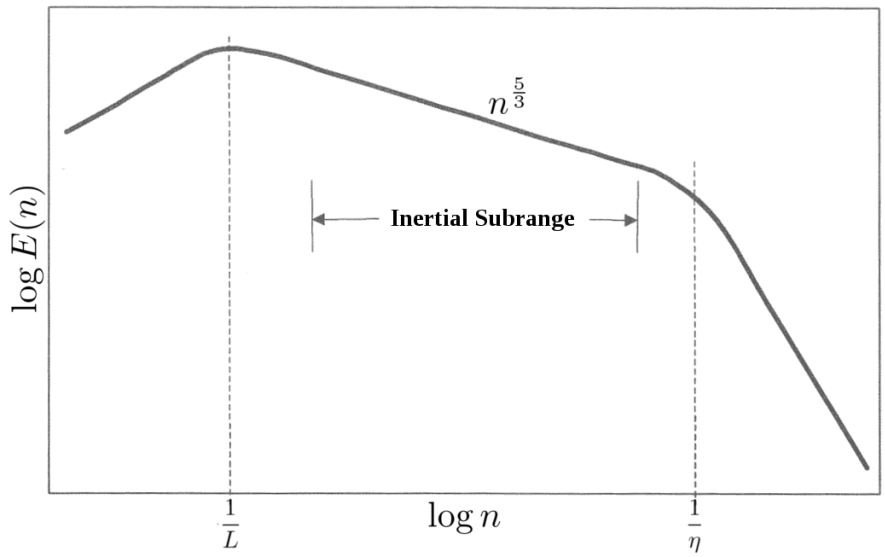

Figure 3.1: Energy spectral density of fully developed turbulence. Adapted from ref. [75].

scale and a sharp drop at the smallest scales.

Kolmogorov, basing his argument on assumptions which are held true to nowadays, was able to identify the scale of the smallest eddies, below which viscous effects become predominant. It can be expressed as:[74,75]

$$\eta = \sqrt[4]{\frac{\nu^3}{\varepsilon}} \tag{3.5}$$

where ν is the kinematic viscosity of the fluid. Expressions can also be given for the characteristic time and velocity scales:[74]

$$\begin{aligned} \Delta t_\eta &= \sqrt{\frac{\nu}{\varepsilon}} \\ v_\eta &= \sqrt[4]{\nu\varepsilon} \end{aligned} \tag{3.6}$$

These Kolmogorov length and time scales represent the smallest scales that must be resolved in a numerical calculation to fully characterise a turbulent flow. It can be proven that the ratio between the largest and the smallest length and time scales increases with the Reynolds number as:[74]

$$\begin{aligned} \frac{L}{\eta} &= \mathrm{Re}^{\frac{3}{4}} \\ \frac{\Delta t_L}{\Delta t_\eta} &= \mathrm{Re}^{\frac{1}{2}} \end{aligned} \tag{3.7}$$

This ratio provides an indicator of the number of divisions a computational grid must

have on any given direction to be fine enough to perform a DNS. A comparable number of time steps will also be needed to guarantee the necessary accuracy in time[72,75]. It follows that, for a three-dimensional problem, the size of the computational mesh increases with the Reynolds number as Re^3. The computing power and memory required by such calculations will increase accordingly significantly limiting the range of applicability of DNS.

For the simulation of most flows, the analyst must rely on a statistically averaged version of Equation 3.2. Due to the non-linear nature of the Navier-Stokes Equations, additional terms appear in the averaged equations, which pose a closure problem for their solution: these terms cannot be eliminated by any manipulation of the equations, and must be modelled under certain physical assumptions, leading to the requirement of *turbulence models*.

Engineering simulations of turbulent flows can be subdivided into two 'families', which differ in the type of the average used in the filtering process: the Reynolds Averaged Navier-Stokes (RANS) approach is based on a time-averaged version of the governing equations, and is discussed in Section 3.1.3, whereas the Large Eddy Simulation (LES) approach, derived by using a spatial filter, is described in Section 3.1.4.

3.1.3 Reynolds Averaged Navier-Stokes Equations

The RANS Equations are obtained by filtering the Navier-Stokes Equations using a time average operator:[72]

$$\bar{\phi} = \lim_{\Delta t \to \infty} \frac{1}{\Delta t} \int_{t_0}^{t_0+\Delta t} \phi(x_i, t) dt \tag{3.8}$$

The resulting equations, written for convenience in the conservative form, are presented below:

$$\frac{\partial \rho \bar{v}_i \bar{v}_j}{\partial x_j} = \frac{\partial \bar{p}}{\partial x_j} + \frac{\partial}{\partial x_j} \mu \left(\frac{\partial \bar{v}_i}{\partial x_j} + \frac{\partial \bar{v}_j}{\partial x_i} \right) - \frac{2}{3} \mu \frac{\partial^2 \bar{v}_j}{\partial x_i \partial x_j} - \frac{\partial \rho \overline{v_i' v_j'}}{\partial x_j} \tag{3.9}$$

where $u_i' = u_i - \bar{u}_i$ is the *fluctuation* of the velocity u_i. The source terms were neglected for simplicity. Note that Equation 3.9 provides a steady state solution for the average velocity field. An unsteady term $\partial \rho \bar{v}_i / \partial t$ is often included, and transient solutions are pursued with some success, an approach termed URANS.

The tensor $\rho \overline{v_i' v_j'}$ is known as the RST and accounts for the momentum transported by the velocity fluctuations. It poses a closure problem for the equations, and an expression for its calculation must be provided to solve Equations 3.9. Many models, of various degree of complexity, have been proposed to determine the Reynolds Stress Tensor (RST).

Many widespread models are based on the assumption that the turbulent diffusion represented by RST can be modelled as a function of the averaged velocity field. The assumption is that it behaves similarly to the molecular diffusion, and can be thus represented using an equivalent viscosity:

$$-\rho\overline{v_i'v_j'} = \mu_t\left(\frac{\partial\bar{v}_i}{\partial x_j} + \frac{\partial\bar{v}_j}{\partial x_i}\right) - \frac{2}{3}\rho k\delta_{ij} \tag{3.10}$$

where $k = \overline{v_i'v_i'}/2$ is named *turbulent kinetic energy*. The term $\frac{2}{3}\rho k\delta_{ij}$ can be added to the time-averaged pressure $\bar{p}$ in Equation 3.9, and treated together to it as a modified pressure. The problem of modelling turbulence is thus reduced to determining the turbulent viscosity μ_t: these models are thus collectively known as Eddy Viscosity Models (EVMs).

Many EVMs have been proposed, with different degrees of complexity and generality. Some models use simple algebraic expressions for μ_t, which allow one to obtain reliable solutions only for specific geometries. Other models employ one, two or more transport equations for some turbulent quantities, which can then be used to calculate the eddy viscosity.

In a number of widespread models the turbulent viscosity at every point in the domain is calculated using the following relation:[75]

$$\mu_t = \rho C_\mu \frac{k^2}{\varepsilon} \tag{3.11}$$

where k is the turbulent kinetic energy and ε is the rate of dissipation of turbulence. A trasport equation is then solved to obtain the distribution of k in the domain:[73]

$$\rho\frac{\partial k}{\partial t} + \rho\bar{v}_j\frac{\partial k}{\partial x_j} = \frac{\partial}{\partial x_j}\left(\mu + \frac{\mu_t}{\sigma_k}\right)\frac{\partial k}{\partial x_j} + P + G - \rho\varepsilon + \Gamma k^{in} + ST_k \tag{3.12}$$

where σ_k is a constant, P and G are the rates of production of k due to shear and buoyancy effects, $\rho\varepsilon$ is the its rate of dissipation, k^{in} is the turbulent kinetic energy associated with the mass source and ST_k represents any additional source term. Equation 3.12 can be derived by noting that:

$$\frac{Dk}{Dt} = \frac{Dv_i'v_i'/2}{Dt} = v_i'\frac{Dv_i'}{Dt} \tag{3.13}$$

where $D\phi/Dt = \partial\phi/\partial t + \overline{v}_i\partial\phi/\partial x_i$ and the implied sum convention is followed. A transport equation for the fluctuating velocities v_i' can be obtained by subtracting the RANS equations from the Navier-Stokes equations, and in turn can be used to obtain the derivative $\frac{Dv_i'}{Dt}$. By further manipulation of Equation 3.13 one can obtain Equation 3.12.[74]

The production terms P and G are calculated as follows:[73]

$$\begin{aligned} P_k &= -\rho\overline{v_i' v_j'}\frac{\partial \overline{v}_j}{\partial x_i} \\ G_k &= \frac{1}{\rho}\frac{\mu_t}{\sigma_k}\nabla\rho\cdot\vec{g} \end{aligned} \tag{3.14}$$

Examples of additional source terms ST_k are those arising in porous media due to the presence of the solid.[39]

The equation for k is commonly used together with an equation for another quantity, such as the dissipation rate ε or the quantity $\omega = k/\varepsilon$:[74,75]

$$\begin{aligned} \rho\frac{\partial \varepsilon}{\partial t} + \rho\overline{v}_j\frac{\partial \varepsilon}{\partial x_j} &= \frac{\partial}{\partial x_j}\left(\mu + \frac{\mu_t}{\sigma_\varepsilon}\right)\frac{\partial \varepsilon}{\partial x_j} + C_{\varepsilon 1}\frac{\varepsilon}{k}P - C_{\varepsilon 2}\rho\frac{\varepsilon^2}{k} \\ \rho\frac{\partial \omega}{\partial t} + \rho\overline{v}_j\frac{\partial \omega}{\partial x_j} &= \frac{\partial}{\partial x_j}\left(\mu + \frac{\mu_t}{\sigma_\omega}\right)\frac{\partial \omega}{\partial x_j} + C_{\omega 1}\frac{\omega}{k}P - C_{\omega 2}\rho\omega^2 \end{aligned} \tag{3.15}$$

where σ_ε, $C_{\varepsilon 1}$, $C_{\varepsilon 2}$, σ_ω, $C_{\omega 1}$ and $C_{\omega 2}$ are constants. EVMs based on more than 2 differential equations have also been proposed.

One of the shortcomings of EVMs is that they fail to model the anisotropy of the RST encountered in many flows of industrial interest. For this reason, RSMs have been developed, which directly solve the transport equations for the Reynolds stresses, plus an additional one for the dissipation ε. Due to the symmetry of the RST, this results in seven transport equations.[72,75] Higher order unresolved terms are still present in the equations and must be modelled. RSMs have been successfully applied to flows in complex geometries, and have proved to be an improvement over simple EVMs in many scenarios. However, this comes at the cost of a higher complexity and resource consumption. Applications of both EVMs and RSMs to problems relevant to nuclear engineering are reviewed in Section 2.2.

To conclude this section, it is worth mentioning two antithetical approaches to the modelling of the flow in proximity of the wall in RANS simulations. In this region, Equation 3.11 does not accurately model the turbulent viscosity.[75] One very popular solution is to assume that the velocity profile near the wall follows the universal law of the wall. In this assumption, the velocity in the boundary layer beyond a viscous sub-layer and a buffer region can be described, in wall units, as:[72,74]

$$v^+ = \frac{1}{\kappa}\log y^+ + B \tag{3.16}$$

where $\kappa = 0.42$ is the Von Karman constant and B is an empirical parameter. Two definitions can be provided for the non-dimensional velocity parallel to the wall, v^+, and

the non-dimensional wall distance, y^+, depending on the choice of a 'one-scale' or a 'two-scale' formulation, both available in Code_Saturne.

In the one-scale formulation one defines the friction velocity $u_\tau = \sqrt{\tau_w/\rho}$, where τ_w is the shear stress at the wall. The non-dimensional velocity and wall distance, v^+ and y^+ are defined as:[73]

$$\begin{aligned} v^+ &= \frac{\overline{v_t}}{u_\tau} \\ y^+ &= \frac{\rho u_\tau y}{\mu} \end{aligned} \tag{3.17}$$

Where $\bar{v_t}$ is the tangential component of the average velocity and y is the dimensional distance from the wall.

In the two-scale formulation, a friction velocity based on the turbulent kinetic energy is defined as:[73]

$$v_k = \sqrt{e^{\sqrt{k}y/11\nu}\frac{\nu\bar{v_t}}{y} + \left(1 - e^{\sqrt{k}y/11\nu}\right)\sqrt{C_\mu}k} \tag{3.18}$$

The friction velocity is then redefined as $u_\tau = \tau_w/(\rho v_k)$. The definitions of v^+ and y^+ become:[73]

$$\begin{aligned} v^+ &= \frac{\bar{v_t}}{u_\tau} \\ y^+ &= \frac{\rho v_k y}{\mu} \end{aligned} \tag{3.19}$$

The standard wall functions approach normally requires that the first node of the mesh lie in the region $y^+ > 30$.[72] It therefore allows the use of relatively coarse meshes. More complex wall functions exist, which have a broader range of validity.[75] Models based on wall functions are known in the literature as High Reynolds Number (HRN) models.

In certain flows, however, the velocity profile near the wall deviates from the universal wall law, for example due to flow separation[72] or gravity effects. In this case one may use another class of models, named Low Reynolds Number (LRN) models, which solve explicitly the equations up to the viscous sub-layer, using damping functions to correct the eddy viscosity given by Equation 3.11. These models require that the node of the mesh closest to the wall be in the region $y^+ < 1$, which results in much finer meshes than those used with HRN models.

3.1.4 Large Eddy Simulation of turbulent flows

A different approach to the simulation of turbulent flow can be conceived by noting that while the large scales of turbulent motions are strongly anisotropic and influenced by the

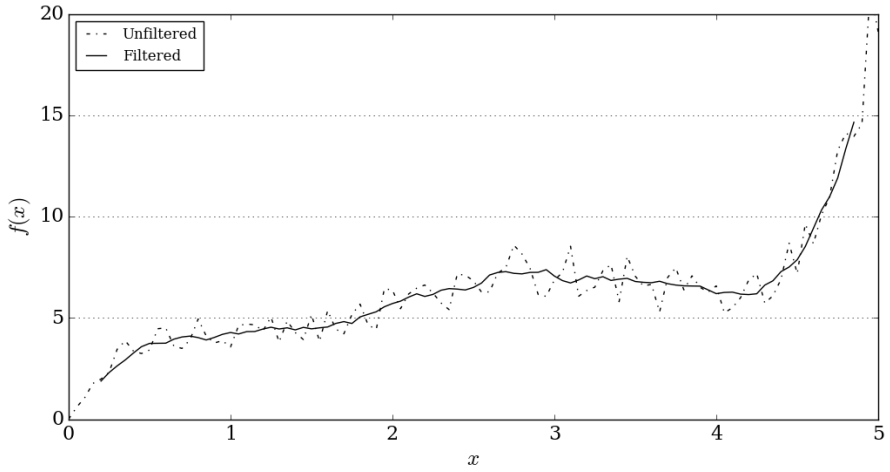

Figure 3.2: Suppression of small scale fluctuations using a one-dimensional box filter.

geometry, the small scales, as observed by Kolmogorov,[74] are by and large isotropic and universal.[75] One could therefore envisage a methodology to explicitly simulate the large structures present in the flow while modelling the influence of the small vortices using general expressions. This approach, which takes the name of Large Eddy Simulation (LES), will be hereby summarised.

Contrary to the time-average approach followed in RANS simulations, LESs are based on the use of spatial filters, defined as:[72,75]

$$\langle \phi(x,t) \rangle = \int G(x,x')\phi(x',t)dx' \tag{3.20}$$

Many choices are available for the filter function $G(x_i, x_i')$ from *box* type moving averages to Gaussian kernels. All can be characterised by a filter width Δ, which determines the dimension of the smallest scales to be resolved. As shown in Figure 3.2, the effect of the filter is to suppress the small scale fluctuations, keeping most of the information relative to lower wave numbers and resulting in a 'smoother' representation of the function.

If the cut-off scale of the filter lies in the *inertial sub-range* of Figure 3.1, the size of the problem can be considerably reduced compared to DNS. However, as will be shown in the following, the effect on the flow of the scales suppressed by the filters, or *sub-filter* scales, must be modelled in order to describe completely the physical phenomenon.

Consider the velocity component v_i. At any point, it can be written as $v_i = \langle v_i \rangle + v_i'$, where v_i' is the sub-filter velocity, analogous to the fluctuation defined for RANS decomposition. If the operator in Equation 3.20 is applied to Equations 3.2, written for simplicity for an incompressible flow, one obtains:[75]

$$\frac{\partial \rho \langle v_i \rangle}{\partial t} + \frac{\partial \rho \langle v_i \rangle \langle v_j \rangle}{\partial x_j} = -\frac{\partial \langle p \rangle}{\partial x_j} + \frac{\partial}{\partial x_j}\mu\left(\frac{\partial \langle v_i \rangle}{\partial x_j} + \frac{\partial \langle v_j \rangle}{\partial x_i}\right) - \frac{\partial \tau_{ij}}{\partial x_j} \tag{3.21}$$

where τ_{ij} is a tensor of additional 'stresses' arising from the non-linearity of the convective terms in Equations 3.2:

$$\tau_{ij} = \rho(\langle v_i v_j \rangle - \langle v_i \rangle \langle v_j \rangle) \tag{3.22}$$

The tensor τ_{ij} can be further decomposed, but it is common practice to model it as a whole.[75] Moreover, in many finite volumes implementation of LES the filter is taken to be the implicit average within the elements of the mesh, a situation in which the additional stress tensor reduces to $\tau_{ij} = \rho\langle u_i' u_j' \rangle$.[75] Incidentally, this implementation of the filter justifies the use in literature of the term *sub-grid* as a synonym for 'sub-filter'.

The most diffused models for τ_{ij} use an EVM approach similar to that followed in RANS modelling:[72,75]

$$\tau_{ij} - \frac{1}{3}\tau_{kk}\delta_{ij} = -2\mu_t\left(\frac{\partial\langle v_i\rangle}{\partial x_j} + \frac{\partial\langle v_j\rangle}{\partial x_i}\right) + \frac{2}{3}\mu_t\frac{\partial\langle v_k\rangle}{\partial x_k}\delta_{ij} \tag{3.23}$$

The term $\frac{1}{3}\tau_{kk}\delta_{ij}$ can be treated by defining a modified pressure $\langle p^* \rangle = \langle p \rangle + \frac{1}{3}\tau_{kk}\delta_{ij}$, and again the model reduces to the determination of μ_t. In the following, a description of some of the models available in the literature will be given, focusing on those available in the CFD solver used in this study, Code_Saturne.

Smagorinsky model

The model developed in the 1960s by J. Smagorinsky is the oldest and, possibly, the most widespread EVM used in Large Eddy Simulations. Based on dimensional considerations, the model proposes for μ_t the following expression:[72,73,75]

$$\mu_t = \rho C_s^2 \Delta^2 \sqrt{2\langle S_{ij}\rangle\langle S_{ij}\rangle} \tag{3.24}$$

where $\langle S_{ij}\rangle = \frac{1}{2}\left(\frac{\partial\langle v_i\rangle}{\partial x_j} + \frac{\partial\langle v_j\rangle}{\partial x_i}\right)$ is the filtered Strain Rate Tensor, Δ is an equivalent width of the filter based on the volume of the mesh cell and C_s is a constant. The value originally proposed for C_s was deducted for isotropic turbulence and it is variedly reported as 0.23,[75] 0.2,[72] or 0.18,[73] the latter being the value used in Code_Saturne.

The constant C_s represents the main liability of the Smagorinsky model. There is no single value that can be used for all possible flows, and for wall bounded flows numbers smaller than those listed above need to be employed, typically 0.065,[72,73] which is default in Code_Saturne. Moreover, damping functions must be used in the near wall region to correctly model the reduction as $\mu_t \sim y^{+3}$.[72,76] One example of such function is the well

known Van Driest function:

$$C_s = C_{s,0}\left(1 - e^{-y^+/25}\right)^2 \tag{3.25}$$

However, the dependence of the constant from a non-local quantity such as the distance from the wall is somewhat undesirable.[72] Moreover, where the wall shear stress and, consequently, u_τ approach zero, such as in proximity of a flow separation point, y^+ will also approach zero at any distance from the wall. Equation 3.25 would thus return C_s, and therefore, μ_t equal to zero, in a region characterised in reality by intense turbulence. The Van Driest model is therefore inadequate for these flow conditions. In the following, two different approaches to eliminate the shortcomings of the Smagorinsky model will be described.

The dynamic model

A more sophisticate model for the sub-grid viscosity can be derived from the assumption that the behaviour of a turbulent flow at scales smaller than the dimension of the filter is similar to that found at the smallest resolved scale.[72,75] A procedure can then be conceived to estimate the sub-grid eddy viscosity from the result of the calculation itself.

Let the velocities $\langle v_i \rangle$ be known at every node from the results of the simulation at a previous iteration and let Δ_G be the width of the filter associated with the computational mesh. One can apply an additional filter, having width $\Delta_F > \Delta_G$, to the computed field. A similar expression to Equation 3.22 can be written for the unresolved stresses at scales smaller than Δ_F:[75]

$$T_{ij} = \rho\{\langle v_i v_j \rangle\} - \{\langle v_i \rangle\}\{\langle v_j \rangle\} \tag{3.26}$$

for which the Smagorinsky model gives, assuming a divergence-free flow for simplicity:

$$T_{ij} - \frac{1}{3}T_{kk}\delta_{ij} = 2\mu_{tF}\{\langle S_{ij} \rangle\} = \rho\left[C_s^2 \Delta_F^2 \sqrt{2\{\langle S_{ij} \rangle\}\{\langle S_{ij} \rangle\}}\right]\{\langle S_{ij} \rangle\} \tag{3.27}$$

This expression can be compared with that for the sub-grid stresses:

$$\tau_{ij} - \frac{1}{3}\tau_{kk}\delta_{ij} = 2\mu_{tG}\langle S_{ij} \rangle = \rho\left[C_s^2 \Delta_G^2 \sqrt{2\langle S_{ij} \rangle \langle S_{ij} \rangle}\right]\langle S_{ij} \rangle \tag{3.28}$$

Let one define a third tensor L_{ij} as:

$$L_{ij} = \rho\{\langle v_i \rangle \langle v_j \rangle\} - \{\langle v_i \rangle\}\{\langle v_j \rangle\} \tag{3.29}$$

for which, combining Equations 3.22 and 3.26, can be trivially shown that:

$$L_{ij} = T_{ij} - \{\tau_{ij}\} \tag{3.30}$$

If it is assumed that a single value of C_s is capable of modelling the turbulent diffusion at both scales, Equations 3.27 and 3.28 can be combined with Equation 3.30 and, neglecting the trace of L_{ij}, the following expression can be written as:[73,75]

$$L_{ij} = -2C_s^2 M_{ij} \tag{3.31}$$

where:

$$M_{ij} = \Delta_F^2 \sqrt{2\{\langle S_{ij}\rangle\}\{\langle S_{ij}\rangle\}}\{\langle S_{ij}\rangle\} - \Delta_G^2\{\sqrt{2\langle S_{ij}\rangle\langle S_{ij}\rangle}\langle S_{ij}\rangle\} \tag{3.32}$$

Both L_{ij} and M_{ij} in Equation 3.31 can be calculated from the computed field. Equation 3.31 can thus be solved for C_s, which in Code_Saturne is done by the least square method, to obtain:[73,75]

$$C_s = -\frac{1}{2}\frac{M_{ij}L_{ij}}{M_{ij}M_{ij}} \tag{3.33}$$

The dynamic model provides a conceptual improvement to the Smagorinsky model in that it does not rely on constants which depend on the specific scenario, and it can correctly predict the reduction of μ_t in the near wall region using only information on the velocity field,[72] and has been applied successfully in different scenarios.[74] However, a major drawback of the model comes from the fact that, in its original formulation, the eddy viscosity it calculates can locally assume negative values, which can strongly affect the numerical stability of the calculation. Commonly used workarounds are clipping the total viscosity to zero[72] or using averaging processes of some kind.[72,73,75]

The WALE model

The Wall-Adapting Local Eddy-Viscosity (WALE) model by Ducros, Nicoud, and Poinsot[76] attempts to provide a general expression for the turbulent viscosity μ_t based only on local quantities. The model aims at improving the performance of the Smagorinsky model in the near wall region and for flows experiencing transition to turbulence.[76,77] It also seeks to account for the contribution to energy dissipation found in regions of high vorticity and low irrotational strain.[77]

The WALE model proposes the following expression for the turbulent viscosity:

$$\mu_t = (C_m \Delta)^2 \frac{(\langle S_{ij}^d \rangle \langle S_{ij}^d \rangle)^{3/2}}{(\langle S_{ij} \rangle \langle S_{ij} \rangle)^{5/2} + (\langle S_{ij}^d \rangle \langle S_{ij}^d \rangle)^{5/4}} \tag{3.34}$$

where C_m is a constant and:

$$\langle S_{ij}^d \rangle = \frac{1}{2}\left(\frac{\partial \langle v_i \rangle}{\partial x_k} \frac{\partial \langle v_k \rangle}{\partial x_j} + \frac{\partial \langle v_j \rangle}{\partial x_k} \frac{\partial \langle v_k \rangle}{\partial x_i} \right) - \frac{1}{3} \frac{\partial \langle v_k \rangle}{\partial x_k} \delta_{ij} \tag{3.35}$$

It can be shown that the product $\langle S_{ij}^d \rangle \langle S_{ij}^d \rangle$ contains information on both the strain rate and the rotation rate, and correctly predicts a negligible eddy viscosity for laminar regions in proximity of the walls, which allows to simulate the instabilities occurring during transition to turbulence.[77] Also, by construction, the turbulent viscosity calculated by Equation 3.34 decreases in the near wall region as $O(y^{+3})$, eliminating the need for a damping function based on non-local quantities.[76,77]

Values for C_m were originally estimated by imposing that the sub-grid energy dissipation be equal to that predicted by the Smagorinsky model, which gave values between 0.5 and 0.6. Later research suggested that better results could be obtained setting $C_m = 0.325$,[a] whereas it appears from inspection of the source code that the value employed in Code_Saturne is $\sqrt[4]{2}/4 \simeq 0.297$.

Two main advantages of the WALE model over the dynamic models can be identified. On the one hand, the WALE models has a reduced overhead compared to dynamic models, as it calculates μ_t from the computed fields without additional filtering. On the other hand, Equation 3.34 never returns negative values for the eddy viscosity, resulting in greater stability and robustness. For this reasons, the WALE model was used for the Large Eddy Simulations carried out in this research and presented in Chapter 4.

3.2 Overview of CFD modelling of porous media

In this section the use of spatial averaging of the governing equations to simplify the study of flows in complex geometries is described briefly, while a more detailed description of the methodology followed in this study can be found in Chapter 5.

The simplification allowed by the porous medium model lies in the macroscopic description of the flow achieved by the use of spatial averaging operators. Considering a control volume (Figure 3.3), large with respect to the microscopic scale of the porous matrix but small compared with the scale of the gradients of the macroscopic flow, one

[a] Information found in `goo.gl/LTY2XV`

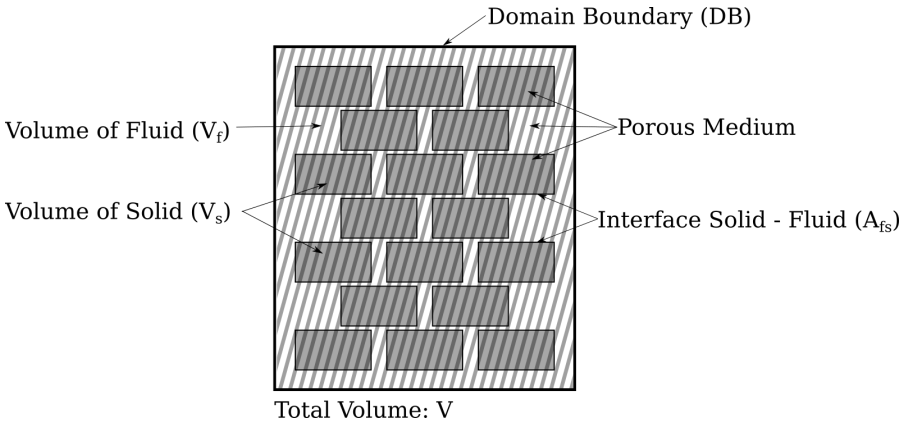

Figure 3.3: Nomenclature of the volume average in a control volume occupied by a fluid and a number of solid bodies.

can define the *phase average* and the *intrinsic phase average* of a quantity y associated with the fluid phase, respectively as:[78]

$$\begin{aligned} \langle y \rangle &= \frac{1}{V} \iiint_V y dV = \frac{1}{V} \iiint_{V_f} y dV \\ {}^i\langle y \rangle &= \frac{1}{V_f} \iiint_{V_f} y dV = \frac{1}{\gamma} \langle y \rangle \end{aligned} \tag{3.36}$$

where V is the total volume, V_f is the volume occupied by the fluid phase and $\gamma = \frac{V_f}{V}$ is called *volumetric porosity*. The quantity y can then be decomposed as a sum of its volumetric average and a deviatoric part:

$$y = {}^i\langle y \rangle + \delta y \tag{3.37}$$

where

$${}^i\langle \delta y \rangle = 0 \tag{3.38}$$

The relationship between the volume average of y and that of its time and space derivatives is given by a pair of theorems, stating:[39,79]

$${}^i\langle \frac{\partial y_i}{\partial t} \rangle = \frac{1}{\gamma} \frac{\delta \gamma \, {}^i\langle y \rangle}{\partial t} \tag{3.39}$$

$$\begin{aligned} {}^i\langle \frac{\partial y_i}{\partial x_i} \rangle &= \frac{1}{\gamma} \frac{\partial \gamma \, {}^i\langle y \rangle}{\partial x_i} + \frac{1}{V_f} \oiint_{A_{fs}} y_i n_i dA_{fs} \quad \text{if y is a vector quantity} \\ {}^i\langle \frac{\partial y_i}{\partial x_i} \rangle &= \frac{1}{\gamma} \frac{\partial \gamma \, {}^i\langle y \rangle}{\partial x_i} + \frac{1}{V_f} \oiint_{A_{fs}} y n_i dA_{fs} \quad \text{if y is a scalar quantity} \end{aligned} \tag{3.40}$$

which allow to derive a set of equations to describe the flow in the porous medium.

By applying the intrinsic average to both sides of the RANS equations, using Equations

3.39 and 3.40, decomposing p, v_i and v_j according to Equation 3.37 and letting the term of the form ${}^{i}\langle \delta y \rangle$ vanish as in Equation 3.38, one obtains:[39]

$$\frac{\partial \gamma^{\,i}\langle \bar{v}_i \rangle}{\partial x_i} = 0 \tag{3.41}$$

$$\begin{aligned}\frac{\partial \gamma^{\,i}\langle \bar{v}_i \rangle}{\partial t} + \frac{\partial \gamma^{\,i}\langle \bar{v}_i \rangle\, {}^{i}\langle \bar{v}_j \rangle}{\partial x_j} \\ = \frac{1}{\rho}\frac{\partial \gamma^{\,i}\langle \bar{p} \rangle}{\partial x_j} + \frac{\partial}{\partial x_j}\left[\nu\left(\frac{\partial \gamma^{\,i}\langle \bar{v}_i \rangle}{\partial x_j} + \frac{\partial \gamma^{\,i}\langle \bar{v}_j \rangle}{\partial x_i}\right)\right] + \\ \frac{1}{Vf}\oiint_{A_{fs}}\left[\nu\left(\frac{\partial \bar{v}_i}{\partial x_j} + \frac{\partial \bar{v}_i}{\partial x_j}\right) + \frac{\bar{p}}{\rho}\delta_{ij}\right] n_j dA_{fs} - \\ \frac{\partial}{\partial x_j}\gamma^{\,i}\langle \delta\bar{v}_i \delta\bar{v}_j \rangle - \frac{\partial}{\partial x_j}\gamma^{\,i}\langle \overline{v_i' v_j'} \rangle\end{aligned} \tag{3.42}$$

which in the literature are sometimes known as *Double-Averaged Navier-Stokes equations*. The two terms in the integral $\frac{1}{Vf}\oiint_{A_{fs}}\left[\nu\left(\frac{\partial \bar{v}_i}{\partial x_j} + \frac{\partial \bar{v}_i}{\partial x_j}\right) + \frac{\bar{p}}{\rho}\delta_{ij}\right] n_j dA_{fs}$ represent respectively the friction and the form drag force exerted by the solid on the fluid and from now on will be indicated as R. R is usually modelled by means of experimental correlations for the pressure drop characteristic of the actual geometry of the matrix. Often, R is modelled together with the term $\frac{\partial}{\partial x_j}\gamma^{\,i}\langle \delta\bar{v}_i \delta\bar{v}_j \rangle$ which accounts for the inertial effects of the sub-grid "dispersion".[39] The macroscopic Reynolds Stress Tensor $\gamma^{\,i}\langle \overline{v_i' v_j'} \rangle$ can be modelled using an Eddy Viscosity Model as:

$$-\gamma^{\,i}\langle \overline{v_i' v_j'} \rangle = \nu_{t,\gamma}\left(\frac{\partial \gamma^{\,i}\langle \bar{v}_i \rangle}{\partial x_j} + \frac{\partial \gamma^{\,i}\langle \bar{v}_j \rangle}{\partial x_i}\right) - \frac{2}{3}\gamma^{\,i}\langle k \rangle \delta_{ij} \tag{3.43}$$

where $\nu_{t,\gamma}$ is the macroscopic turbulent viscosity and ${}^{i}\langle k \rangle$ is the macroscopic turbulent kinetic energy. The calculation of macroscopic turbulent viscosity $\nu_{t,\gamma}$ depends on the specific turbulence model used, see for instance Equations 2.1 and 5.13, the latter used in the model described in this study. The macroscopic turbulent kinetic energy can be conflated with the pressure as described in Section 3.1.3. The equation therefore becomes:

$$\frac{\partial \gamma^{\,i}\langle \bar{v}_i \rangle}{\partial t} + \frac{\partial \gamma^{\,i}\langle \bar{v}_i \rangle\, {}^{i}\langle \bar{v}_j \rangle}{\partial x_j} = \frac{1}{\rho}\frac{\partial \gamma^{\,i}\langle \bar{p} \rangle}{\partial x_j} + \frac{\partial}{\partial x_j}\left[(\nu + \nu_t)\left(\frac{\partial \gamma^{\,i}\langle \bar{v}_i \rangle}{\partial x_j} + \frac{\partial \gamma^{\,i}\langle \bar{v}_j \rangle}{\partial x_i}\right)\right] + R \tag{3.44}$$

which is the form used in this study, where R is calculated using the correlations listed in Appendix B.

Alternative to the approach described above, Equations 3.42 can be obtained by

applying the volume average to the original Navier-Stokes equations, and Reynolds-averaging the result. Pedras and Lemos[79] proved that the two approaches lead to the same form for the mass and momentum equations (Equations 3.42). However, the order of averaging does matter for what concern the transport equation for the turbulent kinetic energy k: Pedras and Lemos[79] proved that only when the Reynolds filter is applied first is the contribution of the turbulent fluctuations at the sub-filter scale accounted for. Therefore, all recent turbulence models used to simulate flows in porous media, some of which are reviewed in Section 2.3, adopt this sequence to derive the equations.

A similar procedure can be used to obtain the Double-Averaged Energy equation. In the hypothesis of constant properties, with no heat generation within the fluid, one can write:[42,78]

$$\rho c_p \gamma \frac{\partial\, {}^{i}\langle T_f \rangle}{\partial t} + \rho c_p \gamma v_i \frac{\partial\, {}^{i}\langle T_f \rangle}{\partial x_i} = \lambda \gamma \frac{\partial^2\, {}^{i}\langle T_f \rangle}{\partial x_i^2} + \frac{1}{V_f} \iint_{A_w} q''_w dA_{fs} \tag{3.45}$$

where q''_w is the heat flux from the solid. If q''_w is calculated with Newton's law of cooling, using the surface averaged wall temperature $T_w = (1/A_w) \iint_{A_w} T dA_{fs}$, Equation 3.45 can be written as:

$$\rho c_p \gamma \frac{\partial\, {}^{i}\langle T_f \rangle}{\partial t} + \rho c_p \gamma v_i \frac{\partial\, {}^{i}\langle T_f \rangle}{\partial x_i} = \lambda \gamma \frac{\partial^2\, {}^{i}\langle T_f \rangle}{\partial x_i^2} + h \frac{A_w}{V_f} \left(T_w - {}^{i}\langle T_f \rangle \right) \tag{3.46}$$

which is the form used in this study, where h is calculated using the correlations listed in Appendix B.

3.3 Software platform

In this section the software employed in the studies presented in this dissertation is described. Most simulations presented in the following chapters modelled the interactions between a fluid domain and a solid domain. The fluid domain was simulated using Code_Saturne, a Finite Volume solver described in Section 3.3.1, while the calculations concerning the solid domain were carried out by SYRTHES, a Finite Element code capable of simulating thermal conduction and radiation, presented in Section 3.3.2. The two solver were coupled to perform conjugate heat transfer analysis. The software system used for the generation of the geometry and the meshing of the domains, SALOME, is finally described in Section 3.3.3

3.3.1 Solver for the fluid domain: Code_Saturne

Code_Saturne is a general purpose, open-source, single-phase CFD code for Unix-like systems, developed by the research and development department of Electricité De France (EDF). It is written mostly in C and Fortran. It is capable of handling flows "which may be steady or unsteady, laminar or turbulent, incompressible or potentially dilatable, isothermal or not."[80] It provides modules named "specific physics" to handle special problems such as particle tracking, combustion, simulation of flows in turbo-machinery and more.

The code is based on the finite volume method for the solution of the Navier-Stokes and scalar transport equations using the co-located scheme used for all the variables and segregate solvers for the velocity-pressure coupling. First and second order discretisation schemes, summarised below, are available for both space and time stepping. Code_Saturne is capable of treating unstructured, body-fitted meshes which may comprise elements of different shapes (tetrahedral, hexahedral, prismatic). Several formats are supported for the meshes, including MED, STAR-CCM+, CGNS, I-deas and others. Non-conformities, periodicities, symmetries, mesh partitioning and joining are treated by the code's preprocessor.[80,73]

The code is heavily programmable: not only can the user write custom subroutines, to carry out actions like defining non-standard boundary conditions or additional source terms, computing statistics and so on, but they can also modify any part of the solver's source code without the need to recompile the whole program,[80] as explained below. To support the programmer, the source code documentation, generated through *Doxygen*, is distributed with the software.[73]

Code_Saturne is free software: EDF released it under GNU GPL and it is freely available, together with its source code, from its website.[b]

Spatial discretisation of the governing equations in Code_Saturne

As mentioned above, Code_Saturne is a CFD solver based on the *finite volume method* which uses the *co-located* formulation for all the flow variable. The *finite volume method* is a discretisation methodology for the solution of partial differential equations which can be summarised in the following steps:

1. The calculation domain is subdivided in a number of finite regions. These regions, or *cells*, form the computational grid or *mesh*. A single value of each of the variables considered is associated with each cell. Several requirements must be fulfilled to guarantee the accuracy and consistency of the numerical solution.

[b] `http://code-saturne.org/cms/download`

2. The governing equations are integrated over each cell, and volume integrals of divergences are converted into surface integrals.

3. The values of the variables and their gradients at the boundaries of each cells are approximated in terms of the values in the neighbouring cells. For transient problems, a time advancement scheme is also applied. This effectively transform the differential equation in a system of algebraic equations, where the unknowns are the cell values of each variable.

4. The system of equations is solved numerically. For transient problems, the calculated fields are used as a starting point for the calculation at the following time step.

In the description given above it was implicitly used the *co-located* formulation, which assigns all the flow variables to the same locations, namely the cells centres. The alternative approach, the *staggered grid* formulation, which defines the fluid velocity on the faces between the cells, is not discussed here.

To illustrate the methodology, one shall take the moves from the general transport equation for a variable Y, written in non-conservative form:[81]

$$\rho\frac{\partial Y}{\partial t}+\rho v_k\frac{\partial Y}{\partial x_k}-\frac{\partial}{\partial x_k}K\frac{\partial Y}{\partial x_k}=S_I Y+S_E+\Gamma(Y^{in}-Y) \tag{3.47}$$

Where S_I and S_E denote the explicit and implicit contributions to the volumetric source term.[c] If one drops, for simplicity, the term related to the mass source, one can write the integral of the equation over a cell i as:

$$\underbrace{\iiint_{V_i}\rho\frac{\partial Y}{\partial t}dV_i}_{\text{Inertial term}}+\underbrace{\iiint_{V_i}\rho v_k\frac{\partial Y}{\partial x_k}dV_i}_{\text{Convective term}}-\underbrace{\iiint_{V_i}\frac{\partial}{\partial x_k}K\frac{\partial Y}{\partial x_k}dV_i}_{\text{Diffusive term}}=\underbrace{\iiint_{V_i}(S_I Y+S_E)dV_i}_{\text{Source term}} \tag{3.48}$$

The 'convective' and 'diffusive' terms are best treated by transforming the volume integrals in surface integrals over the cell boundary, as will be illustrated shortly. One can approximate the remaining volume integrals by assuming that the distribution of all variable and physical properties is constant within the domain, and equal to the value on

[c] As a rule, in this dissertation the documentation of the version of Code_Saturne employed in the reported studies has been used as a reference. However, ref. [73] reports a slightly different equation which does not appear to be correct. In particular, the term '$-(\partial(\rho v_k)/\partial x_k)Y$' appears on the left hand side, despite being already accounted for in the term 'ΓY'. The term does not appear in ref. [81] which documents a later version of the code.

the centroid I of the cell. This allows one to write:

$$\begin{aligned} \iiint_{V_i} \rho \frac{\partial Y}{\partial t} dV_i &= \rho^I \frac{\partial Y^I}{\partial t} V_i \\ \iiint_{V_i} (S_I Y + S_E) dV_i &= (S_I Y^I + S_E) V_I \end{aligned} \tag{3.49}$$

Figure 3.4 illustrates the nomenclature used in the following to describe the discretisation schemes used in Code_Saturne for the convective and diffusive term:

- I and J indicate the cells centres of cells i and j.
- V_i and V_j are the volumes of the cells.
- F is the centre of the face between cells i and j or a boundary face adjoining cell i.
- A_{ij} is the area of the internal face between cells i and j.
- A_b is the area of a boundary face adjoining cell i.
- O is the point where the line between I and J intercepts the internal face.
- I' and J' are the projections of I and J on a line normal to the face and passing through F.

In the following, the evaluation of the convective and diffusive terms in the interior of the domain will be described. The treatment of the boundary conditions will be discussed in a later section.

Convective term The term $\iiint_{V_i} \rho v_k \frac{\partial Y}{\partial x_k} dV_i$ represents the contribution to the decrement of variable Y in the cell due to the quantity transported by the outgoing flow. It can be written as:[73]

$$\iiint_{V_i} \rho v_k \frac{\partial Y}{\partial x_k} dV_i = \iiint_{V_i} \frac{\partial Y \rho v_k}{\partial x_k} dV_i - \iiint_{V_i} Y \frac{\partial \rho v_k}{\partial x_k} dV_i \tag{3.50}$$

If one assumes that Y can be approximated within the cell by a single value Y_i taken at the cell centre, one can use the divergence theorem to write:[73]

$$\iiint_{V_i} \rho v_k \frac{\partial Y}{\partial x_k} dV_i \simeq \oiint_{A_i} Y \rho v_k n_k dA_i - Y_i \oiint_{A_i} \rho v_k n_k dA_i \tag{3.51}$$

where A_i is the area of the surface delimiting cell i and n_k is the unit vector normal to the element surface. Noting that the boundary of the cell consists of all the faces between

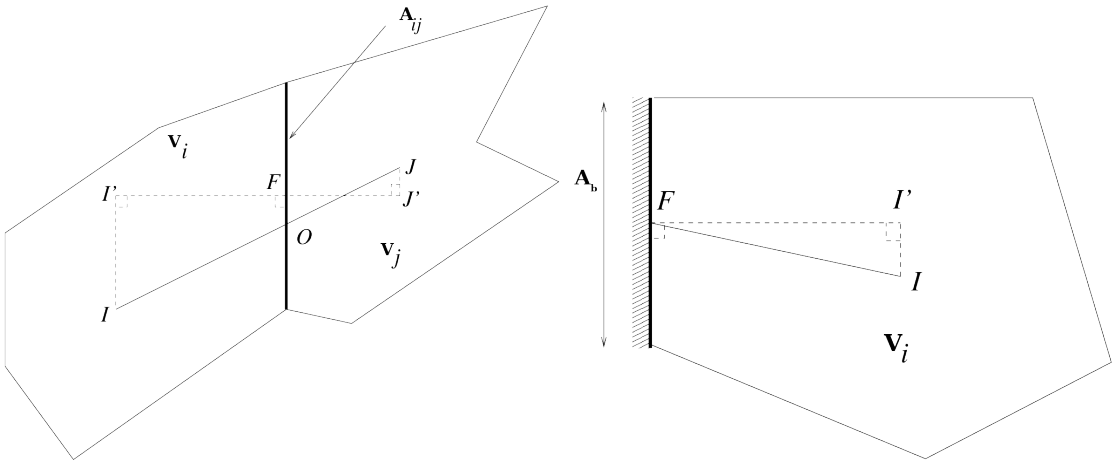

(a) Internal face. (b) Boundary face.

Figure 3.4: Nomenclature used in the description of the spatial discretisation. Adapted from ref. [73].

the cell itself and its neighbours, and assuming that Y can be approximated on each face by a single value $Y_{f_{ij}}$ taken at the face centre, one can finally write:[73]

$$\iiint_{V_i} \rho v_k \frac{\partial Y}{\partial x_k} dV_i \simeq \sum_j \left[(Y_{f_{ij}} - Y_i) \oint_{A_{f_{ij}}} \rho v_k n_k dA_i \right] = \sum_j \dot{m}_{f_{ij}} (Y_{f_{ij}} - Y_i) \quad (3.52)$$

where the cells j are all the neighbours of cell i, $A_{f_{ij}}$ is the area of the face between cells i and j and $\dot{m}_{f_{ij}} = (\rho v)_{f_{ij}} A_{f_{ij}}$ is the mass flow rate crossing face f_{ij} from cell i to cell j. If cell i is a boundary cell, one should alter the expression derived above to include the contributions from the boundary faces:[73]

$$\iiint_{V_i} \rho v_k \frac{\partial Y}{\partial x_k} dV_i \simeq \sum_j \dot{m}_{f_{ij}} (Y_{f_{ij}} - Y_i) + \sum_b \dot{m}_{ib} (Y_{ib} - Y_i) \quad (3.53)$$

where the index b represents the boundary faces adjoining cell i.

In Code_Saturne, three numerical schemes are available for the evaluation of the face values $Y_{f_{ij}}$ and Y_{ib}, namely the *Upwind* scheme, the *Central Differencing Scheme (CDS)*, or *centred* scheme, and the *Second Order Linear Upwind (SOLU)* scheme. Note that $\dot{m}_{f_{ij}}$ and $\dot{m}_{ib}$ depend on the face values for the velocity and thus on the choice of the convective scheme used in its calculation.

The Upwind scheme is a first order approximation in which the face value $Y_{f_{ij}}$ is taken

equal to the value in the cell upstream of the face:[73]

$$Y_{f_{ij}}^{\mathrm{UW}} = \begin{cases} Y_i & \text{if } \dot{m}_{f_{ij}} \geq 0 \\ Y_j & \text{if } \dot{m}_{f_{ij}} < 0 \end{cases} \tag{3.54}$$

As a first order scheme, it is not as accurate as the schemes described below, particularly on coarse meshes. It has the effect of introducing an additional numerical diffusivity in the calculation, as one can notice by expanding Y in Taylor series:

$$Y_{f_{ij}} = Y_i + \overrightarrow{\nabla} iY \cdot \overrightarrow{IF} + O(\overrightarrow{IF}^2) \tag{3.55}$$

and noting that $\overrightarrow{\nabla} iY \cdot \overrightarrow{IF}$ can be added to the diffusive term described below. Nonetheless, the estimates it provides are always bounded by the values in the adjoining cells, and it is therefore, in general, more stable than the second order schemes which do not possess this property. In Code_Saturne, a slope test can be employed to switch to the Upwind scheme from a second-order scheme when this would enhance stability. This test compares the cell gradients of neighbouring cells to identify regions where the variable considered varies irregularly, and switches locally to the Upwind scheme in the attempt to stabilise the solution.

The Centred scheme is a second-order scheme in which the value at an internal face is interpolated linearly from the values in the adjoining cells. Its implementation in Code_Saturne takes into account stability considerations:[73]

$$Y_{f_{ij}}^{\mathrm{CDS}} = \alpha_{f_{ij}} Y_i + (1 - \alpha_{f_{ij}}) Y_j + \frac{1}{2} \left(\overrightarrow{\nabla} iY + \overrightarrow{\nabla} jY \right) \cdot \overrightarrow{OF} \tag{3.56}$$

where $\alpha_{f_{ij}} = \overline{FJ'}/\overline{I'J'}$ is a weight factor. The last term is included to ensure second order convergence to the scheme for non-orthogonal meshes.[73]

The SOLU scheme can be derived from Equation 3.55 written for the upstream cell, by retaining the first derivative term, which results in a second-order approximation. This is the numerical scheme employed in the Large Eddy Simulations presented in Chapter 4. It can be formally written as follows:[73]

$$Y_{f_{ij}}^{\mathrm{SOLU}} = \begin{cases} Y_i + \overrightarrow{\nabla} iY \cdot \overrightarrow{IF} & \text{if } \dot{m}_{f_{ij}} \geq 0 \\ Y_j + \overrightarrow{\nabla} jY \cdot \overrightarrow{JF} & \text{if } \dot{m}_{f_{ij}} < 0 \end{cases} \tag{3.57}$$

Note that both the CDS and the SOLU scheme require the evaluation of the gradient of the quantity Y for each cell, which is discussed later in this section.

Diffusion term The diffusion term $\iiint_{V_i} \frac{\partial}{\partial x_k} K \frac{\partial Y}{\partial x_k} dV_i$ represents the transport of the variable Y due to diffusive phenomena, both molecular and turbulent. It can be manipulated under the same assumption as the convective term to give:[73]

$$\iiint_{V_i} \frac{\partial}{\partial x_k} K \frac{\partial Y}{\partial x_k} dV_i = \oiint_{A_i} K \frac{\partial Y}{\partial x_k} n_k dA_i \simeq \sum_j K_{f_{ij}} \left(\frac{\partial Y}{\partial x_k} n_k \right)_{f_{ij}} A_{f_{ij}} \tag{3.58}$$

Equation 3.58 contains two quantities which need to be evaluated at the face centre, namely the face diffusivity $K_{f_{ij}}$ and the gradient normal to the face $(\partial Y / \partial x_k n_k)_{f_{ij}}$.

In Code_Saturne, two schemes are available to estimate the former:[73]

- The *harmonic mean*, which ensures that the flux exiting a cell from one face is equal to the one entering the adjoining cell from the same face:

$$\frac{1}{K_{f_{ij}}^{\text{h.m.}}} = \frac{1 - \alpha_{f_{ij}}}{K_i} + \frac{\alpha_{f_{ij}}}{K_j} \tag{3.59}$$

- The *arithmetic mean*, which is sometimes used for its grater stability:

$$K_{f_{ij}}^{\text{a.m.}} = \frac{1}{2}\big(K_i + K_j\big) \tag{3.60}$$

To evaluate the gradient on the face centre, a natural approach would be to write:[73]

$$\left(\frac{\partial Y}{\partial x_k} n_k \right)_{f_{ij}} = -\frac{Y_{I'} - Y_{J'}}{\overline{I'J'}} = -\frac{(Y_i + \overrightarrow{\nabla} iY \cdot \overrightarrow{II'}) - (Y_j + \overrightarrow{\nabla} jY \cdot \overrightarrow{JJ'})}{\overline{I'J'}} \tag{3.61}$$

In facts, a modified expression is used in Code_Saturne, which ensures second order convergence to the scheme:[73]

$$\left(\frac{\partial Y}{\partial x_k} n_k \right)_{f_{ij}} = -\frac{Y_i - Y_j}{\overline{I'J'}} - \frac{1}{2} \frac{(\overrightarrow{\nabla} iY + \overrightarrow{\nabla} jY) \cdot (\overrightarrow{II'} - \overrightarrow{JJ'})}{\overline{I'J'}} \tag{3.62}$$

The evaluation of the cell gradients, required by the calculation of the diffusive term as well as the convective term, is described below.

Gradient calculation In Code_Saturne, two algorithms for the evaluation of the cell gradients are available:[73]

1. An *iterative* process, stable and accurate but relatively computational intensive.

2. An approximate algorithm based on the least square method, faster but less accurate.

The second methodology was not used in the studies presented in this dissertation and it will not be discussed here. In the following the iterative algorithm is illustrated with some simplification, with reference to a scalar variable. A more complete description, as well as information on the treatment of vector variables and on the least square technique can be found in reference [73].

The cell gradient of variable can be defined as the volume average of the gradient within the cell:[73]

$$\overrightarrow{\nabla} iY = \frac{1}{V_i} \iiint_{V_i} \overrightarrow{\nabla} dV_i = \frac{1}{V_i} \oiint_{V_i} Y n_k dV_i \tag{3.63}$$

Assuming that Y can be approximated throughout each face by a single value $Y_{f_{ij}}$ taken at the face centre, the expression above can be approximated as:[73]

$$\frac{1}{V_i} \oiint_{A_i} Y n_k dA_i = \frac{1}{V_i} \sum_j Y_{f_{ij}} n_k A_{f_{ij}} = \frac{1}{V_i} \sum_j (Y_O + \overrightarrow{\nabla} OY \cdot \overrightarrow{OF}) n_k A_{f_{ij}} \tag{3.64}$$

where the subscript 'O' indicates quantities evaluated at point O in Figure 3.4a. These are calculated as follows:[73]

- Y_O can be estimated by linear interpolation from the cell values:

$$Y_O = \alpha_{f_{ij}} Y_I + (1 - \alpha_{f_{ij}}) Y_J \tag{3.65}$$

- $\overrightarrow{\nabla} OY$ is evaluated, in a first-order approximation, as an arithmetic mean between the cell values:

$$\overrightarrow{\nabla} OY = \frac{1}{2} (\overrightarrow{\nabla} iY + \overrightarrow{\nabla} jY) \tag{3.66}$$

Equation 3.64 can then be rewritten as:

$$\overrightarrow{\nabla} iY = \sum_j \left[\alpha_{f_{ij}} Y_I + (1 - \alpha_{f_{ij}}) Y_J + \frac{1}{2} (\overrightarrow{\nabla} iY + \overrightarrow{\nabla} jY) \cdot \overrightarrow{OF} \right] n_k A_{f_{ij}} \tag{3.67}$$

which, when written for all the N cells of the mesh results in a system of $3 \times N$ equations.

Equation 3.67 can be rewritten in a form that makes it possible to solve it iteratively by replacing the terms $\overrightarrow{\nabla} jY$ with their estimate at the generic iteration n, and the terms $\overrightarrow{\nabla} iY$ with the updated values at iteration $n + 1$. Rearranging Equation 3.67 one can

write:

$$\overrightarrow{\nabla} i^{n+1}Y - \frac{1}{2}\sum_j (\overrightarrow{\nabla} i^{n+1}Y \cdot \overrightarrow{OF}) n_k A_{f_{ij}} = \sum_j \left[\alpha_{f_{ij}} Y_I + (1-\alpha_{f_{ij}}) Y_J\right] n_k A_{f_{ij}} + \sum_j \left[\frac{1}{2}\overrightarrow{\nabla} j^n Y \cdot \overrightarrow{OF}\right] n_k A_{f_{ij}} \tag{3.68}$$

which can be solved when paired with an initial estimate obtained suppressing the last term from Equation 3.67:[73]

$$\overrightarrow{\nabla} i^0 Y = \sum_j \alpha_{f_{ij}} Y_I + (1-\alpha_{f_{ij}}) Y_J n_k A_{f_{ij}} \tag{3.69}$$

Equation 3.68 is iterated until a target tolerance is reached, or when the maximum number of iterations is hit.

Time discretisation

To integrate numerically Equation 3.47 in time, a finite difference approximation of the inertia term can be written as:

$$\rho^I \frac{\partial Y^I}{\partial t} V_i = \rho^I \frac{Y^{I,n+1} - Y^{I,n}}{\Delta t} V_i \tag{3.70}$$

A number of numerical methods can be concieved which differ for the time at which the variable Y is evaluated in the remaining terms. Two of these numerical schemes are available in Code_Saturne, namely:[73]

- The first order Forward Euler scheme, in which $Y = Y^{n+1}$.
- The second order Crank-Nicholson scheme, which assumes that Y varies linearly during the time step and evaluates the variable at $t = t^n + \frac{1}{2}\Delta t$:

$$Y = Y^{n+\frac{1}{2}} = \frac{Y^{n+1} + Y^n}{2} \tag{3.71}$$

Both time schemes can be written as $Y^{n+\theta} = \theta Y^{n+1} + (1-\theta) Y^n$ with $\theta = 1$ for the Euler scheme and $\theta = 0.5$ for the Crank-Nicholson scheme. Note that both schemes are *implicit*, in that the unknown value Y^{n+1} appears in the equation in association with the neighbouring cells, thus requiring the solution of an algebraic system at each time step.

Beside the variable itself, the solution of Equation 3.47 requires the knowledge of the face mass fluxes, physical properties and source terms. Time discretisation schemes are

required to evaluate them at a given instant. The schemes available in Code_Saturne are summarized below:

Mass fluxes During the solution of the momentum equations, the mass fluxes between the cells are not known at the new time step and must be expressed in terms of the values at previous time steps. Two possibilities are allowed in Code_Saturne:[73]

- The mass fluxes calculated at time step n are employed.
- The mass fluxes are evaluated at time step $n + \frac{1}{2}$, estimating them by means of an extrapolation:

$$(\rho v)^{n+\frac{1}{2}} = 2(\rho v)^{n-\frac{1}{2}} + (\rho v)^{n-\frac{3}{2}} \tag{3.72}$$

After the momentum equations are solved, the mass fluxes at time step $n + 1$ are known. Therefore, during the solution of the equations for the turbulent quantities and the transported scalars, other options are available:[73]

- If the mass fluxes at time step n were used in the momentum equations, the same values can be employed.
- Alternatively the newly calculated mass fluxes at $n + 1$ can be used, which is the default choice.
- If the extrapolation at $n + \frac{1}{2}$ was used, the mass fluxes are re-evaluated at the same instant by the interpolation:

$$(\rho v)^{n+\frac{1}{2}} = \frac{2}{3}(\rho v)^{n+1} + \frac{1}{3}(\rho v)^{n-\frac{1}{2}} \tag{3.73}$$

Physical properties and source terms The physical properties are in general known only after the solution of the scalar equations. Therefore, during the solution of the equations they can only be estimated from values at the preceding time steps. The time schemes for their evaluation available in Code_Saturne can be summarised by the general Adam-Bashforth extrapolation:[73]

$$\Phi^{n+\theta_\phi} = (1 + \theta_\phi)\Phi^n - \theta_\phi \Phi^{n-1} \tag{3.74}$$

Values allowed for θ are 0 and 1, with which one obtains a first order discretisation, and 0.5, with which the scheme becomes second-order.

The same considerations are valid for the explicit source term, replacing θ_ϕ with the appropriate parameter θ_S. The implicit contribution follows the same discretisation as

the computed variable if $\theta_S \neq 0$, otherwise it is estimated at time step $n+1$. This exception is justified by stability requirements.[73]

Boundary conditions

Boundary conditions imposed by the user are stored in Code_Saturne as pairs of coefficient, used to account for their contributions to the discretised equations. Two pairs of coefficients are stored for each boundary face and for each variable, which contribute respectively to the discretised convective and diffusive term. The first pair, (A_c, B_c), is used to express the value of the variable at the face as a function of the value at the cell centre:[73]

$$Y_F = A_c + B_c Y_{I'} \tag{3.75}$$

Where Y_F and $Y_{I'}$ are respectively the values at the boundary face and at point I' in Figure 3.4b. The second pair, (A_d, B_d), is used to express the flux of the variable at the face:[81]

$$q''_F = -(A_d + B_d Y_{I'}) \tag{3.76}$$

With the same meaning of the subscripts as above.

As an example, let the boundary facelet with centre in F represent a solid wall. The heat flux through the wall can be represented as:[73]

$$q''_F = -\lambda \frac{\partial T}{\partial n} \simeq -\lambda \frac{T_{I'} - T_F}{\overline{I'F}} \tag{3.77}$$

A Dirichlet boundary condition $T_F = T_w$ can thus be represented by the pairs:

- $(A_c, B_c) = (T_w, 0)$
- $(A_d, B_d) = (-\lambda T_w / \overline{I'F}, \lambda / \overline{I'F})$

If a Neumann boundary condition $q''_F = q''_w$ is imposed, the pairs become as follows:

- $(A_c, B_c) = (q''_w \overline{I'F}/\lambda, 1)$
- $(A_d, B_d) = (-q''_w, 0)$

In Code_Saturne, standard shorthands are provided for the most common boundary conditions, which automatically impose the appropriate condition for each governing equation. A description of those employed in the simulations presented in this study is given below:[73]

Wall Solid walls of the domain can usually be treated as no-slip surfaces. This correspond to imposing a homogeneous Dirichlet boundary condition for all the velocity

components. For pressure, the default treatment is imposing a homogeneous Neumann boundary condition (zero gradient normal to the surface), while for scalars the user can choose between Dirichlet, Neumann or convective boundary condition, in which an external fluid temperature and a heat transfer conditions are imposed. The boundary conditions are internally modified according to the wall functions used if the simulation includes them.

Symmetry Planes of symmetry are defined by imposing homogeneous Neumann boundary conditions for all variables. It can be used to model no-shear wall boundary conditions, modifying the condition for the scalar if required.

Inlet At the inlets of the domain the standard treatment is to prescribe Dirichlet conditions for all the variables except the pressure, for which a homogeneous Neumann condition is applied.

Outlet At the outlets of the domain the standard treatment is to prescribe homogeneous Neumann conditions for all the variables except the pressure, for which a Dirichlet condition is applied.

Structure of a Code_Saturne study

Code_Saturne uses an organised structure for the analysis based on a hierarchy of *studies* and *cases*, which is mirrored by the standard directory tree generated by the code. Before starting the simulation campaign, the structure is created by running the command `code-saturne create` followed by the required options. For instance, to create a study called "*Channel*", which comprises of a case named "*LowReynoldsNumber*", one would run the command:

```
code-saturne create --study Channel --case LowReynoldsNumber
```

To open the graphical interface one must run the command:

```
code-saturne gui
```

from within the case directory.

Once created, the study directory contains the following subdirectories:

- A `MESH` folder in which the meshes for the simulations are stored;
- A `POST` folder, which can be used to store the scripts used for post processing the results, but is not directly used by Code_Saturne;
- One or more case folders (in this example `LowReynoldsNumber`).

In turn, each case folder contains four subdirectories:

- A `DATA` folder in which the data needed for the calculations and the set-up file generated by the graphical interface are stored;
- A `SCRIPT` folder, which contains the launch script;
- A `SRC` folder where the source code of the user subroutines, as well as of every portion of the solver which has been modified, are saved;
- A `RESU` in which the working directories for each run of the solver are created.

When a calculation is run, either through the graphical interface or from the command line, a working folder is created into `RESU`, and all the content of `DATA` is copied into it. An executable of the solver is then created in the working folder: if any source file is found inside `SRC`, it is compiled and linked to the executable. Finally, the calculation starts, and can be monitored from the `listing` file generated in the working folder.

3.3.2 Solver for the solid domain: SYRTHES

To carry out the calculation of thermal conduction in the solid domains and thermal radiation between their surfaces, the model described in Chapter 5 relies on SYRTHES, a finite element thermal analysis software developed by EDF research and development department. Like Code_Saturne, SYRTHES is free software covered by GNU GPL. In the following, a brief description is given of its capabilities, limited to those employed in the studies presented in this work.

Conduction solver

SYRTHES' conduction solver is capable of performing conduction calculations on two-dimensional, axisymmetrical and three-dimensional domains on meshes made out of triangular or tetrahedral elements. The elements are of the type *iso-P2*, characterised by an additional node in the middle of each edge, which divide the triangular or tetrahedral element respectively in four or eight sub-regions. The base function for each sub-region is linear.[82] The subdivision is carried out internally by the code.

The solver is capable of simulating isotropic and non-isotropic materials. In the latter case, the thermal conductivity represented by either a diagonal matrix (orthotropic material, in SYRTHES' terminology) or a full symmetric matrix (anisotropic material). The distinction between the orthotropic and anisotropic materials does not mirror a physical difference, since it originates from a choice of coordinate frames, but it is nonetheless

relevant to the implementation.[83] A first order time advancing scheme is used to simulate transients.[82]

Neumann, Dirichlet and convective boundary conditions can handled by the solver, as well as symmetry and periodicity conditions. At the interface between two solid regions, a contact resistance can be specified. An additional boundary condition type, termed 'infinite radiation', is also allowed. When it is imposed, the heat flux from the surface is calculated assuming that it exchanges thermal radiation with an infinite medium at a given temperature.[83] Coupling with a fluid solver such as Code_Saturne can replace the boundary conditions on one or more surfaces, providing effectively a convective condition. On the contrary, coupling with the radiation solver described below does not replace a boundary condition, but can complement it.

Thermal radiation solver

The three-dimensional model for thermal radiation is based on the assumptions that radiative exchange occurs between opaque solid surfaces in a transparent medium. Therefore it does not account for radiation absorption in the space between the surfaces, nor for transmission through the solid bodies. It is based on the radiosity method, which is summarised below.

The surfaces involved in the radiative exchange are discretised using a mesh made out of segments (for two-dimensional simulations) or triangular elements (for three-dimensional calculations). This mesh is independent from that used in the conduction calculation, which allows for the use of a coarser mesh for the radiation computation. Conversion between the values of the temperatures on the nodes of the conduction mesh and those on the surface elements of the radiation mesh is carried out through a table of interpolation.

For the sake of simplicity, one can assume that the solid bodies involved behave like grey bodies, i.e. their properties do not depend on the wavelength of the radiation. Under this assumption, at each time step the temperature on the face i can be used to estimate the emittance $E_i = \varepsilon\sigma T_i^4$, where ε is the surface emissivity and σ is the Stefan-Boltzmann constant.[82] For problems where the emissivity varies with the wavelength, it is possible to subdivide the spectrum in bands and define a constant emissivity for each band.

The radiosity J_i, i.e. the total energy radiated by the surface, is given by the sum of the face emittance and the reflected portion of the incident radiation. Thus, after some manipulation, the following expression can be written:[82]

$$J_i - \rho_i \sum_{j=1}^{N} F_{ij} J_j = E_i \tag{3.78}$$

where F_{ij} is the view factor between the face i and the face j. When this balance is written for all the N faces, the system allows to determine the radiosity for every face. Since the net flux leaving the solid through the face i is, for a grey body:

$$q''_{rad,i} = E_i - \varepsilon_i \sum_{j=1}^{N} F_{ij} J_j \tag{3.79}$$

it is possible to calculate a boundary condition for the conduction problem from the knowledge of J_i for each face. This is done using an implicit formulation, by defining an auxiliary temperature T_{aux} so that $\sum_{j=1}^{N} F_{ij} J_j = \sigma T_{\text{aux}}^4$. Equation 3.79 can thus be manipulated to write the radiated heat flux as:[82]

$$q''_{rad} = h_{\text{rad}}^n (T_i^{n+1} - T_{\text{aux}}) \tag{3.80}$$

where $T_i^n + 1$ is the temperature in the facelet at time step $n + 1$ and h_{rad}^n is calculated using quantities evaluated at the previous time step.

The view factors are numerically estimated by using an optimised formulation of the "method of the line integral", where the surface integral used in their calculation is replaced by a pair of two line integrals (Figure 3.5):[82]

$$F_{ij} = \frac{1}{\pi S_i} \iint_{S_i} \iint_{S_j} \frac{\cos\theta_i \cos\theta_j}{\pi l^2} dS_i dS_j = \frac{1}{2\pi S_i} \oint_{C_i} \oint_{C_j} \log l dl_i dl_j \tag{3.81}$$

The view factors calculated in this manner must be corrected to account for the shadows cast by other surfaces, i.e. the obstacles encountered by radiation while travelling from one facelet to another. This is a rather costly operation which is carried out by considering a set of lines between the facelets and identifying the surfaces intersected.[82] Due to the computational intensity of the task, the view factors are saved in a binary file which can be reused in all the following calculations which use the same mesh.[83]

Coupling with Code_Saturne

The code is designed to be easily coupled with Code_Saturne to carry out conjugate heat transfer calculations: in normal use, it is sufficient to specify the coupling surfaces to both the programs in order to establish a coupled simulation.[80] However, when the interface between the solid and the fluid domains is not resolved, as in the porous model described in this work (see Chapter 5), the built-in capabilities are not sufficient: although a "volumetric coupling" capability is available in the code, this is aimed at the simulation of scenarios where the solid domain undergoes the same simplification described in as the fluid, and is not satisfactory for scenarios where the solid model resolves the details

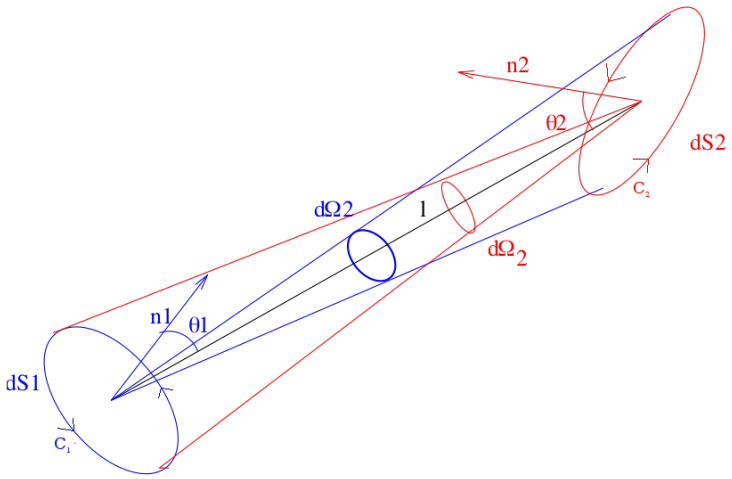

Figure 3.5: Schematics of the calculation of the view factors. Adapted from ref. [82].

of the geometry. A patch was therefore developed to adapt the coupling infrastructure to the requirements of the porous model, as described in Appendix A.

For the surface coupling, used at the boundaries of the porous region (e.g along the graphite sleeve), the communication occurs through the existing interface. SYRTHES receives from Code_Saturne the fluid temperatures for the cells adjoining the walls and the heat transfer coefficients evaluated according to the turbulence model used. In turn, it transfers the temperatures at the solid surface to the fluid solver. Since mesh nodes are not required to be coincident at the shared surfaces, the solvers carry out an interpolation of the quantities received before applying the boundary conditions on the appropriate node.

3.3.3 Geometry and mesh generation: SALOME

SALOME is a cross-platform suite of utilities for scientific calculations developed jointly by EDF, Open Cascade and the French Commissariat à l'Energie Atomique (CEA). It provides a number of tools to support the computational analysis from the generation of the geometry to the post-processing of the results which include the following (this is not a complete list):[84]

- *Geometry*, to create and edit geometrical models;
- *Mesh*, to generate computational grids from a model created with *Geometry*;
- *YACS*, for the integration of different solvers in a coupled calculation;
- *Parametric*, which allows to run parametric studies using a specified solver;

- *ParaViS*, a visualisation tool based on *ParaView*

In this study, *Geometry* and *Mesh* are used jointly to create the meshes for the fluid and the solid domains (see Sections 5.2). Both utilities provide Python APIs to script the generation of the model. This allows the flexibility of varying the size of the geometry and the mesh by changing the values of a set of parameters. Through the APIs it is possible to perform all the operations allowed in the graphical interface, including drawing points, lines, surfaces and volumes, performing boolean operations between shapes, extrusions, transformations on both the geometric model and the mesh and so on.[84]

SALOME is open-source software, distributed under GNU LGPL, and it is freely available, together with its source code, from its website.[d]

[d] `http://www.salome-platform.org/downloads/current-version`

Chapter 4

Large Eddy Simulation of natural convection in an enclosed fuel pin bundle

In this chapter the results of a Large Eddy Simulation of buoyancy driven flow in an enclosed pin bundle are presented for a scenario, in which a constant and uniform heat flux is provided to the fluid from the pins.

In Sections 4.1 a physical and geometric description of the scenario under examination is outlined. A description of the results obtained in the case simulated is found in Section 4.2. An evaluation of the quality of the calculation according to two parameters proposed in the literature is presented in Section 4.2.1. Sections 4.2.2 and 4.2.3 provide a discussion of the general features observed in the simulated flows, while in Section 4.2.4 the region in the immediate vicinity of the walls is analysed in more detail. Finally, in Section 4.3 an attempt to provide correlations for heat transfer is presented.

4.1 Description of the scenarios

The study presented in this chapter concerns natural convection along an enclosed pin bundle, where heat is provided from the pins and removed from the outer sleeve. Although the arrangement of the pins corresponds to that found in AGR stringers, the geometry considered is considerably simplified: the computational domain is $250\,\mathrm{mm}$ tall, about one quarter of the size of a single fuel element. Moreover, the roughness of the outer surface of the claddings was entirely neglected.

The mesh employed is shown in Figure 4.1. It represents a 60° sector, or one sixth of the bundle, discretised with about 11.7 million elements. The regions adjoining the boundaries corresponding to the guide tube, the pins and the sleeve walls are discre-

Property	Symbol	Value	Units
Density	ρ	$\sum_{i=0}^{5} \rho_i T_k^i$	$\mathrm{kg\,m^{-3}}$
	ρ_0	4.561×10^{2}	$\mathrm{kg\,m^{-3}}$
	ρ_1	-2.350	$\mathrm{kg\,m^{-3}\,K^{-1}}$
	ρ_2	5.369×10^{-3}	$\mathrm{kg\,m^{-3}\,K^{-2}}$
	ρ_3	-6.196×10^{-6}	$\mathrm{kg\,m^{-3}\,K^{-3}}$
	ρ_4	3.535×10^{-9}	$\mathrm{kg\,m^{-3}\,K^{-4}}$
	ρ_5	-7.925×10^{-13}	$\mathrm{kg\,m^{-3}\,K^{-5}}$
Dynamic viscosity	μ	2.314×10^{-5}	$\mathrm{Pa\,s}$
Specific heat	c_p	1.097×10^{3}	$\mathrm{J\,kg^{-1}\,{}^{\circ}C^{-1}}$
Thermal conductivity	λ	3.700×10^{-2}	$\mathrm{W\,m^{-1}\,{}^{\circ}C^{-1}}$
Prandtl number	Pr	6.860×10^{-1}	

Table 4.1: Physical properties imposed to the fluid in the study presented in Chapter 4. T_k is the gas temperature in K.

tised by structured, hexahedral sub-meshes, while the rest of the mesh is formed by automatically generated prismatic cells. The mesh was generated by extrusion from a two-dimensional discretisation of the cross-section. In the extrusion direction the mesh consists of a total of 210 divisions, of which 30 are found in each of the $10\,\mathrm{mm}$ long layers adjoining the top and bottom boundary, with a progressive refinement towards the walls. The remaining 150 are uniformly distributed in the $230\,\mathrm{mm}$ long central region. Similarly, the cross-sectional mesh is progressively refined in the region next to the vertical boundaries, with a $1.6\,\mathrm{mm}$ thick layer adjoining the guide tube, pins and sleeve boundary, discretised respectively by 14, 28 and 50 divisions. The non-dimensional distance y^+ of the first node from the wall was between 0.022 and 0.483 along the pins, between 0.010 and 0.238 along the guide tube, and between 0.006 and 0.257 along the sleeve. Figure 4.2 shows a schematic depiction of the cross section, with an outline of the blocks which form the mesh. As a reference for the following discussion, the lines used in the post-processing phase to extract the profiles of the quantities of interest are also indicated.

All physical properties except for density were set to constants. A fifth-order polynomial fit was used for the density, obtained from tabular data for carbon dioxide at the pressure of $4.2\,\mathrm{MPa}$. The values of all the properties and the coefficients of the density fitted are reported in Table 4.1. An eddy viscosity is defined to account for turbulent diffusion, calculated using the WALE LES model described in Section 3.1.4.

The choice of modelling a 60° sector of the domain allowed the use of rotational periodicity on the two azimuthal vertical boundaries, which is deemed to be more suitable than a symmetry boundary condition, in that it does not impose artificial constraints on the variable calculated. Figure 4.3 provides a depiction of the domain, showing the

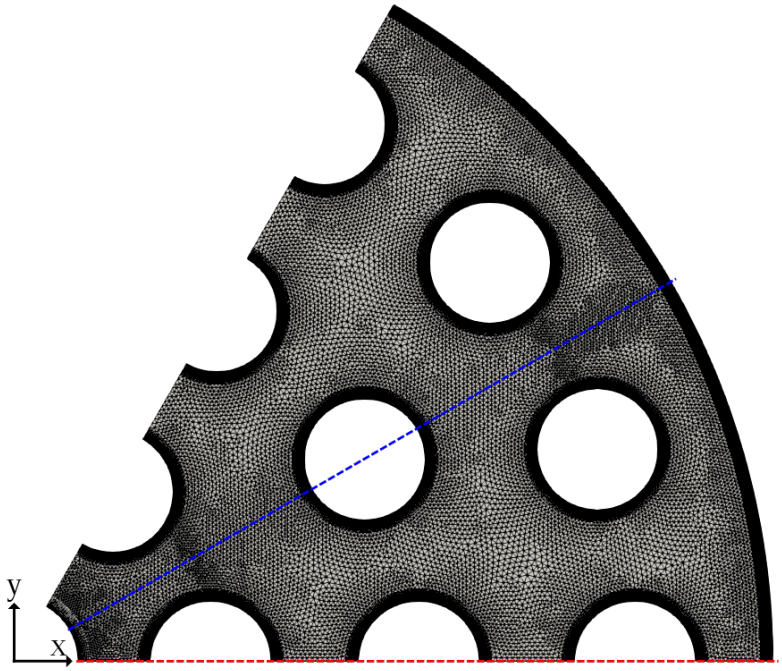

Figure 4.1: Mesh used in the LES studies described in Chapter 4. The figures show the cross section normal to the z axis. The dashed lines indicate the traces of the slices used in the post-processing stage.

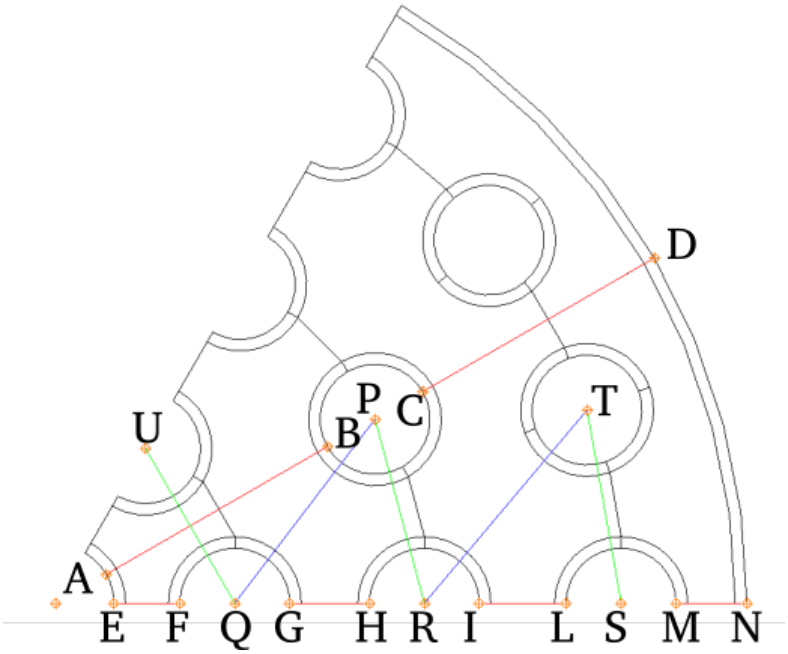

Figure 4.2: Outline of the sub-meshes in the discretisation of the cross-section, and the lines used in the post-processing phase to extract the profiles of the quantities of interest.

Non-dimensional number	Value
$\mathrm{Gr}_{q''}$	1.722×10^{13}
$\mathrm{Ra}_{q''}$	1.181×10^{13}
$\mathrm{Gr}_{\Delta T_w}$	1.133×10^{11}
$\mathrm{Ra}_{\Delta T_w}$	7.772×10^{10}
U_b	$4.198\,\mathrm{m\,s^{-1}}$

Table 4.2: Grashof and Rayleigh numbers and buoyant velocity for the scenario presented in Chapter 4.

boundary condition imposed in the calculation. The top and bottom boundaries of the domain were treated as adiabatic no-shear walls by imposing symmetry boundary conditions on them. An adiabatic no-slip boundary condition was imposed on the surface corresponding to the Guide Tube wall, whilst the boundary corresponding to the sleeve wall is treated as a no-slip wall with a convective boundary condition imposed on it, with an exchange coefficient of $100\,\mathrm{W\,m^{-2}\,^{\circ}C^{-1}}$ and an external temperature of $22\,^{\circ}\mathrm{C}$. The value chosen for the heat transfer coefficient is arbitrary, but plausible for forced convection in a gas[85]. Finally, no-slip boundary condition were applied to the pin surfaces. In the case presented in this chapter a uniform heat flux, equal to $324.5\,\mathrm{W\,m^{-2}}$, was imposed on the pin boundaries. It is possible to use two definitions for the Grashof number and, equivalently, for the Rayleigh number $\mathrm{Ra} = \mathrm{GrPr}$. One definition is based on the value of the heat flux through the pins:

$$\mathrm{Gr}_{q''} = \frac{g\beta_f H^4 q''}{\nu^2 \lambda} \tag{4.1}$$

where g is the acceleration due to gravity, β_f is the volumetric expansion coefficient of the fluid, H is the height of the domain, q'' is the heat flux from the pins and $\nu = \mu/\rho$ is the kinematic viscosity. The second definition is based on the difference between the average temperatures of the pins and the sleeve walls, ΔT_w:

$$\mathrm{Gr}_{\Delta T_w} = \frac{g\beta_f H^3 \Delta T_w}{\nu^2} \tag{4.2}$$

A related quantity is the buoyant velocity:

$$U_b = \sqrt{\frac{g\beta_f H^2 q''}{\lambda}} \tag{4.3}$$

Employed in the following as a reference velocity for the normalisation of the velocities and turbulent kinetic energies. Table 4.2 reports the values of the Grashof and Rayleigh numbers obtained following both definitions.

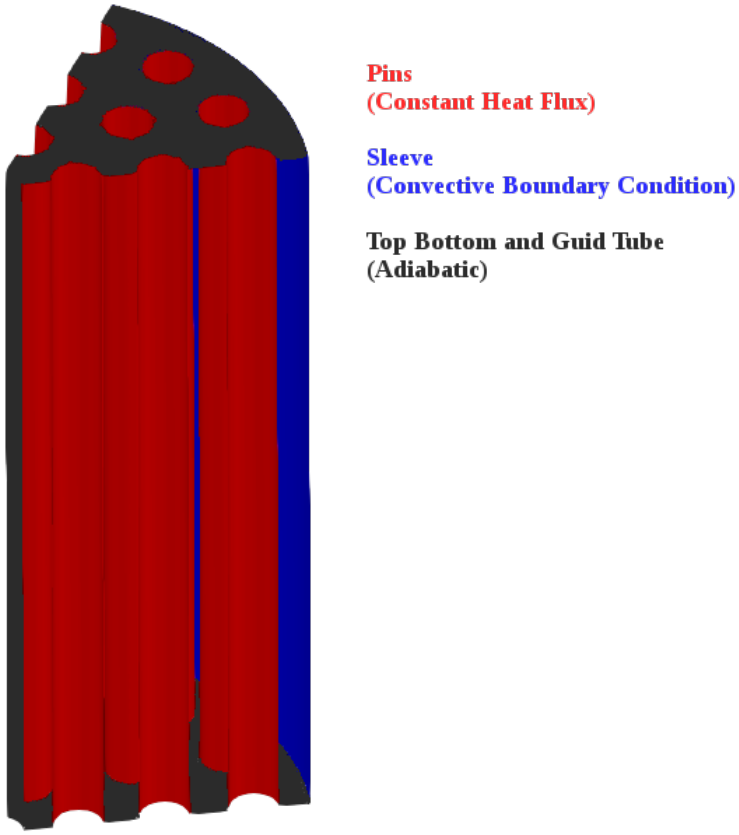

Figure 4.3: Boundary conditions for the simulation described in Chapter 4. To enhance clarity, the periodicity surface were not included.

The second ordered centred scheme described in Section 3.3.1 was used to evaluate the velocity and temperature at the interfaces between cells. After an initial stage in the calculation, where a time step of $2.0 \times 10^{-3}\,\mathrm{s}$ was used to speed up the transient, the time step was reduced to $2.5 \times 10^{-4}\,\mathrm{s}$, which corresponded to a maximum Courant number oscillating between 0.25 and 0.98. Although the time advancing scheme used was implicit, and therefore there was no stability requirement on the value of the Courant number, this time step was deemed to give a good compromise between the rapidity of the simulation and the accuracy of the results.A preliminary RANS calculation was carried out to provide an initial condition for the simulation.

The time averages of the temperature, pressure, density, velocity component and their mutual products were calculated within Code_Saturne, and formed part of the output of the simulation. Their values were monitored at different points in the domain, and the transient was considered to be completed when they became appreciably stationary. After this state was achieved, the time step was reduced and the calculation was continued to build a sufficient statistical sample. The instant when this phase began will be labelled t_0 in the following.

The averaged fields output by Code_Saturne at time t refer to the time interval $[0; t]$. In order to calculate the average in the interval $[t_0; t]$, and therefore to exclude the contribution of the transient to the average, the following manipulation was necessary. Let:

$$\overline{\phi}_{[t_i,t_j]} = \frac{1}{t_j - t_i} \int_{t_i}^{t_j} \phi dt \tag{4.4}$$

be the average of the quantity ϕ between the instant t_i and t_j, where $t_j > t_i$. The average in the interval $[t_0; t]$ can be written as:

$$\overline{\phi}_{[t_0,t]} = \frac{1}{t - t_0} \int_{t_0}^{t} \phi dt = \frac{1}{t - t_0} \left(\int_0^t \phi dt - \int_0^{t_0} \phi dt \right) \tag{4.5}$$

This expression can be rewritten making use of the averages calculated by Code_Saturne:

$$\overline{\phi}_{[t_0,t]} = \frac{1}{t - t_0} \left(t\,\overline{\phi}_{[0,t]} - t_0\,\overline{\phi}_{[0,t_0]} \right) \tag{4.6}$$

The covariances of the velocity, $\overline{v_i' v_j'}$, were calculated from the averaged velocities and products of velocities, according to the relation:

$$\overline{v_i' v_j'} = \overline{v_i v_j} - \overline{v_i'}\,\overline{v_j'} \tag{4.7}$$

In turn, they were used in the calculation of the turbulent kinetic energy, $k = \overline{v_i' v_i'}/2$.

The calculation was continued until the averages calculated according to Equation

4.6 ceased to evolve. Figures 4.4 and 4.5 show the evolution of the average velocity, temperature, and non-dimensional turbulent kinetic energy profiles along two of the lines shown in Figure 4.2. It can be observed that after a period of adjustment the velocity and temperature profiles do not change appreciably. It must be noted, however, that small but noticeable variation in the turbulent kinetic energy are still observed at the end of the calculation. This, and the roughness of its distribution noted in the following sections, seems to suggest that the second order momenta would require significantly longer computations to achieve complete convergence in this natural convection scenario.

4.2 Results

In this section, the results of the simulation described in Section 4.1 are presented. As mentioned above, a uniform heat flux of $324.5\,\mathrm{W\,m^{-2}}$ was imposed through the walls of the pins.

4.2.1 Quality of the simulation

In Section 3.1.4, it was pointed out that the LES approach to the simulation of turbulent flow is based on the application of a spatial filter, which remove the information relative to the smallest eddies while allowing one to simulate the largest scales of the flows. Many Sub Grid Scale models are available to the analyst to take into account the contribution of the small vortices to the overall diffusion, some of which are presented in Section 3.1.4.

The Sub Grid Scale models are based on assumptions whose validity depends on the width of the filter adopted, which in the majority of applications coincides with the local size of the mesh. Moreover, by their own nature, however advanced they may be models represent an approximation of the real behaviour of a fluid, and therefore introduce a *modelling error* in the calculation.

Therefore, it is desirable for an accurate simulation that the influence of the model be kept to a minimum. A 'high-quality' LES will therefore be one that employs a mesh fine enough that the contribution of the unresolved scales should be relatively small compared to that of the vortices which are explicitly simulated.

In this study, two criteria proposed by Celik, Cehreli, and Yavuz[86] are used to assess the quality of the calculation. Both are based on the comparison of the turbulent diffusion due to the unresolved scales to the molecular diffusion in the fluid. An estimate of the numerical diffusion due to the mesh coarseness is also included.

The first estimator used is the s^* parameter, the ratio of the sub-grid and numerical

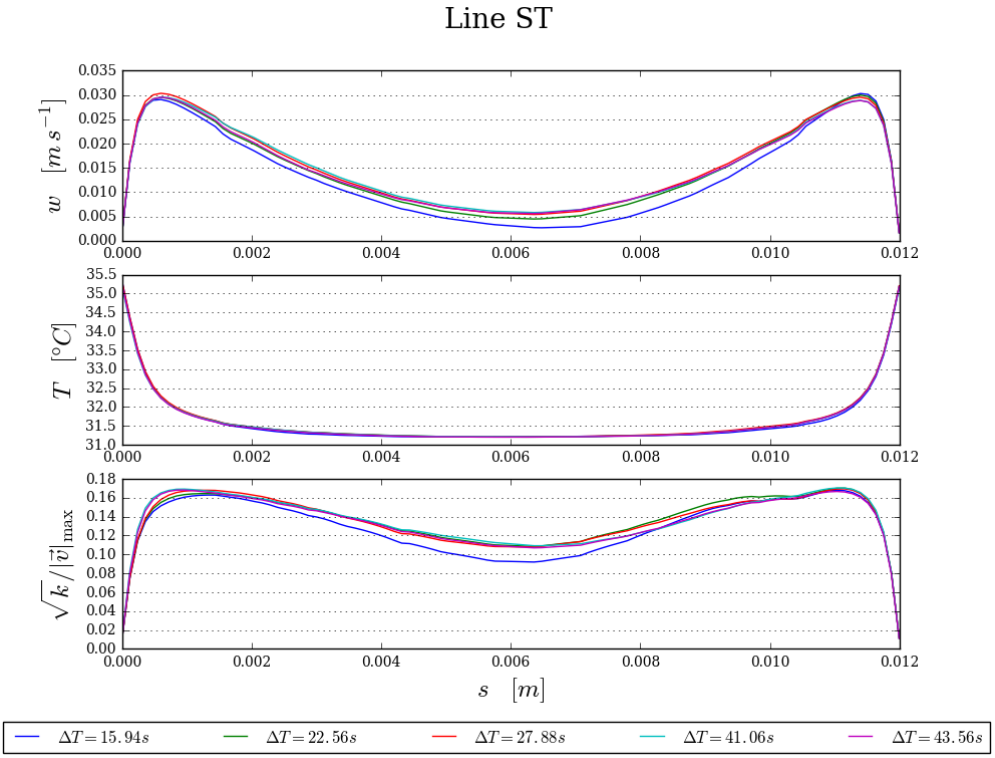

Figure 4.4: Evolution of the time averaged axial velocity and temperature along line ST of Figure 4.2 at $z = \frac{4}{5}H$, for different length of the averaging interval.

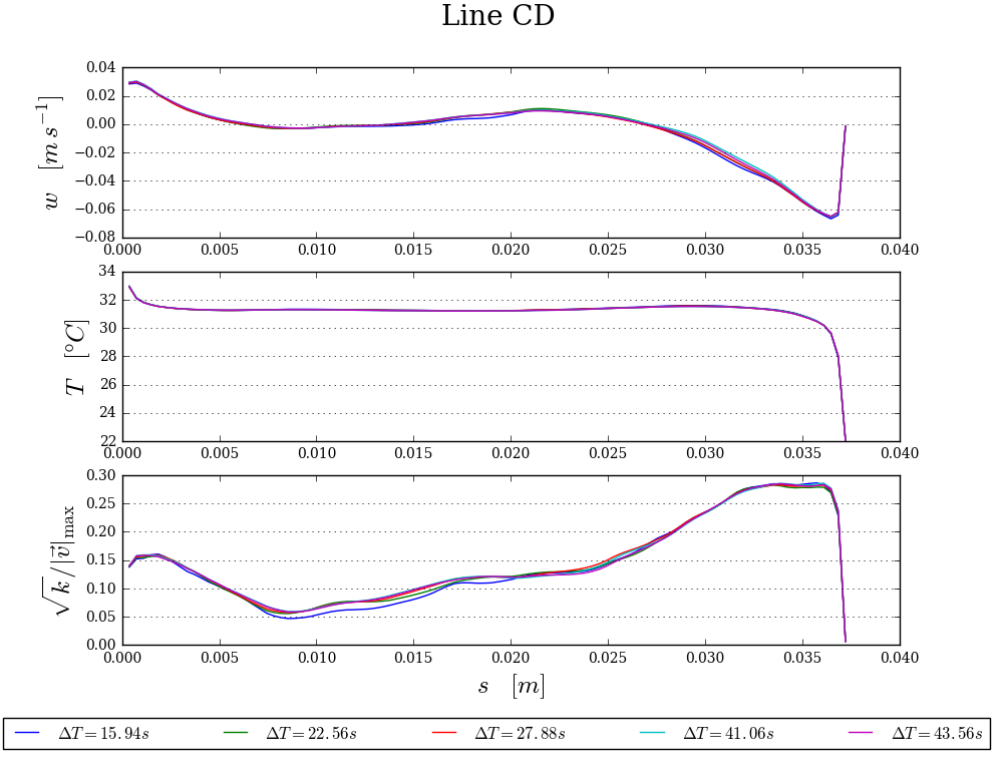

Figure 4.5: Evolution of the time averaged axial velocity and temperature along line CD of Figure 4.2 at $z = \frac{4}{5}H$, for different length of the averaging interval.

diffusivity to the total diffusivity in the calculation:[86]

$$s^* = \frac{\mu_{sg} + \mu_{num}}{\mu_{sg} + \mu_{num} + \mu} \tag{4.8}$$

where μ_{sg} is the sub-grid dynamic viscosity predicted by the model, μ_{num} is the numerical 'viscosity' produced by the mesh, and μ is the molecular dynamic viscosity of the fluid. The parameter $s*$ thus indicates the relative influence of the model on the calculation. It takes values in the range $[0; 1[$ with high values indicating a calculation sensitive to modelling errors.

By manipulation of the expressions provided by Celik, Klein, and Janicka[87] for the sub-grid and numerical viscosities and kinetic energies, one can conclude that, when the width of the filter is equal to the local size of the mesh, in first approximation it can be assumed $\mu_{sg} \simeq \mu_{num}$.

Figure 4.6 shows the distribution of s^* on two vertical planes, whose traces are shown as a red and a blue line in 4.1. Higher values of the parameter are found in the regions where intense turbulence is observed (see Section 4.2.2) and lower in the regions with less intense mixing.

A shortcoming of the parameter s^* as a quality indicator is that for poor quality calculations it assumes values very close to 1, at the upper end of the range. A second estimator, the $\mathrm{LES_{iq}}$ parameter, was thus proposed by Celik, Cehreli, and Yavuz,[86] to obviate to this flaw:[86]

$$\mathrm{LES_{iq}} = \frac{1}{1 + \alpha_v \left(\frac{s^*}{1 - s^*} \right)^n} \tag{4.9}$$

where $\alpha_v = 0.05$ and $n = 0.53$. The information it provides is analogous to that provided by s^*, but it is more sensitive to differences between poor quality simulations. Contrary to s^*, high values of $\mathrm{LES_{iq}}$ indicate high quality of the calculation. Values above 0.8, corresponding to $s^* \lesssim 0.954$, indicate a good quality LES.

Figure 4.7 shows the distribution of $\mathrm{LES_{iq}}$ on the same vertical planes mentioned above. Lower values of the parameter are again found in the regions of higher turbulence. $\mathrm{LES_{iq}}$ is greater than the recommended value everywhere, and hence the distribution indicates a high mesh resolution throughout the domain.

Figure 4.8 details the distribution of the indicators across the volume of the domain, by showing the fraction of the volume in which the indicators assume values in different ranges. Figure 4.8a shows that intermediate values of s^* are predominant throughout the domain, with values lower than $s^* = 0.5$ found in $51.9\,\%$ of the domain and volume average equal to 0.47. As noted above, $\mathrm{LES_{iq}}$ assumes values greater than $85\,\%$ in $100\,\%$ of the domain, (Figure 4.8b), confirming the quality of the discretisation used.

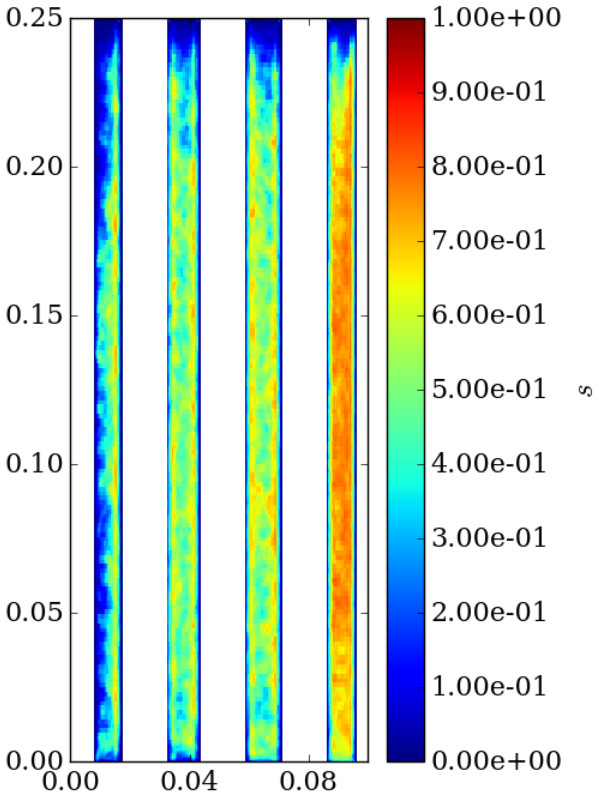

(a) Periodicity plane.

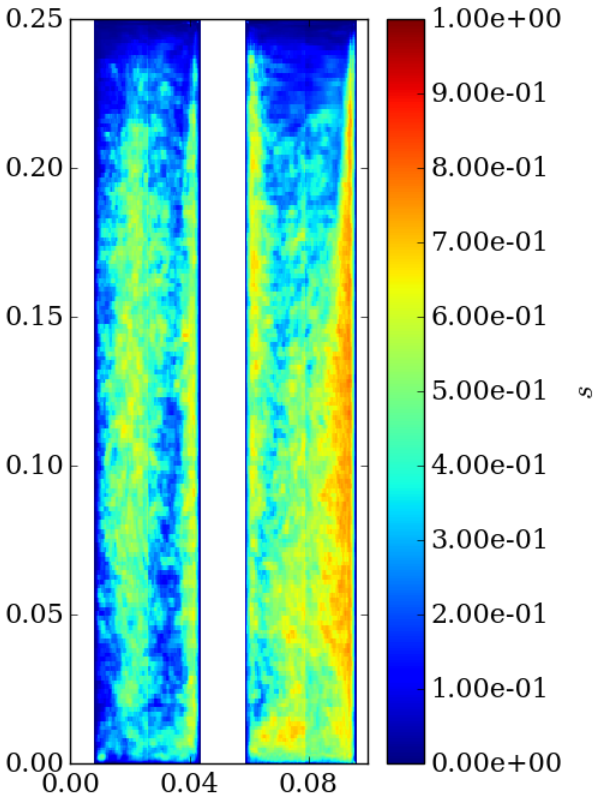

(b) Symmetry plane.

Figure 4.6: Maps of the quality indicator s^* of Equation 4.8 on the periodicity plane (trace in red in Figure 4.1) and on the symmetry plane (trace in blue in Figure 4.1) of the domain.

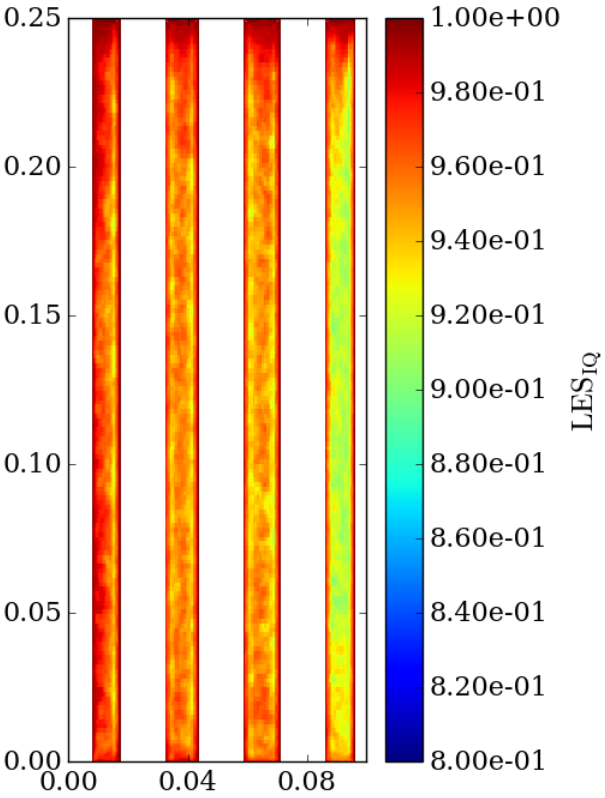

(a) Periodicity plane.

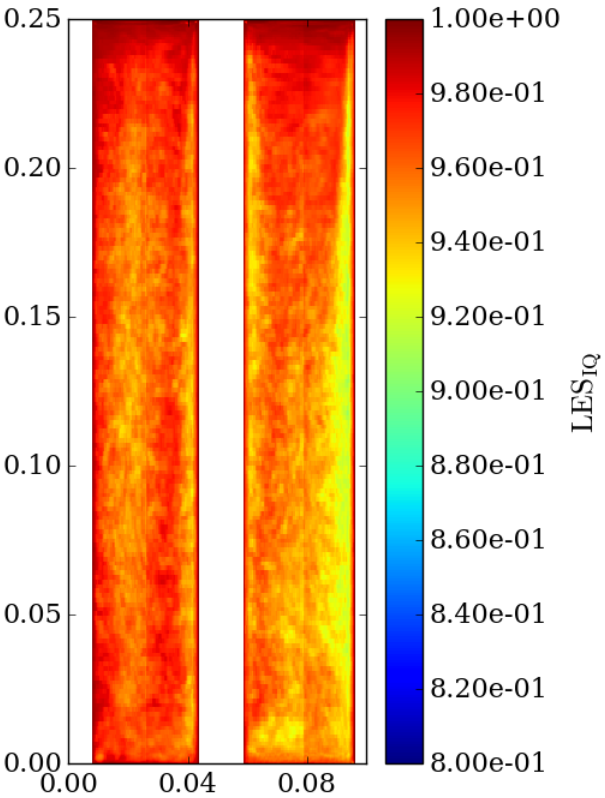

(b) Symmetry plane.

Figure 4.7: Maps of the quality indicator $\mathrm{LES}_{\mathrm{iq}}$ of Equation 4.9 on the periodicity plane (trace in red in Figure 4.1) and on the symmetry plane (trace in blue in Figure 4.1) of the domain.

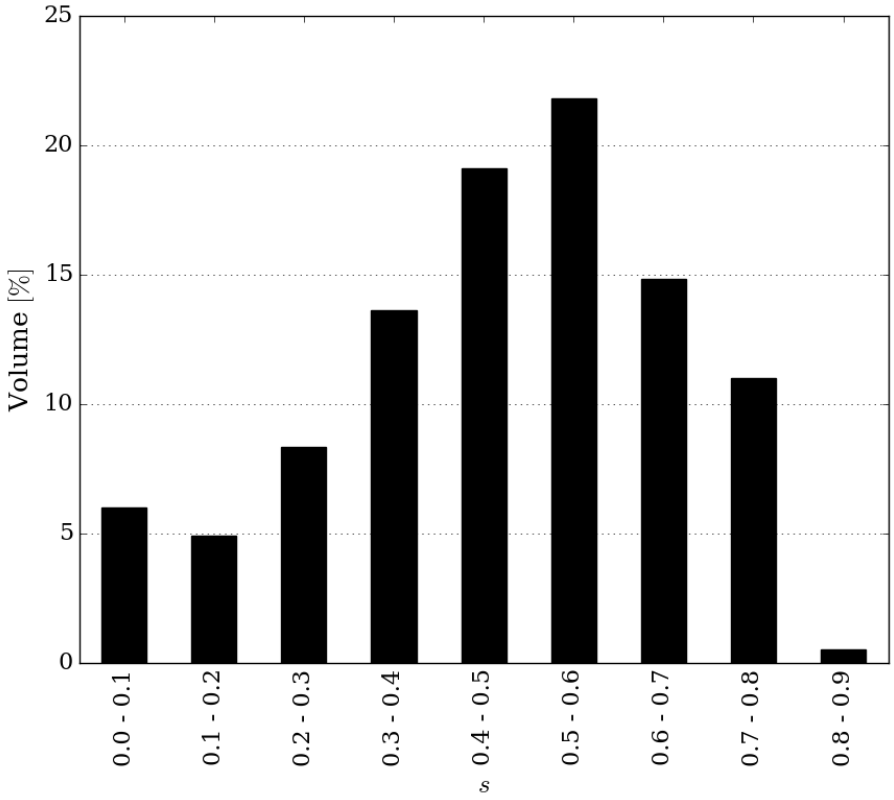

(a) s^*.

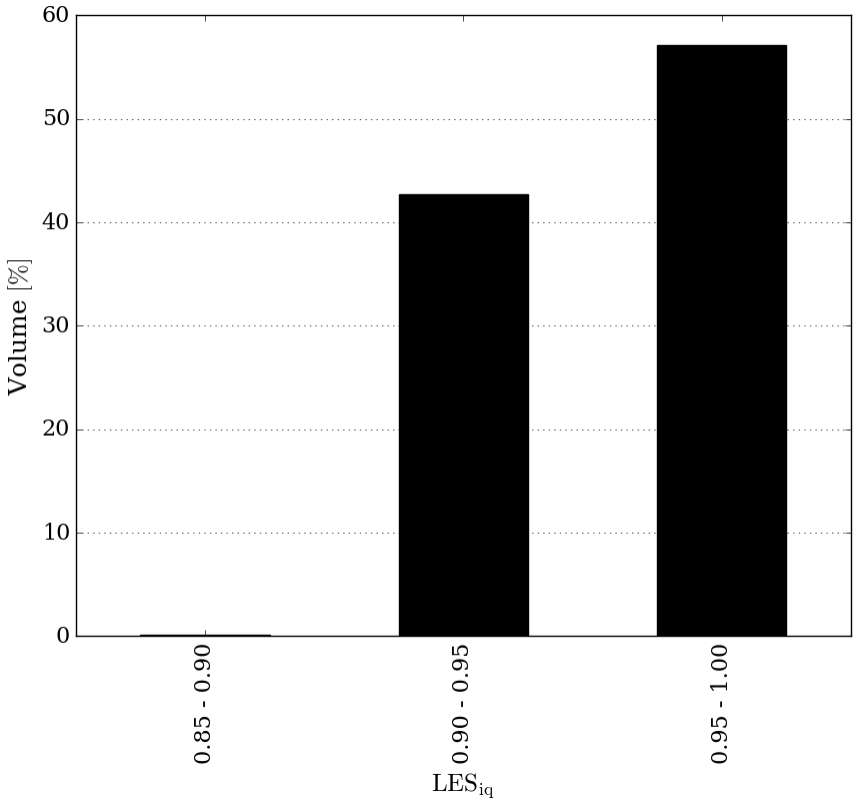

(b) $\mathrm{LES}_{\mathrm{iq}}$.

Figure 4.8: Subdivision of the volume of the domain according to the values taken by the quality indicators s^* (Equation 4.8) and $\mathrm{LES}_{\mathrm{iq}}$ (Equation 4.9).

4.2.2 General features

Figures 4.9 and 4.10 show the distribution of the instantaneous and average temperature and velocity, and of the turbulence intensity on two vertical planes. The turbulence intensity was defined as the ratio between the square root of the local turbulent kinetic energy and the buoyant velocity U_b. The velocities, here and in the rest of the section, were also normalised by dividing them by U_b. The slice shown in Figure 4.9 lies on the xz plane and corresponds to the periodicity surface defined in the calculation (trace drawn in red in Figure 4.1), whilst the plane in Figure 4.10 is rotated from the former by an angle of 30° around the z axis and represents a symmetry plane for the domain (in blue in Figure 4.1).

Observation of the velocity and temperature distributions (Figures 4.9a, 4.9b, 4.10a and 4.10b) show the existence of a vast stagnant region in the core of the domain, whilst significant fluid motion is found only in thin layers adjoining the active walls, where velocities are predominantly vertical, and at the top and the bottom of the domain, where cross-flow is most relevant. Ascending velocities are found along the heated surfaces (pins), while downward flow takes place along the cooled surface (sleeve). Thermal stratification is clearly visible, with small variation of the vertical temperature gradient throughout the domain, except at the extrema. This is shown evidently in the axial profile of the mass-averaged gas temperature in Figure 4.11. The figure also shows the average pin surface temperature as a function of the height. No appreciable difference is found between the three ranks, in agreement with the findings of Rao and Glakpe.[70]

These features are typical of the laminar *Boundary Layer* flow regime described in Section 2.4. However, the flow deviates from a purely laminar behaviour in the vicinity of the active walls of the domain. At the sleeve walls, a sizeable region of intense turbulent mixing is found next to the fast descending flow in the boundary layer, as highlighted by the region of higher turbulence intensity visible in Figures 4.9c and 4.10c. The extension of this region reaches the outermost rank of pins, and merges into the turbulent region originated by the latter (the blue-green area in Figure 4.10c). At the pin walls, where lower velocities are found, instabilities are encountered in the form of travelling waves (Figure 4.12), possibly related to the 'wall waves' described by Elder[56] in his study of transition to turbulence (Figure 2.6a).

Figures 4.13, 4.14 and 4.15 show the distributions of the velocity, temperature and turbulence intensity on six cross-sectional planes regularly spaced along the domain. Since the quantities considered vary significantly with the axial position, different scales were used for different vector and contour plots in order to exaggerate the variation of the quantities considered across the cross-section.

The color scale in Figure 4.13 represents the axial velocity of the gas, while the cross-

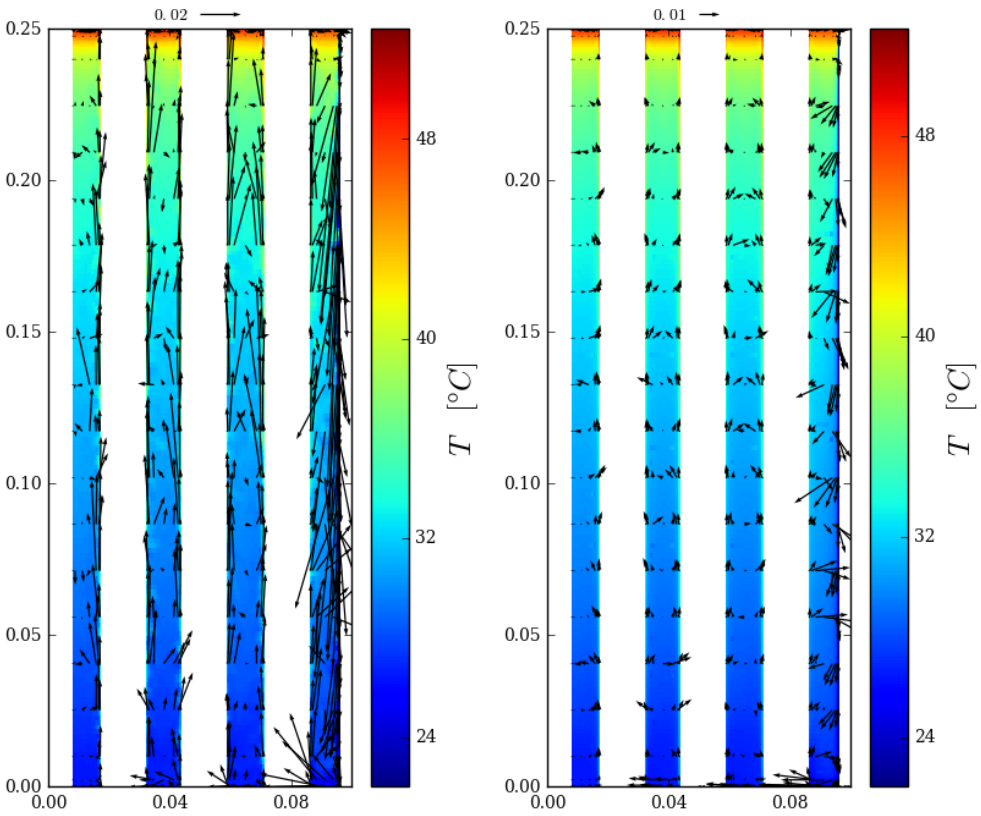

(a) Instantaneous velocity and temperature. (b) Time averaged velocity and temperature.

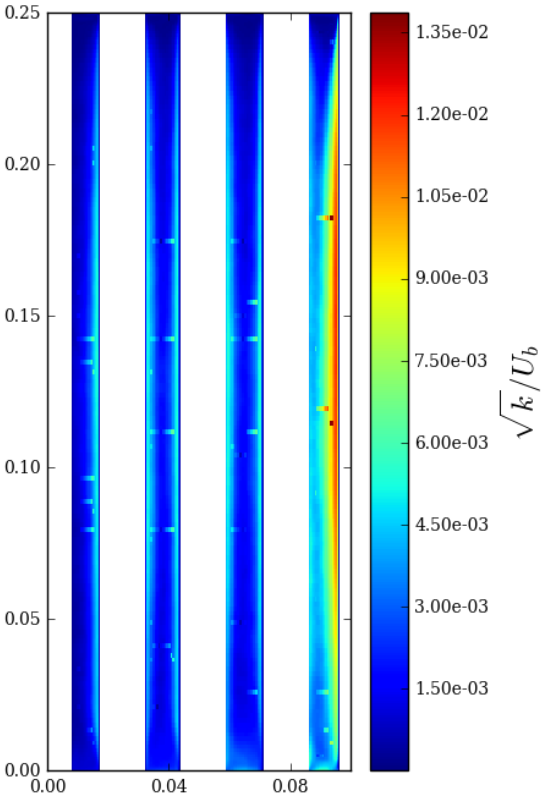

(c) Turbulent intensity (see caption to Figure4.15).

Figure 4.9: Maps of some quantities of interest on the vertical periodicity plane (trace in red in Figure 4.1).

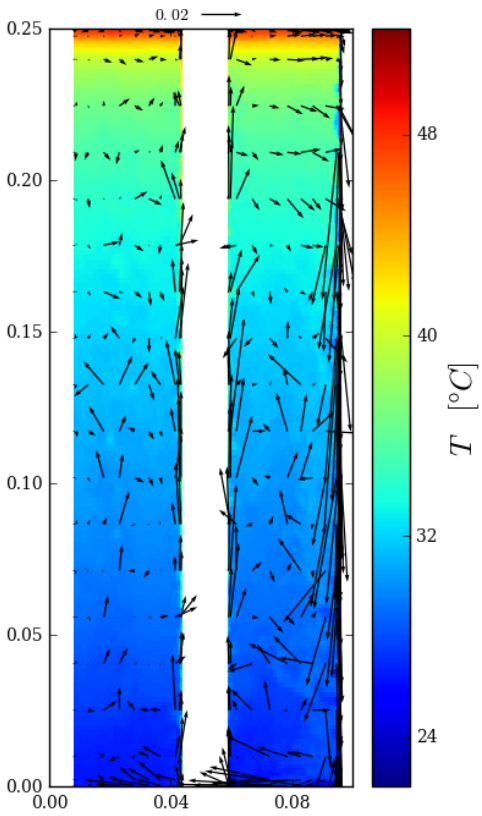

(a) Instantaneous velocity and temperature.

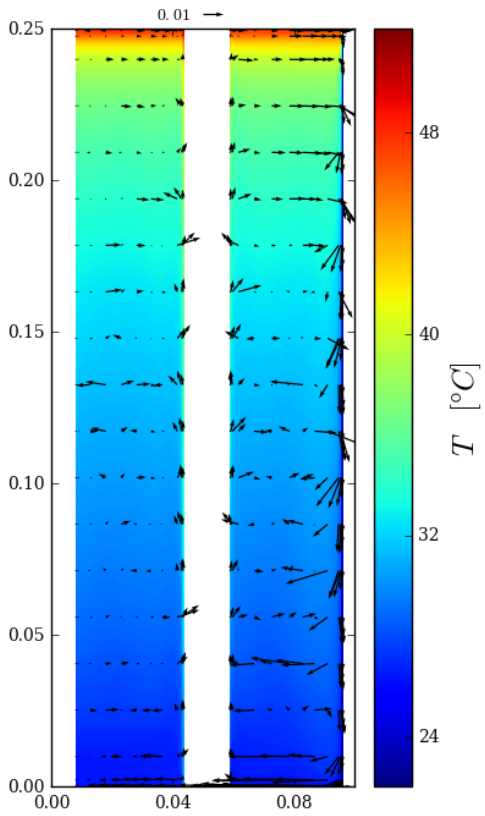

(b) Time averaged velocity and temperature.

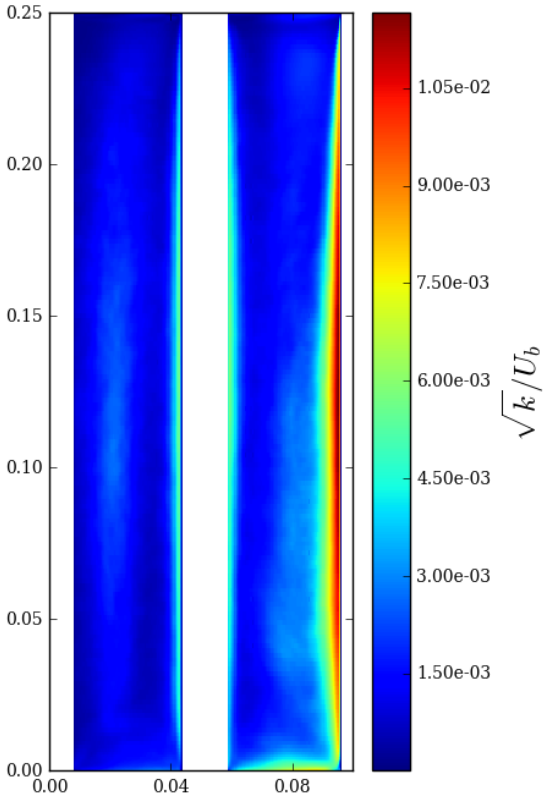

(c) Turbulent intensity (see caption to Figure4.15).

Figure 4.10: Maps of some quantities of interest on the vertical symmetry plane (trace in blue in Figure 4.1).

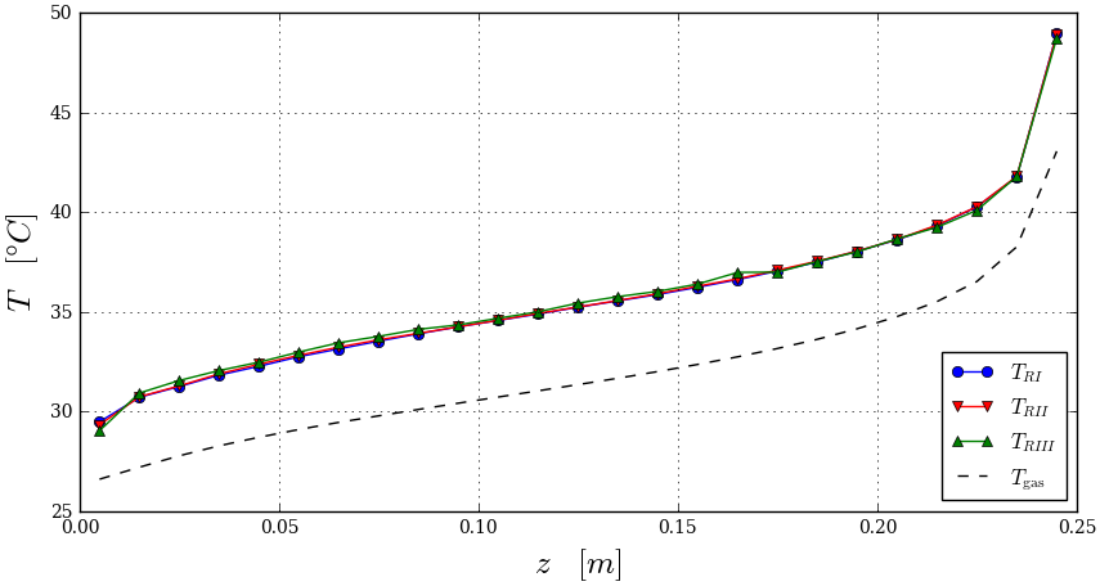

Figure 4.11: Axial profile of the average surface temperature of the three ranks of pins and of the mass averaged gas temperature.

sectional velocities are depicted as vectors. The plots confirm that, except at the top and bottom of the domain, significant gas motion takes place exclusively in thin layers along the active walls, whereas in most of the cross-sections both axial and transversal velocities are very small or negligible. The scale of the vectors used in in Figure 4.13a is different from that used in the remaining plot, due to the large difference in magnitude between the transversal velocity at the bottom and in the rest of the domain. The black contour lines mark the loci of the points where the axial velocity is $0\,\mathrm{m\,s^{-1}}$. It shows the presence of very small downward velocities in the core of the fluid domain, in agreement with the experimental observations reported by Keyhani, Kulacki, and Christensen[64].

The distribution of the gas temperature presented in Figure 4.14 is relatively uniform within each cross section, with observable temperature gradients found only in the vicinity of the active surfaces. Different colour scales are used in slices placed at different height. Despite this, a shift towards the top of the scale is observed as the position of the slice moves towards the top. This is due to the boundary condition placed on the sleeve, which causes the temperature on its surface to be close to $30\,^{\circ}\mathrm{C}$ at all heights, thus keeping the minimum of the scale almost constant. Azimuthal variations of the temperature around the pins tend to be small, except at the bottom of the domain where strong cross-flow from the sleeve to the centre takes place and local maxima can be found on the leeward side of the pins.

Figure 4.15 shows the distribution of the turbulence intensity. As mentioned in Section 4.1, the distribution does not appear entirely smooth, suggesting that a longer simulation time would be required in order to achieve the complete convergence of the second

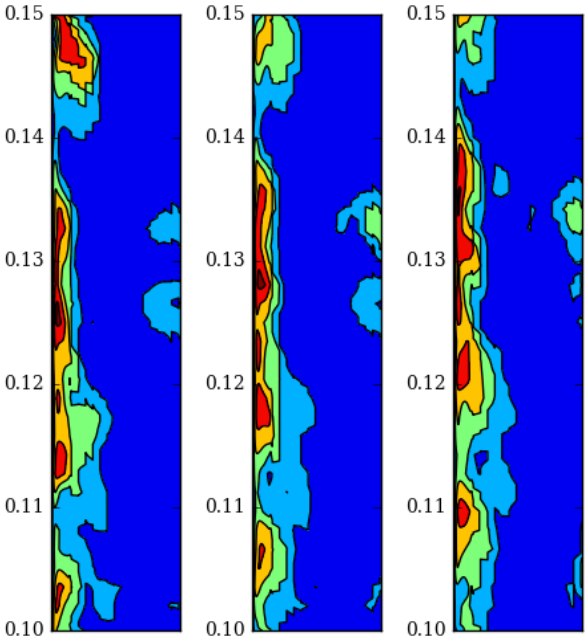

(a) t_0. (b) $t_0 + 125\,\mathrm{ms}$. (c) $t_0 + 250\,\mathrm{ms}$.

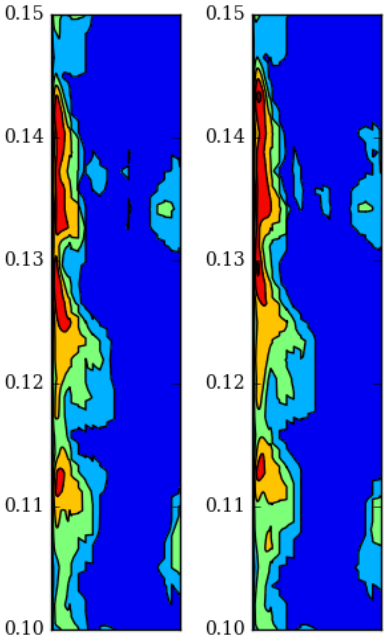

(d) $t_0 + 375\,\mathrm{ms}$. (e) $t_0 + 500\,\mathrm{ms}$.

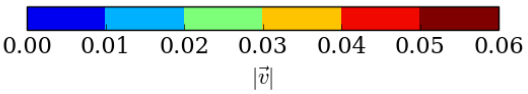

(f) Colour scale

Figure 4.12: Magnitude of the velocity in proximity of one of the fuel pins in the second rank at $100\,\mathrm{mm} \leq z \leq 150\,\mathrm{mm}$, showing the presence of travelling waves.

order momenta. To make the cross-sectional patterns more visible, different colour scales were used for different plots. In all planes except at the top higher values of k are found in annular regions surrounding the pins, decreasing towards the core. The highest values are found next to the sleeve, due to the higher velocities encountered there and, presumably, to the proximity of the boundary layer of the pins in the third rank flowing in the opposite direction. The overall turbulence in the cross-sections appears to decrease in the top section of the domain, where the regions of intense mixing decrease in extension.

At the bottom of the domain (Figure 4.15a) local maxima are also found in the wake generated by the pins, particularly those in the outermost rank, on the cross-flow shown in Figure 4.13a. Very small values are encountered across the top cross section (Figure 4.15f).

4.2.3 Profiles of velocity, temperature and turbulent kinetic energy

Figures 4.16, 4.17 and 4.18 show qualitatively the evolution of the profiles of the axial velocity, temperature, and turbulence intensity along four of the lines depicted in Figure 4.2. The development of the same profiles in the bottom $20\,\mathrm{mm}$ of the domain is shown in Figures 4.19, 4.20 and 4.21, whilst in Figures 4.22, 4.23 and 4.24 the behaviour in the top $20\,\mathrm{mm}$ is illustrated. For comparison, in all figures the profile at mid-height is plotted as a dashed line at every position. The temperature profiles were altered by subtracting the minimum temperature found along the line or, in the case of line CD, the temperature at the centre of the line. It can be observed that the profiles of velocity and temperature, for the gas flowing upwards, develop rapidly in a region at the bottom of the domain ($z \lesssim 75\,\mathrm{mm}$, Figures 4.19 and 4.20), with the velocity forming two peaks in the vicinity of the walls separated by stagnant gas. Out of this region ($75\,\mathrm{mm} \lesssim z \lesssim 175\,\mathrm{mm}$) they remain essentially unchanged until the flow reaches the proximity of the top wall, where the velocity decreases. This points to the existence of a region of developed flow, which is typical of natural convection in enclosures. The profiles for the downward flow follows a similar pattern, developing within a short distance from the top wall, although the velocity of the cold gas remains significant up to a very short distance from the floor.

The profiles of $\sqrt{k}/U_b$ follow a similar evolution, although as mentioned above the profile do not show the smoothness usually associated with full statistical convergence. The profiles assume a shape characteristic of internal flows, with peaks near the pin walls and progressively decreasing towards the centre of the line. Higher peaks are found near the sleeve. The profiles assume different shapes at the bottom of the domain, where the impingement of the downward flow against the floor generates intense turbulence, creating a large peak close to the sleeve in line CD and smaller peaks on the leeward side of the pins, as shown in Figure 4.18c

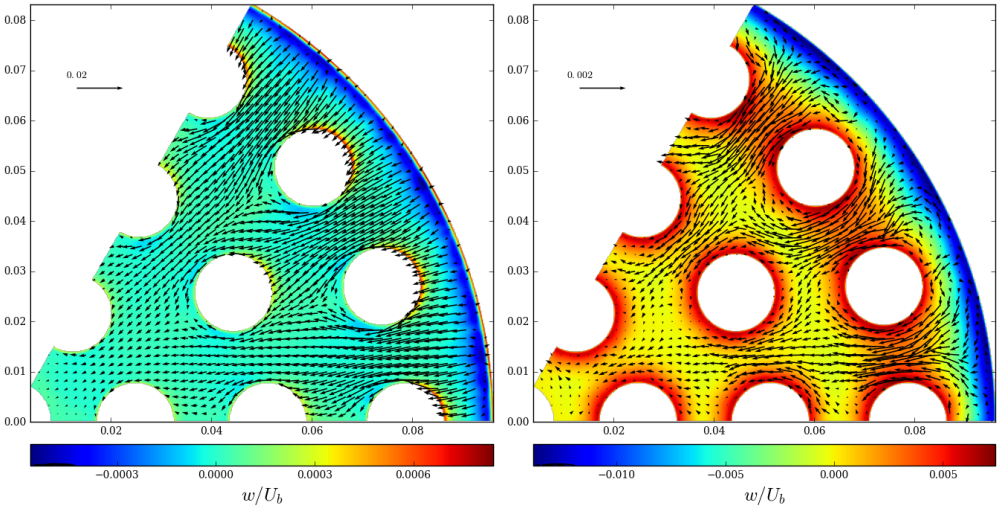

(a) $z = 0.1\,\mathrm{mm}$.

(b) $z = 50\,\mathrm{mm}$.

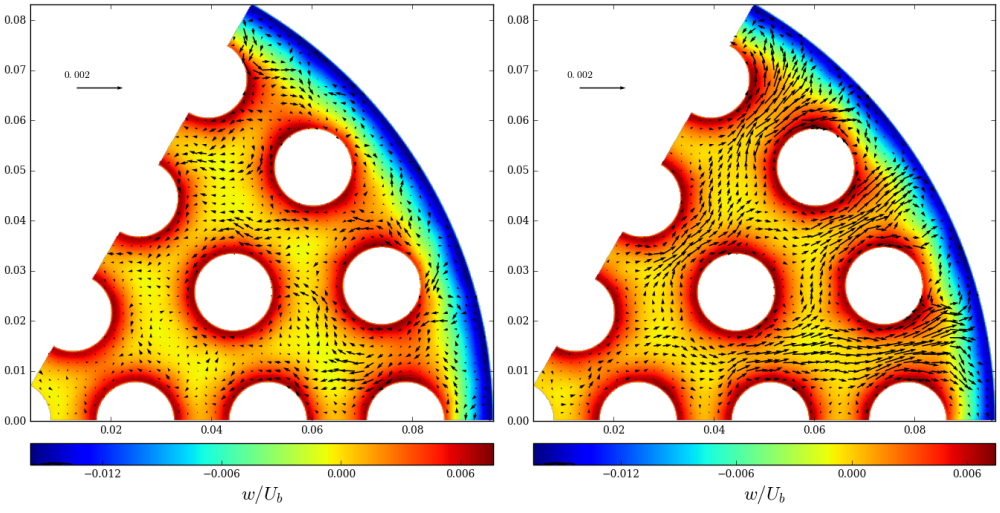

(c) $z = 100\,\mathrm{mm}$.

(d) $z = 150\,\mathrm{mm}$.

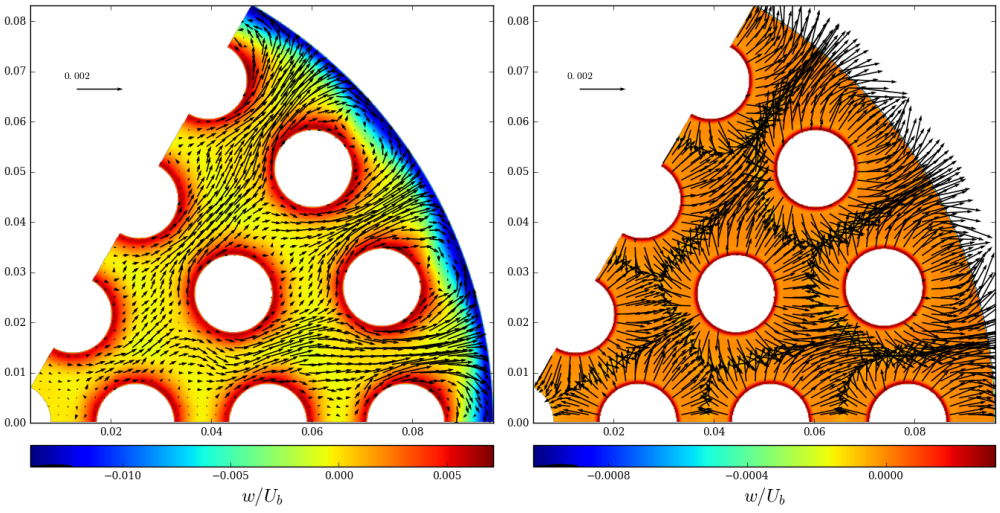

(e) $z = 200\,\mathrm{mm}$.

(f) $z = 249.9\,\mathrm{mm}$.

Figure 4.13: Maps of the average velocity on horizontal planes placed at different heights. The colour scale represents the axial component, while the black contour line separates positive and negative velocities. Note that the vector and colour scales change with the height.

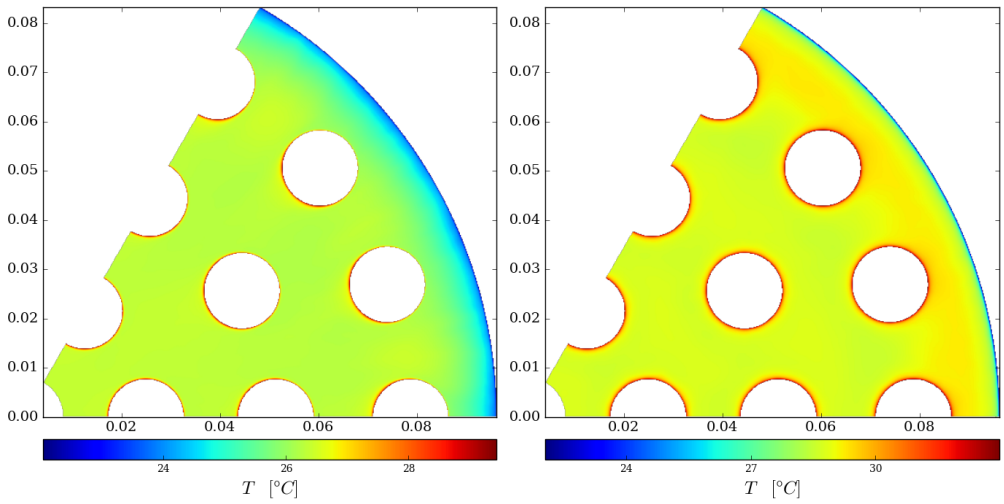

(a) $z = 0.1\,\mathrm{mm}$.

(b) $z = 50\,\mathrm{mm}$.

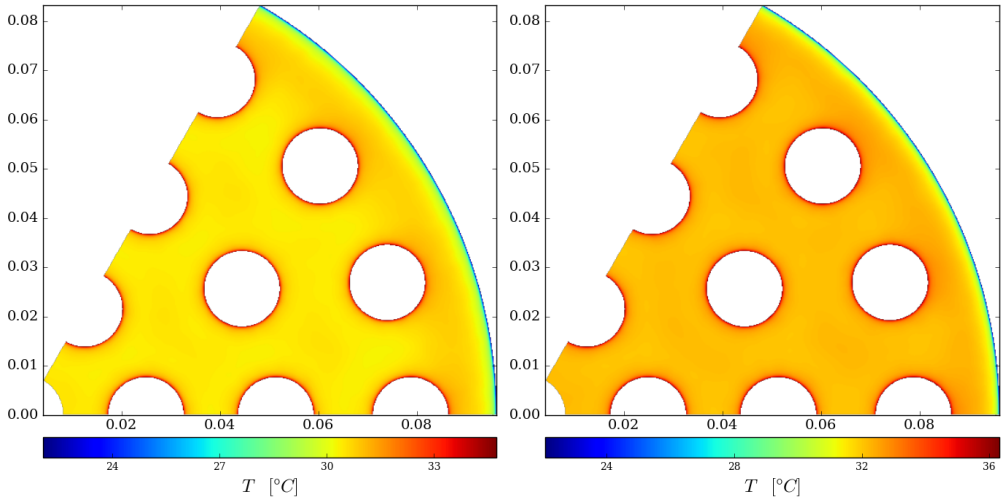

(c) $z = 100\,\mathrm{mm}$.

(d) $z = 150\,\mathrm{mm}$.

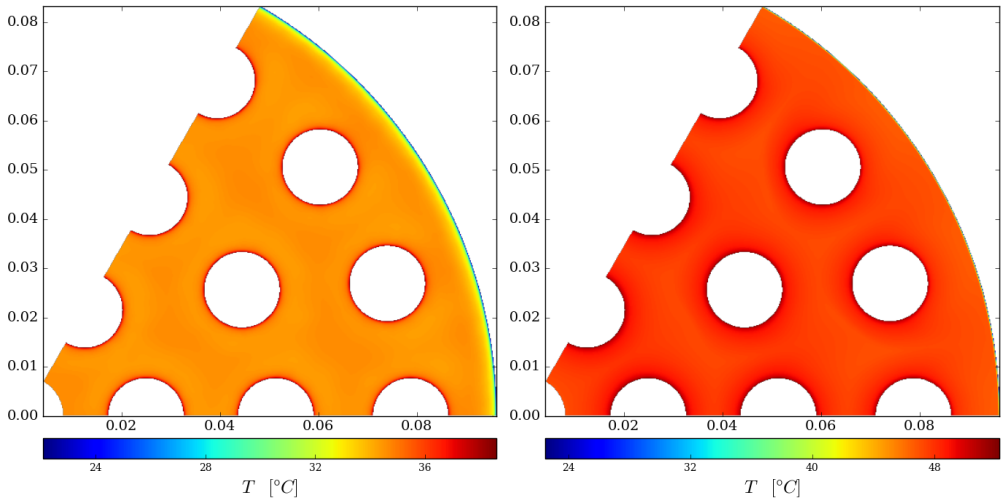

(e) $z = 200\,\mathrm{mm}$.

(f) $z = 249.9\,\mathrm{mm}$.

Figure 4.14: Maps of the average temperature on horizontal planes placed at different heights. Note that the colour scale changes with the height.

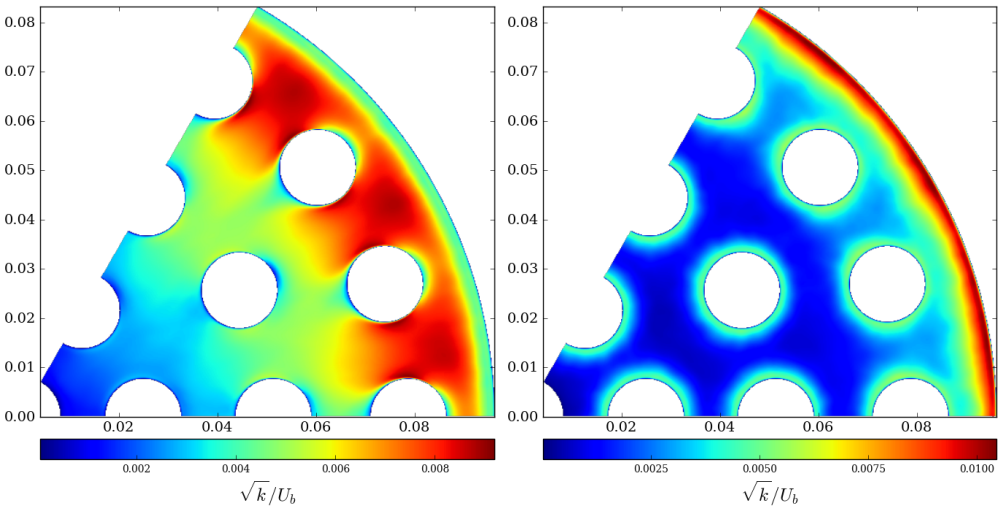

(a) $z = 0.1\,\mathrm{mm}$.

(b) $z = 50\,\mathrm{mm}$.

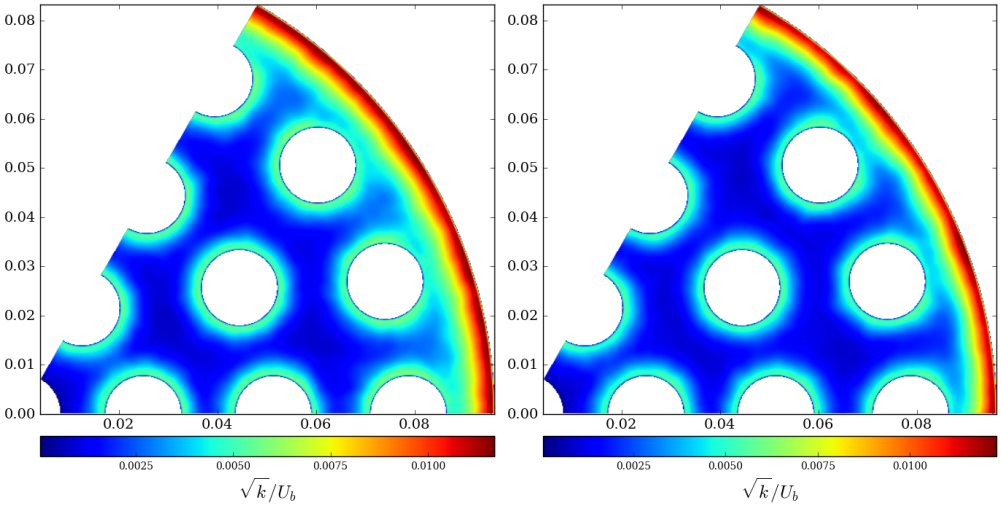

(c) $z = 100\,\mathrm{mm}$.

(d) $z = 150\,\mathrm{mm}$.

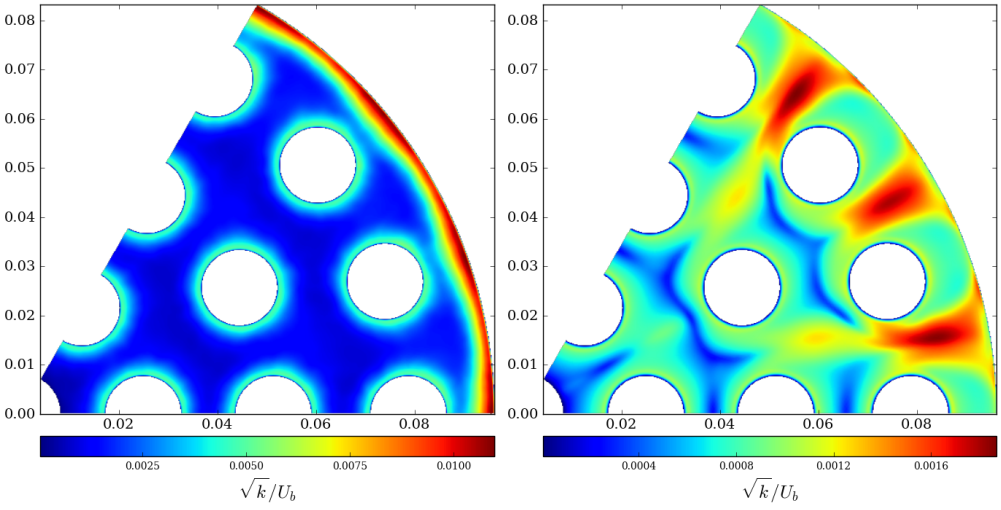

(e) $z = 200\,\mathrm{mm}$.

(f) $z = 249.9\,\mathrm{mm}$.

Figure 4.15: Maps of the turbulent intensity, defined as the ratio between the square root of the turbulent kinetic energy and the maximum magnitude of the time-averaged velocity in the domain, on horizontal planes placed at different heights. Note that the colour scale changes with the height.

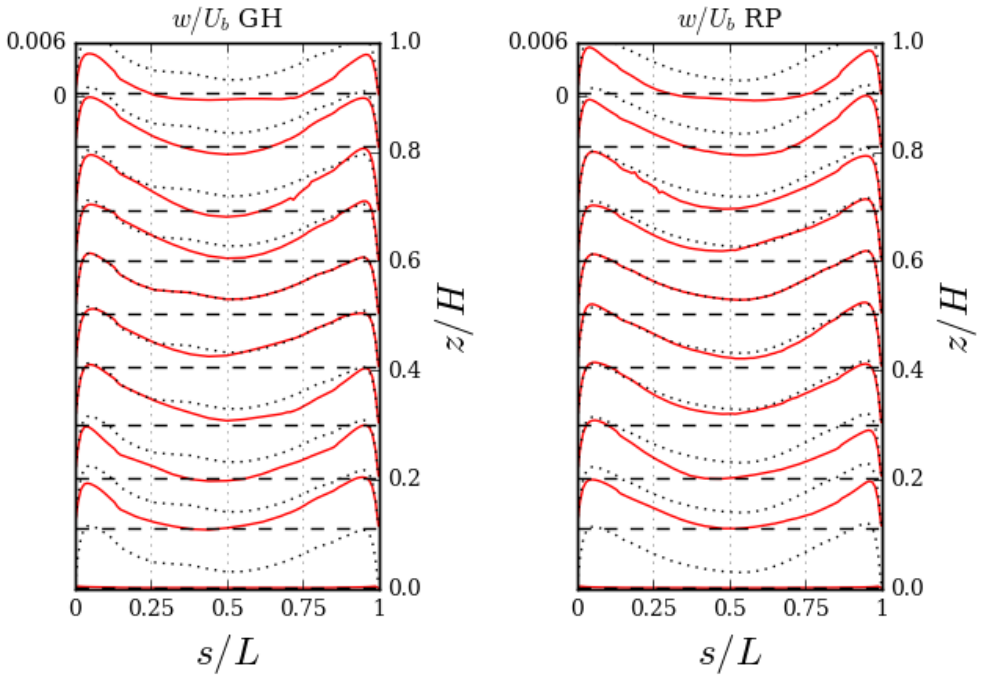

(a) GH.

(b) RP.

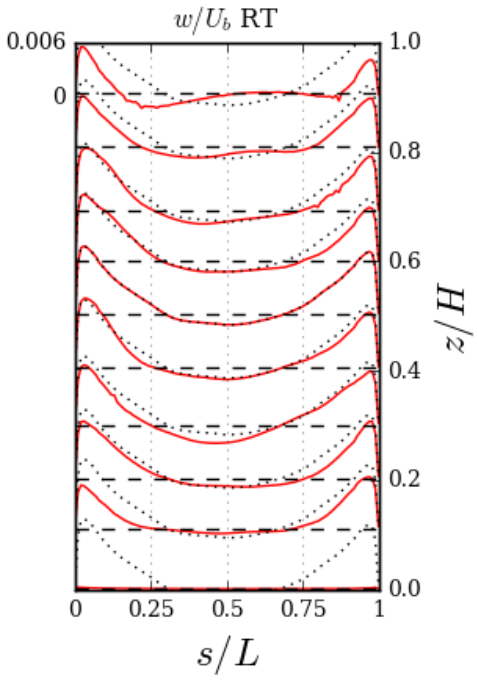

(c) RT.

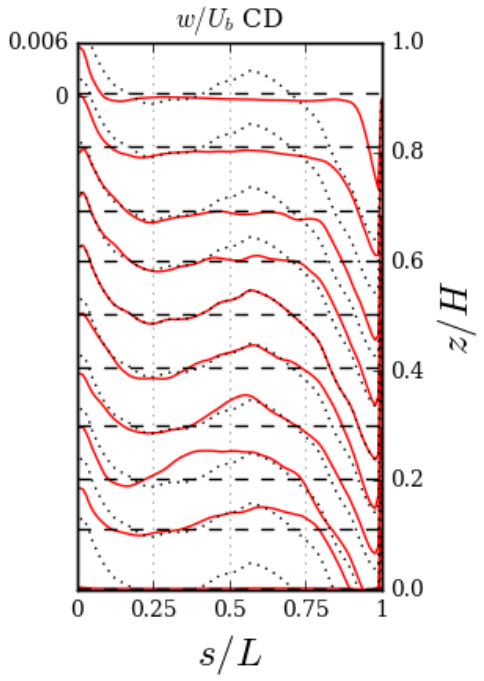

(d) CD.

Figure 4.16: Evolution of the vertical velocity profiles with increasing height, in four of the lines defined in Figure 4.2. The dotted lines show the profile at $z = 0.5H$, s is the linear coordinate along the line, L is the length of the line, z is the axial coordinate and $H = 0.25\,\mathrm{m}$ is the height of the channel. The scale is provided at the top left corner.

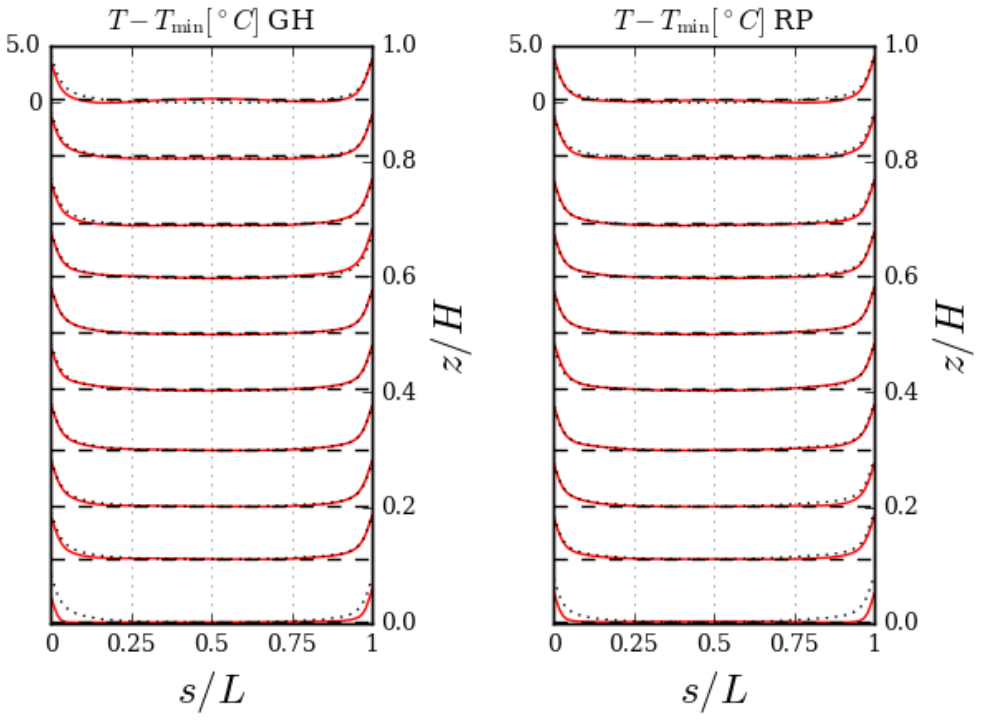

(a) GH.

(b) RP.

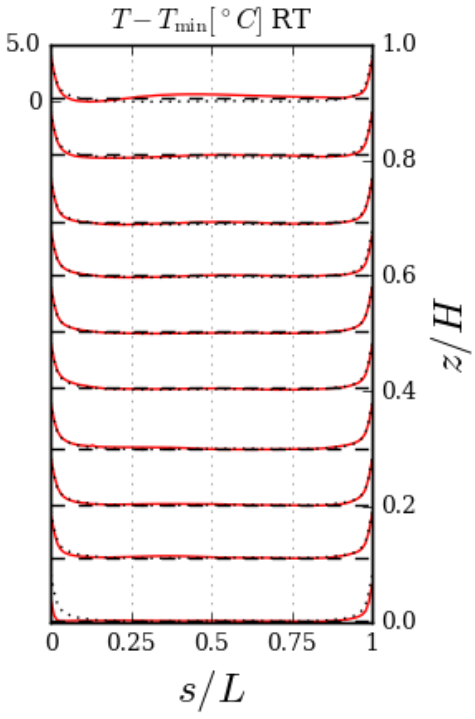

(c) RT.

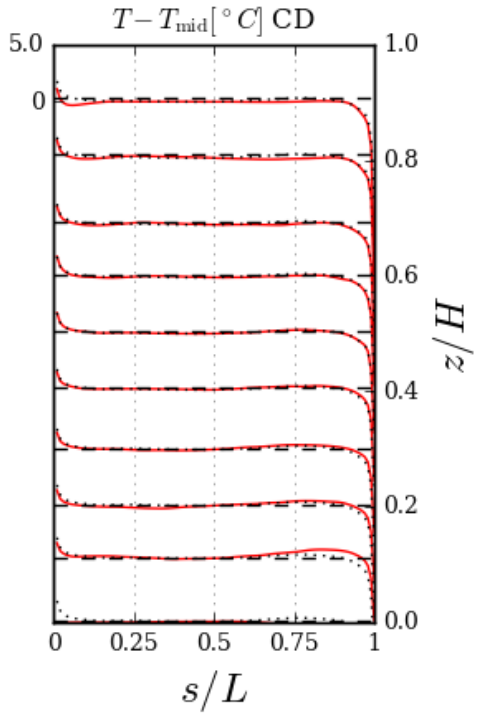

(d) CD.

Figure 4.17: Temperature profiles at different heights, in four of the lines defined in Figure 4.2. The minimum temperature along the line (or the temperature in the middle of line CD) was subtracted to the profile. The dotted lines show the profile at $z = 0.5H$, s is the linear coordinate along the line, L is the length of the line, z is the axial coordinate and $H = 0.25\,\mathrm{m}$ is the height of the channel. The scale is provided at the top left corner.

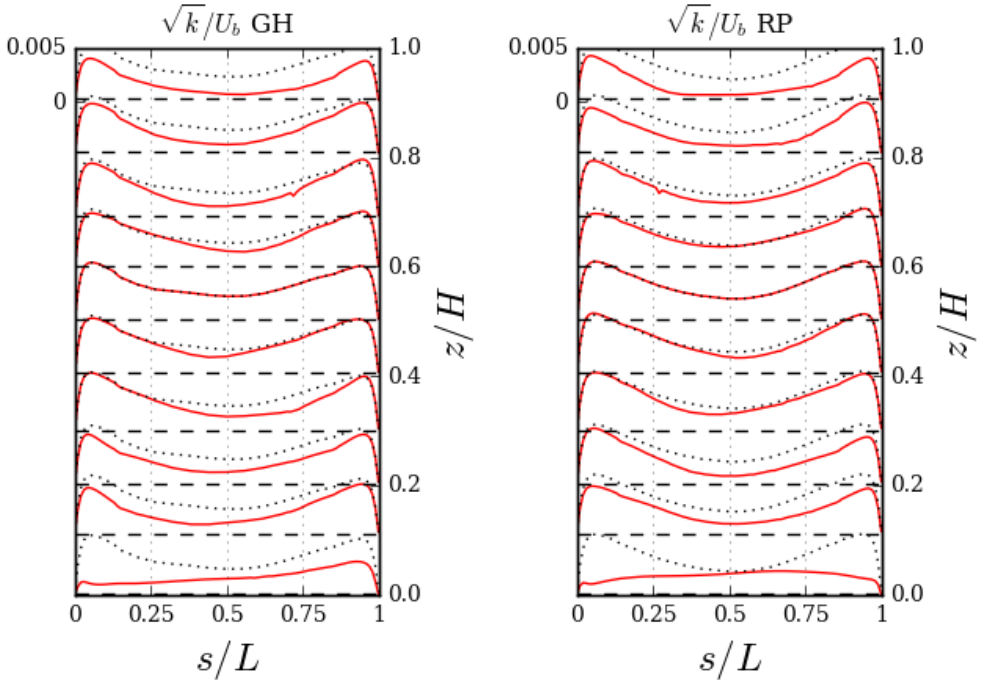

(a) GH.

(b) RP.

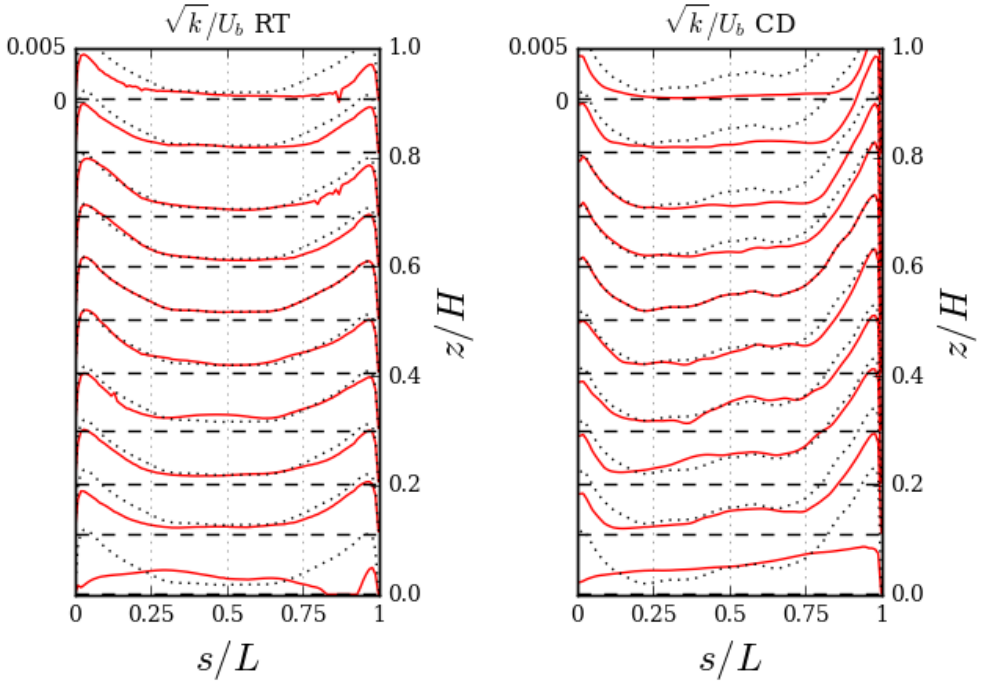

(c) RT.

(d) CD.

Figure 4.18: Evolution of the profiles of the turbulent kinetic energy with increasing height, in four of the lines defined in Figure 4.2. The dotted lines show the profile at $z = 0.5H$, s is the linear coordinate along the line, L is the length of the line, z is the axial coordinate and $H = 0.25\,\mathrm{m}$ is the height of the channel. The scale is provided at the top left corner.

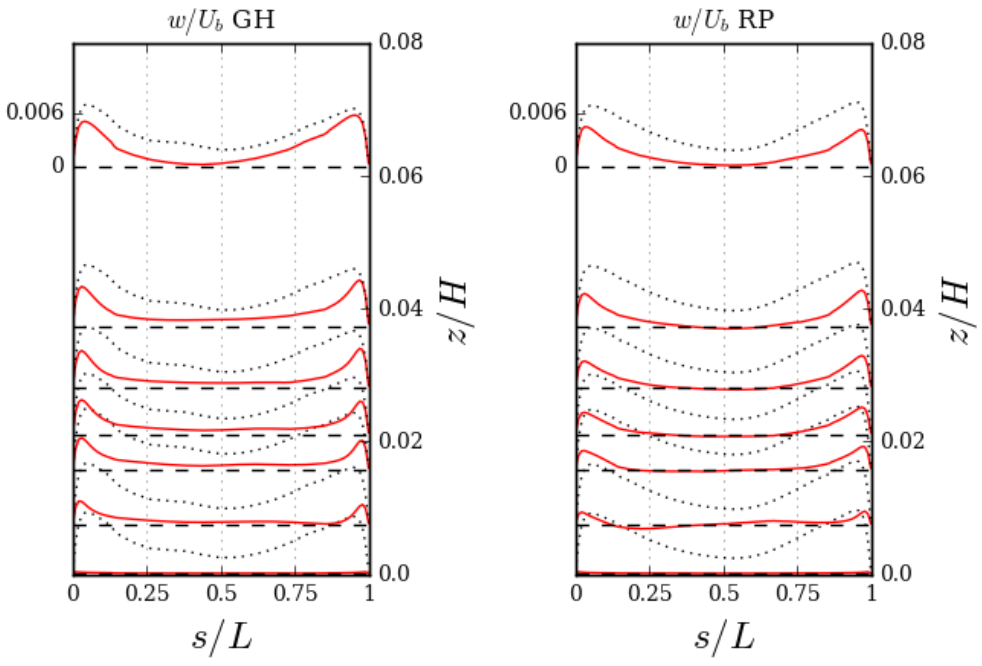

(a) GH.

(b) RP.

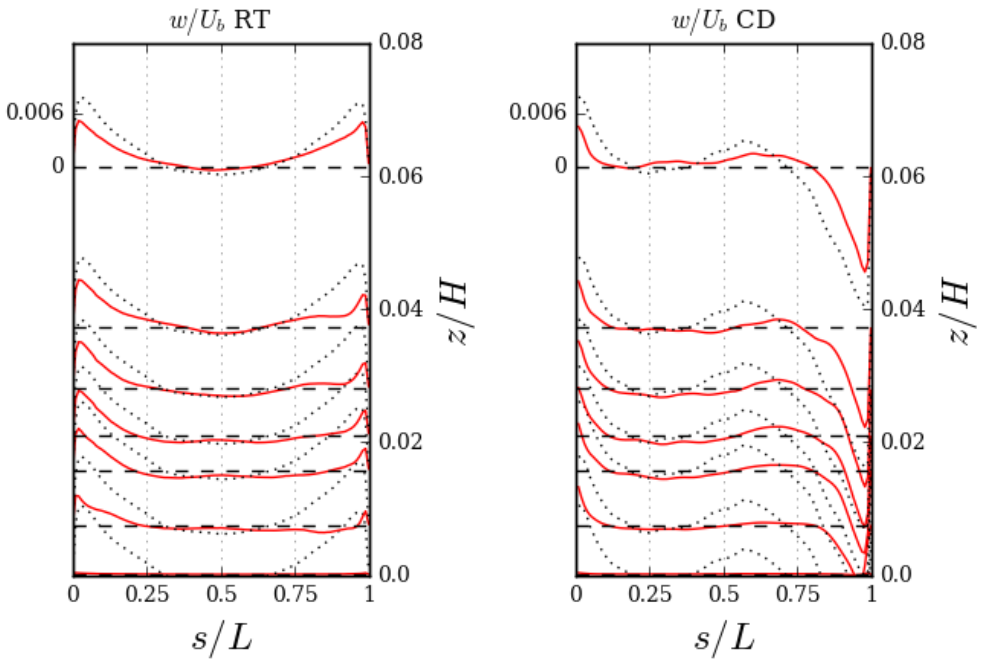

(c) RT.

(d) CD.

Figure 4.19: Evolution of the vertical velocity profiles along the bottom $20\,\mathrm{mm}$, in four of the lines defined in Figure 4.2. The dotted lines show the profile at $z = 0.5H$, s is the linear coordinate along the line, L is the length of the line, z is the axial coordinate and $H = 0.25\,\mathrm{m}$ is the height of the channel. The scale is provided at the top left corner.

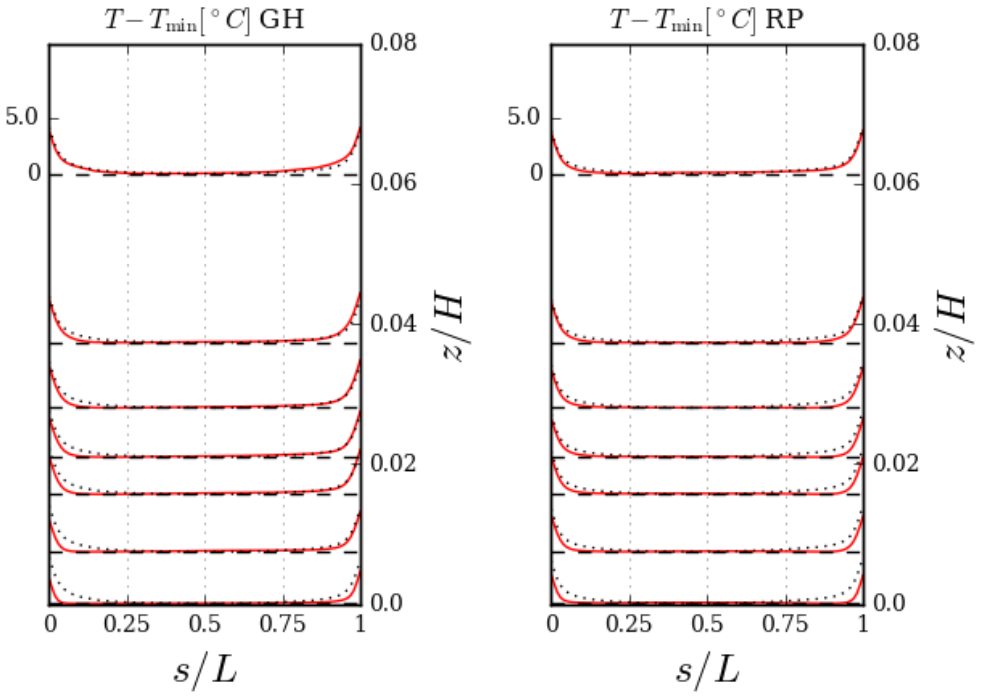

(a) GH.

(b) RP.

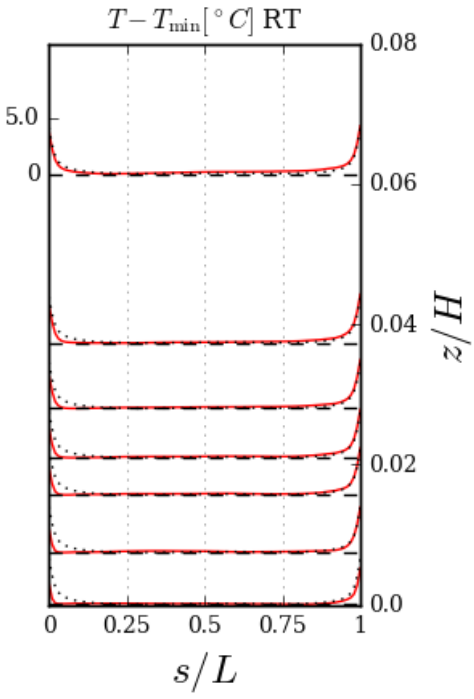

(c) RT.

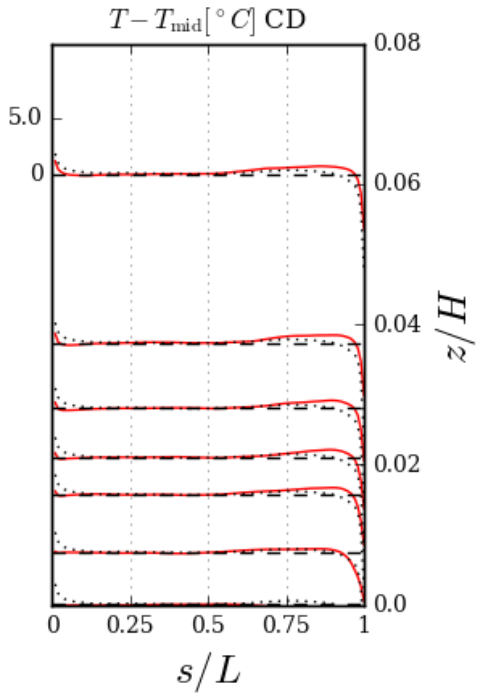

(d) CD.

Figure 4.20: Temperature profiles along the bottom $20\,\mathrm{mm}$, in four of the lines defined in Figure 4.2. The minimum temperature along the line (or the temperature in the middle of line CD) was subtracted to the profile. The dotted lines show the profile at $z = 0.5H$, s is the linear coordinate along the line, L is the length of the line, z is the axial coordinate and $H = 0.25\,\mathrm{m}$ is the height of the channel. The scale is provided at the top left corner.

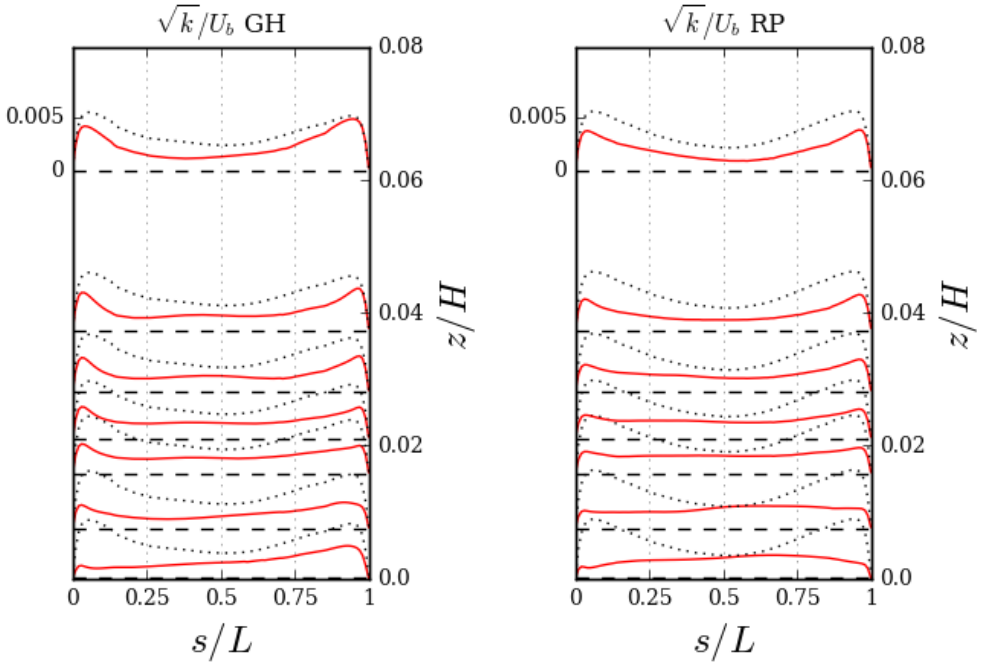

(a) GH.

(b) RP.

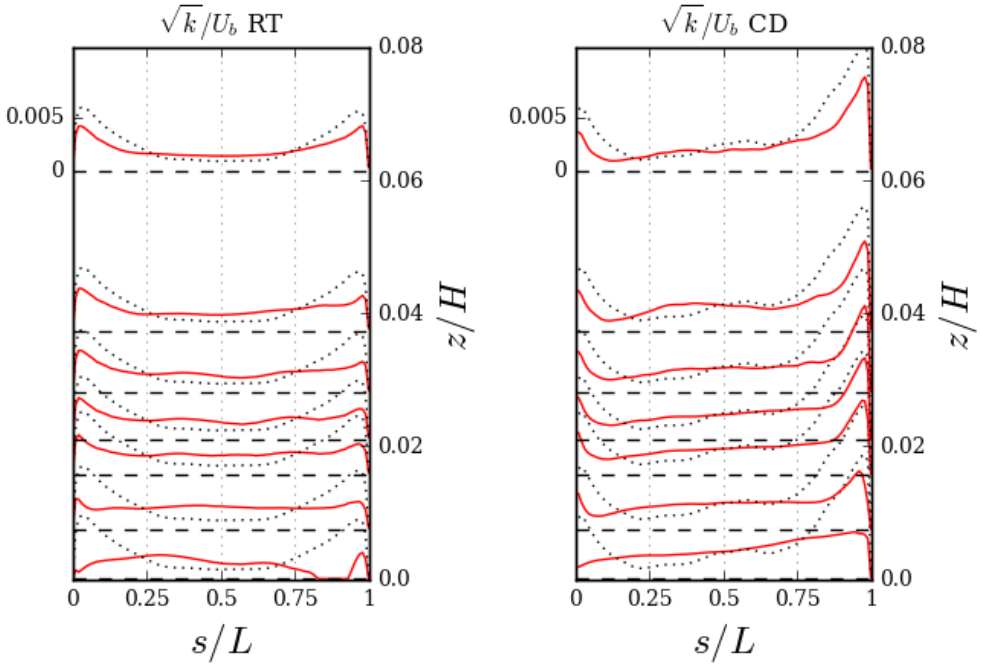

(c) RT.

(d) CD.

Figure 4.21: Evolution of the profiles of the turbulent kinetic energy along the bottom $20\,\mathrm{mm}$, in four of the lines defined in Figure 4.2. The dotted lines show the profile at $z = 0.5H$, s is the linear coordinate along the line, L is the length of the line, z is the axial coordinate and $H = 0.25\,\mathrm{m}$ is the height of the channel. The scale is provided at the top left corner.

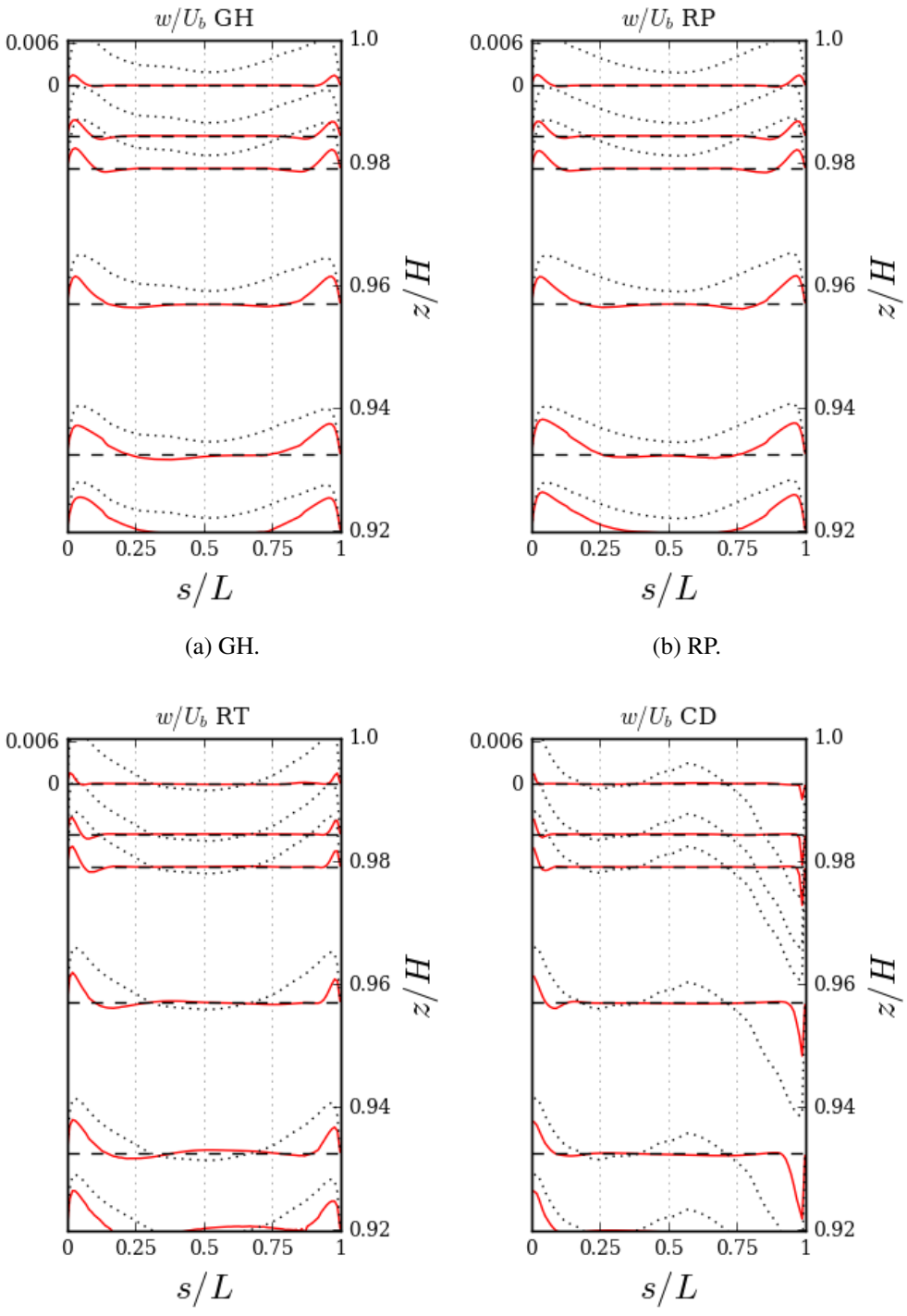

(a) GH.

(b) RP.

(c) RT.

(d) CD.

Figure 4.22: Evolution of the vertical velocity profiles along the top $20\,\mathrm{mm}$, in four of the lines defined in Figure 4.2. The dotted lines show the profile at $z = 0.5H$, s is the linear coordinate along the line, L is the length of the line, z is the axial coordinate and $H = 0.25\,\mathrm{m}$ is the height of the channel. The scale is provided at the top left corner.

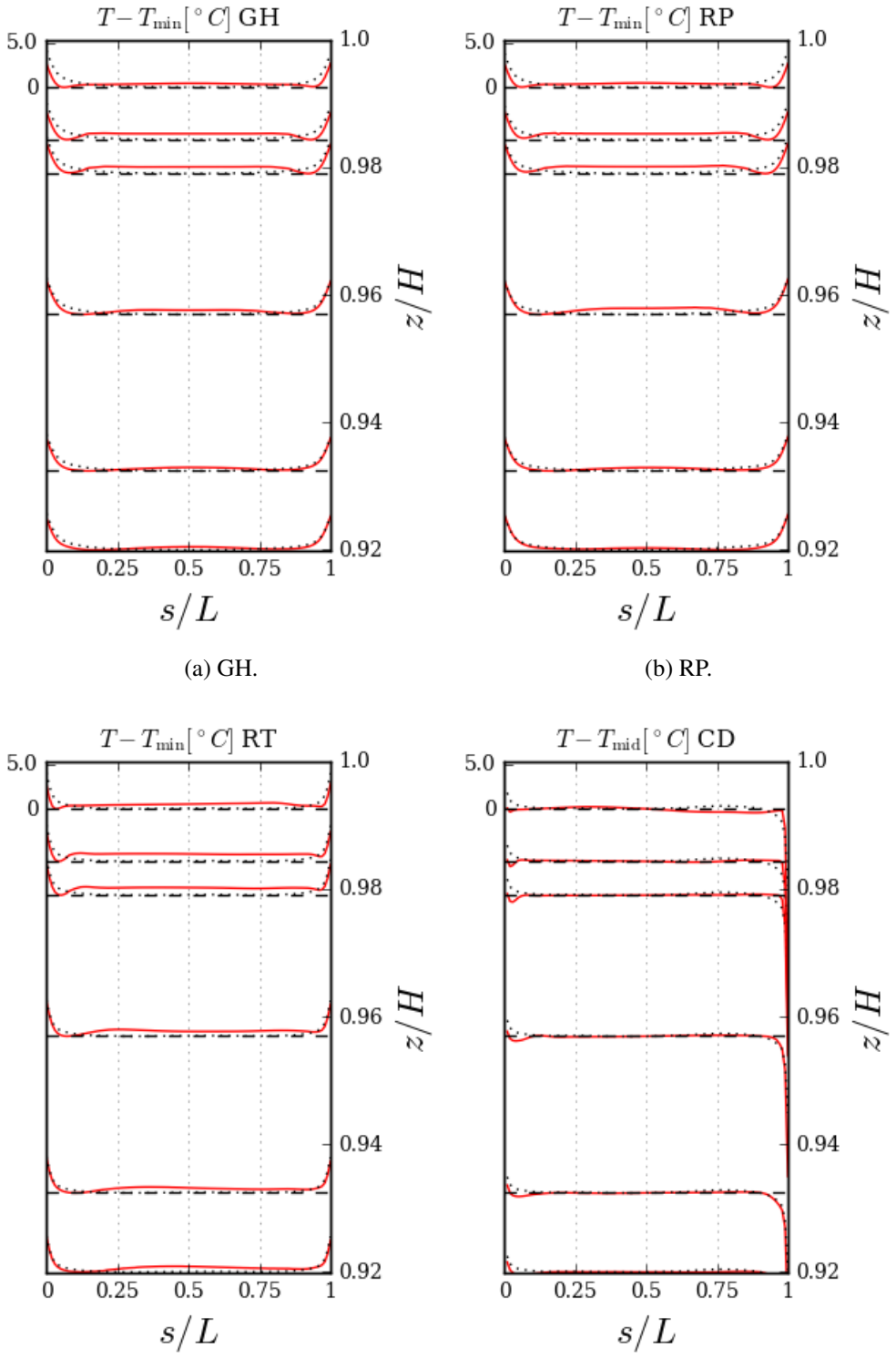

(a) GH.

(b) RP.

(c) RT.

(d) CD.

Figure 4.23: Temperature profiles along the top 20 mm, in four of the lines defined in Figure 4.2. The minimum temperature along the line (or the temperature in the middle of line CD) was subtracted to the profile. The dotted lines show the profile at $z = 0.5H$, s is the linear coordinate along the line, L is the length of the line, z is the axial coordinate and $H = 0.25\,\mathrm{m}$ is the height of the channel. The scale is provided at the top left corner.

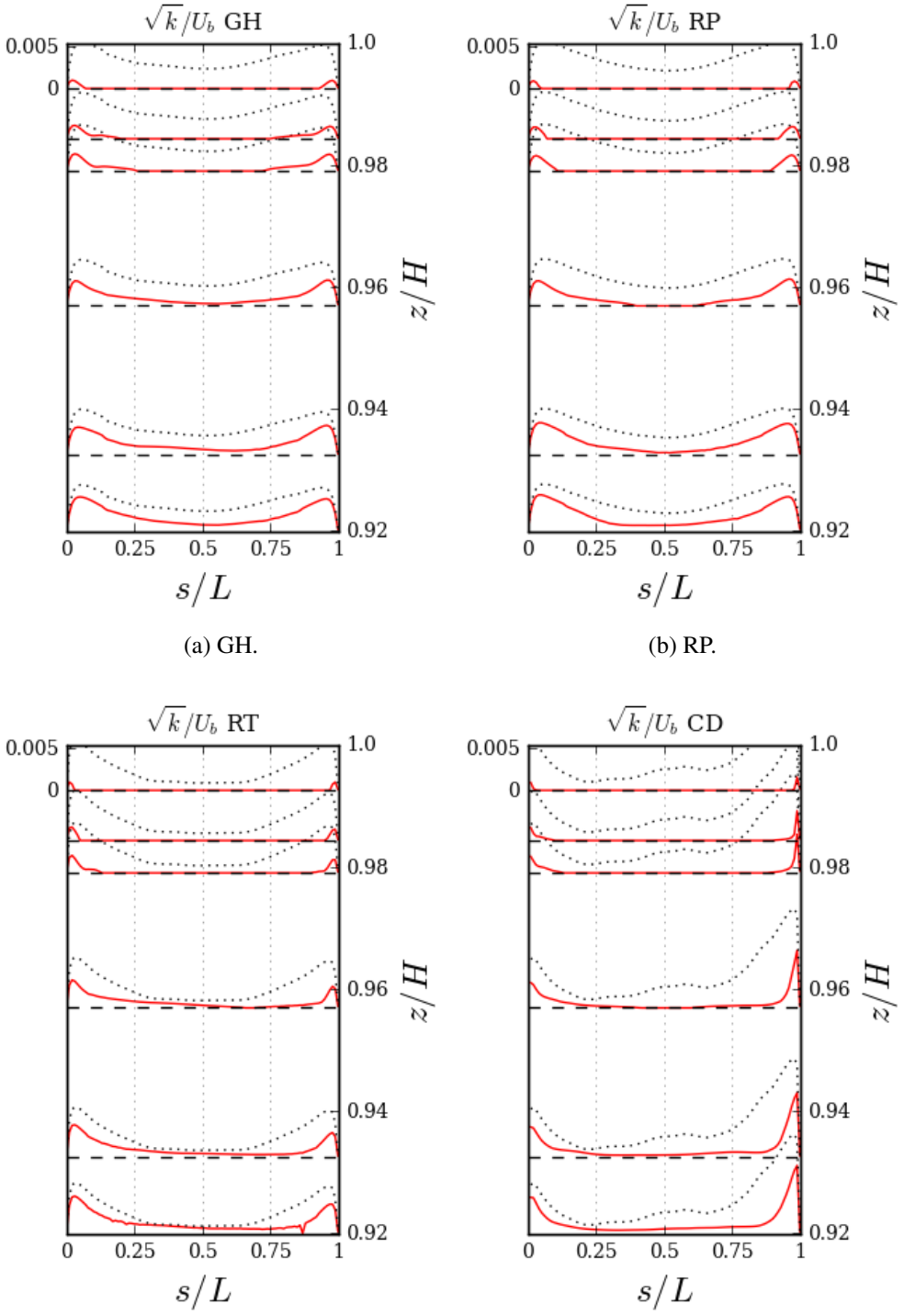

(a) GH.

(b) RP.

(c) RT.

(d) CD.

Figure 4.24: Evolution of the profiles of the turbulent kinetic energy along the top 20 mm, in four of the lines defined in Figure 4.2. The dotted lines show the profile at $z = 0.5H$, s is the linear coordinate along the line, L is the length of the line, z is the axial coordinate and $H = 0.25\,\mathrm{m}$ is the height of the channel. The scale is provided at the top left corner.

Non-dimensional quantity	Definition
y^+	$\rho u_\tau y/\mu$
w^+	$\overline{w}/u_\tau$
T^+	$(T_{\text{wall}} - T)\rho c_p u_\tau/q''$
$k^{1/2+}$	$\sqrt{k}/u_\tau$
$\langle w'w' \rangle^{1/2+}$	$\sqrt{\langle w'w' \rangle}/u_\tau$

Table 4.3: Definition of the non-dimensional quantities plotted in Figures 4.25 and 4.26.

4.2.4 Non-dimensional near-wall profiles

Figures 4.25 and 4.26 shows the near-wall profiles of some relevant non-dimensional quantities at representative locations, placed at different axial positions in the computational domain. The plots shown are relative to lines normal to the wall respectively at points C and D in Figure 4.2. The definitions of the quantities are provided in Table 4.3. The data presented concern the regions discretised by structured meshes, to avoid the inevitable interpolation problems caused by the prismatic discretisation used further from the walls.

The non-dimensional profiles in the vicinity of the pins are illustrated in Figure 4.25. The non-dimensional axial velocity along the pins shows a peak at values of y^+ between 9 and 20 at all height. The development of the velocity profiles at both ends of the domain, as described above, is apparent, with the magnitude of the peak increasing from the bottom up to $z = 100\,\text{mm}$.

The development is accompanied by a shift of the location of the peak towards higher values of y^+. From that position, the profiles remain very close to each other, with a maximum value of $w^+ \lesssim 5$, up to $z = 175\,\text{mm}$, where the magnitude of the peak begins to decrease and its location shift back to lower values of y^+. Comparison with the curve representing $w^+ = y^+$, shown as a black dashed line in the plots, reveals that the profiles tend to conform to the law of the wall up to values of y^+ slightly larger than 1.

The evolution of the non-dimensional temperature at different height is consistent with the trend described for the axial velocity, with the development and anti-development of the profiles evident for values of y^+ greater than $\sim$10, whilst closer to the wall, the profiles do not show any appreciable difference at different heights. Contrary to the velocity profiles, the temperature seems to be well described by the law of the wall, $T^+ = \text{Pr}y^+$, up to $y^+ \simeq 3$.

The non-dimensional turbulence intensity, $k^{1/2+}$, and root mean square of the axial velocity fluctuation $\langle w'w' \rangle^{1/2+}$, both expressed in wall units, follow qualitatively similar trends, showing a certain variability even in the the central region of the domain. It must be noted that the profile of the turbulent quantities at $z = 125\,\text{mm}$ does not show a peak

in the region considered, compatibly with the flatter profile assumed by the turbulence intensity at this axial position (Figure 4.18). In all cases, the peak in the turbulent quantities is located slightly farther from the wall than the peak in velocity, at values of y^+ greater than 10.

The non-dimensional profiles along the sleeve wall are presented in Figure 4.26. Since the flow in this region is oriented downwards, the profiles show a developing trend from the top of the domain towards a central region, where they tend not to vary significantly. The velocity profiles, in this case, do not show signs of decelerating markedly in proximity of the bottom. Note that the values assumed by both w^+ and T^+ are somewhat higher than the peaks observed near the pins.

In the developed region, the peak in w^+ occurs at $y^+ \gtrsim 20$. The velocity profile deviates from the curve $w^+ = y^+$ for values of y^+ higher than 1, while the temperature profile follows the law $T^+ = \mathrm{Pr} y^+$ closely up to $y^+ \simeq 6$. Similarly to the profiles next to the pins, the turbulent quantities show peaks further from the wall compared to w^+, at $y^+ \gtrsim 30$ for $z \leq 175\,\mathrm{mm}$.

4.3 Correlations for heat transfer

In this section the relations between the local Nusselt numbers and the local flow conditions are explored. Correlations for Nu are proposed following two approaches.

The first approach attempts to draw a parallel between the flow profiles on the planes presented in Section 4.2.3 and those established in natural convection in two-dimensional rectangular enclosures. The second approach correlates the average Nusselt and Rayleigh numbers in each sub-channel within the bundle.

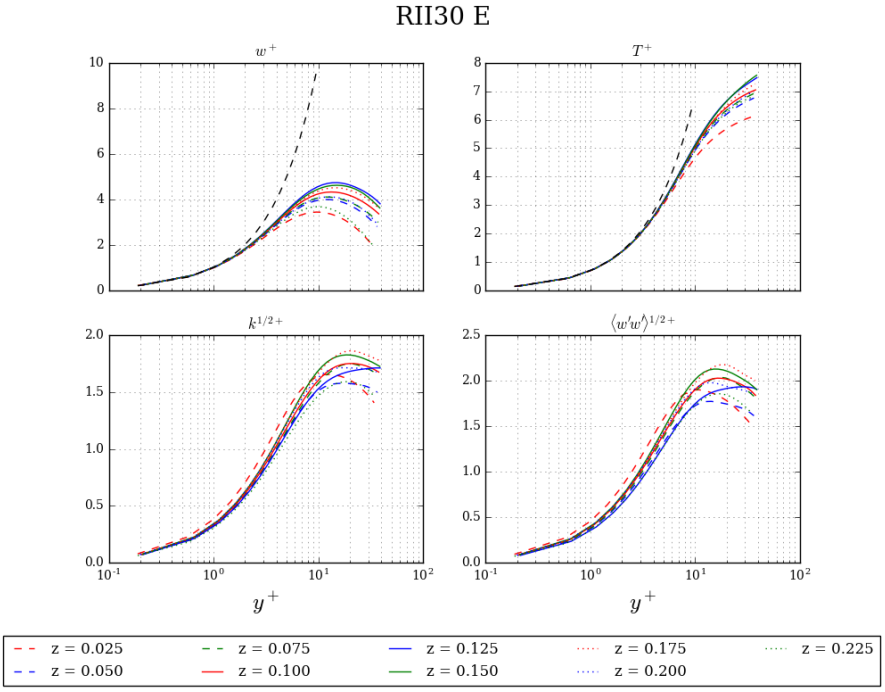

Figure 4.25: Near-pin non-dimensional profiles of some quantities of interest. The profiles are relative to a line normal to a pin in the second rank, with the origin in point C of Figure 4.2.

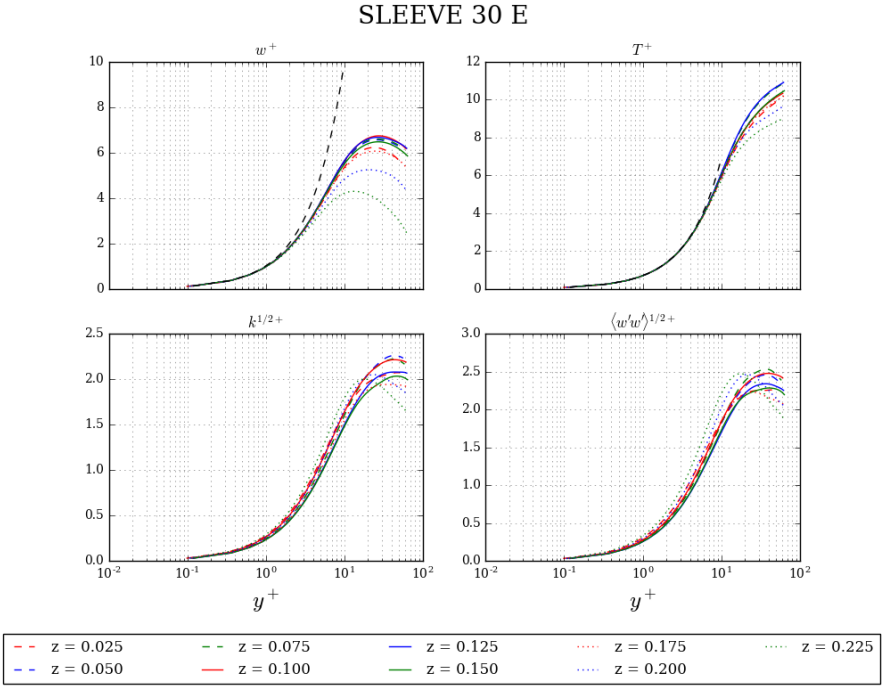

Figure 4.26: Near-sleeve non-dimensional profiles of some quantities of interest. The profiles are relative to a line normal to the sleeve, with the origin in point D of Figure 4.2.

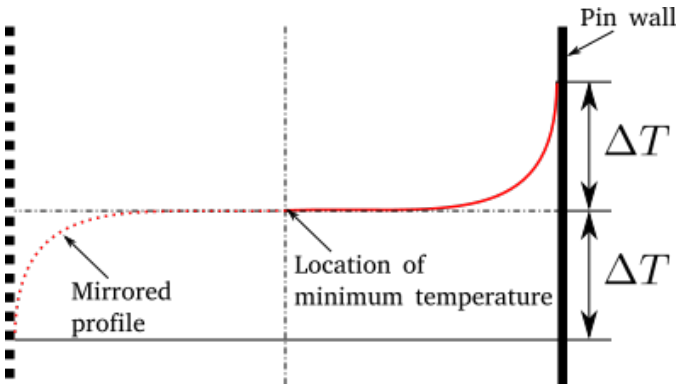

Figure 4.27: Schematics of the hypothesis used in the definition of the Rayleigh and Nusselt numbers in the inter-pin gaps, as described in Section 4.3.1.

4.3.1 Inter-pin gaps

The hypothesis behind the first approach can be described as follows: let one consider a typical temperature profile in the gaps between the fuel pins, along one of the lines in Figure 4.2 (Figure 4.27). If one splits the line at the location of the minimum temperature, the profiles on each segment can be considered as one half of the symmetric profile across a rectangular enclosure where the temperature difference $2\Delta T = 2(T_w - T_{min})$ is applied. It is thus assumed that the temperature distribution around a pin is not influenced by its surrounding, except for a thin boundary layer. The Rayleigh and Nusselt numbers are calculated according to this definition and the correlations obtained in this formulation can be compared with one commonly used for rectangular enclosure. The aspect ratios H/L, where $H = 250\,\mathrm{mm}$ is the height of the domain and L is the length of the profile are between 12 and 27. Under this assumption, the Nusselt and Rayleigh numbers are defined as follows:

$$\begin{aligned} \mathrm{Nu} &= \frac{q'' L}{2\Delta T \lambda} \\ \mathrm{Ra} &= \frac{g\beta L^3 (2\Delta T)}{\nu\alpha} \end{aligned} \tag{4.10}$$

where q'' is the heat flux from the pin, λ is the thermal conductivity, g is the acceleration due to gravity, β is the volumetric expansion coefficient, ν is the kinematic viscosity and α is the thermal diffusivity.

The results of the analysis described above are depicted in Figure 4.28 for the developed flow region ($75\,\mathrm{mm} < z < 175\,\mathrm{mm}$). Each point in the scatter plots represents a $(\mathrm{Ra}, \mathrm{Nu})$ pair for one half of a profile line at different axial positions, each line thus contributing two points to the plot. The colour of the point corresponds to the colour of the line in Figure 4.2. Lines AB, CD, EF and MN, which have one of the extrema not laying on a fuel pin, were not considered.

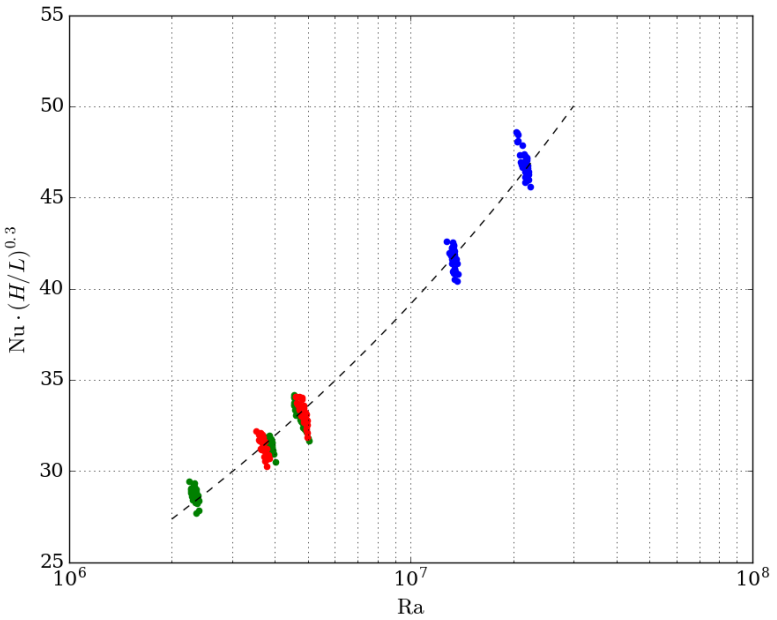

(a) With Nusselt scaling (Equation 4.11a).

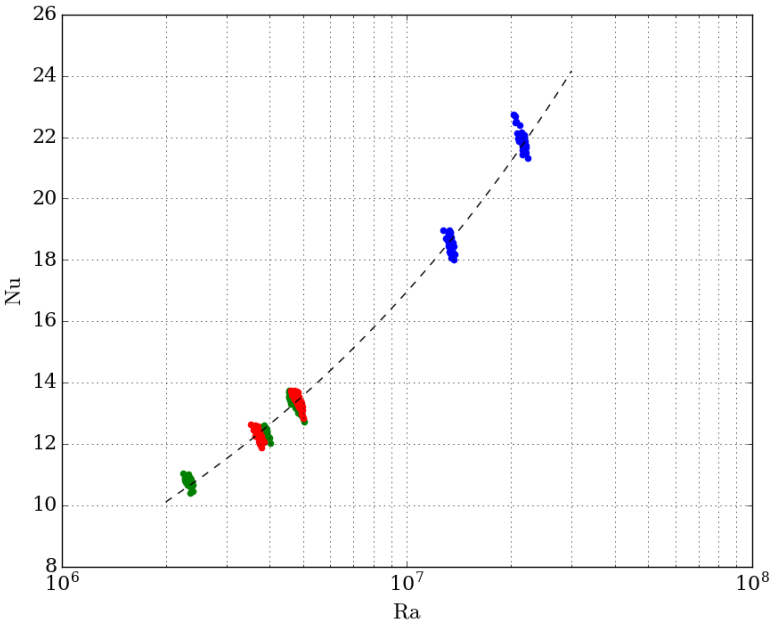

(b) Without Nusselt scaling (Equation 4.11b).

Figure 4.28: Correlations between Nu and Ra in the gaps between the fuel pins. The dotted lines show the fit obtained from the data using the expressions shown in Equation 4.13.

Incropera and DeWitt[85] reported two correlations for tall enclosures (height-to-width ratio up to 40):

$$\mathrm{Nu}_L = \frac{hL}{\lambda} = 0.42\mathrm{Ra}_L^{0.250}\mathrm{Pr}^{0.012}\left(\frac{H}{L}\right)^{-0.3} \tag{4.11a}$$

$$\mathrm{Nu}_L = 0.046\mathrm{Ra}^{0.333} \tag{4.11b}$$

where L and H are respectively the width and the height of the enclosure. Equation 4.11a is valid for H/L between 10 and 40, Prandtl number between 1 and 2×10^4 and Rayleigh number between 1×10^4 and 1×10^7. Equation 4.11b is valid for H/L between 1 and 40, Prandtl number between 1 and 20 and Rayleigh number between 1×10^6 and 1×10^9.

To fit the data presented in Figure 4.28, an expression similar to that shown in Equation 4.11 has been used:

$$\mathrm{Nu}_L = \frac{hL}{\lambda} = a_1\mathrm{Ra}_L^{b_1}\mathrm{Pr}^{0.012}\left(\frac{H}{L}\right)^{-0.3} \tag{4.12a}$$

$$\mathrm{Nu}_L = a_2\mathrm{Ra}^{b_2} \tag{4.12b}$$

Points corresponding to profiles within $75\ \mathrm{mm}$ from the top and bottom of the domain were not used to obtain the correlation, to limit the scope to the region where the flow field is fully developed. In Figure 4.28a the Nusselt number in each point has been divided by $\left(H/L\right)^{-0.3}$ where in this case L is the length of the corresponding line, to obtain a correlation in the form of Equation 4.12a. In Figure 4.28b the Nusselt number has not been scaled, and the correlation obtained is in the form of Equation 4.12b. The following expression was obtained:

$$\mathrm{Nu}_L = \frac{hL}{\lambda} = 1.081\mathrm{Ra}_L^{0.223}\mathrm{Pr}^{0.012}\left(\frac{H}{L}\right)^{-0.3} \tag{4.13a}$$

$$\mathrm{Nu}_L = 0.095\mathrm{Ra}^{0.322} \tag{4.13b}$$

It is noted that, while the coefficients a_i differ from those proposed for rectangular enclosures by a factor greater than 2, the exponents b_i are very close, indicating a similar dependence of Nu from Ra in the two scenarios, despite the significantly different geometries.

4.3.2 Sub-channels

In this section the dependence of the average Nusselt number in the sub-channels of the stringer on the average sub-channel Rayleigh number is investigated. This is the

formulation used in the classical sub-channel approach common in nuclear engineering, where correlations are employed to account for heat transfer between the fuel and the coolant within each sub-channel.

To obtain the correlations, the computational domain was divided in 25 axial blocks and 5 annular sub-channels (Figure 4.29). The results of the calculation were then filtered using the intrinsic average operator:

$$^{i}\langle\phi\rangle = \frac{1}{V_f}\iiint_{V_f}\phi dV \tag{4.14}$$

where ϕ is a generic variable and V_f is the volume occupied by the fluid. The Nusselt and Rayleigh numbers are defined as follows:

$$\begin{aligned}\mathrm{Nu} &= \frac{q'' D_h}{(\langle T_w\rangle - {}^{i}\langle T_f\rangle)\lambda} \\ \mathrm{Ra} &= \frac{g\beta D_h^3(\langle T_w\rangle - {}^{i}\langle T_f\rangle)}{\nu\alpha}\end{aligned} \tag{4.15}$$

where D_h is the hydraulic diameter of the sub-channel, $\langle T_w\rangle$ is the average wall temperature in the sub-channel and $^{i}\langle T_f\rangle$ is the intrinsic averaged fluid temperature.

The relation between the sub-channel Rayleigh number and the sub-channel Nusselt number for the developed region is shown in the scatter plot presented in Figure 4.30. Points corresponding to profiles within $75\,\mathrm{mm}$ from the top and bottom of the domain were removed, to limit the scope to the region where the flow field is fully developed. The outermost sub-channel, where no pins are present, was not included among the points used. The dashed line represent the power law used to fit the data:

$$\mathrm{Nu}_{sc} = 0.295\mathrm{Ra}_{sc}^{0.315} \tag{4.16}$$

It can be noted that all points tend to cluster along the best-fit line, with the notable exception of Sub-channel 4 which presents a broader spread of the relative points, which may be explained by its peculiar geometry and its proximity to the fluid region influenced by the sleeve. This supports the assumptions behind sub-channel analysis for buoyancy dominated flow, although a larger set of data, corresponding to a broader variation in the flow conditions, would be needed to draw more general conclusions.

As a comparison, a correlation obtained for the artificially roughened pin bundle found in AGR fuel is reported below (see Appendix B):

$$\mathrm{Nu}_{sc,rough} = 0.068\mathrm{Ra}_{sc}^{0.37} \tag{4.17}$$

As shown in Figure 4.30, the values of Nu predicted by the correlation are consistently

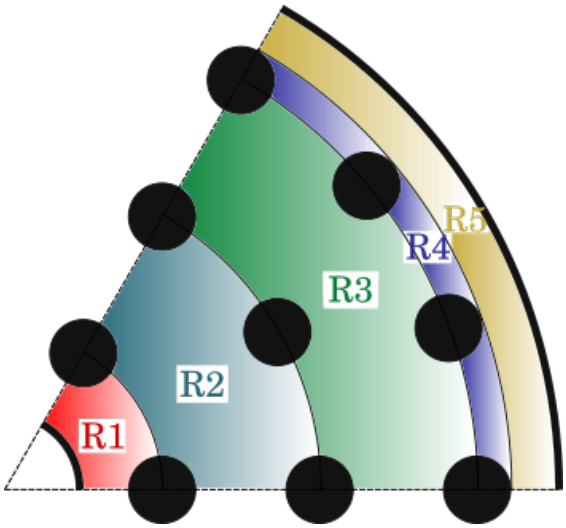

Figure 4.29: The five annular sub-channels used in the averaging operations.

lower than those output by the simulation, which signals a detrimental effect of the ribs on heat transfer in this natural convection scenario.

4.4 Concluding remarks

In this chapter a Large Eddy Simulation of natural convection in an enclosed pin bundle was presented. The computational domain represented the region occupied by the coolant gas in a shortened model of the AGR fuel element. Although features such as the artificial roughness of the pins' surfaces were neglected, to the author's knowledge this represents the first investigation of turbulent natural convection in this geometry.

The predicted flow field shows the presence of a stagnant core region, while non-zero vertical velocities are found exclusively next to the active surfaces. Along the pins, ascending flow is observes in a thin boundary layer, traversed by disturbances in the form of travelling waves. High negative velocities are found close to the sleeve wall, through which heat is removed from the domain. Intense turbulence is observed in this region. A region of fully-developed flow, where the thickness of the boundary layer does not change, is observed in the central portion of the domain, far from the top and bottom boundaries. The study of heat transfer correlations in the gaps between the pins showed a similar dependence of the Nusselt number from the local Rayleigh number to that observed in tall rectangular enclosures. In an alternative formulation, correlations for the heat transfer based on average sub-channel quantities were extracted, corroborating the methodology followed in the following chapters.

The calculation presented above was limited to a single set of parameters. It is therefore recommended that future studies should explore the effects of different values of the

heat flux imposed at the pins, as well as of different heights of the channel. The effect of the roughness of the pins in natural convection conditions would also be an interesting, though challenging, object of investigation.

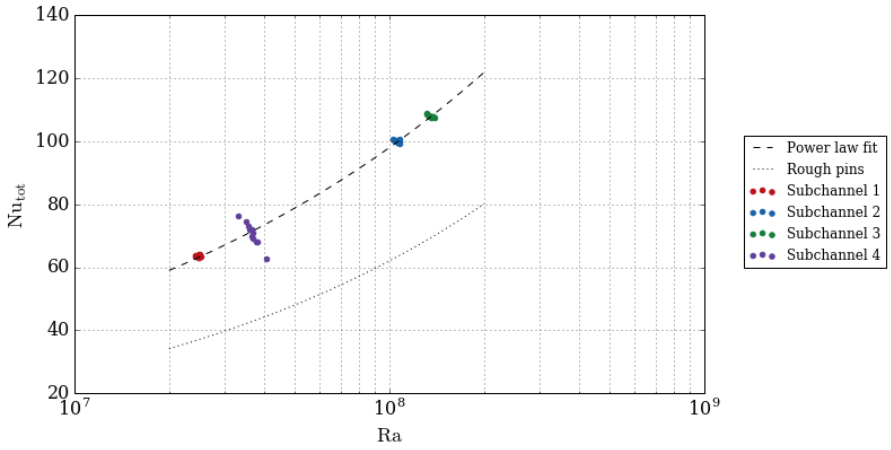

Figure 4.30: Correlations between Nu and Ra in the domain's sub-channels. The dotted lines show the fit obtained from the data (Equation 4.16).

Chapter 5

Development of POSTR - a numerical tool for refuelling cooling in AGRs

In this chapter, the methodology that will be used in the course of the project is discussed. Section 5.1 enunciates the premises of this study, outlining the the features the model developed was required to possess, while Section 5.2 contains a description of the 'porous' model developed.

5.1 Requirements for the model

As stated in the Introduction to this study, a purpose of this project is to develop, in partnership with EDF Energy, a three-dimensional model for the gas flow and heat transfer in the AGR fuel stringer and its surroundings (Figure 5.1). The model should simulate the cooling of the fuel during the handling operations taking place between the extraction of the irradiated fuel stringer from the reactor channel and its handling in the fuel disposal cell. It is desirable that the model be capable of simulating both normal operations and incidental deviations, and that it balances its complexity with time and resource constrains.

In order to provide reliable results in a range of scenarios, the model must cover the following aspects:

- Thermal hydraulics of the flow inside the graphite sleeve, along the pin bundle;
- Thermal hydraulics of the flow in the surrounding region, e.g. the gas outlet and the annular region of the reactor channel between the moderator wall and the graphite sleeve;
- Conduction within the fuel, tie bar and other solid parts of the domain;

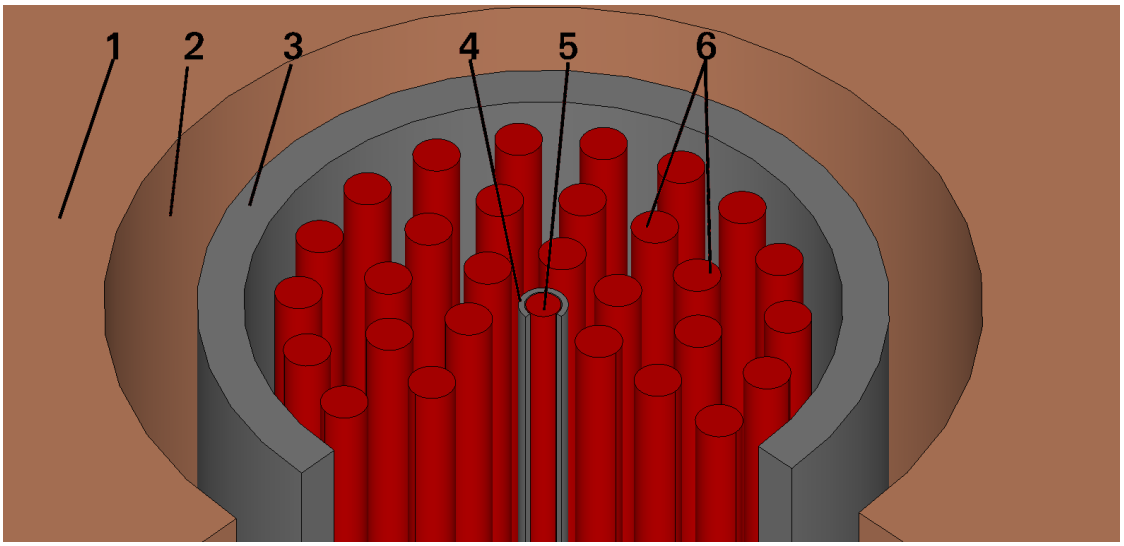

Figure 5.1: Schematics of the AGR stringer and its surroundings: 1) Delimiting wall, corresponds to different components in different scenarios (e.g. moderator, standpipe walls, etc.); 2) Gap between the sleeve and the delimiting wall; 3) Graphite sleeve; 4) Guide tube; 5) Tie bar; 6) Fuel pins

- Conjugate heat transfer between the solid and the fluid domain;
- Natural convection and thermal radiation.

In particular, a reliable treatment of natural convection and thermal radiation is of capital importance, due to their significant contribution to the overall heat transfer at the low flow rates involved in most of the scenarios of interest.

The purpose of the three-dimensional model is to provide additional capability to the analyses of the one-dimensional thermal-hydraulics codes used currently for Refuelling Cooling calculations at EDF Energy, when neglecting three-dimensional effects can lead to missing important aspects of the flow. One-dimensional results may indeed suffer from excessive pessimism in several situations that can occur during the refuelling operations. For instance, one-dimensional analysis provides very pessimistic results when the flow rate is very low or zero. A typical example occurs in the case of a total blockage of one of the stringers ends. In this scenario, while the net flow rate must drop to zero, internal recirculation still takes place due to natural convection and can contribute to heat removal. One-dimensional codes, taking into account the first phenomenon but not the latter, would thus over-predict the severity and the rate of the temperature increase that would result.

To implement the required features and at the same time maintaining the computational cost low enough for the use of the model in industrial practice, the overall strategy of the model developed is the following:

1. The flow and convective heat transfer in the fuel bundle are modelled using the

porous approximation.

2. The detailed solid geometry is represented for the purpose of conduction and radiation calculations. The resulting model is described in Section 5.2.

Finally, the model makes use of software developed, completely or in part, by EDF, a choice that would guarantee the availability of the solver to the company analysts in the years to come. The software chosen is presented in section 3.3. It consists of the SALOME platform, used for the generation and the discretisation of the domain, Code_Saturne, the solver for the calculation on the fluid domain and finally SYRTHES, used for the simulation of diffusive and radiative heat transfer in and between the solid domains.

5.2 The porous model: POSTR

In Section 2.3, it was shown that an alternative approach to the use of body fitted meshes to model complex geometries is often used when the focus of the simulation is on the global effect the component has on the flow, rather than the local details of the flow field. In this approach, the geometry under exam is modelled as an equivalent porous medium: this allows for the use of simpler, coarser meshes, thus reducing the computational resources needed for the calculation. The method models the effects of the solid surface as a body force and a volumetric heat generation term. This approach was applied to the AGR fuel stringer by Fung,[11] who developed the COOLFUEL-3D code on behalf of Nuclear Electric in 1995. As discussed in Section 1.3.2 COOLFUEL-3D consisted of a set of input files and subroutines for the CFD solver PHOENICS from CHAM ltd. In the course of the project discussed in this work, a replacement for COOLFUEL-3D based on Code_Saturne and SYRTHES was developed, to provide refuelling cooling analysts with a three-dimensional tool to support the current established methodology, particularly in low flow rate scenarios.

The model is based on a two-scale approach, in which separate meshes are used for the filtering and the solution of the governing equations (Section 5.2.1). The effect of the presence of the fuel on the fluid is modelled by a porosity field (Section 5.2.2) and additional source terms (Section 5.2.3), calculated on the coarser (*filtering*) grid, while the solution of the equations is performed on the finer (*solution*) mesh. Coupling between Code_Saturne and SYRTHES is established to simulate heat transfer between the solid and fluid domains (Section 5.2.4), while a simple turbulence model is employed to consider turbulent effects (Section 5.2.5). The mutual influence between the stringer and the rest of the system of interest is simulated by coupling the three-dimensional CFD calculation with a one-dimensional solver for a flow network. Conduction and radiation

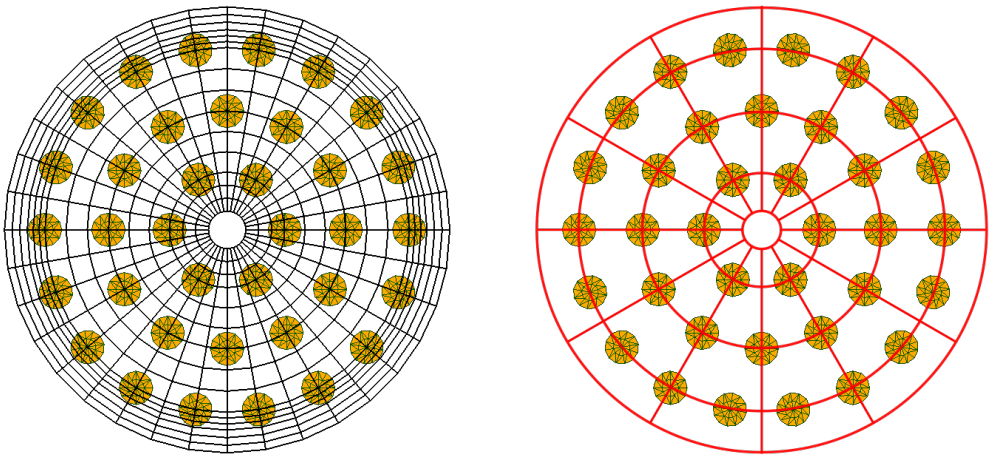

(a) Computational grid for the fluid (black) and the pins (golden).

(b) Filtering grid for the fluid (red) and position of the pins (golden).

Figure 5.2: Meshes used in the 'porous' model. The computational mesh in black is used in Code_Saturne for the solution of the equations for the fluid domain, whilst the mesh in black is used in SYRTHES to simulate conduction within the pins (other components, such as the claddings and the sleeve, can be included). The filtering mesh, shown in red, divides the fluid domain in blocks within which the porosity, hydraulic diameter and source terms are calculated. Each block can contain several cells of the computational mesh (Figure 5.3).

in the solid domain are simulated to provide accurate predictions for the solid temperature distribution (Section 5.2.7).

In the rest of this section the principles and the modelling choices followed in the development of the model are detailed.

5.2.1 Meshing and filtering

The methodology illustrated in Section 3.2 avoids the use of a body fitted mesh to represent the fluid domain around the fuel pins. Instead, the porous medium approximation is used. Here a much simpler mesh is employed for the gas inside the stringer, represented as an annular channel contained between the guide tube outer wall and the graphite sleeve inner wall (Figure 5.2). The presence of the solid components is accounted for by means of additional source terms, calculated using experimental correlations for the friction factor and the Nusselt number. The solid domain is meshed separately for conduction and radiation calculations. The coupling between the two domains is described in Section 5.2.4.

The calculation requires three computational meshes: one for the fluid domain, one for the solid surfaces for the radiation calculation, and one for conduction within the solid components. The latter may include the pins and their claddings, the graphite sleeve, the tie bar and its guide tube. Inert sections can be included in the solid mesh to simulate the

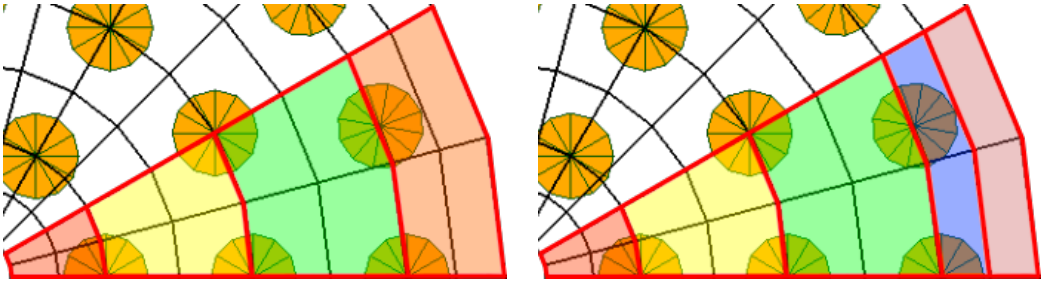

(a) 4 radial subdivisions. (b) 5 radial subdivisions.

Figure 5.3: Filtering grid (red) and computational mesh (black).

gaps between the fuel bundle at the interfaces between the elements. All the meshes are generated in SALOME using Python scripts for greater flexibility.

The geometry of the porous matrix, i.e. the fuel bundle, is represented in the fluid domain by spatially non-uniform quantities such as porosity γ, hydraulic diameter D_h and area of the solid surfaces A_w. This allows a more accurate description of the conditions encountered by the flow, but poses a fundamental question regarding the validity of the porous medium approximation in such a scenario. It is stated in Section 3.2 that this methodology is based on the averaging of the governing equations in a control volume of a suitable size, i.e. big compared to the dimension of the pores (Equations 3.42). If the computational mesh were used also as a filtering grid, it would necessarily be very coarse, in that a single cell would need to encompass, roughly, one of the sub-channels between the pins. In the case of the AGR stringer, that would mean that the mesh used could not have more than 4 or 5 divisions radially and 12 azimuthally.

In order to be able to refine the mesh, it was decided that the filtering grid and the computational mesh be separated (Figures 5.2 and 5.3). The latter can thus be refined without being constrained by the size of the pores, allowing the calculation to benefit from the improved discretisation and making it possible to run a mesh convergence study to reduce numerical errors. The filtering grid is instead chosen so that each of its blocks has size comparable to the pores: in the implementation used in this study, its radial divisions were made coincident with the space between the centrelines of the pin ranks. The space between the third rank of pins and the sleeve can be divided in a sub-region extending to the edge of the pins and a clear ($\gamma = 1$) annular region next to the sleeve wall (Figure 5.3b). The number of azimuthal division was chosen so as to divide the bundle in sectors containing the same number of pins (6 or 12 divisions in the studies presented).

This approach, however, leaves an open question regarding the interpretation of the microscopic variations of the variables obtained from the calculations, on scales smaller than the resolution of the filter. In the present study, a simple and relatively safe view is taken, which considers the size of the filter as the smallest scale of interest. The modelled

terms of the equations, i.e. the source terms and the turbulent viscosity are calculated at this scale, using quantities averaged on the filtering grid, as discussed below. For this reason, the intrinsic average operator (Equation 3.36) is applied to the computed fields before they are presented or used for any analysis. This operation also allows to compare the results of the porous model with those of the 'detailed' model, as shown in Section 6.1. A more sophisticated approach, aimed at predicting the features of the flow field with better approximation, would require a more complex distribution of the modelled quantities and may be suggested as a topic for further research.

It is noted that the size of the filtering blocks has been chosen to make them coincident to the sub-channels between the pins, in order to be able to use correlations for sub-channel flow to calculate the source terms. There is therefore a similarity between the methodology described herein and the established techniques of sub-channel analysis long employed in nuclear thermal-hydraulic analysis.[78] This observation justifies the abuse of terminology followed for the rest of this work, where the term '*sub-channel*' will be used as a synonym of 'filtering block'. For quantities referring to the computational mesh, the adjective '*local*' will be occasionally used.

5.2.2 Calculation of the porosity field

For the calculation of the porosity field, shown in Figure 5.4, two methods were employed in this study. The first to be developed used a numerical approach, which allowed for greater flexibility and it is now used, in a parallel project, for simulations of the cooling of fuel debris. With this technique, the volume of each pin is discretised in several blocks, and the coordinates of the centres of each block are calculated. For each centre, the algorithm locates the cell of the filtering grid where it lies and the volume of the block is assigned to that cell (Figure 5.5a). The volumes of the blocks assigned to a cell are summed, and the local porosity is calculated according to the formula:

$$\gamma = 1 - \frac{\sum V_{blocks}}{V_{cell}} \tag{5.1}$$

where V_{cell} is the volume of the filtering cell and V_{blocks} are the volumes of the solid blocks assigned to the cell.

The downside of the algorithm described above is that it can be relatively time consuming when a fine discretisation is used for the pins. For this reason, and since the flexibility it offers is not crucial for the case of intact fuel analysed in this study, a faster method has been devised based on an analytical solution. The nomenclature used below is illustrated in Figure 5.5b. The cross section of the stringer is divided in annular subregions, delimited by circles passing through the centres of the pins where the porosity is

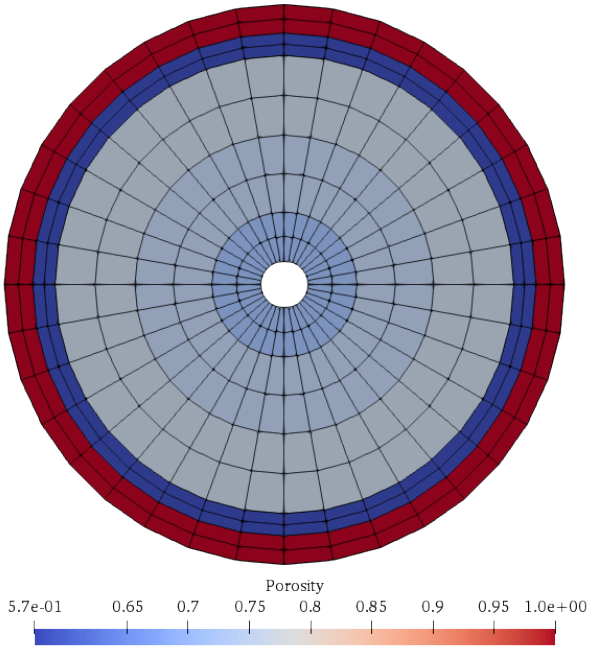

Figure 5.4: Porosity field, with the computational grid shown in black.

assumed to be uniform. Since for intact fuel both the volumes of the fluid and the pins are proportional to the height of the block, ratios of volumes are equivalent to ratios of cross sectional areas: $V_{pin}/V_{fluid} = A_{pin}/A_{fluid}$. For each sub-channel, the portion of the cross sectional area of a pin centred on its external boundary is given by (see Appendix C):

$$A_{p,ext} = R_p^2 \arccos \frac{R_p}{2R_{ext}} + R_{ext}^2 \arccos \frac{2R_{ext}^2 - R_p^2}{2R_{ext}^2} - \frac{R_p}{2}\sqrt{4R_{ext}^2 - R_p^2} \tag{5.2}$$

The residual part of the pin's cross section is then assigned to the adjoining region. By denoting with $A_{p,tot}$ the total solid area assigned to the region and with A_{fluid} the area of the annulus itself, the porosity of each annulus can be calculated as:

$$\gamma = 1 - \frac{A_{p,tot}}{A_{fluid}} \tag{5.3}$$

5.2.3 Friction and heat transfer

In Section 3.2, it was stated that after the averaging of the governing equations, additional terms appear that require modelling by means of experimental correlations. In the model described herein, these terms account for the friction exerted by the fuel pins on the fluid, in the momentum equations, whilst in the energy equation they model the heat exchange

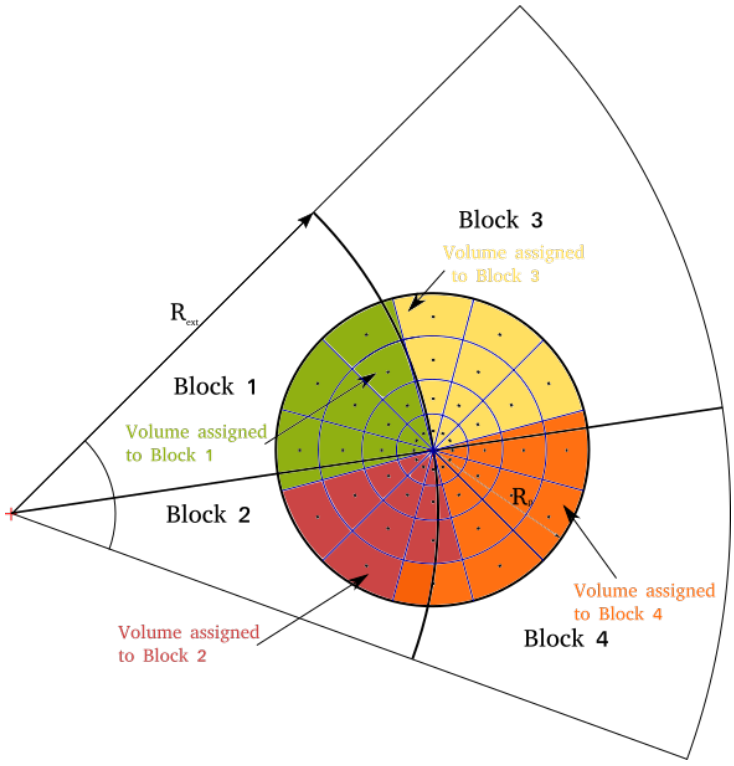

(a) Numerical algorithm. Each subdivision of the solid is assigned to the block where its centre lies.

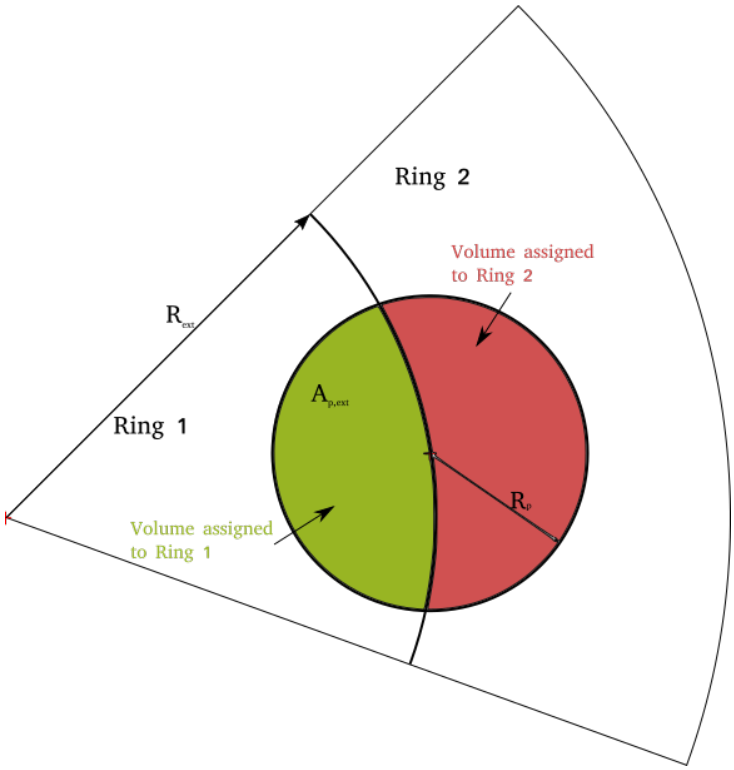

(b) Geometrical algorithm. The volumes assigned to each ring are calculated according to Equation 5.2

Figure 5.5: Algorithms for the calculation of the porosity field.

between the two domains. In integral form one can write:

$$F_{sc} = \int_{A_w} \tau_w dA_w \tag{5.4}$$

$$\dot{Q}_{sc} = \int_{A_w} q''_w dA_w \tag{5.5}$$

where R_{sc} and $\dot{Q}_{sc}$ are respectively the resistance exerted and the thermal power transferred from the fuel to the coolant in the sub-channel, while τ_w and q''_w are respectively the shear stress and the heat flux on the pins wall and A_w is the surface area of the pins contained in the sub-channel. Sub-channel averages for the latter two quantities can be calculated as:

$$\tau_{w,sc} = C_f \frac{{}^i\langle U \rangle^2}{2} \tag{5.6}$$

$$q''_{w,sc} = h\big({}^i\langle T_w \rangle - {}^i\langle T_f \rangle\big) \tag{5.7}$$

where C_f is the average Fanning friction factor in the sub-channel, h the average heat transfer coefficient, U, T_w and T_f are respectively the flow velocity and the solid and fluid temperatures, and the operator ${}^i\langle\cdot\rangle$ represents intrinsic averages in the sub-channel. Correlations for C_f and $\mathrm{Nu} = hD_h/\lambda$ are then necessary. In the studies presented in this work different sets of correlations are used for flow along smooth rod bundles and rough AGR fuel pins.

As pointed out, the quantities in Equation 5.4 are integrated over each sub-channel. These must be distributed among the computational cells belonging to the same filtering block to be imposed as a source term in the solver. The distribution is carried out proportionally to the volume of the cells.

In the calculation of the source terms, the contribution of the main flow and local buoyancy effects are considered. The correlations used express C_f and Nu as functions of sub-channel Reynolds Number $\mathrm{Re} = UD_h/\nu$ and Grashof Number $\mathrm{Gr} = g\beta(T_w - T_f)\delta^3/\nu^2$. These two parameters are also used to evaluate the flow regime and select the appropriate correlations. The contribution due to forced convection in turn considers separate contributions from axial and transversal flows. In the correlations for the latter, Re, Gr and Nu are based on the diameter of the pins D_p instead of D_h. The procedure followed can be thus summarised:

1. The sub-channel Reynolds number Re and the Grashof number Gr are evaluated for every sub-channel, to evaluate the flow regime and select the correlations to be used.

2. Sub-channel C_f and Nu due to forced and free convection are calculated from the

correlations presented in Appendix B.

3. The values of wall shear stress τ_w (from C_f) and Nu obtained for free and forced convection are blended using a composite expression of the form:[11]

$$X = \sqrt[3]{X_{forced}^3 + X_{free}^3} \tag{5.8}$$

These steps are undertaken for both the axial and the cross-flow. To blend the two contributions, the approach proposed by Romero[88] is followed, which combines the values for the axial and cross-flow contributions multiplied by '*yaw factors*' derived from fitting experimental data. For the friction, a coefficient Eu_c is defined, which has the dimensions of a loss coefficient per unit length. It is calculated as:[88]

$$\mathrm{Eu}_c = \sqrt{\left(\frac{4 f_{ax}}{D_h}\cos^{14}\psi\right)^2 + \left(\Omega\frac{\mathrm{Eu}_{cf}}{\mathrm{Pitch}}\sin^{1.32}\psi\right)^2} \tag{5.9}$$

where f_{ax} is the axial friction factor, Eu_{cf} is the cross flow loss coefficient (or Euler number), $\psi = \arccos(v_z/|\vec{v}|)$ is the angle of the flow velocity with the axial direction, and Ω is a tuning coefficient introduced to make the expression a good approximation for both in-line and staggered arrays of pins.[88] The pressure gradient in the i-th direction can then be written as:

$$\frac{\partial p}{\partial x_i} = \frac{1}{2}\mathrm{Eu}_c \cdot \rho|\vec{v}|^2\cos\phi_i \tag{5.10}$$

where ϕ_i is the angle between the velocity vector and the i-th direction. Details on the implementation can be found in Appendix A.

For the Nusselt number, the same principle was applied by Romero, albeit, admittedly, with limited backing from experimental data. It was observed that experimental investigation of the effect of yaw on heat transfer over banks of cylinders, for instance the work of Žukauskas,[89] shows little dependence of the Nusselt number from the axial flow in the range of ψ explored, down to $30°$. Therefore, it was postulated that the contribution of the axial flow should die out rapidly with increasing ψ. In COOLFUEL-3D and in the model described in this work the compound heat transfer coefficient is calculated as:

$$h = \sqrt{h_{ax}^2\cos\psi + h_{cf}^2\sin\psi} \tag{5.11}$$

5.2.4 Coupling

It is mentioned in Section 3.3 that the volumetric coupling capability provided by SYRTHES and Code_Saturne is not suitable for a scenario where the details of the solid geometry are resolved. This is due to the fact that, in the approach used in the unmodified code,

every point of the solid domain, including those in the interior of the components, exchange heat with the fluid. Consequently, it is necessary to develop a new coupling infrastructure to model the heat exchange only at the surfaces wet by the coolant. With the new methodology, implemented by means of patches to SYRTHES and subroutines for Code_Saturne, the sub-channel heat transfer coefficient h and average fluid temperature ${}^{i}\langle T_f \rangle$ are communicated by Code_Saturne to SYRTHES, where they are used as boundary conditions on the coupling faces. In turn, SYRTHES sends the temperatures ${}^{i}\langle T_w \rangle$ of the surface elements to Code_Saturne, where they are averaged in the respective sub-channel and used to calculate the heat source term for the fluid domain:

$$q''' = q''_{w,sc} \cdot \frac{A_w}{V_f} = h \frac{A_w}{V_f} \left(T_w - {}^{i}\langle T_f \rangle \right) \tag{5.12}$$

where V_f is the volume of the fluid in the sub-channel. The 'PLE' libraries, distributed together with Code_Saturne, are responsible for associating the data transferred between the domains to the correct location within the meshes.

Since the contact surfaces between the fluid domain and the sleeve, or the guide tube, are part of the boundaries of the fluid mesh, the built-in surface coupling provided by the solvers is used at these interfaces. However, as explained below, the heat transfer coefficient calculated by Code_Saturne is replaced by a value obtained from correlations.

5.2.5 Turbulence model

A simple zero-equations eddy viscosity turbulence model is used in the model, with the turbulent viscosity calculated as:[90]

$$\mu_t = \alpha_1 \sqrt{\frac{C_f}{2}} \rho |w| D_h \tag{5.13}$$

where α_1 is a coefficient equal to 0.035, C_f is the Fanning friction factor, ρ is the fluid density, $|w|$ is the absolute value of the vertical velocity, and D_h is the hydraulic diameter. An additional tuning coefficient is provided for sensitivity studies. The turbulent thermal conductivity is obtained by dividing μ_t by a turbulent Prandtl number σ_t, usually set equal to 1 to match the default value used in the turbulence models implemented in Code_Saturne.[80]

The model does not include any special treatment for the near-wall region of the flow: this would result in an over-prediction of the turbulent shear stress and heat flux at the surfaces where no-slip boundary conditions are imposed. To overcome this issue, two separate solutions were devised for the friction and heat transfer aspects.

The friction on the walls is modelled as an additional distributed source term in the

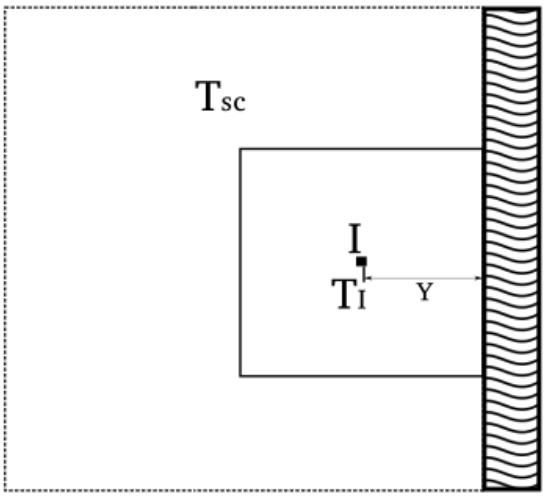

Figure 5.6: Correction to near-wall turbulent conductivity

sub-channels adjoining the boundary. A wall friction factor is calculated by correlations and used to calculate the wall shear stress, which is multiplied by the area of the wall surface touched by the sub-channel. Since the friction due to the boundary wall is accounted for in the source term, imposing a no-slip boundary condition would double-account for its contribution to the pressure drop. To avoid this, a no-shear boundary condition ($\tau_w = 0$) is imposed on those surfaces.

Since heat transfer at the surfaces involves coupling with the solid domain, a somewhat more complex adjustment had to be implemented to correct its behaviour. Heat transfer at the no-shear walls, in Code_Saturne, is considered to be purely due to molecular and turbulent diffusion and calculated as (Figure 5.6):

$$q'' = (\lambda + \lambda_t)\frac{T_w - T_I}{Y} \tag{5.14}$$

where λ_t is the eddy thermal conductivity. All quantities are defined on the computational mesh. T_w and T_I are respectively the temperatures at the face centre and at the cell centre, while Y is the distance between the cell centre I and the wall. A local heat transfer coefficient can thus be written as $h_{diff} = \frac{\lambda+\lambda_t}{Y}$. The heat flux from the wall calculated by Code_Saturne, if no correction is made, is therefore given by:

$$q''_{CS} = h_{diff}(T_w - T_I) \tag{5.15}$$

It is evident that, in absence of damping of λ_t, heat exchange would be overestimated. Using an experimental correlation for the heat transfer coefficient h_{sc}, one could obtain

an average value for the sub-channel and compute the 'real' heat flux as:

$$q''_{real} = h_{sc}(T_w - {}^{i}\langle T_f \rangle) \tag{5.16}$$

The local wall temperature is still used, instead of the average, since when integrated across the surface it will result in the same thermal power. Comparing Equations 5.15 and 5.16 one derives a an effective h_{diff}:

$$h_{diff} = h_{sc}\frac{T_w - {}^{i}\langle T_f \rangle}{T_w - T_I} \tag{5.17}$$

which in turn gives, for the turbulent conductivity at the wall:

$$\begin{aligned} \lambda_t &= h_{sc}\frac{T_w - {}^{i}\langle T_f \rangle}{T_w - T_I}Y - \lambda \\ &= h_{sc}K_T Y - \lambda \end{aligned} \tag{5.18}$$

This value replaces the value from Equation 5.13 in the cells next to the wall. Details on the implementation are given in Appendix A.

5.2.6 Surroundings of the stringer

In many scenarios of interest, the flow within the stringer is strongly influenced by the condition in its surrounding, and it is not always possible to decouple the two domains. A situation of this type was encountered in the course of this study in the simulation of a set of experiments carried out at the MEL, performed to study the cooling of AGR fuel during low power refuelling.[91] The simulation campaign and the experimental set-up are described in Section 6.3. In a first approach to the problem, an attempt was made to include all the regions of interest in the three-dimensional model, defining separate regions which offered different resistances to the flow, and using Code_Saturne to solve the governing equations in the whole system. This approach was found impractical due to the apparent difficulty of suppressing the spatial oscillations in the pressure and velocity field arising at the interface between the regions. Reports by other workers suggest that this issue is common when using finite volume solvers, and would require specific numerical solvers to be mitigated.[92]

To overcome this issue an alternative method was adopted, which coupled a three-dimensional model for the stringer with a one-dimensional resistance network for the external environment. In the campaign described in Section 6.3 an *ad hoc* network solver was developed, which took advantage of the simplicity of the circuit. The subroutines implementing it, described in Appendix A, provide a frame which can be adapted to other

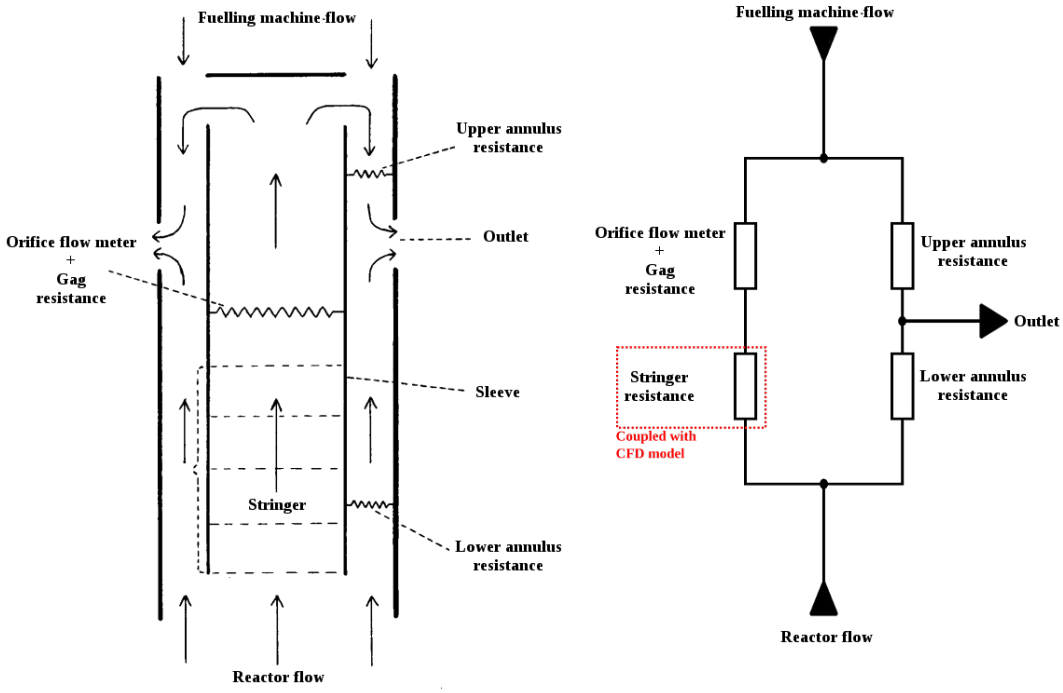

(a) Model of the MEL test facility. Adapted from ref. [91]

(b) Resistance network.

Figure 5.7: Model of the surroundings of the fuel stringer used in the MEL experiments' simulation campaign.

scenarios, always on a case-by-case basis. Coupling with a more complex and flexible solver may be desirable, but the feasibility of the endeavour has not been assessed. In the following, a conceptual description of the model for the MEL rig is provided.

Figure 5.7a shows a schematic representation of the test rig used in the MEL experiments. Moore[91] provides the compound flow resistance in the three main legs of the circuit outside the stringer, defined as

$$R = \frac{\rho \Delta p}{\dot{m}^2} \tag{5.19}$$

These values were provided as constants for each of the test cases considered. They were used to build the network shown in Figure 5.7b, from which the following system of equations was derived:

$$\begin{cases} \dot{m}_{\mathrm{ua}} = \dot{m}_{\mathrm{str}} + \dot{m}_{\mathrm{fm}} & \text{Continuity - Upper plenum} \\ \dot{m}_{\mathrm{ua}} + \dot{m}_{\mathrm{la}} = \dot{m}_{\mathrm{out}} = \dot{m}_{\mathrm{re}} + \dot{m}_{\mathrm{fm}} & \text{Continuity - Outlet} \\ \left(\frac{R_{\mathrm{str}}}{\rho_{\mathrm{str}}} + \frac{R_{\mathrm{gag}}}{\rho_{\mathrm{gag}}} \right) \dot{m}_{\mathrm{str}}^2 + \frac{R_{\mathrm{ua}}}{\rho_{\mathrm{ua}}} \dot{m}_{\mathrm{ua}}^2 + \frac{R_{\mathrm{la}}}{\rho_{\mathrm{la}}} \dot{m}_{\mathrm{la}}^2 = 0 & \text{Pressure balance} \end{cases} \tag{5.20}$$

where the subscripts 'ua' and 'la' refer respectively to the upper and lower annulus, 'gag' to the compound gag unit and flow meter and 'str' to the stringer. The subscripts 're' and 'fm' refer respectively to the incoming flow from the reactor and the fuelling machine (or, more precisely, their equivalents in the experimental rig).

The system of Equation 5.20 is solved iteratively at every time step to obtain $\dot{m}_{\mathrm{str}}$, using the Newton-Raphson method to linearise the pressure balance, followed by a fixed number of iterations of the Gauss-Seidel method. When the solution converges, the flow rate calculated is used as an inlet boundary condition for the CFD calculation in the stringer. The solution for the pressure and density fields thence obtained are used to calculate the resistance $R_{\mathrm{str}}/\rho_{\mathrm{str}}$, which forms the feedback to the one-dimensional solver. A lumped parameter model is used for the heat transfer from the graphite sleeve to the lower annulus, in which the average gas temperature is calculated as:

$$T_{\mathrm{la}} = T_{\mathrm{re}} + \frac{1}{2}\frac{\dot{Q}_{\mathrm{sleeve}}}{\dot{m}_{\mathrm{la}} c_{p,\mathrm{la}}} \tag{5.21}$$

where T_{la} and T_{re} are the average temperature in the lower annulus and the temperature of the reactor flow, $\dot{Q}_{\mathrm{sleeve}}$ is the power crossing the sleeve outer wall as calculated by SYRTHES and $c_{p,\mathrm{la}}$ is the specific heat of the gas in the lower annulus. The heat transfer coefficient is calculated from correlations, and the two parameters are communicated to SYRTHES, where they are imposed as boundary conditions on the sleeve outer wall. In turn, SYRTHES sends back the total power from the sleeve and the average wall temperature.

Details on the implementation are provided in Appendix A. The latter includes recommendations concerning the adaptation of the methodology to different scenarios.

5.2.7 The solid domain

The solid model comprises of computational domains for conduction and thermal radiation (Figures 5.8 and fig:radiation-domain). It can include the fuel pins, their claddings, the graphite sleeve, the tie bar and its guide tube. Any of these components can be excluded if not required in the calculation. The mesh for the radiation solver is usually coarser than that for the conduction, due to the computationally intense calculation of the view factors, although they can be stored in a file and reused in all the simulations involving the same mesh.

The model for the fuel pin is typically composed by a cylinder representing the fuel and an annulus representing the cladding. A contact resistance is defined between the outer surface of the fuel and the inner surface of the cladding. A volumetric heat source term is assigned to the fuel region, while the outer surface of the cladding exchanges heat

with the fluid domain through the volume coupling methodology described in Section 5.2.4.

The graphite sleeve is modelled as an annulus, the inner surface of which receives its boundary condition from the fluid through the built-in surface coupling methodology provided by the solvers. At the outer surface, a range of boundary conditions can be chosen to suit the scenario: in the simulation campaign regarding the MEL experiment (Section 6.3), they were provided by a lumped parameters model indirectly coupled with the fluid model. Heat generation in the sleeve due to absorption of nuclear radiation can be simulated as a volumetric heat source.

5.3 Concluding remarks

In this chapter the development of POSTR, a three-dimensional model for the AGR fuel stringer, based on the porous medium approximation, has been described. The model was conceived to support the thermal-hydraulic analysis of scenarios occurring during refuelling, which is based chiefly on one-dimensional system codes, by allowing practitioners to estimate the influence of internal circulation in refuelling cooling scenarios characterised by very low or zero net flow rate through the stringer.

A novel two-scale approach was adopted for the discretisation of the domain to fulfil the requirements of the porous medium approximation while allowing the refinement of the computational mesh. Source terms for the momentum and energy equations are calculated from empirical correlation at the largest scale, corresponding to the dimensions of the sub-channels within the bundle. The solution of the equations is subsequently performed on a finer mesh.

The coupling methodology available in the solvers employed was modified to allow realistic predictions of the temperature distribution in the solid components. A simple zero-equation turbulence model was used with modifications applied in the vicinity of the walls to account for the lack of damping of the turbulent viscosity.

In the following chapter, the predictions of POSTR are compared with the results of detailed RANS calculations, the output of legacy software and data from a large-scale experiment. A discussion of its performance and recommendations on its usage will be presented therein.

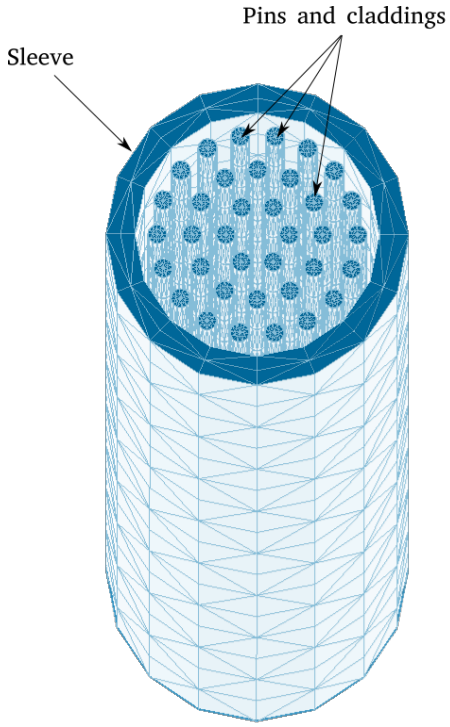

Figure 5.8: Computational grid for conduction in the solid domain.

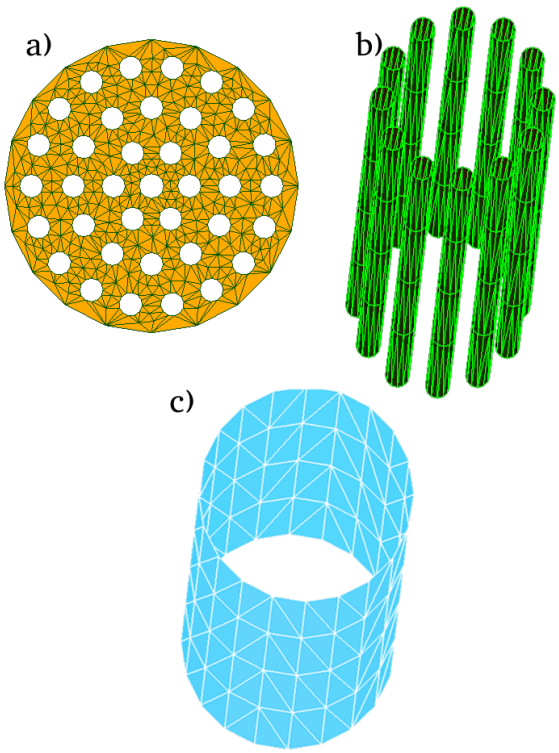

Figure 5.9: Computational grid for radiation in the solid domain: a) mesh for the top and bottom openings; b) mesh for the pins surfaces (Rank 2 is depicted); c) mesh for the sleeve.

Chapter 6

Validation and demonstration of potential applications of POSTR

In this chapter, the results obtained using the model described in Chapter 5 are compared with the results of other calculations and with available experimental data. The objective is to evaluate the potential and limitation of the numerical tool for thermal-hydraulic calculations concerning the AGR Stringer. Section 6.1 presents a comparison between POSTR and RANS calculations in body fitted meshes for the simulation of forced flow along a fuel bundle; in Section 6.2 a comparison is presented between POSTR and pre-existing software for refuelling cooling, for a case of natural convection in a full-sized AGR stringer; finally, in Section 6.3, the simulation of a refuelling cooling experiment is discussed.

6.1 Forced flow in smooth and rough fuel bundles - Comparison with detailed RANS results

6.1.1 Description of the scenario and overview of the model

In the study presented in this section, forced convection along a fuel bundle was simulated using POSTR and traditional RANS techniques. The aim was to evaluate the ability of the porous model to approximate the temperature and velocity distribution in the stringer.

The domain considered was a $3\,\mathrm{m}$ long channel, containing a bundle of 36 heat generating pins, representing a shortened version of the AGR stringer. The solid domain was limited to the unclad pins, and was discretised by a mesh of 38880 tetrahedral elements. The discretisation of the fluid domain was carried out differently for the 'detailed' and 'porous' simulations, as shown in Figure 6.1. The different settings used in the two models are discussed in the following.

Property	Symbol	Value	Units
Density	ρ	39.936	$\mathrm{kg\,m^{-3}}$
Dynamic viscosity	μ	2.70×10^{-5}	$\mathrm{Pa\,s}$
Specific heat	c_p	1080.24	$\mathrm{J\,kg^{-1}\,{}^{\circ}C^{-1}}$
Thermal conductivity	λ	4.07×10^{-2}	$\mathrm{W\,m^{-1}\,{}^{\circ}C^{-1}}$
Prandtl number	Pr	0.72	

Table 6.1: Physical properties imposed to the fluid in the study presented in Section 6.1.

An annular mesh of the type described in Section 5.2.1 was used (Figures 6.1a and 6.2a) for the 'porous' calculation. The inlet was placed on the bottom surface, with a uniform velocity and temperature distribution imposed, respectively of $5.5\,\mathrm{m\,s^{-1}}$ and $30\,^{\circ}\mathrm{C}$. At the top surface an outlet boundary condition was imposed, which correspond to a Dirichlet boundary condition for the pressure and a homogeneous Neumann boundary condition for all the other variables. The boundaries corresponding to the sleeve and guide tube walls were adiabatic and were treated as no-shear surfaces. The conjugate heat transfer simulation used the coupling method described in Section 5.2.4. Correlations for smooth pin bundles were used. The heat generation in the pins was $7 \times 10^7\,\mathrm{W\,m^{-3}}$, which corresponds to a total channel power of $\sim 1.4\,\mathrm{MW}$.

The constant physical properties assigned to the fluid are summarised in Table 6.1. Taking them into account, and given the boundary conditions detailed above, one can calculate the mass flow rate and temperature increase in the channel as $\dot{m} = 4.875\,\mathrm{kg\,s^{-1}}$ and $\Delta T_{\mathrm{ch}} = 264.48\,^{\circ}\mathrm{C}$.

A body-fitted mesh is used in the 'detailed' calculation, formed by 38 'near-wall' sub-regions discretised with hexahedral cells, and a 'bulk' region made out of prismatic elements (Figures 6.1b and 6.2b).

The simulations were carried out with the standard $k - \varepsilon$ turbulence model and, for comparison, with a Reynolds Stress Model (the $R_{ij} - \varepsilon$ SSG model). Two-scales wall functions were used, with the non-dimensional distance y^+ of the wall from the first node lying in the range $20 - 50$ in all calculations. The Single Gradient Diffusion Hypothesis was used in all the calculations presented for the turbulent heat fluxes, while the Generalised Gradient Diffusion Hypothesis was tested in one RSM calculation and was proved uninfluential. No-slip boundary conditions were applied at all walls, which were considered smooth. Surface coupling with the solid domain was employed to simulate heat exchange with the pins. The same conditions as in the 'porous' simulations were set on the remaining boundaries.

A pseudo-transient method was used, where only the final fields of an unsteady simulation were retained for the analysis. The default first-order time advancement schemes were used for all the discretised quantities, with the implicit Euler scheme used for the

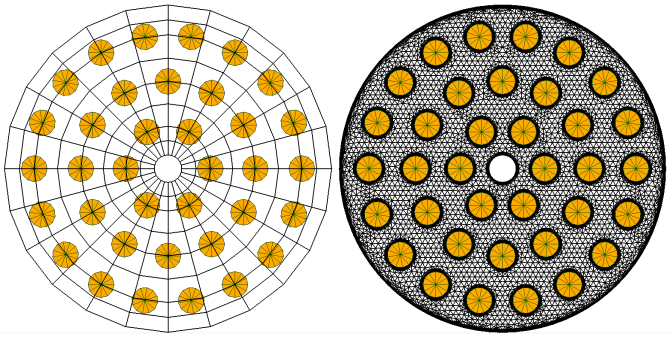

(a) Simplified mesh for 'porous' calculations.

(b) Body fitted mesh for 'detailed' calculations.

Figure 6.1: Comparison between the meshes used in the 'detailed' and 'porous' simulations (solid mesh shown in yellow). The figures show the cross sections normal to the z axis.

solved variables. The time step size was $10^{-3}\,\mathrm{s}$ for the 'detailed' simulations and $10^{-2}\,\mathrm{s}$ for the 'porous' calculations. For timing purposes, all simulations were carried out for 1000 time steps, which were more than sufficient to achieve a converged solution. All calculations used the SOLU discretisation scheme for velocity and temperature, with the possibility to switch locally to the Upwind scheme based on the result of a slope test.

A mesh independence study was carried out to minimize the discretisation error. Four meshes of increasing fineness were employed for each model. Their size is reported in Table 6.2. The filtering grid for the porous model (see Section 5.2.1) had 30 division on the axial direction, 12 on the azimuthal direction and 5 on the radial direction.

Figure 6.3 shows an example of the computed velocity and temperature fields calculated by the 'detailed' and 'porous' models at a cross section placed at $z = 2.55\,\mathrm{m} = 0.85H$. It is apparent that a direct comparison between the two solutions would be difficult. Therefore, the intrinsic average operator:

$$ {}^{i}\langle y \rangle = \frac{1}{V_f} \iiint_{V_f} y dV \tag{6.1}$$

is applied to the computed field during post-processing. The filtering grid was the same used in the porous calculation. An example of filtered results is presented in Figure 6.4.

6.1.2 Influence of the computational mesh.

In this section the results of the mesh independence study carried out on the 'porous' and 'detailed' calculation are presented. The study was carried out running four calculations for each model, on the meshes reported in Table 6.2, keeping constant all other settings. All the 'detailed' calculations employed the $k-\varepsilon$ turbulence model. For post-processing purposes, the intrinsic average operator is applied to the results, over the five annular

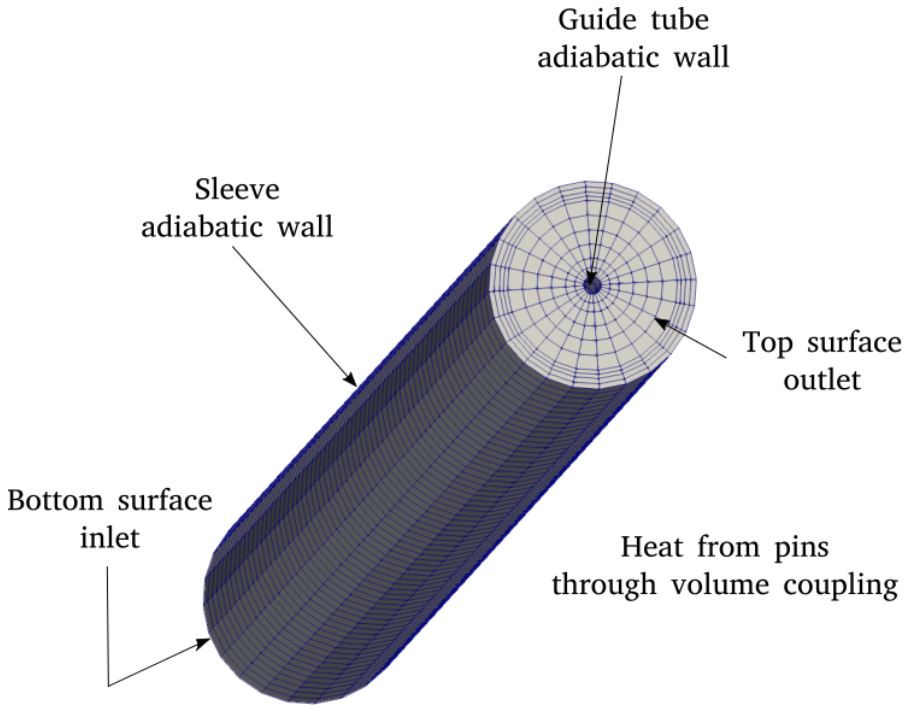

(a) Fluid domain for the ‘porous’ calculation.

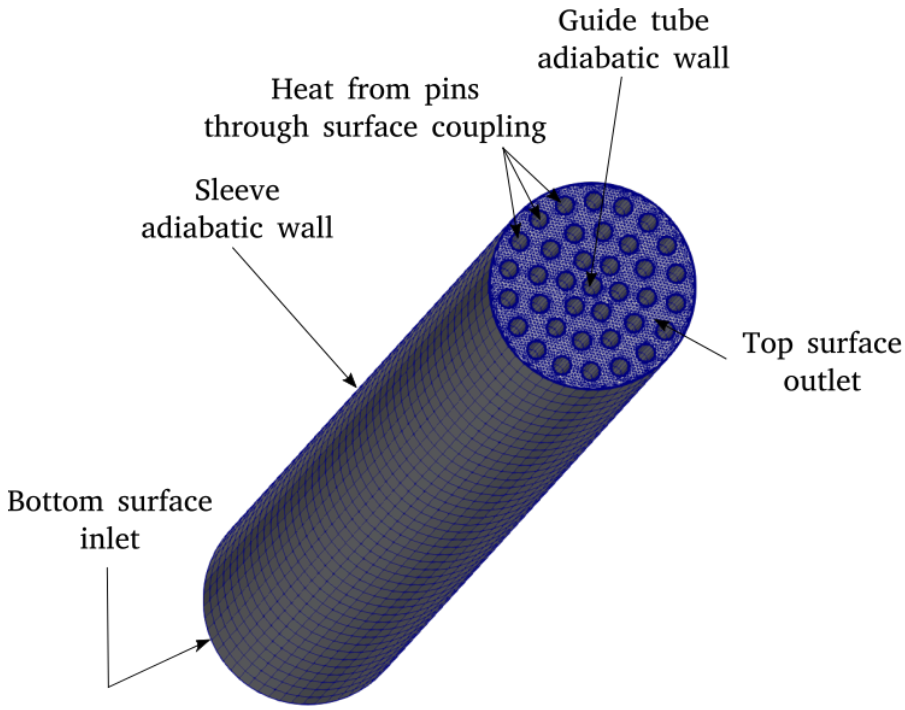

(b) Fluid domain for the ‘detailed’ calculation.

Figure 6.2: Fluid domains for the calculations presented in Section 6.1, annotated with the boundary conditions imposed.

Mesh	Number of elements
A1	125640
B1	332304
C1	610886
D1	1973740

(a) 'Detailed' calculations.

Mesh	Number of elements
A2	1800
B2	14400
C2	48600
D2	115200

(b) 'Porous' calculations.

Table 6.2: Number of elements in the meshes used in the study presented in Section 6.1.

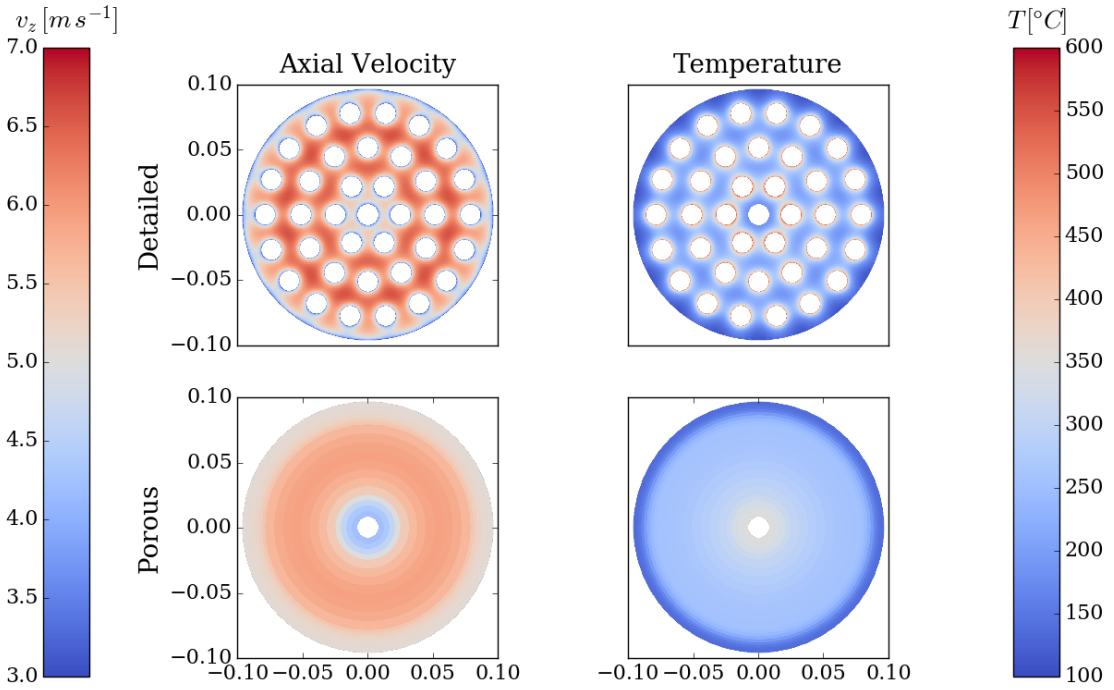

Figure 6.3: Velocity and temperature fields on a cross sectional plane at $z = 2.55\,\mathrm{m}$ as calculated by the 'detailed' and 'porous' models using meshes D1 and D2 (see Table 6.2.

Variable	Detailed [%]	Porous [%]	Variable	Detailed [%]	Porous [%]
ΔP	0.09	−0.76	T_{w3}	−0.23	−0.04
T_{f_1}	1.13	−0.30	T_{w4}	−0.25	−0.14
T_{f_2}	0.07	−0.25	w_1	−0.45	0.21
T_{f_3}	0.76	−0.14	w_2	0.12	−0.03
T_{f_4}	0.42	−0.44	w_3	−0.15	−0.06
T_{f_5}	−0.77	0.16	w_4	0.01	0.11
T_{w1}	−0.17	−0.15	w_5	0.21	0.03
T_{w2}	−0.25	−0.07			

Table 6.3: Relative variation $\frac{Y_D - Y_C}{Y_D}$ of the values of a number of integral quantities in the last refinement for the 'detailed' and 'porous' models. The subscripts C and D refer to the finest meshes in Table 6.2.

regions defined in Figure 6.5. The sub-channels are numbered from 1, the innermost, to 5, the outermost.

Figures 6.6, 6.7, 6.8 and 6.9 show the evolution of, respectively, the pressure drop and the sub-channel averages of the axial velocity, fluid and wall temperature calculated with the 'detailed' model on progressively finer meshes. Figures 6.10, 6.11, 6.12 and 6.13 show the same trends for the 'porous' calculations. The size of the mesh is represented in the horizontal axis by the cubic root of the number of elements. The sub-channel averages are calculated at an axial position of $z = 2.55\,\mathrm{m}$. All the plots show a converging trend, indicating the reduction of the numerical error due to the discretisation. The relative variations between the two finest meshes for each quantity are listed in Table 6.3. It can be concluded that mesh independence is achieved in this scenario. Mesh D2 will be employed in the following for all POSTR calculations, while for the detailed simulations the results obtained using mesh C1 will be used. This was decided in order to reduce the computational time of the subsequent calculations, especially those run using the RSM model.

The increase in calculation time for each mesh refinement is shown in Figure 6.14. All calculations were run on a Personal Computer, using 5 CPU cores for Code_Saturne and 1 for SYRTHES. It can be observed that, for similar mesh sizes, the 'porous' model runs are in general slower than the 'detailed' calculations, due to the additional overhead introduced by the model. However, the possibility to use coarser meshes makes the model competitive even against fast $k - \varepsilon$ calculations as those presented here. The execution time of the RSM calculation discussed in next section is also included for comparison: the simulation lasted for 229', a significant increase from the 182' required by the $k - \varepsilon$ model to run on the same mesh.

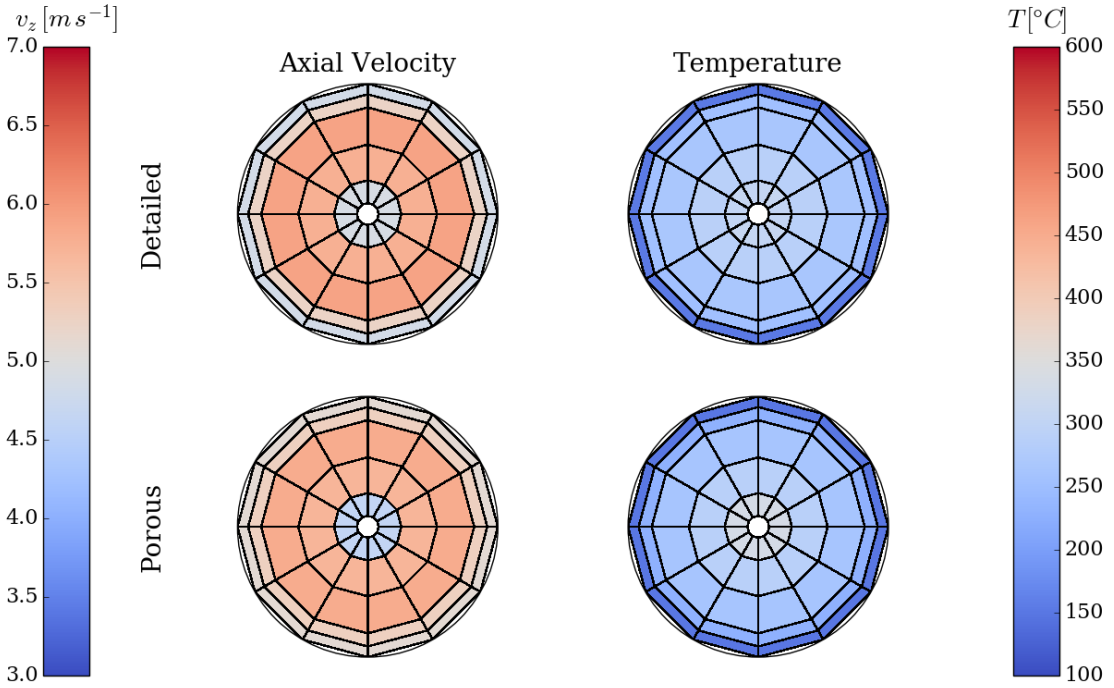

Figure 6.4: Velocity and temperature fields of Figure 6.3 after applying the intrinsic average operator of Equation 6.1.

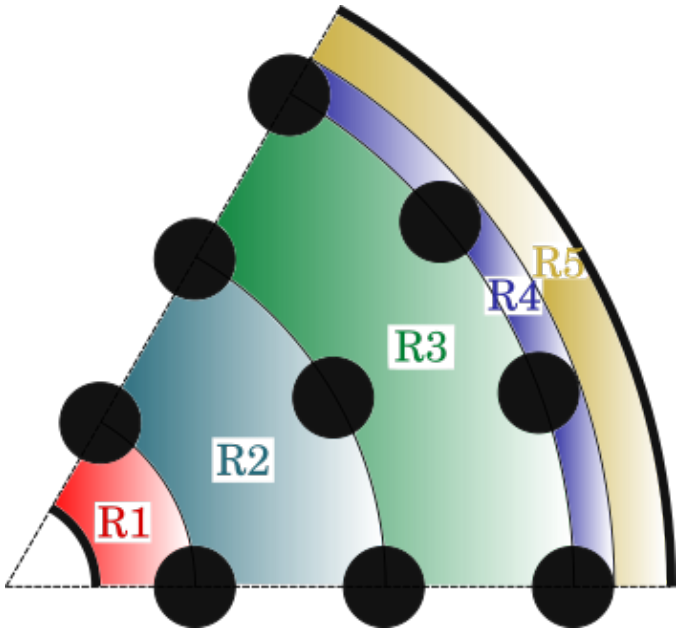

Figure 6.5: The five annular sub-channels used in the averaging operations.

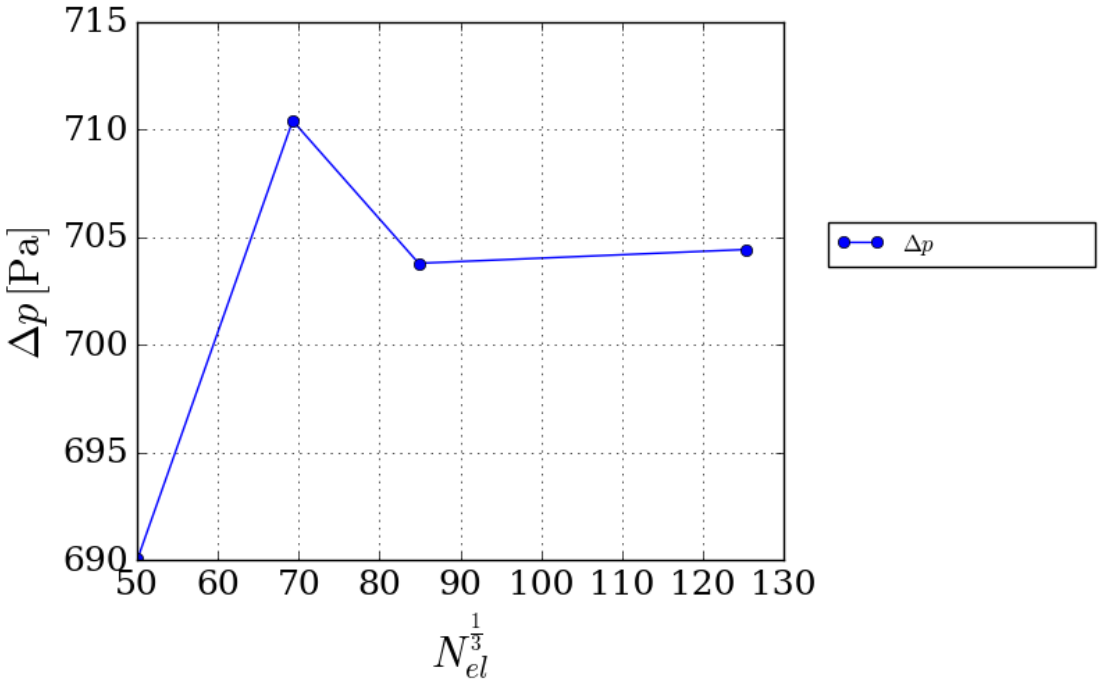

Figure 6.6: Predictions of the pressure drop obtained with the 'detailed' model through successive refinements of the fluid mesh.

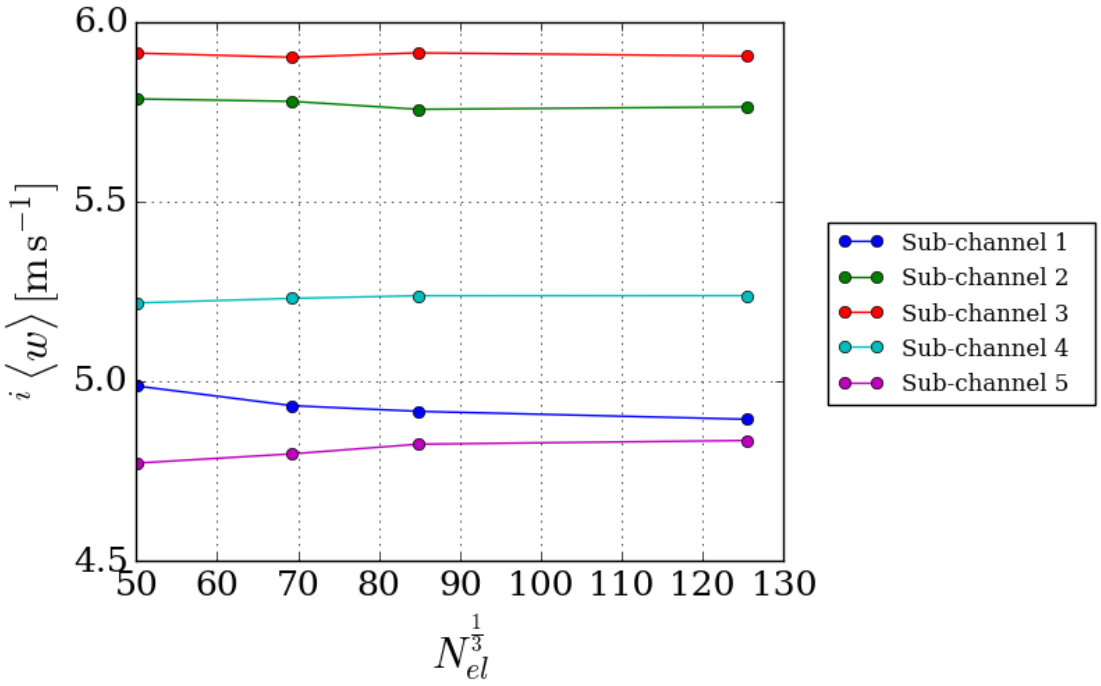

Figure 6.7: Predictions of the average sub-channel velocity at $z = 2.55\,\mathrm{m}$ obtained with the 'detailed' model through successive refinements of the fluid mesh.

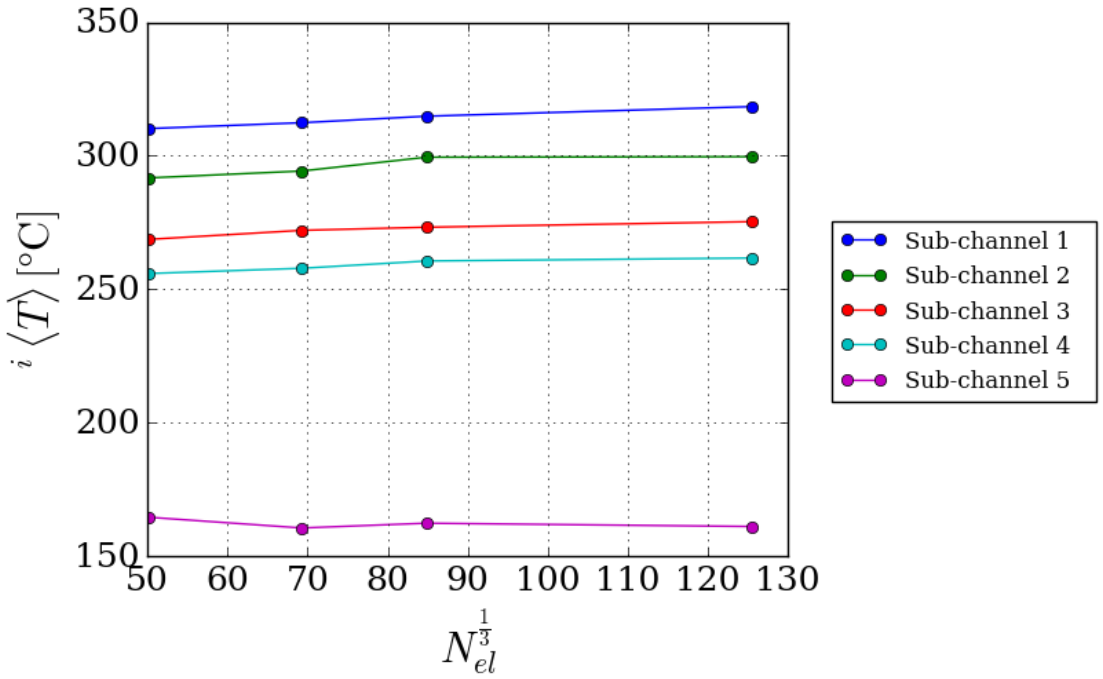

Figure 6.8: Predictions of the average sub-channel fluid temperature at $z = 2.55\,\mathrm{m}$ obtained with the 'detailed' model through successive refinements of the fluid mesh.

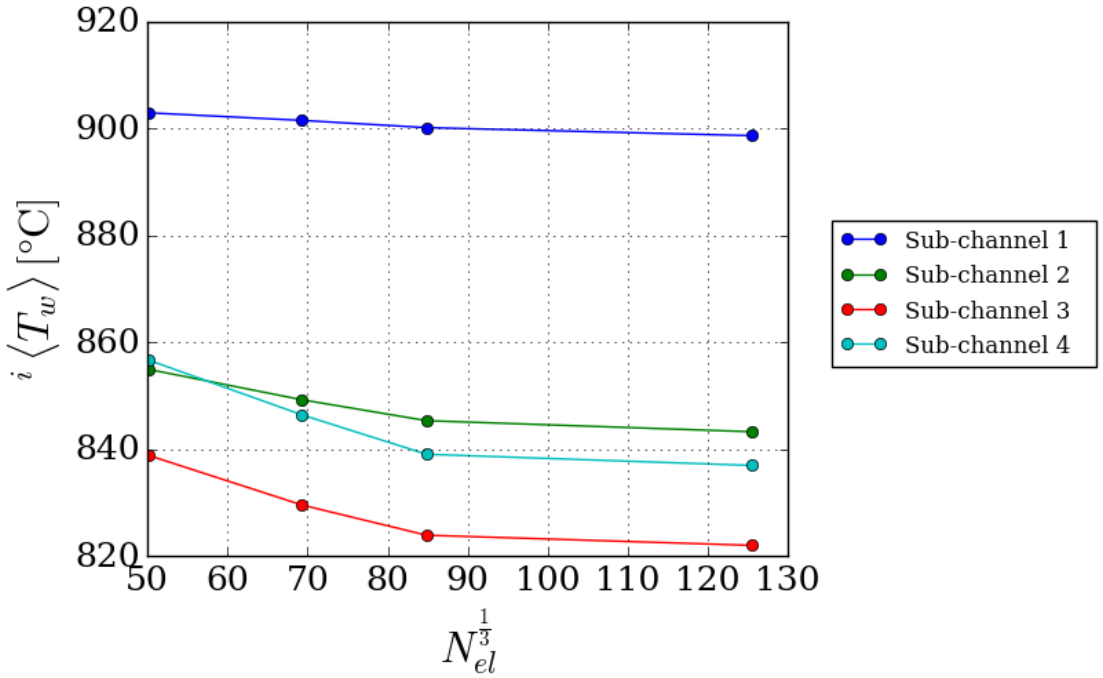

Figure 6.9: Predictions of the average sub-channel solid wall temperature at $z = 2.55\,\mathrm{m}$ obtained with the 'detailed' model through successive refinements of the fluid mesh.

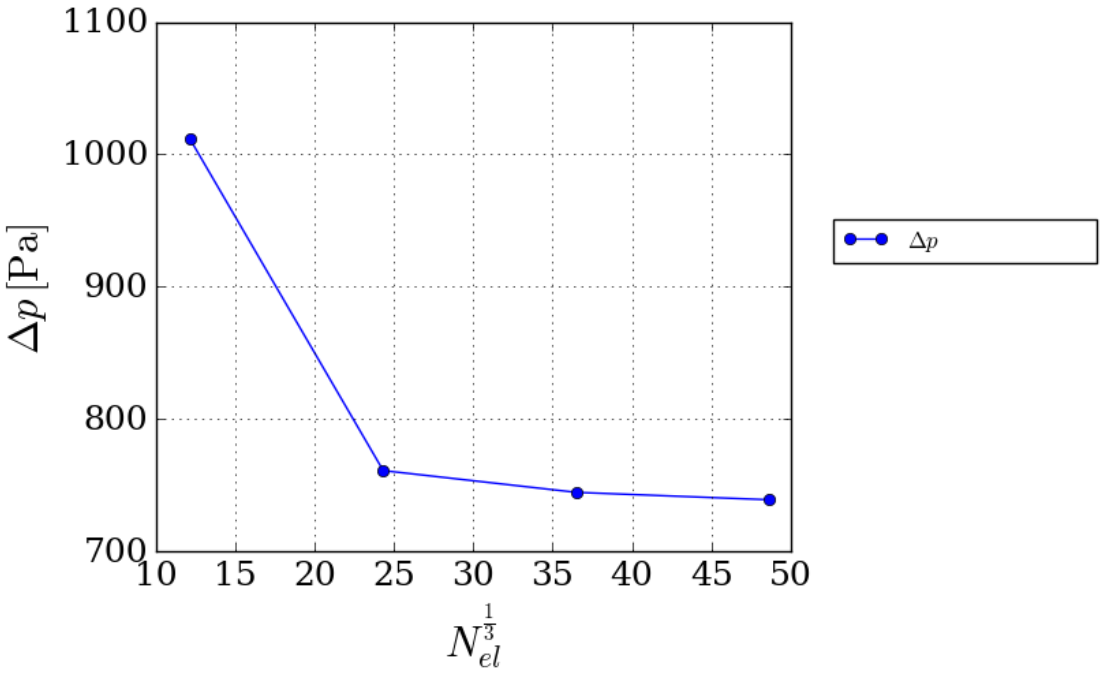

Figure 6.10: Predictions of the pressure drop obtained with the 'porous' model through successive refinements of the fluid mesh.

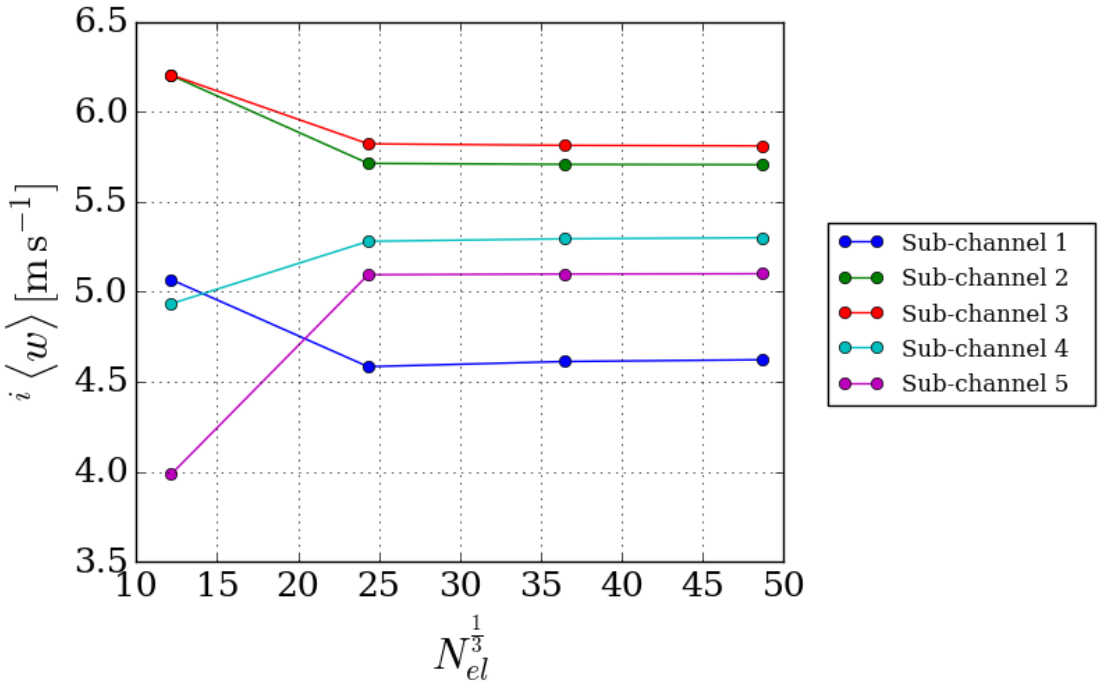

Figure 6.11: Predictions of the average sub-channel velocity at $z = 2.55\,\mathrm{m}$ obtained with the 'porous' model through successive refinements of the fluid mesh.

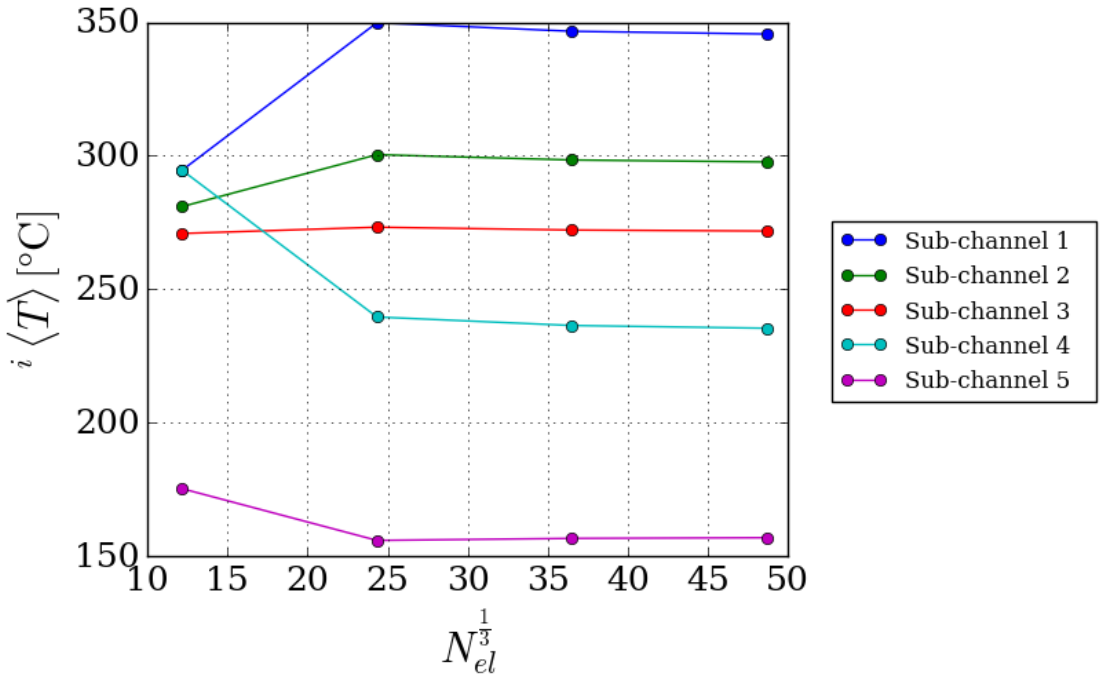

Figure 6.12: Predictions of the average sub-channel fluid temperature at $z = 2.55\,\mathrm{m}$ obtained with the 'porous' model through successive refinements of the fluid mesh.

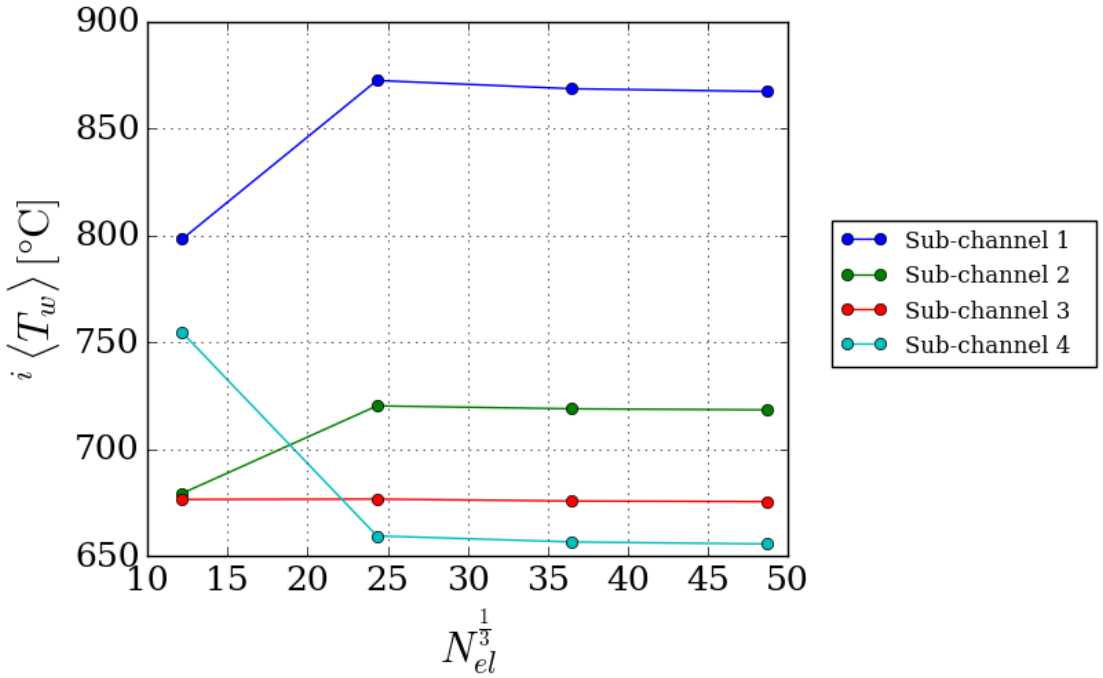

Figure 6.13: Predictions of the average sub-channel solid wall temperature at $z = 2.55\,\mathrm{m}$ obtained with the 'porous' model through successive refinements of the fluid mesh.

6.1.3 Sub-channel quantities

The sub-channel averages were computed using a set of Python scripts based on the *pandas* libraries for data analysis. Numerical integration on the cells of the filtering grid is performed by means of pivot tables calculated by pandas. In the following a comparison is presented between the results produced by POSTR and those output by two 'detailed' calculations, which employed the $k-\varepsilon$ and $R_{ij}-\varepsilon$ SSG turbulence models. The data shown were extracted from the calculation performed on mesh D2 of Table 6.2 for the POSTR run, while for the detailed calculation mesh C1 was chosen to allow the comparison with the RSM model.

Figures 6.15 and 6.16 show the intrinsic averages of the axial velocity and the fluid temperature for the five annular sub-channels at two different axial positions. It can be observed that, for the velocity, the agreement between the 'porous' and 'detailed' model tends to be better in the three 'internal' sub-channels, R2 to R4 of Figure 6.5, while the discrepancy tends to increase close to the boundaries. For the temperature, the largest differences are found in sub-channels R1 and R4.

To quantify the discrepancy, one can define a normalized velocity and temperature difference as:

$$\begin{aligned} \varepsilon_w &= \frac{w_{\mathrm{det}} - w_{\mathrm{por}}}{w_{\mathrm{ref}}} \times 100\,\% \\ \varepsilon_T &= \frac{T_{\mathrm{det}} - T_{\mathrm{por}}}{T_{\mathrm{ref}}} \times 100\,\% \end{aligned} \tag{6.2}$$

were $w_{\mathrm{ref}} = w_{\mathrm{in}}$ is the inlet velocity ($5.5\,\mathrm{m\,s^{-1}}$) and $T_{\mathrm{ref}} = T_{\mathrm{in}} + \frac{z}{H}\Delta T_{\mathrm{ch}}$ is the bulk temperature in the cross section estimated from the global energy balance. In the following, the results from POSTR are compared with those from the $k-\varepsilon$ calculation. The predicion from the RSM simulation are close to the $k-\varepsilon$.

At $z = 0.52H$ the velocity discrepancy ranges between $-3.91\,\%$ in sub-channel R5, next to the sleeve, and $5.48\,\%$ in sub-channel R1, which surrounds the guide tube. The other sub-channels show better agreement, with a maximum discrepancy of $1.04\,\%$ in R3. At $z = 0.85H$ similar results are observed, with a discrepancy of $5.35\,\%$ in R1, $-5.00\,\%$ in R5 and $1.88\,\%$ in R3.

The maximum discrepancies are somewhat bigger in the temperature distributions. At $z = 0.52H$ the temperature discrepancy ranges between $-10.78\,\%$ in R1 and $13.07\,\%$ in R4, while at $z = 0.85H$, in the same sub-channels, the error is respectively $-11.68\,\%$ and $9.56\,\%$. In the other sub-channels the results were closer, with a maximum discrepancy, at the cross sections considered, of $2.07\,\%$

The predictions of the sub-channel averages of the velocity and fluid temperature are therefore in reasonably good agreement, considering the fundamental difference in the

two approaches. However, the same cannot be said when the predictions for the solid domain are compared. Figures 6.17, 6.18 and 6.19 show the maximum solid temperature in each rank of pins, together with the gas temperature, at different axial positions. It can be observed that, when comparing POSTR with the $k-\varepsilon$ model, significant discrepancies are observed, with differences as big as $175\,^{\circ}\mathrm{C}$ in the third rank (the outermost). These differences are mirrored in the distribution of the sub-channel Nusselt number, shown in Figures 6.20 and 6.21. Nonetheless, in relative terms the maximum discrepancy between the temperatures is somewhat limited, less than $23\,\%$ of the solid-fluid temperature difference predicted by the porous model. The axial trends of the solid temperature are also very similar in all the simulations.

One should be careful not to interpret the discrepancy in the results as a proof of the inadequate performance of the 'porous' model. To illustrate this, the results obtained in the RSM calculations are included in the comparison. It can be observed that significant differences exist between the two 'detailed' calculations, with discrepancies up to $61\,^{\circ}\mathrm{C}$. It is probably safer to deduce that this analysis shows how model validation against reliable experimental data cannot easily be replaced with comparisons between different models. In Section 6.3 the performances of POSTR are assessed by a comparison with data from a large scale experiment.

6.1.4 Effect of roughness on the velocity and temperature distribution

In this section the effect of roughness on the results is briefly presented. A comparison between POSTR and a 'detailed' calculation for a bundle of rough pins is problematic: while the correlations used in POSTR were specifically obtained for AGR fuel, in a 'detailed' calculation, if wall functions are used, roughness is assumed to be of the 'sandpaper' type. Therefore, the effects on the flow would not necessarily be comparable. For this reason, only the qualitative effects of roughness will be considered here. The roughness height used was $0.125\,\mathrm{mm}$, which was found to match the pressure drop across the channel predicted by correlations for AGR fuel.[93]

Figure 6.22 shows the profile of the sub-channel averages of the axial velocity and fluid temperature obtained by including the roughness of the pins in the calculation. The most apparent feature is the dramatic change in the velocity distribution, which is now strongly shifted towards the sleeve due to the increased resistance along the bundle.

The effect of roughness on the solid temperature is shown in Figure 6.23 for the innermost rank of pins. Comparison with Figure 6.17 shows a dramatic drop in the solid temperature, due to the enhanced heat exchange. Note that while in the case with smooth pins the 'detailed' model predicted a higher temperature than POSTR, here the opposite

is true, a sign that the heat transfer improvement predicted by the $k - \varepsilon$ model using wall functions is much bigger than that calculated by POSTR, using heat transfer correlations.

6.1.5 Concluding remarks

In this section a usage test for the simulation of a forced convection scenario using POSTR was presented. 'Detailed' RANS simulations have been carried out for comparison. Mesh independent results were achieved with both models and moderate differences were observed in the predictions of the velocity and temperature fields, although fundamental agreement was observed for what concerns the trends and the discrepancy in the predictions never exceeded $23\,\%$ of the temperature difference between the pins and the gas. It is noted that the discrepancies observed are not necessarily due to the shortcomings of the porous model, which highlights the necessity of reliable experimental data for the validation and tuning of POSTR.

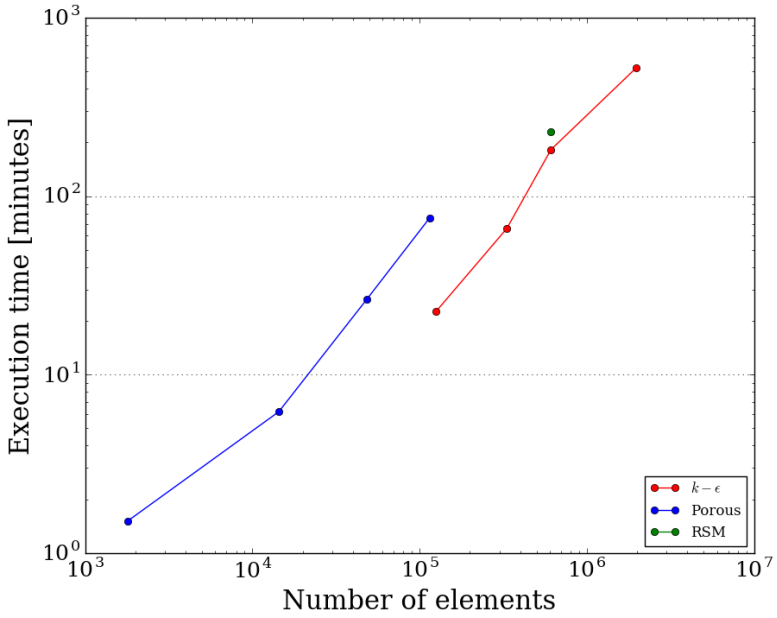

Figure 6.14: Execution time for the ‘detailed’ and ‘porous’ models for different mesh sizes.

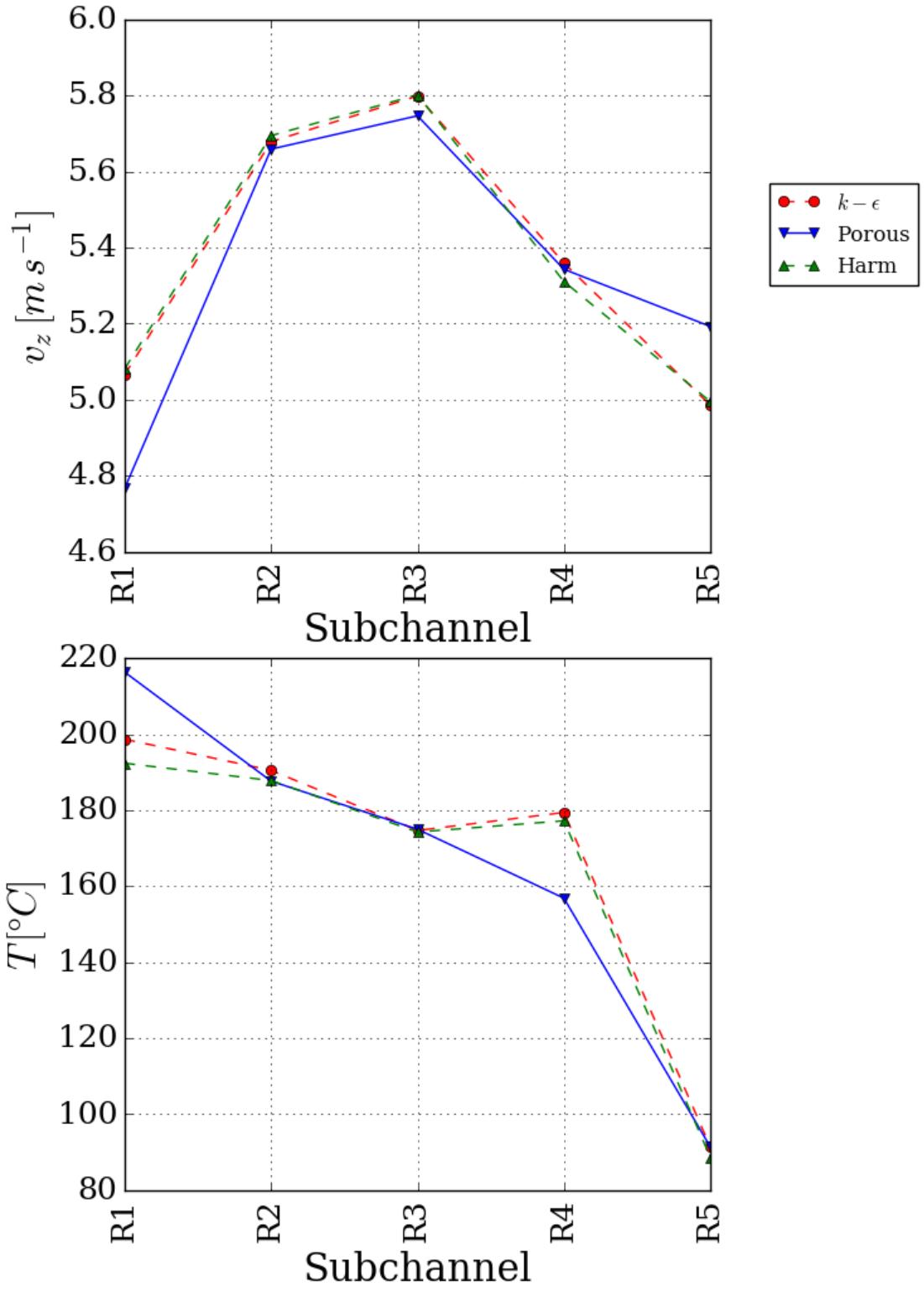

Figure 6.15: Comparison between predictions of sub-channel averages obtained with POSTR with two 'detailed' calculations at $z = 0.52H$.

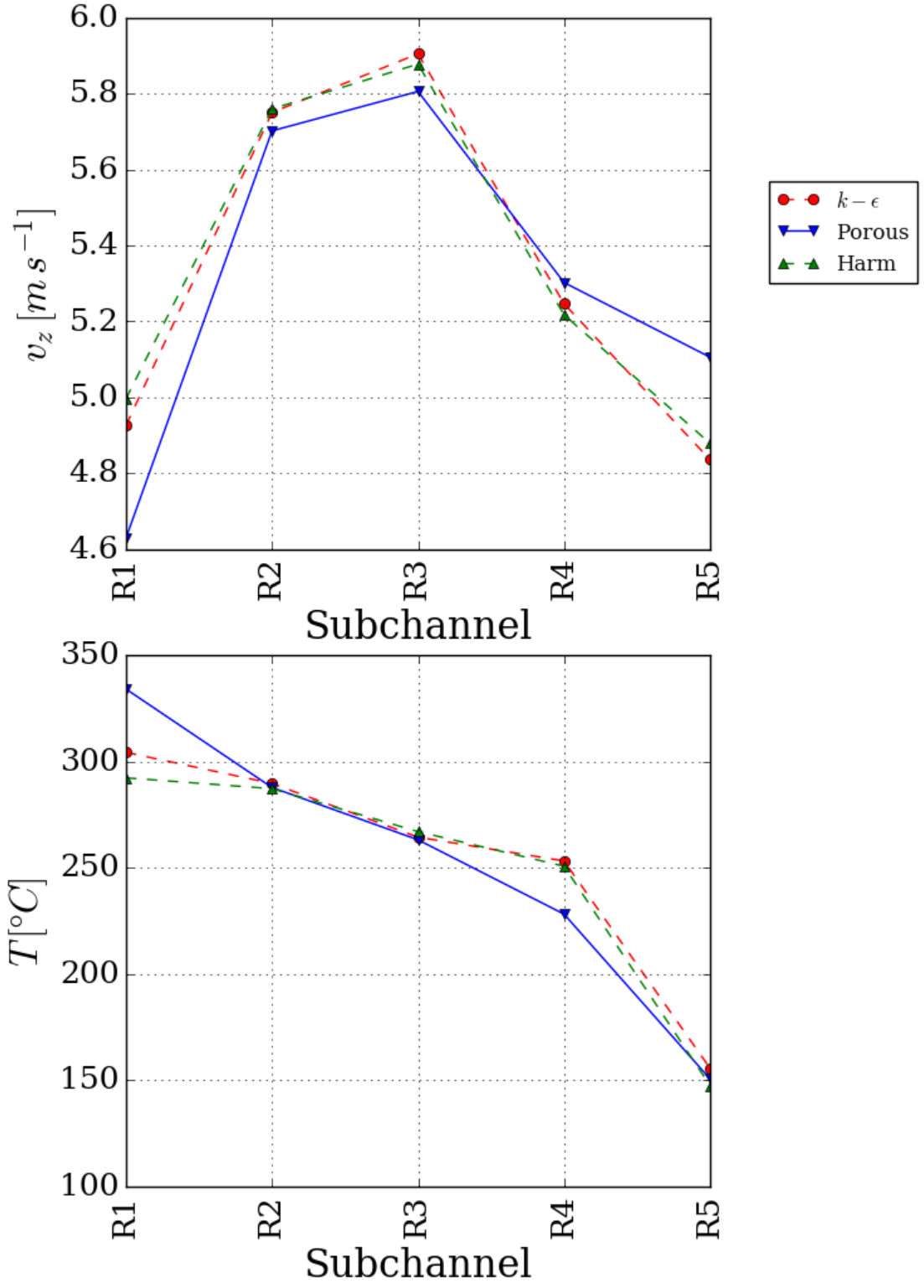

Figure 6.16: Comparison between predictions of sub-channel averages obtained with POSTR with two 'detailed' calculations at $z = 0.85H$.

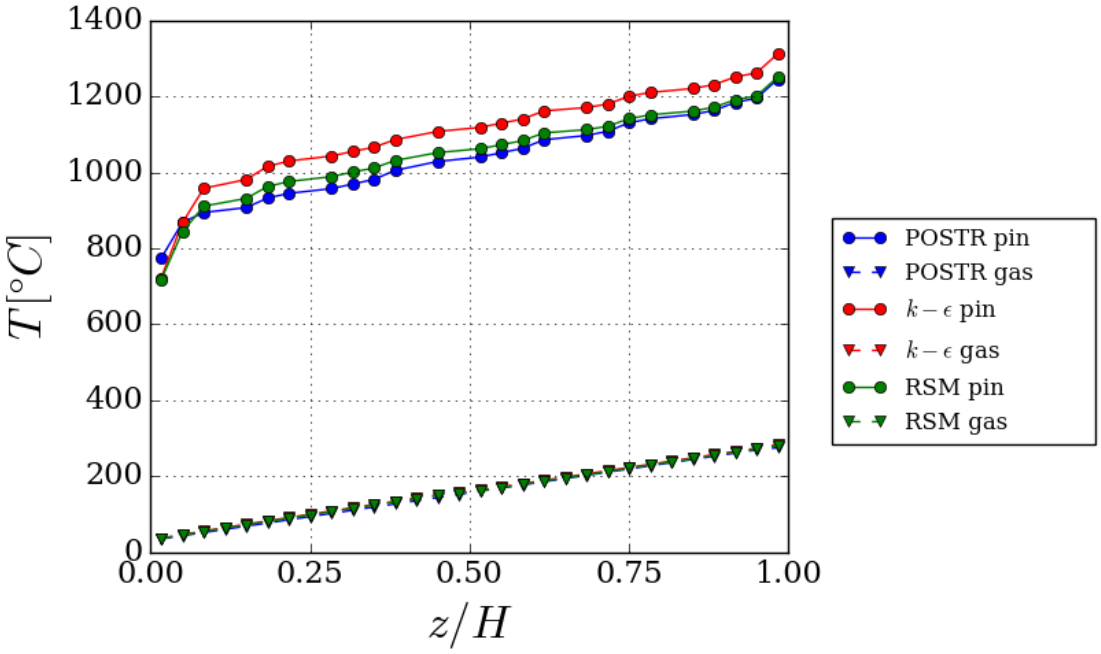

Figure 6.17: Average gas temperature and maximum cladding temperature in the first rank of pins at different axial positions, as predicted by POSTR and two 'detailed' calculations.

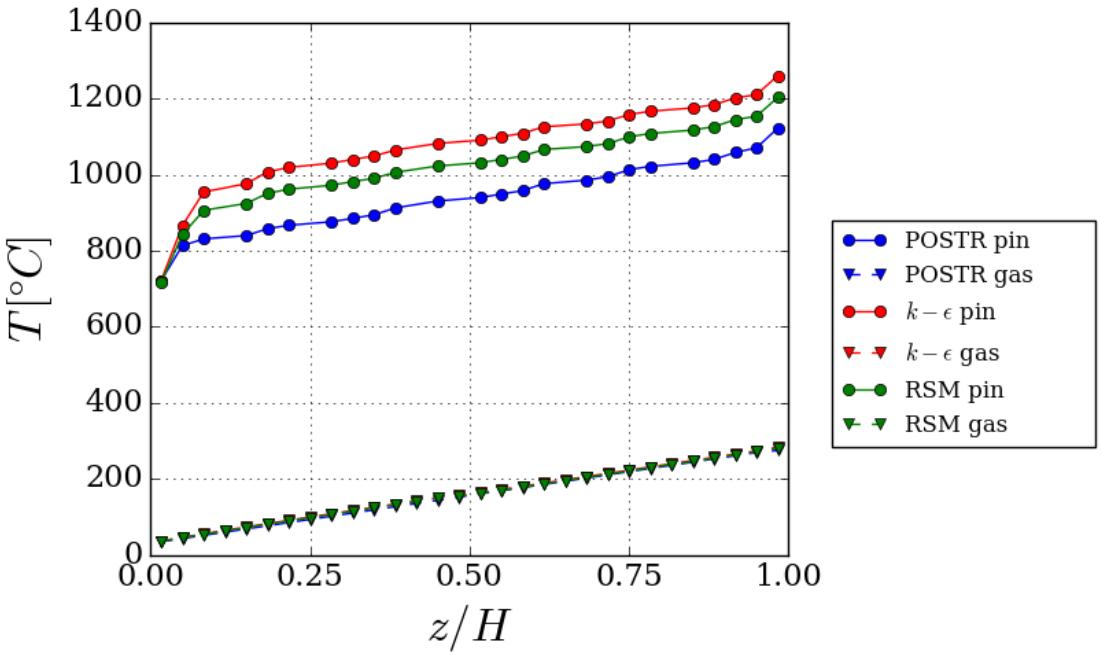

Figure 6.18: Average gas temperature and maximum cladding temperature in the second rank of pins at different axial positions, as predicted by POSTR and two 'detailed' calculations.

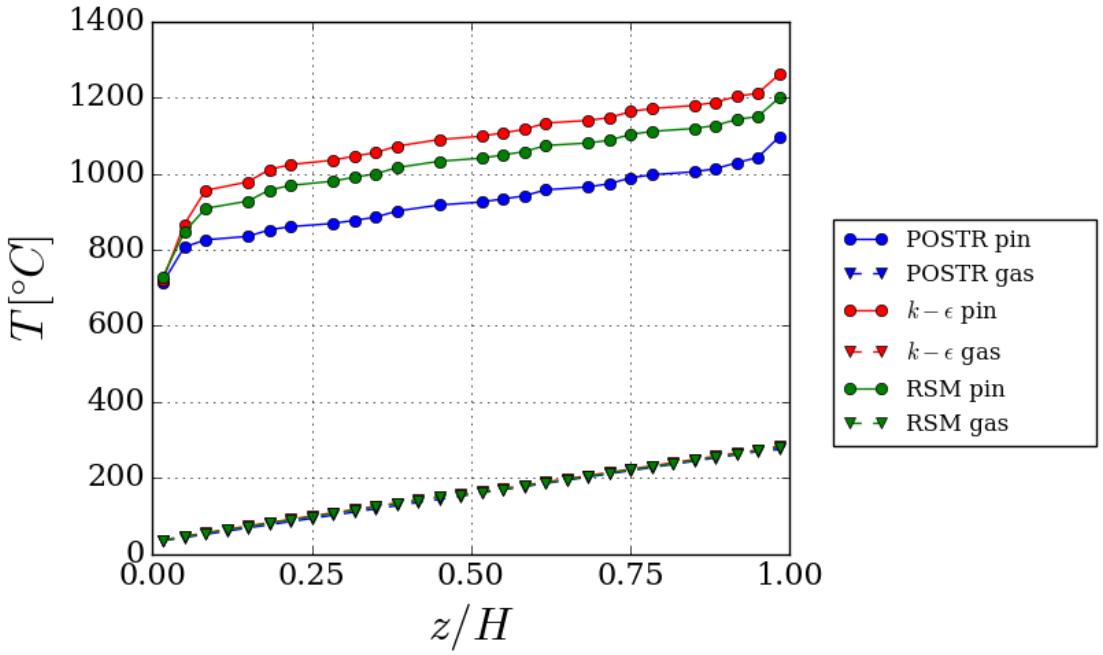

Figure 6.19: Average gas temperature and maximum cladding temperature in the third rank of pins at different axial positions, as predicted by POSTR and two 'detailed' calculations.

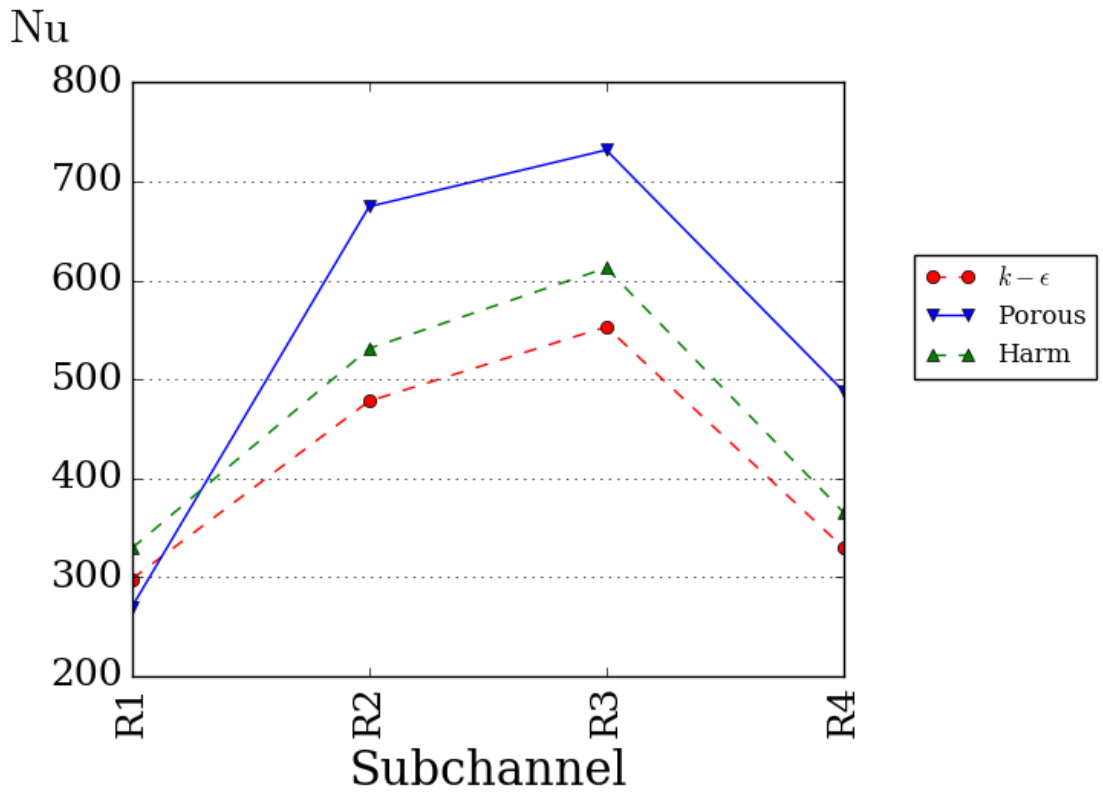

Figure 6.20: Comparison between predictions of sub-channel Nusselt number obtained with POSTR with two 'detailed' calculations at $z = 0.52H$.

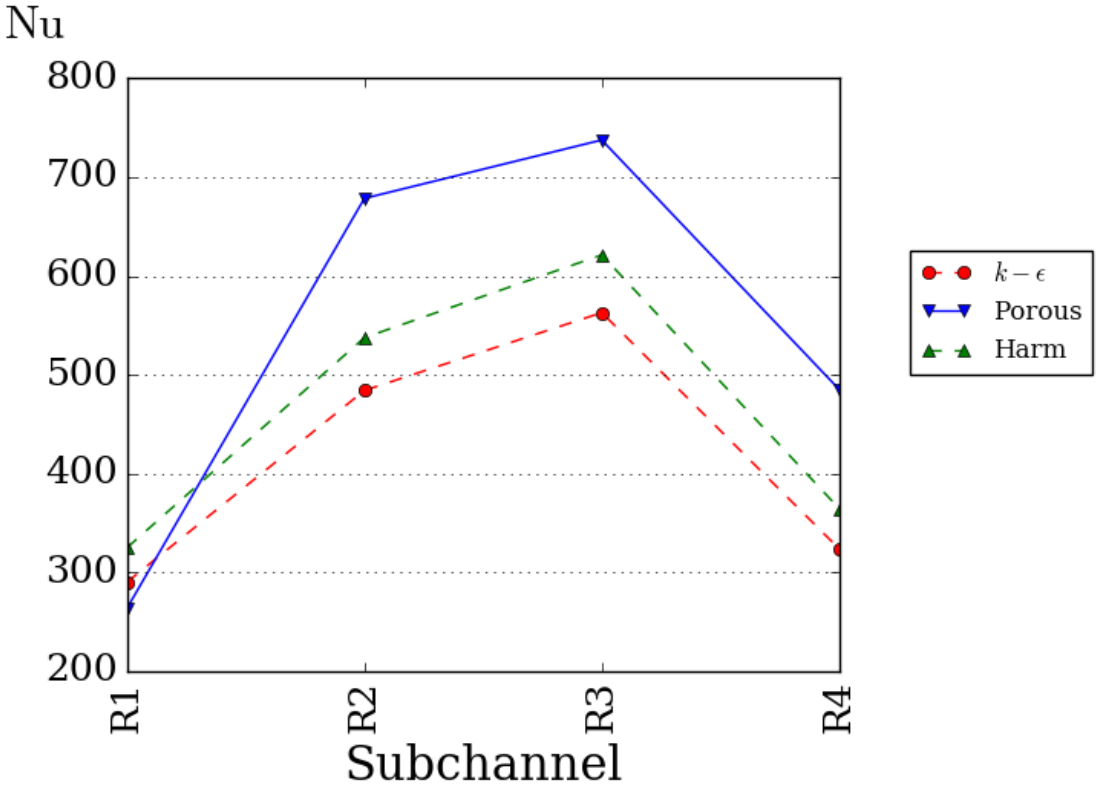

Figure 6.21: Comparison between predictions of sub-channel Nusselt number obtained with POSTR with two 'detailed' calculations at $z = 0.85H$.

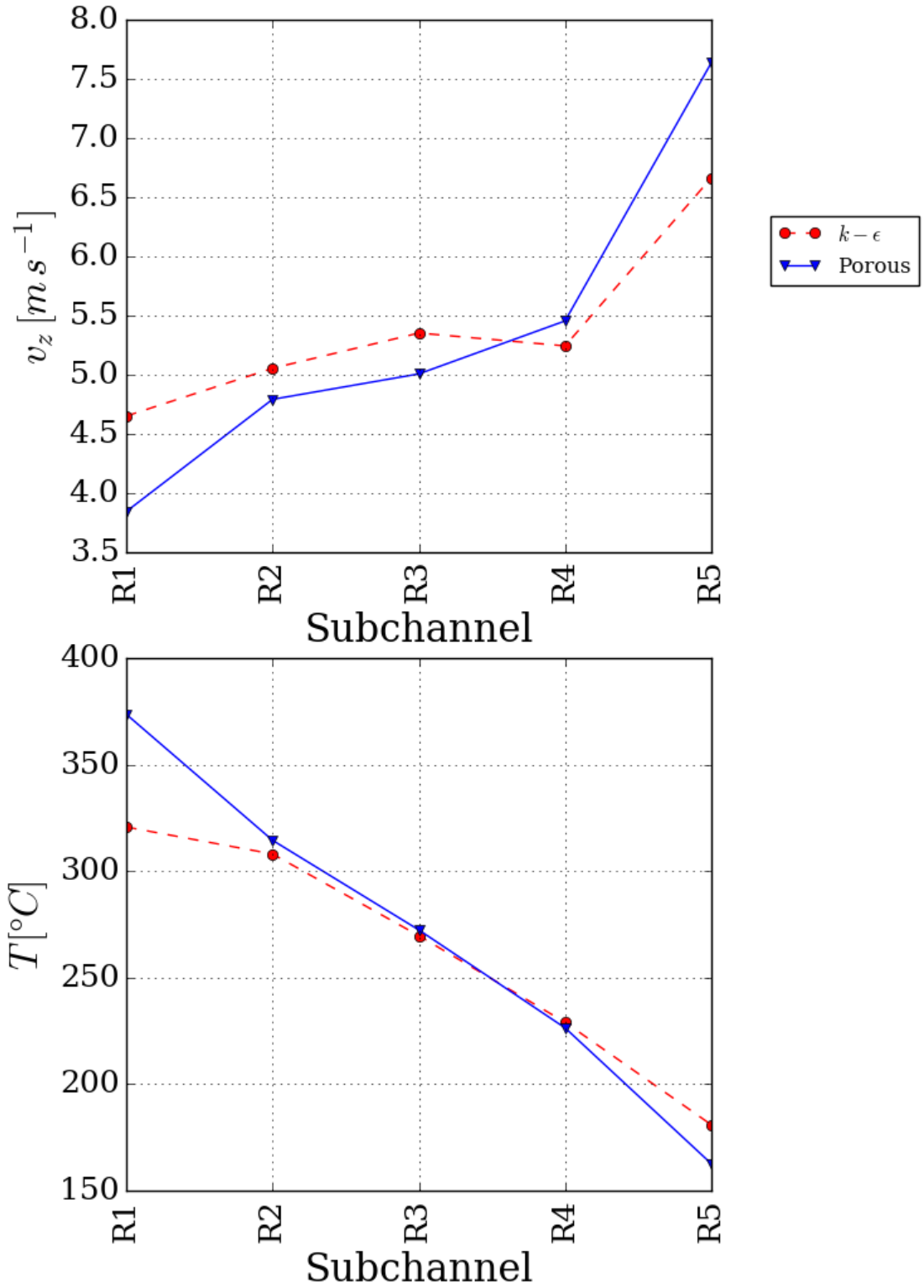

Figure 6.22: Effect of roughness on the sub-channel averages predicted with POSTR and a $k-\varepsilon$ calculation. Cross section at $z = 0.85H$.

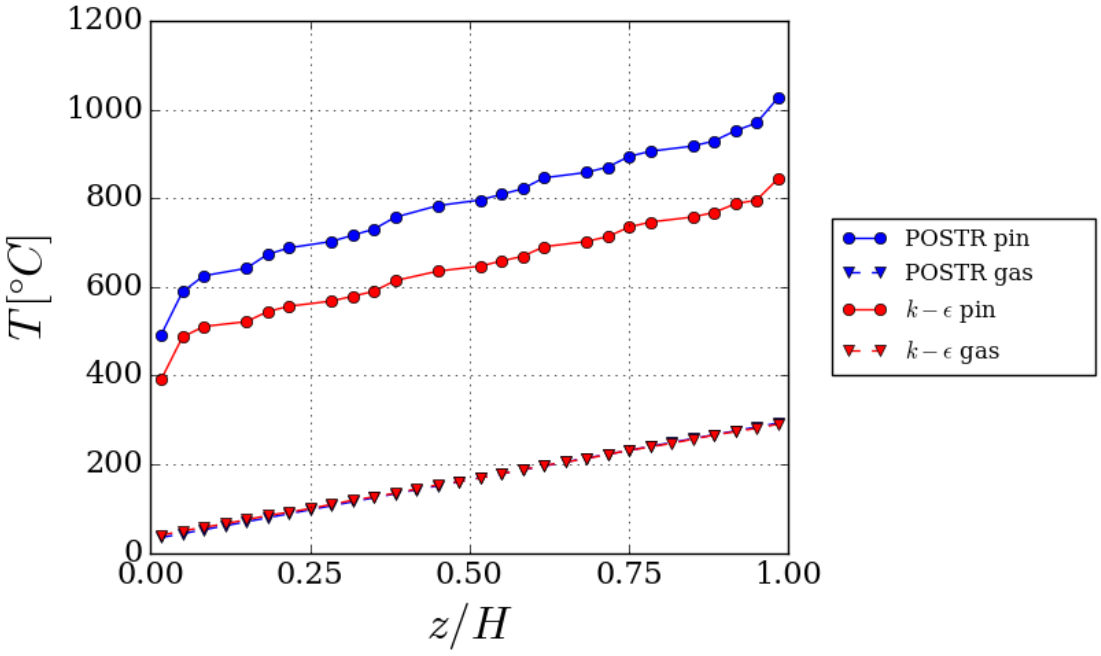

Figure 6.23: Effect of roughness on the maximum temperatures in the first rank of pins.

6.2 Natural convection in an enclosed AGR stringer - Case NATURAL-FS

6.2.1 Description of the scenario and model overview

This section presents the simulation of natural convection in a full-sized model for the stringer, in which the top and bottom are sealed (Figure 6.24). The net flow through the stringer is therefore zero and the decay heat generated in the fuel can only be removed through the graphite sleeve. The case is labelled NATURAL-FS, as it simulates natural convection in a full stringer.

Albeit abstract, the scenario can be considered a conservative model for a credible incident that may occur during the extraction of the stringer from the reactor, in which the hoist stops while the stringer bottom nose have entered the standpipe above the reactor channel. In such a situation, two opposing mechanisms co-exist and determine the flow through the stringer:

- An upward contribution is provided by the buoyancy forces acting on the gas.
- A downward driving force is provided by the Fuelling Machine Cooling System (FMCS), which in this phase of the extraction is normally predominant.

If a stop occurs in this phase, the contribution from the buoyancy forces can build up as the gas temperature increases. This can cause the net flow to stagnate, which may lead to increased fuel and tie bar temperatures.

One-dimensional analysis of the scenario assumes that, in this scenario, the fuel is cooled by thermal radiation alone. In reality, internal recirculation driven by buoyancy can significantly reduce the maximum temperature reached. A three-dimensional model can thus help evaluating the degree of conservativity of one-dimensional solutions. In this study, the predictions of POSTR are compared with the result obtained in a 1994 investigation carried out with COOLFUEL-1D and -3D for the simplified scenario outlined above.[94] In Section 6.3 another potential deviation will be investigated employing a more complex model and compared with experimental data.

The computational domain comprises of an $8\,\mathrm{m}$ long annular enclosure, containing a bundle of 36 clad pins and surrounded by a sleeve. The domain was divided in 8 blocks, representing approximately the 8 fuel elements which form the stringer. The top and bottom of the fluid domain, as well as the inner cylindrical surface representing the guide-tube wall, were adiabatic no-shear walls. At the outer wall surface coupling was defined between the fluid domain and the SYRTHES model for the sleeve. The nominal power generated by the stringer was $40\,\mathrm{kW}$, distributed as follows, using the same setup as reported in Reference [94]:

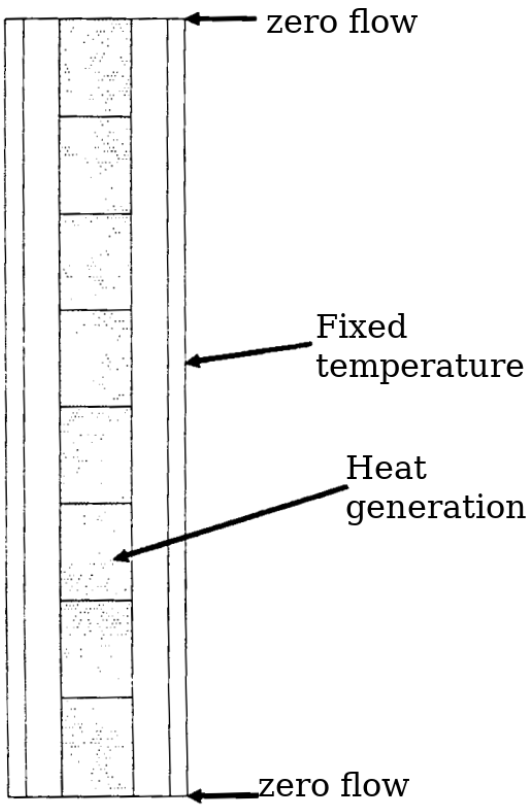

Figure 6.24: Schematics of the geometry simulated in case NATURAL-FS.

Fluid Mesh	Number of Elements	Solid Mesh	Number of Elements
A	2400	1	142000
B	19200	2	814682
C	64800	3	1628454
D	153600		

Table 6.4: Number of elements in the meshes used in case NATURAL-FS.

- $13.624\,\%$ in the first rank of pins.
- $28.213\,\%$ in the second rank of pins.
- $45.597\,\%$ in the third rank of pins.
- $2.000\,\%$ in the sleeve.
- $10.566\,\%$ neglected.

Although, the nature of the power neglected is not reported in Reference [94], a reasonable interpretation could be that it corresponds to the power deposited by ionizing radiation into the structural elements surrounding the stringer. A non uniform power distribution among the pins was also used. Constant temperatures where imposed on the outer wall of the stringer, again with a non uniform distribution among the elements.

The thermal conductivity of the solid material was taken from reference [94], whereas, since only the steady state solution was of interest, reduced density and specific heat were used to accelerate the transient. The physical properties of the fluid were obtained from tables for carbon dioxide at the pressure of $34\,\mathrm{bar}$, with the dependence from the temperature modelled with linear fits except for the density, for which Charles' law is used.

The time step for the calculation in Code_Saturne was $0.1\,\mathrm{s}$ while on SYRTHES it was set to $1\,\mathrm{s}$, also to speed up the transient. Most calculations were run for 5000 time steps. The Upwind scheme was used to improve the stability of the calculation, which was affected by intense oscillations of the solved variables. Similarly to the scenario discussed in Section 6.3, the effect of these oscillations on the solid temperature was minor.

6.2.2 Influence of the computational meshes

The influence of the computational meshes for the fluid and solid domains was studied in a series of calculation runs. The sizes of the meshes used are reported in Table 6.4. The filtering mesh was kept fixed, with 40 axial, 12 azimuthal and 5 radial divisions.

Figures 6.25, 6.26 and 6.27 show how the average gas temperature at mid-height, the average sub-channel velocities and the average clad temperature at mid-height in each

Variable	Fluid M.I. [%]	Solid M.I. [%]
T_f	-2.08	-6.93
W_1	9.98	21.10
W_2	18.64	31.85
W_3	54.79	73.89
W_4	25.85	57.65
W_5	22.80	55.02
T_{w1}	-1.31	1.22
T_{w2}	-1.13	0.76
T_{w3}	-1.16	0.45

Table 6.5: Relative variation $\frac{Y_{\mathrm{finest}}-Y_{\mathrm{chosen}}}{Y_{\mathrm{finest}}}$ in the values of a number of integral quantities at mid-height between the mesh chosen for the analysis and the finest tested. The subscripts finest and chosen refer respectively to the fluid meshes D and B, and to the solid meshes 3 and 1 in Table 6.4.

rank of pins change as the fluid mesh is refined. It is apparent that no converging trend has emerged from the tests, with relatively large variations between one mesh to the other. Similar considerations can be drawn for what concerns the dependence from the solid mesh, as shown in Figures 6.28, 6.29 and 6.30. The calculations performed for the fluid mesh dependence study used Mesh 1 for the solid domain, whilst those for the solid mesh dependence study employed Mesh B for the fluid domain. In the following section the calculation performed on these two meshes is used in the analysis of the results and referred to as 'reference calculation'. However, the relatively strong dependence on the mesh employed should be borne in mind when discussing the results. The relative differences between the predictions made on these meshes and those made on their finest counterparts are shown in Table 6.5.

Figures 6.31 and 6.32 show the predictions of maximum temperature at the surface of the cladding at different axial positions obtained by varying respectively the fluid and the solid mesh. Similar trends are output by all calculations, with the temperature increasing significantly in the bottom half of the enclosure and remaining roughly uniform in the top half. Noticeable deviations from the trend are predicted by the calculation using Mesh C in the fluid mesh dependence study and, less significantly, by that using Mesh 2 in the solid mesh dependence study: in these two simulations the temperature reaches a maximum above mid-height, then decreases to reach a local minimum close to the top. One can observe that the calculated temperatures tend to be closer in the bottom half of the stringer and tend to increase with increasing height. This trend is quantitatively shown in Figure 6.33: the discrepancies plotted are obtained by considering the maximum surface clad temperature at each height, regardless of the pins rank, and calculating the difference between the maximum and minimum prediction among all the simulations. The spread

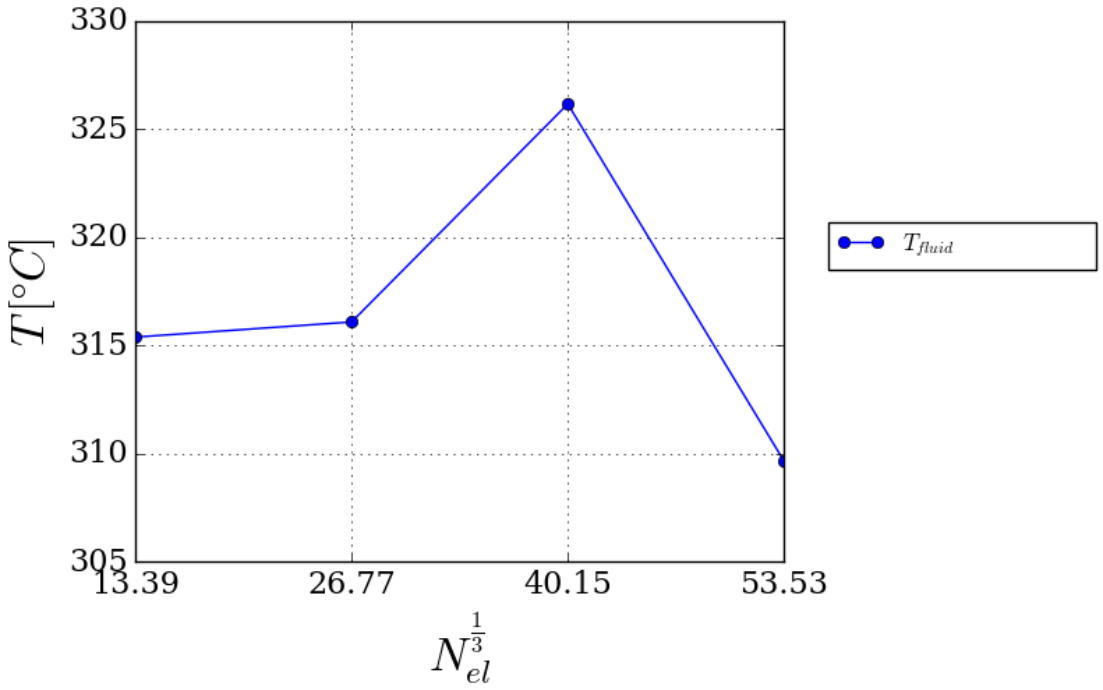

Figure 6.25: Predictions of the average temperature in a cross-section at $z = 0.5H$ for case NATURAL-FS, obtained through successive refinements of the fluid mesh.

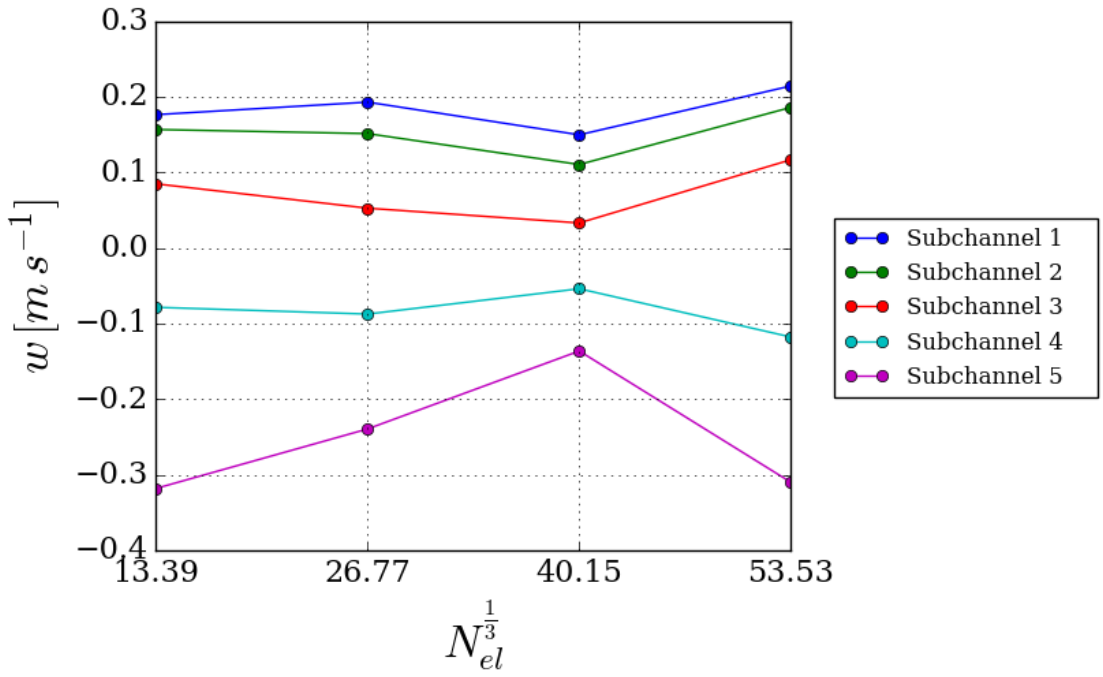

Figure 6.26: Predictions of the sub-channel velocities in a cross-section at $z = 0.5H$ for the case described in Section 6.2, obtained through successive refinements of the fluid mesh.

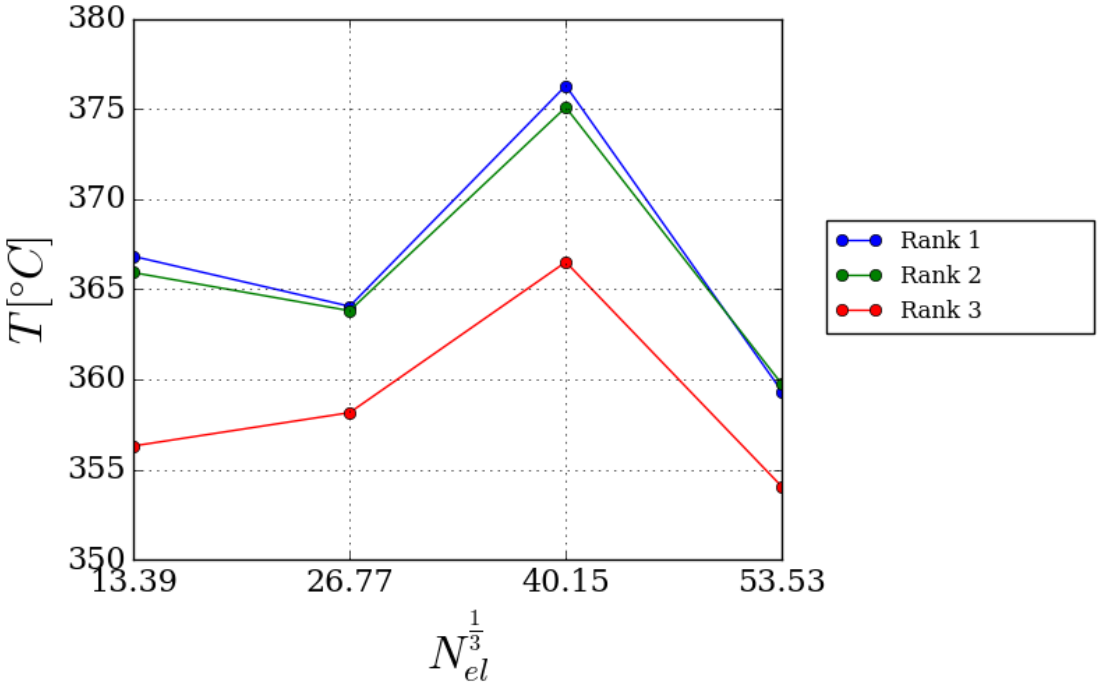

Figure 6.27: Predictions of the average solid temperature between $z = (0.5 \pm 0.05)H$ for case NATURAL-FS, obtained through successive refinements of the fluid mesh.

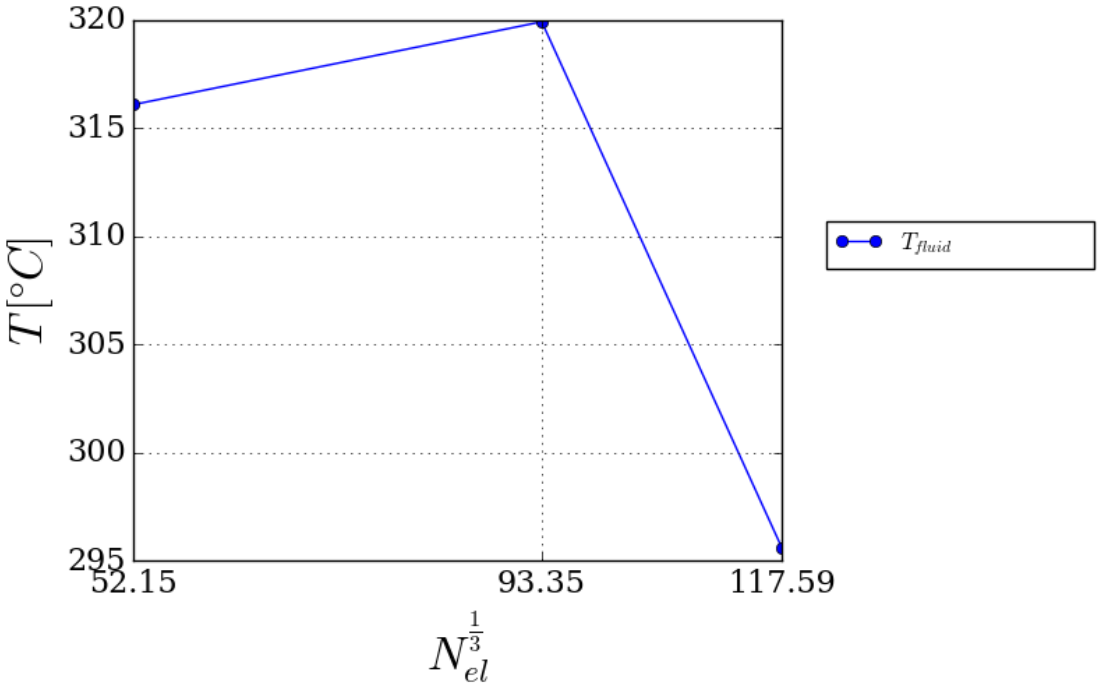

Figure 6.28: Predictions of the average temperature in a cross-section at $z = 0.5H$ for case NATURAL-FS, obtained through successive refinements of the solid mesh.

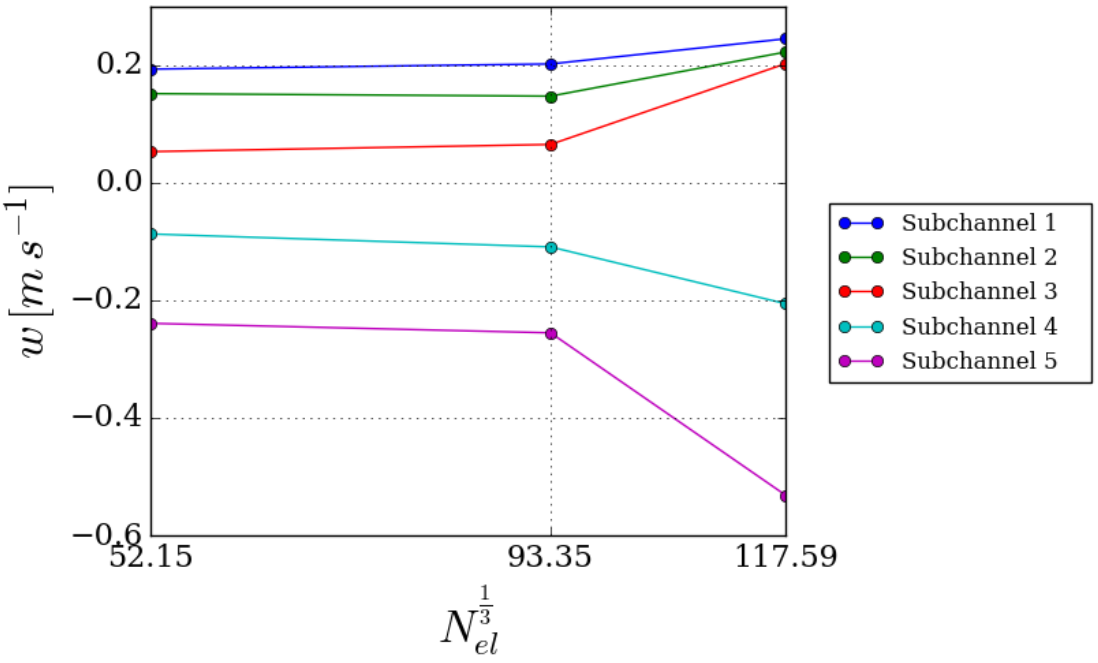

Figure 6.29: Predictions of the sub-channel velocities in a cross-section at $z = 0.5H$ for case NATURAL-FS, obtained through successive refinements of the solid mesh.

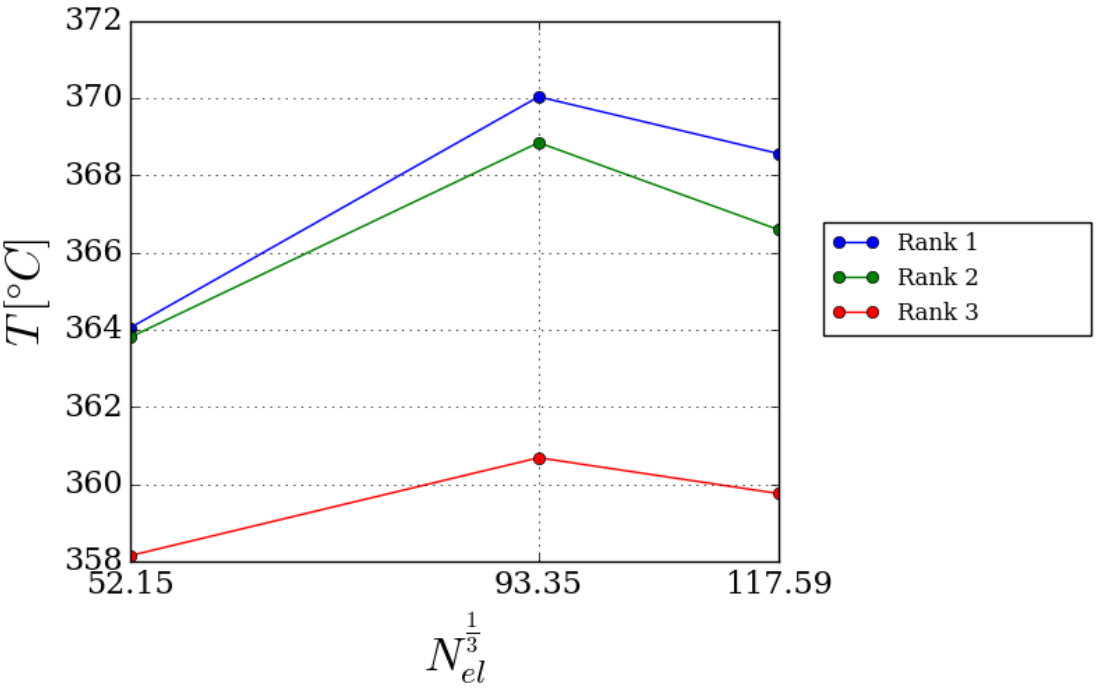

Figure 6.30: Predictions of the average solid temperature between $z = (0.5 \pm 0.05)H$ for case NATURAL-FS, obtained through successive refinements of the solid mesh.

between the prediction reaches a maximum of $32.44\,^{\circ}\mathrm{C}$ at $z = 0.84H$, which is $17.32\,\%$ of the temperature increase in the reference calculation.

6.2.3 Discussion of results

In the following, the results for the reference calculation are presented. The profiles of axial velocity and temperature at different heights will be shown, and the predictions for the temperature of the claddings will be compared to the results obtained by Hornby and Fung[94] using COOLFUEL-1D and COOLFUEL-3D.

Figures 6.34, 6.35 and 6.36 show the profiles of temperature and axial velocities output by the calculation at three different cross sections, located respectively at a height of $0.25H$, $0.50H$ and $0.75H$ of the total height of the domain. Due to the oscillations in the calculation, the calculated quantities were averaged in time before applying the spatial filter.

The presence of internal recirculation is evident from the axial velocity plot, which shows a separation between the innermost sub-channels, where the net flow is directed upward, and those closest to the sleeve, where the cooling effect of the boundary conditions drives the flow downwards due to the increased density. For what concerns the temperature distribution, one can observe that while the radial temperature variation at $0.25H$ and $0.50H$ of the total height is less than $15\,^{\circ}\mathrm{C}$, in the plane at $0.75H$ there is a difference of $49.30\,^{\circ}\mathrm{C}$ between the innermost and the outermost sub-channel. This can be put in relation with the more intense circulation pointed out by the velocity profiles, which show higher ascending and descending velocities, which in turn would result in more intense heat transfer and temperatures closer to the adjoining solid surfaces.

Figure 6.37 shows a comparison between the maximum cladding temperatures at different heights obtained with POSTR and those obtained with COOLFUEL-1D and COOLFUEL-3D, as reported by Hornby and Fung[94]. Each point in the plot represents the maximum temperature occurring at a given cross-section, regardless of the rank of pins in which it occurs. The line plotted for the POSTR results represents the output of the reference calculation. However, given the broad variations in the predictions obtained with different meshes, the whole span of the computed values is shown in the plot as a shaded area. The breadth of the area at each axial position is reported in Figure 6.33. It appears that the predictions obtained with POSTR, at least for what concerns the reference calculation, are closer to those obtained with COOLFUEL-1D than those by COOLFUEL-3D, despite the model used being similar to the latter. In general, POSTR predicts lower temperatures than COOLFUEL-3D and, as a trend, higher temperatures than COOLFUEL-1D.

As mentioned above, the purpose of a three-dimensional model as that implemented in POSTR and COOLFUEL-3D is to overcome the limitations of one-dimensional solvers,

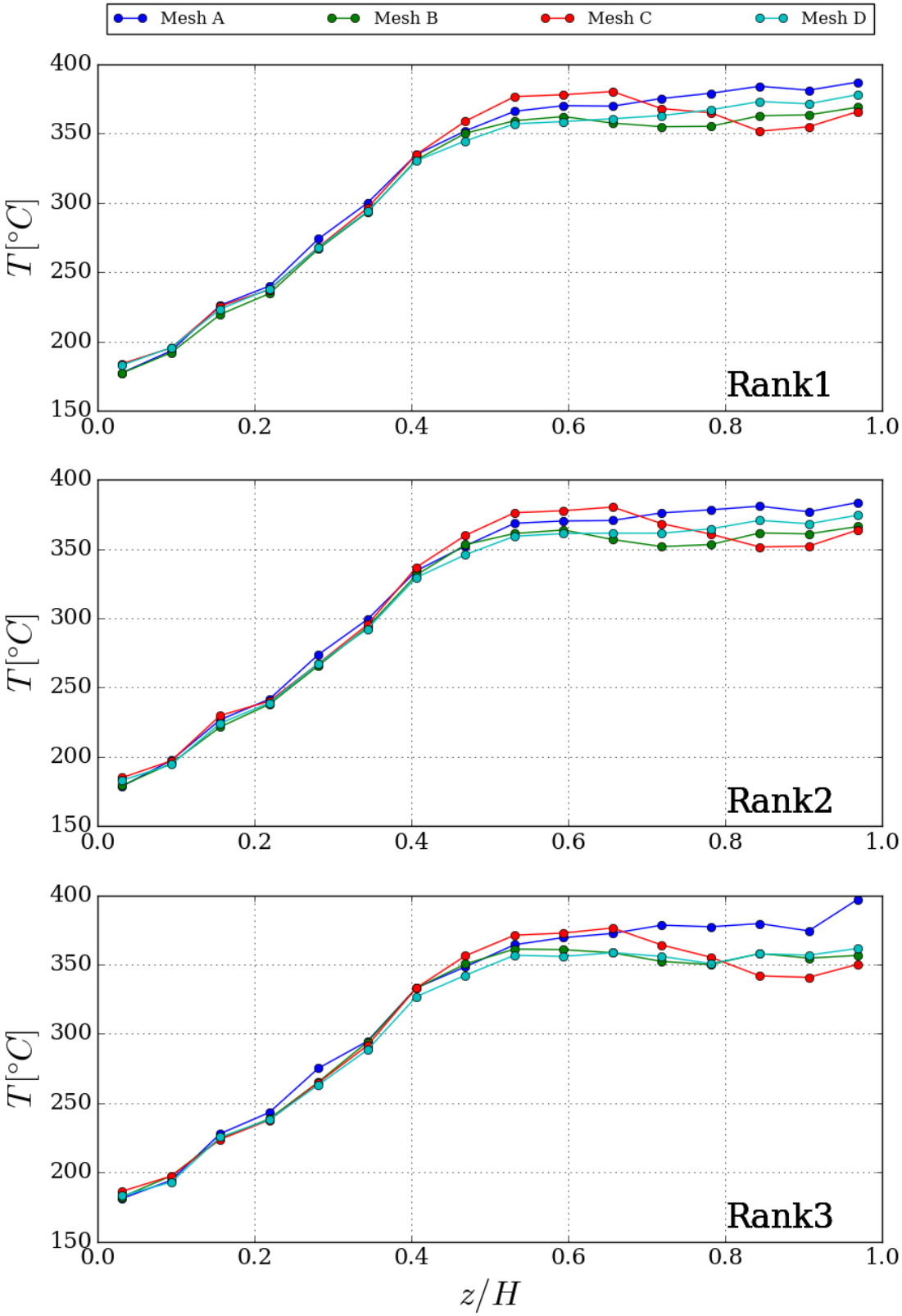

Figure 6.31: Predictions of the maximum surface cladding temperature for each rank of pins at different heights for case NATURAL-FS, obtained by varying the fluid mesh employed.

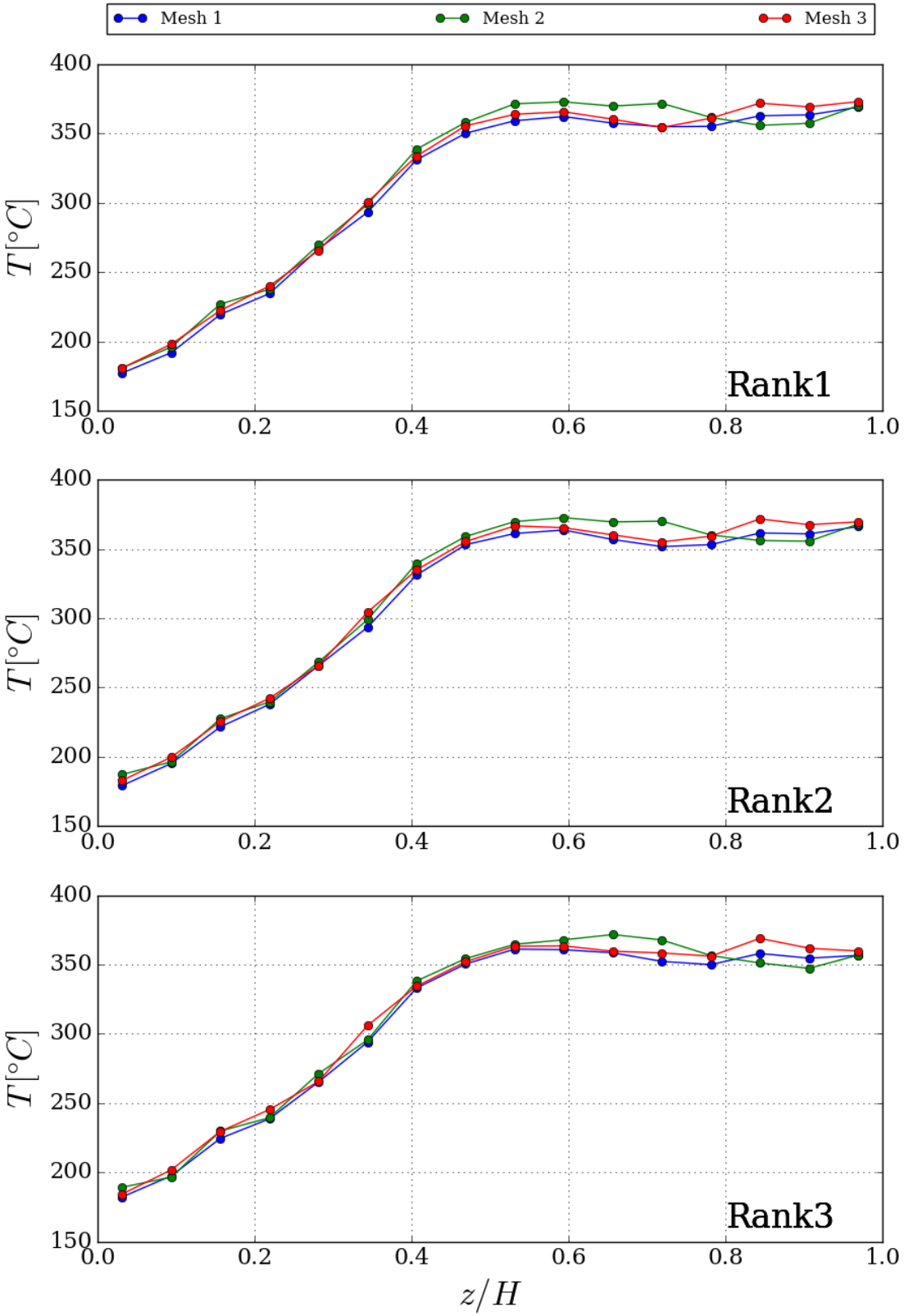

Figure 6.32: Predictions of the maximum surface cladding temperature for each rank of pins at different heights for case NATURAL-FS, obtained by varying the solid mesh employed.

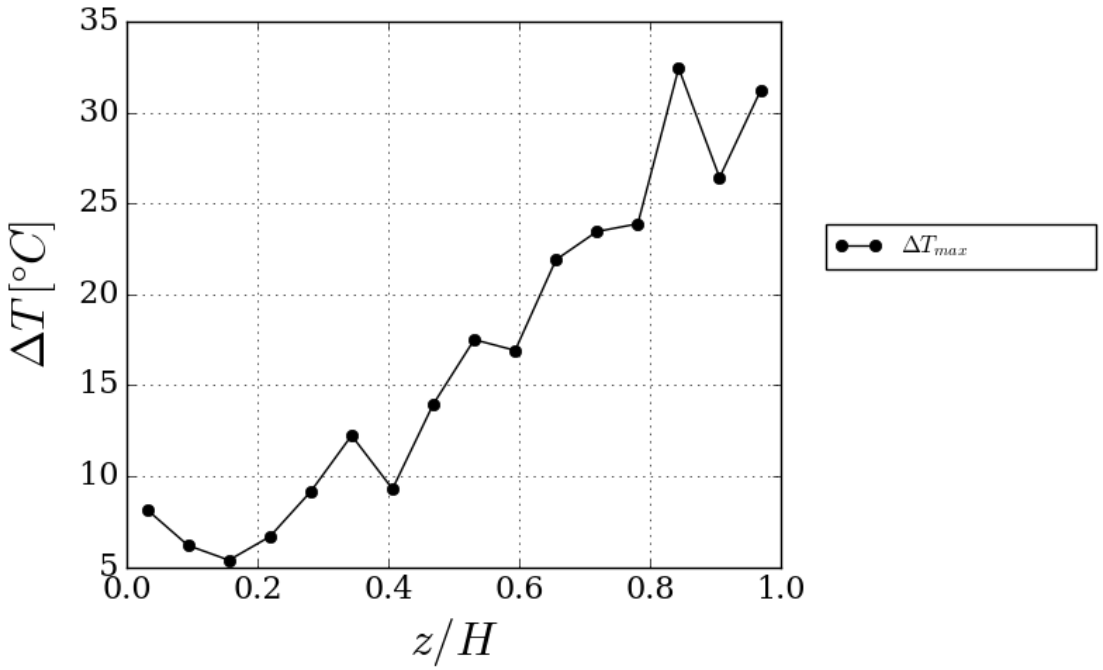

Figure 6.33: Spread in the predictions of the maximum surface cladding temperature at different heights among all the calculations performed for case NATURAL-FS.

which in scenarios such as the one presented in this section cannot take into account internal recirculation and would over-predict the temperatures reached. This situation can be simulated by suppressing the buoyancy forces in the calculation, e.g. by defining a constant density for the fluid. The maximum surface cladding temperatures at different axial positions calculated under these conditions by POSTR and COOLFUEL-3D are shown in Figure 6.38. The results of the two codes are in good agreement, and show an increase in the predicted temperatures compared to those shown in Figure 6.37. The maximum temperature predicted by COOLFUEL-3D increases from $407.50\,°\mathrm{C}$ to $548.97\,°\mathrm{C}$, while that calculated by POSTR increases from $369.01\,°\mathrm{C}$ to $545.19\,°\mathrm{C}$.

6.2.4 Concluding remarks

In this section the predictions of POSTR were compared with results obtained using COOLFUEL-3D and COOLFUEL-1D, codes deemed reliable enough to be used in refuelling cooling analysis in industrial practice. Some oscillations in the fluid temperature and velocity were observed, which are judged to be related to the physical characteristics of the flow. In addition, the model predictions show some sensitivity to the mesh density. Nevertheless, the fuel pin temperature was in good agreement with the predictions of COOLFUEL-3D and COOLFUEL-1D.

Although the observed similarities in the predictions of POSTR with those given by the

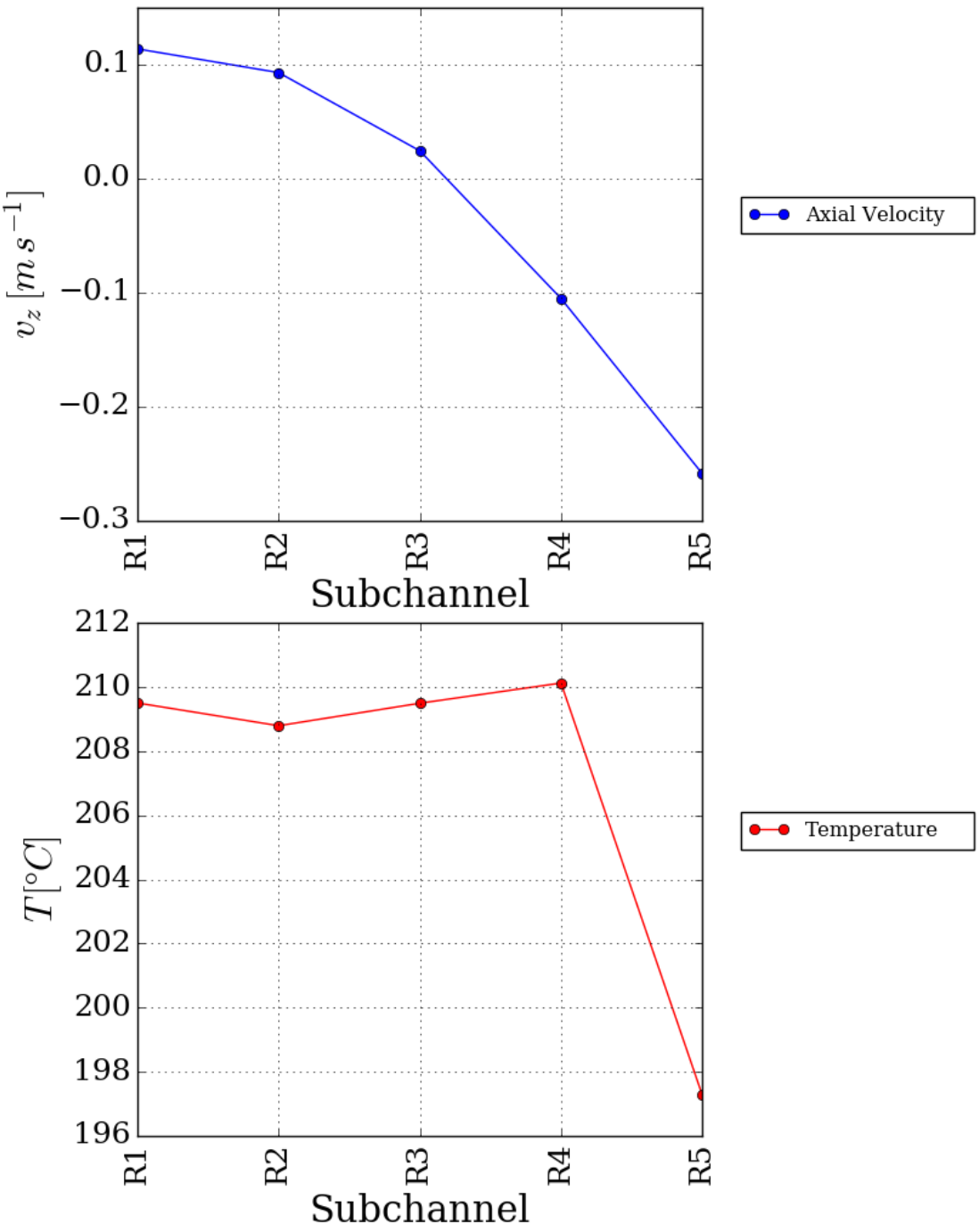

Figure 6.34: Predictions of sub-channel averages obtained with POSTR in the enclosed stringer at $z = 0.25H$.

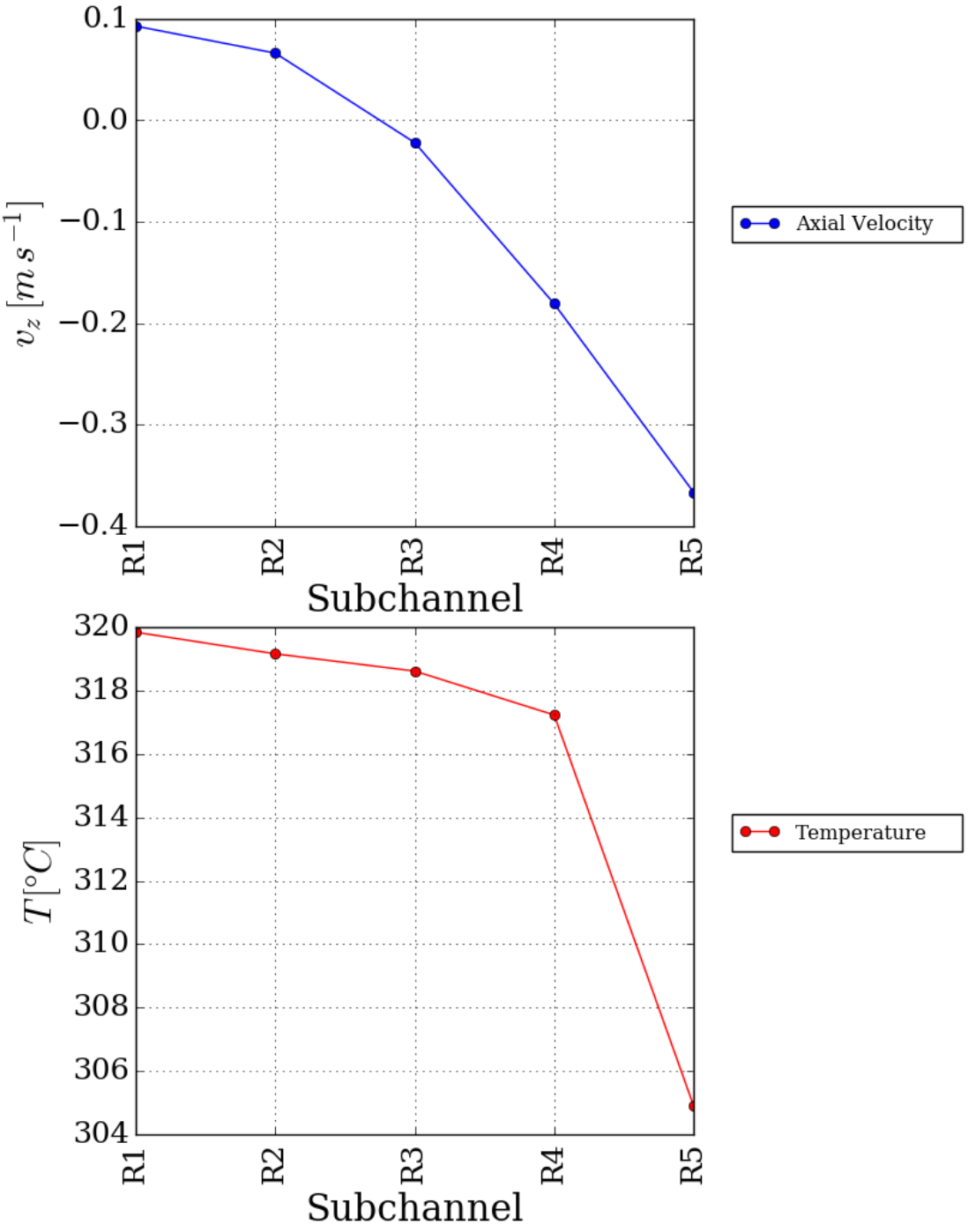

Figure 6.35: Predictions of sub-channel averages obtained with POSTR in the enclosed stringer at $z = 0.50H$.

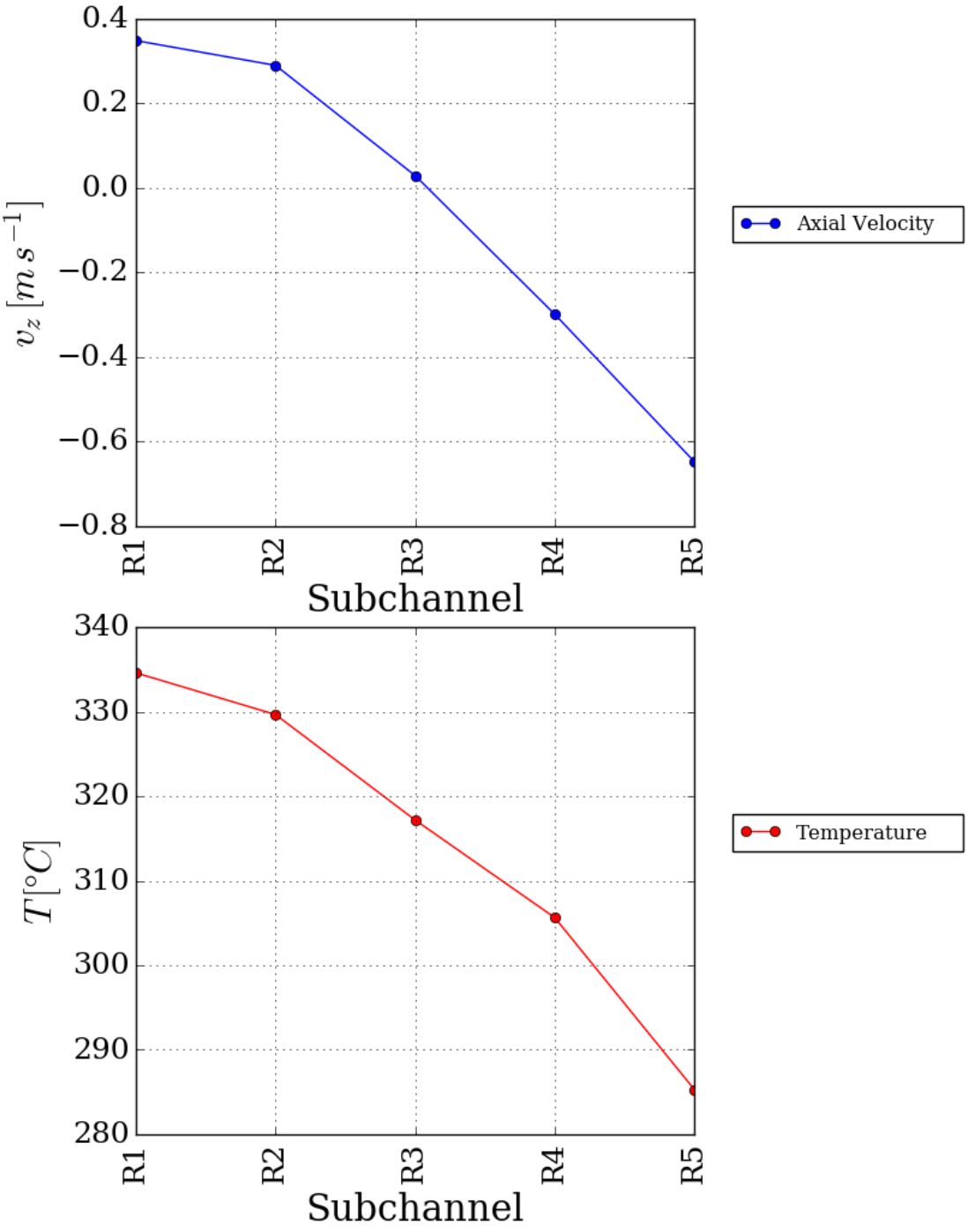

Figure 6.36: Predictions of sub-channel averages obtained with POSTR in the enclosed stringer at $z = 0.75H$.

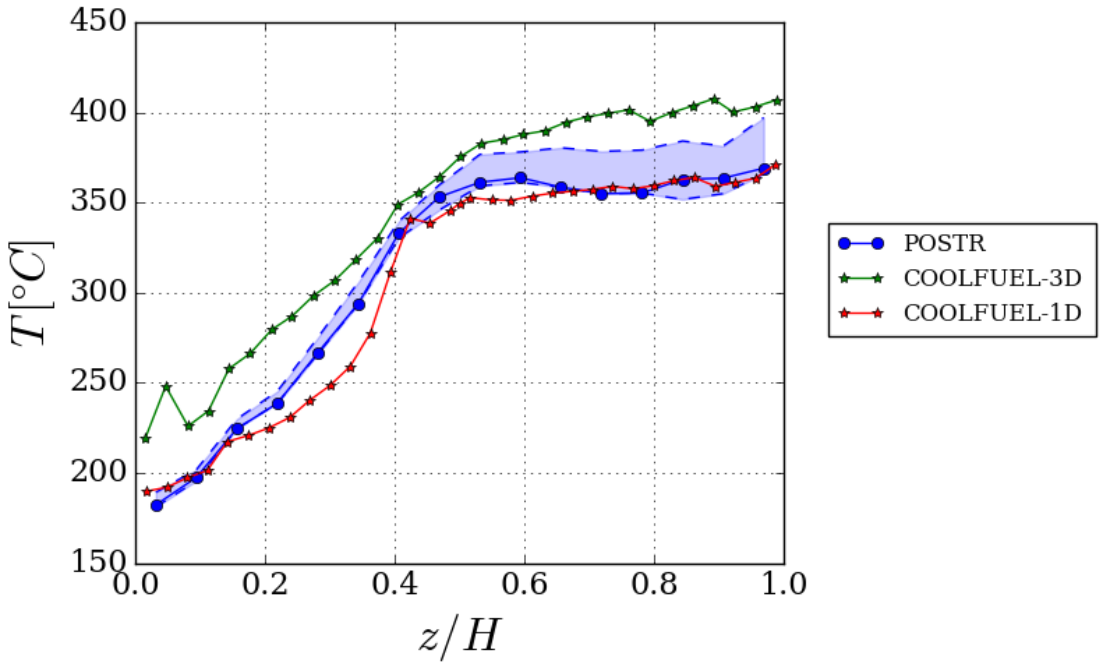

Figure 6.37: Comparison between the predictions of the maximum surface cladding temperature at different heights for case NATURAL-FS output by POSTR, COOLFUEL-1D and COOLFUEL-3D. The shaded area represents the range of predictions obtained with POSTR with different meshes.

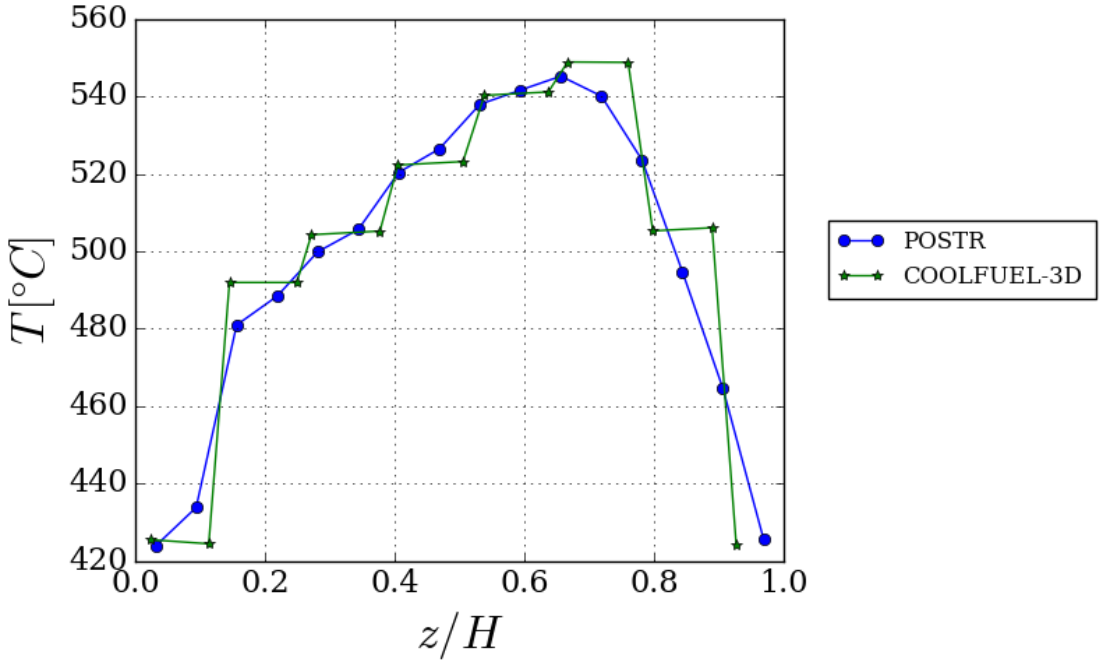

Figure 6.38: Comparison between the predictions of the maximum surface cladding temperature at different heights for case NATURAL-FS output by POSTR and COOLFUEL-3D, when buoyancy is suppressed.

other solvers supports the confidence in the model used, this comparison cannot replace validation with reliable experimental data, which is carried out in the next section.

6.3 Stringer in a hydraulic loop - The MEL experiment

6.3.1 Description of the scenario and model overview

Another potential deviation than the one described in Section 6.2 occurs when a fault during the extraction from the reactor causes the stringer to stop with its bottom nose below the standpipe, rather than inside it. This scenario was investigated experimentally in the 1990s at the Marchwood Engineering Laboratories (MEL). The data gathered were later used to validate the use of COOLFUEL-3D to simulate the scenario. This section describes the simulations with POSTR of three test runs carried out in the MEL facility. The results are compared with the experimental measurements as well as with the predictions given by COOLFUEL-3D.

The test facility represented an AGR stringer partially extracted from the reactor channel, with the outlet ports already in the stand pipe and the piston seals still in the hotbox. A stringer mock-up, which consisted of four fuel element replicas provided with electrical heaters inserted in the pins, was housed in an annular space provided with two inlets. The upward CO_2 flow coming from the bottom inlet represented the coolant flow from the reactor, whereas that from top inlet represented the downward flow from the Fuelling Machine Cooling System (FMCS) (Figure 6.39a). The rig was equipped with an orifice flow meter to measure the resulting flow rate through the stringer, while thermocouples were housed in grooves in the pins claddings to provide readings for the can temperature. Flow resistances across the plug-unit, the upper and lower section of the annulus surrounding the stringer were calculated as $R = \rho\Delta p/\dot{m}^2$ for every test case.[91]

In Reference [91] three test runs were selected as validation cases for COOLFUEL-3D, which differed by the relative influence of buoyancy: Test 60 presented a strong net flow through the stringer and is considered a purely forced convection case, while in Tests 123 and 137 the very small net flow makes buoyancy driven recirculation in the stringer non-negligible. The flow conditions for each case are reported in Table 6.6. This section presents comparisons between POSTR, COOLFUEL-3D and experimental data for these three cases.

It was mentioned in Section 5.2.6 that an attempt was made to simulate the entire domain using a three-dimensional CFD model, as was done in the original COOLFUEL-3D calculation. This approach gave rise to severe numerical oscillations that made the calculation unreliable and was abandoned in favour of the use of a one-dimensional resistance network coupled with a CFD model for the stringer (Figure 5.7b). The fluid domain thus

included only the interior of the stringer, modelled according to the porous approximation, whereas the solid model included the pins, with their cladding, and the graphite sleeve. For simplicity, gravity effects were neglected in the one-dimensional network: as shown in Section 6.3.4, the calculated flow rates were sufficiently close to those reported for the experiment to support this assumption.

The one-dimensional calculation provided the flow rate through the stringer, imposed as an inlet boundary condition applied at the bottom surface of the fluid domain. In turn, the CFD computation provided a new estimate for the stringer resistance to be used by the network solver. A convective boundary condition was imposed at the outer surface of the sleeve, with the fluid temperature of the lower annulus and the heat transfer coefficient calculated using a lumped parameters calculation, which required communication with SYRTHES by means of auxiliary files. At the outer wall of the outer annulus, COOLFUEL-3D used a constant temperature boundary condition. The actual values used were not reported, and in the lumped parameter model used in POSTR the wall was assumed to be adiabatic, in the conservative assumption that heat lost through it would be negligible compared to that transported by the net flow. The tie bar and its guide tube were not included in the solid model in the POSTR calculation, replaced by an adiabatic slip wall boundary condition at the corresponding wall. At the top surface of the stringer, an outlet boundary condition was imposed. Heat generation took place exclusively in the stringer, with the volumetric rate assumed constant and uniform. The inlet flow rates and resistances reported by Moore[91] were imposed to the one-dimensional model, with the resistance due in the plug unit and across the orifice plate modelled together. The fluid density varied according to the ideal gas law, while linear fits from tabular data were used for the other properties. The average solid conductivity from the case presented in Section 6.2 was used, while a reduced thermal inertia was applied to speed up the transient.

All the calculations were run for 5000 variable time steps for the fluid domain, to achieve a faster steady state. The time step for the solid calculation was $1\,\mathrm{s}$. The Upwind scheme was used to increase the stability of the calculation.

A word of warning must be written on the results obtained for Test 137, where the buoyancy influence was the strongest. It was observed that, when the mesh was refined, the solutions for the fluid domain began to oscillate strongly, as shown in Figure 6.40a. The thermal inertia of the solid helped stabilise the fluctuations in that domain (Figure 6.40b), so the predictions of the solid temperatures were considered trustworthy. Nonetheless, for this reasons and for the reduced computational cost it allowed, the results presented in the last section were obtained on a coarser mesh, where the oscillations in the temperatures, although not in the velocities, were minor. This is justified by the close predictions obtained with most meshes for the solid temperature, as will be shown

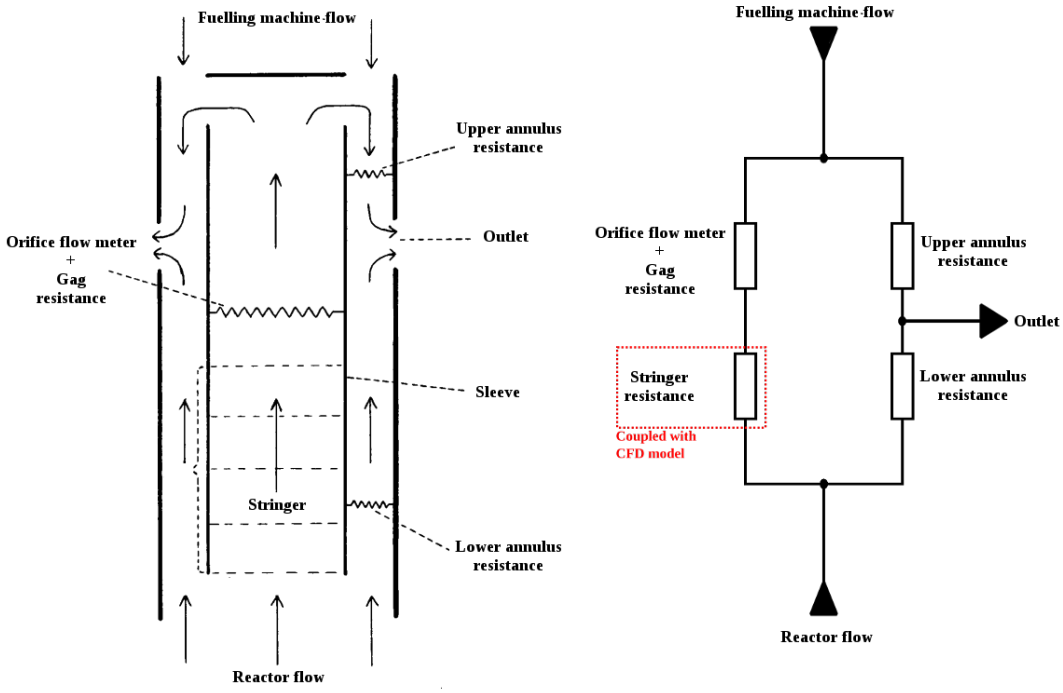

(a) Model of the MEL test facility. Adapted from ref. [91]

(b) Resistance network.

Figure 6.39: Model of the surroundings of the fuel stringer used in the MEL experiments' simulation campaign.

in next section.

Most of the results shown in this section were obtained using a simplified mesh for the solid domain, in which the pins are considered to be continuous throughout the stringer. An alternative mesh modelled the gap between the pin bundles of adjoining fuel elements as non-active sections of the mesh. In the following, this mesh is referred to as 'discontinuous', while the word 'continuous' refers to the simplified mesh.

6.3.2 Influence of the computational meshes

The dependence of the solution from the fluid mesh was investigated for Tests 60 and 137, whilst the influence of the solid mesh was studied for Test 137 only. Table 6.7 reports the number of elements that form the meshes used in the study. For the fluid mesh dependence study, the 'continuous' mesh was used in the solid domain, whereas the meshes used to study the influence of the solid mesh were of the 'discontinuous' type. The filtering mesh used in these simulations had 16 divisions in the axial direction, 12 in the azimuthal direction and 5 in the radial direction.

Figures 6.41, 6.42 and 6.43 show the variations of, respectively, the average tem-

	Test 60	Test 123	Test 137
Stringer Power [kW]	14.1	6.75	2.44
Gas Pressure [bar]	5.15	2.03	2.08
Reactor Flow Rate [$\mathrm{kg\,s^{-1}}$]	0.633	0.0485	0.0303
Reactor Flow Temperature [°C]	59.5	18.6	13.3
FM Flow Rate [$\mathrm{kg\,s^{-1}}$]	0.258	0.1646	0.1025
FM Flow Temperature [°C]	40.6	22.9	20.7

Table 6.6: Parameters used in the set-up of the three calculations presented in Section 6.3.

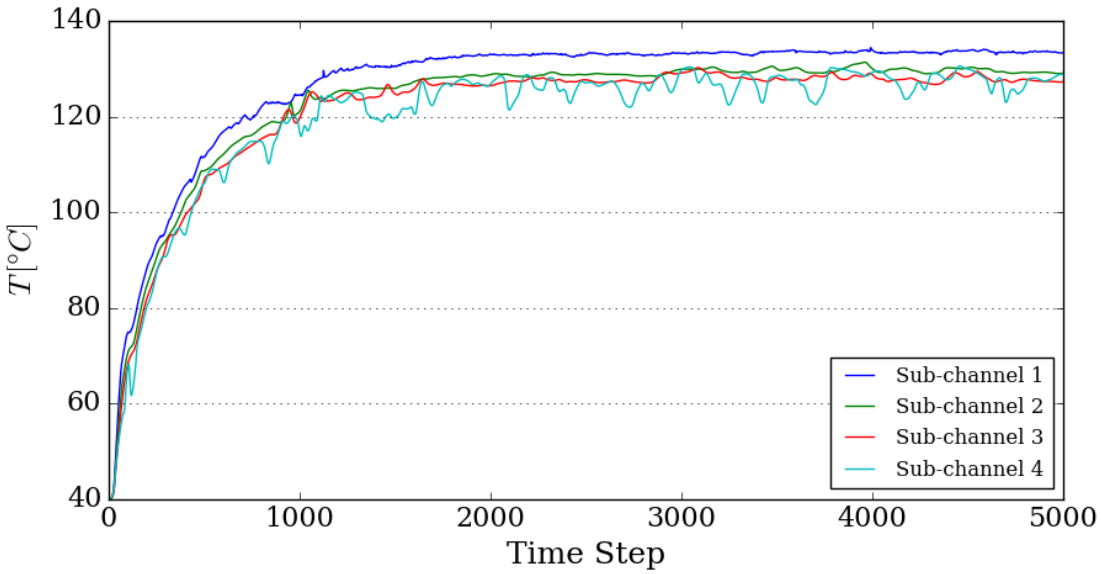

(a) Fluid temperature

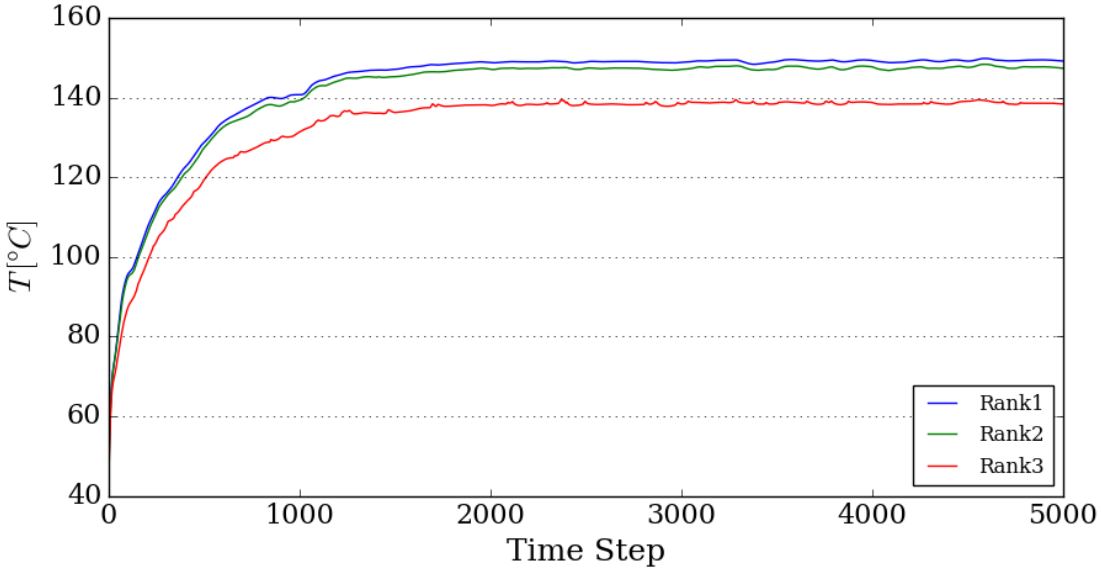

(b) Solid temperature.

Figure 6.40: Oscillations in case T137. The temperatures plotted are the output of probes placed at different positions at $z = 2\,\mathrm{m}$

Fluid Mesh	Number of Elements	Solid Mesh	Number of Elements
A	4608	1	316429
B	17280	2	858078
C	25920	3	1980833
D	61440		

Table 6.7: Number of elements in the meshes used in the study presented in Section 6.3.

Variable	Test 60, Fluid M.I. [%]	Test 137, Fluid M.I.[%]	Test 137, Solid M.I.[%]
T_f	-0.16	-1.04	0.41
w_1	0.35	29.11^*	-14.77^*
w_2	0.06	36.54^*	-7.99^*
w_3	-0.32	11.52^*	-13.00^*
w_4	1.59	-6.18^*	-6.07^*
w_5	-0.24	-44.72^*	-16.90^*
T_{w1}	-0.22	-1.99	0.71
T_{w2}	-0.30	-2.22	0.44
T_{w3}	-0.65	-2.30	0.27

Table 6.8: Relative variation $\frac{Y_{\mathrm{finest}}-Y_{\mathrm{chosen}}}{Y_{\mathrm{finest}}}$ in the values of a number of integral quantities at mid-height between the mesh chosen for the analysis and the finest tested. The subscripts finest and chosen refer respectively to the fluid meshes D and B, and to the solid meshes 3 and 1 in Table 6.7. Velocities marked with a star (*) were scaled against $w_{1,\mathrm{finest}}$ to avoid amplifying the error in sub-channels with very low velocity.

perature of the gas at mid-height, the average sub-channel velocity and the average clad temperature in each rank, for subsequent refinements of the fluid mesh. The plots show a converging trends, with very close predictions from all meshes, except for the coarsest. The relative variation in the prediction between mesh B and D is shown in Table 6.8. The predictions of mesh B will be used for the comparisons in the last section.

The influence of the fluid mesh on the results for Test 137 is shown in Figures 6.44, 6.45 and 6.46. It can be observed that larger variations are found for subsequent mesh refinements. Furthermore the trend shown by the sub-channel velocities appears strongly irregular, which can perhaps be put in relation with the oscillations shown in Figure 6.40a. Nevertheless, the small variation in the solid temperature (see Table 6.8) observed between meshes B and D supported the use of the former in subsequent calculations.

Figures 6.47, 6.48 and 6.49 show the influence of the solid mesh in the predictions for Test 137. Mesh B was used for the fluid domain in all the calculations. As mentioned above, this study was conducted on the 'discontinuous' geometry for the solid mesh, i.e. modelling the gaps between the pins as unheated regions. It can be observed from the figures and from Table 6.8 that the effect of different solid meshes appears to be relatively minor compared to that from the refinement of the fluid mesh. The relatively

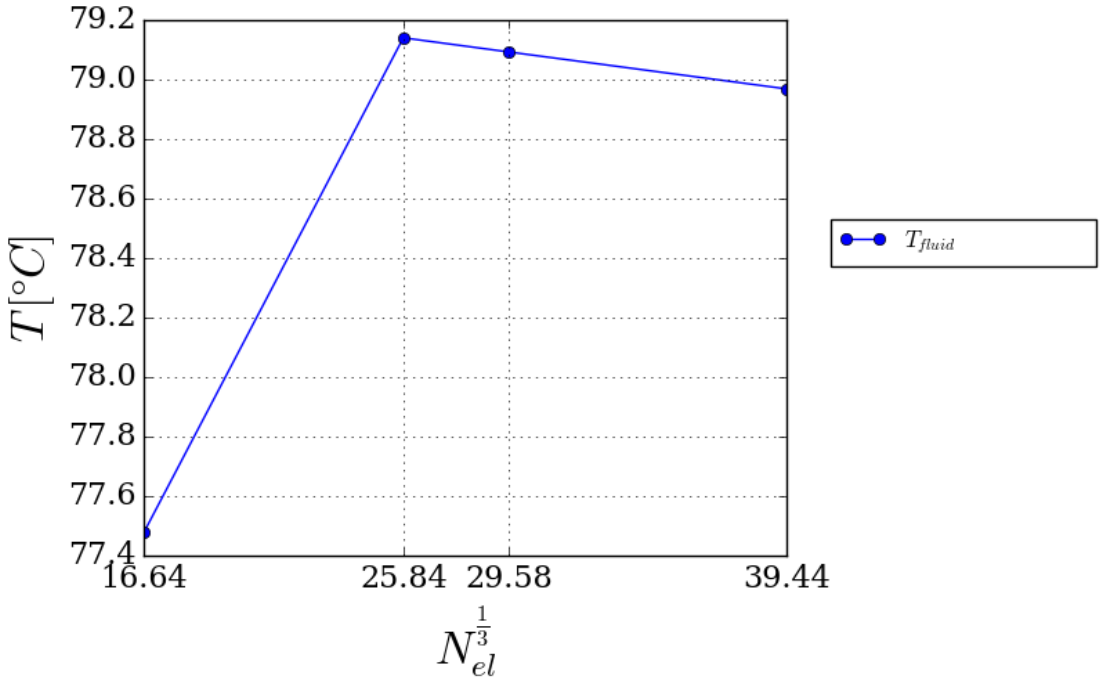

Figure 6.41: Predictions of the average temperature in a cross-section at $z = 0.5H$ for case T60, obtained through successive refinements of the fluid mesh.

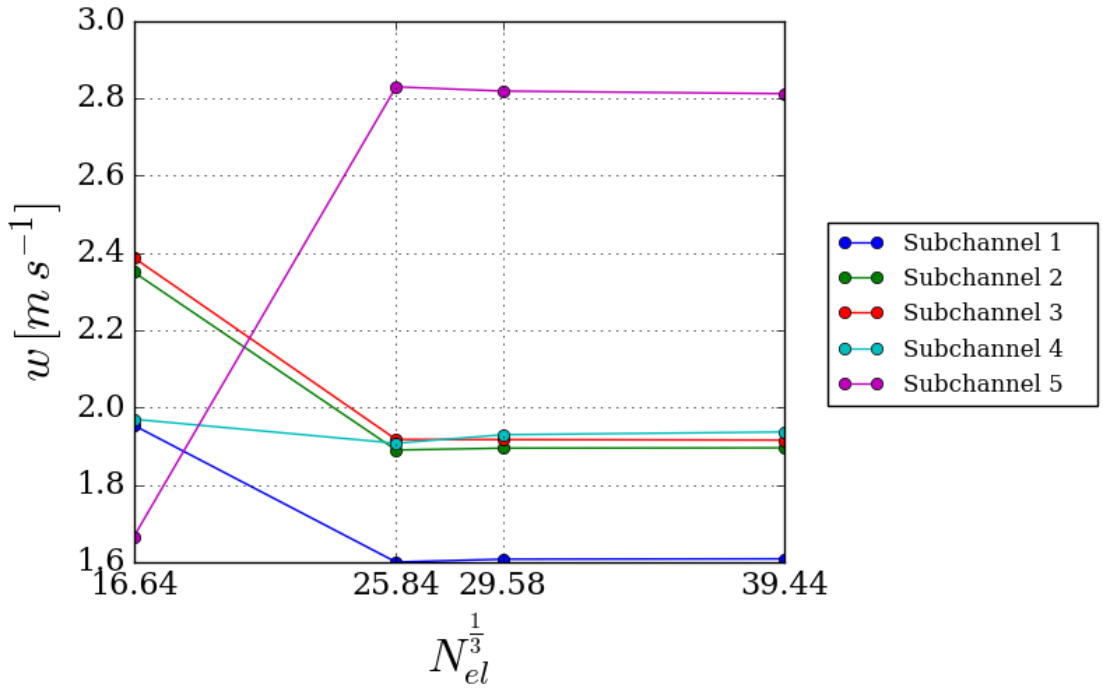

Figure 6.42: Predictions of the sub-channel velocities in a cross-section at $z = 0.5H$ for case T60, obtained through successive refinements of the fluid mesh.

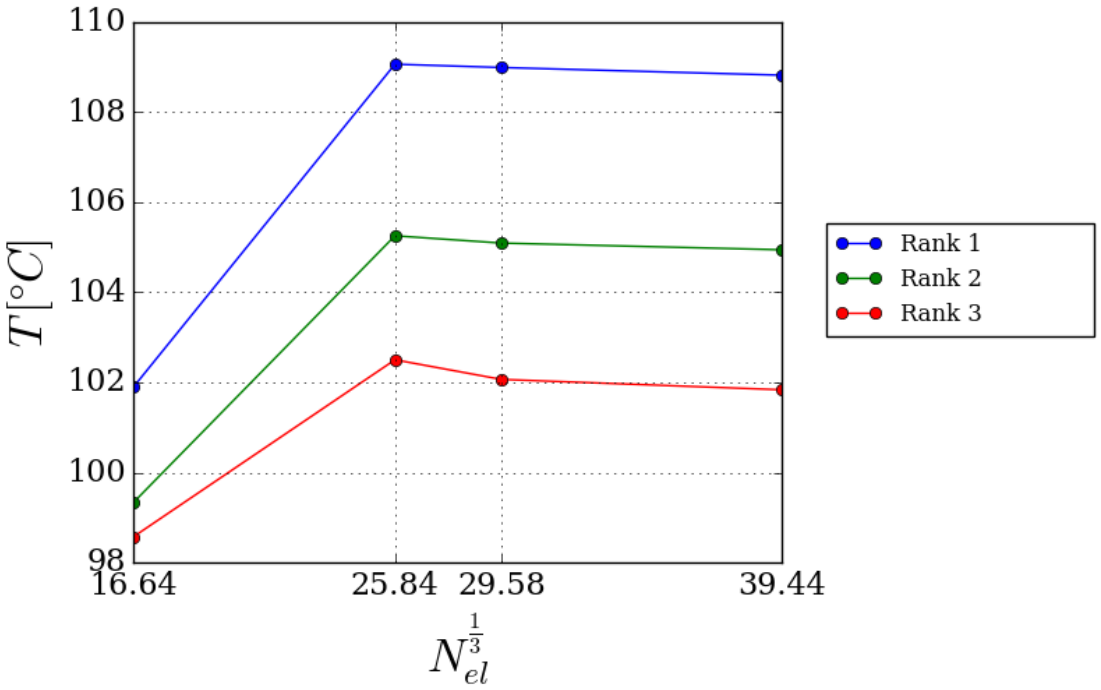

Figure 6.43: Predictions of the average solid temperature between $z = (0.5 \pm 0.05)H$ for case T137, obtained through successive refinements of the fluid mesh.

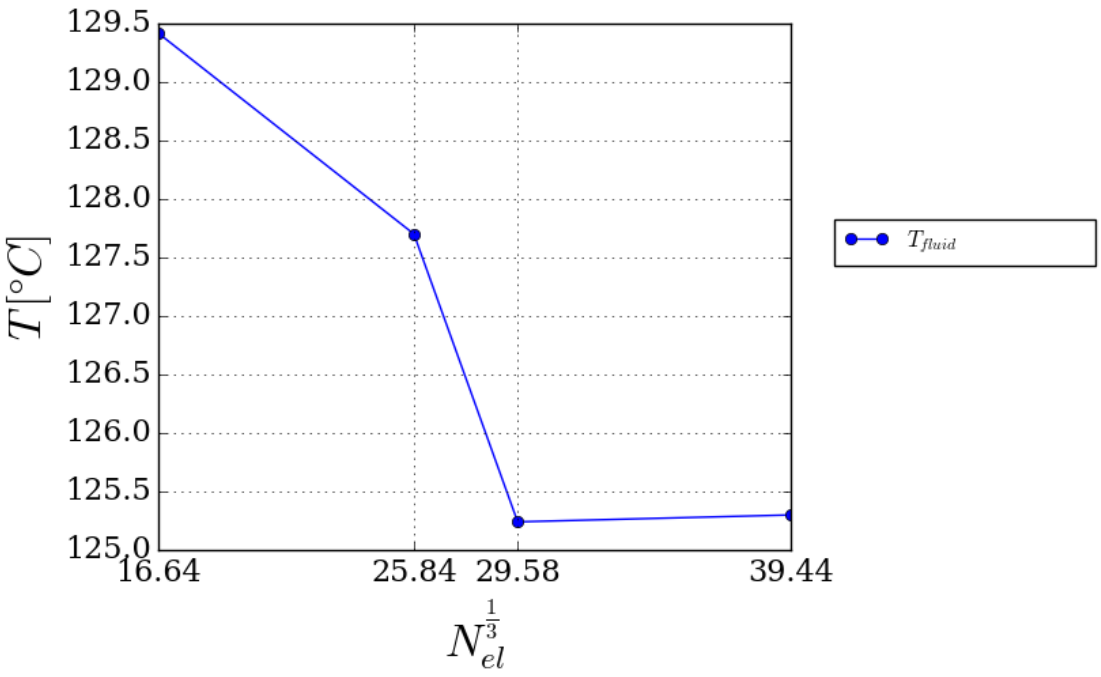

Figure 6.44: Predictions of the average temperature in a cross-section at $z = 0.5H$ for case T137, obtained through successive refinements of the fluid mesh.

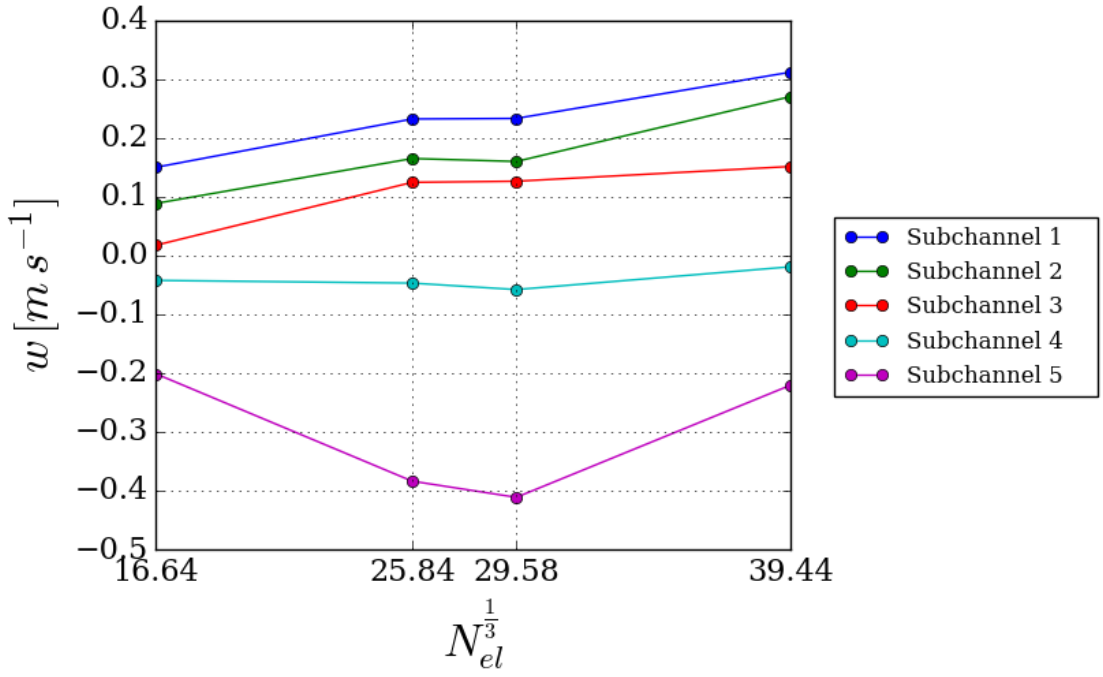

Figure 6.45: Predictions of the sub-channel velocities in a cross-section at $z = 0.5H$ for case T137, obtained through successive refinements of the fluid mesh.

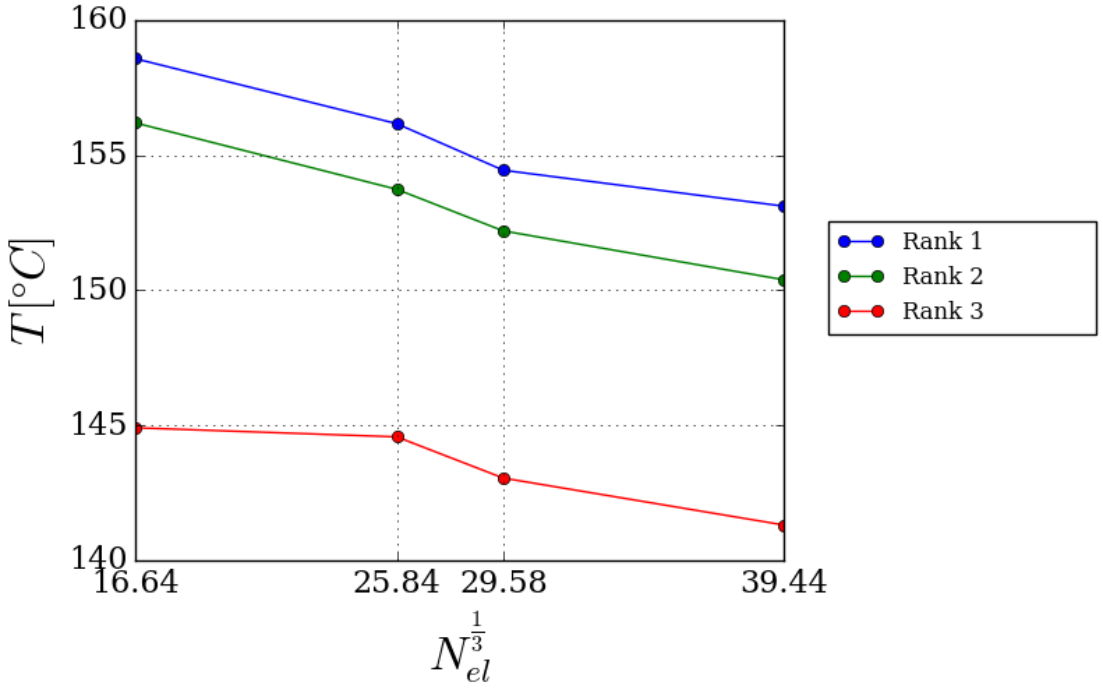

Figure 6.46: Predictions of the average solid temperature between $z = (0.5 \pm 0.05)H$ for case T137, obtained through successive refinements of the fluid mesh.

Axial Refinement	NZ	NAZ	NR
Grid 1	4	12	5
Grid 2	6	12	5
Grid 3	8	12	5
Grid 4	10	12	5
Azimuthal Refinement	NZ	NAZ	NR
Grid 3	8	12	5
Grid 5	8	6	5
Grid 6	8	3	5

Table 6.9: Number of elements in the filtering meshes used in the study presented in Section 6.3.

large variations in the sub-channel velocities despite the use of the same mesh for the fluid domain support the hypothesis that the discrepancy could be due to the oscillations in the velocity predictions.

6.3.3 Influence of the filtering mesh

Beside the effect of the computational mesh, the influence of the filtering grid on the solution was assessed in a series of calculations in which the computational meshes were kept constant. The dependence on the axial and azimuthal subdivision was explored.

The computational meshes used were different from those employed in the studies described above. The fluid mesh comprised of 120 divisions in the axial direction, 10 in the radial direction and 24 in the azimuthal direction. The solid mesh was formed by total of 416224 tetrahedra, with 120 divisions in the axial directions for the pins. This discretisation was chosen to allow the use of different filtering grid while maintaining a uniform distribution of the computational cells in the filtering blocks.

Six computational grids were tested, with different subdivision in the axial and azimuthal directions. The scenario investigated was that of Test 137. Figures 6.50, 6.51 and 6.52 show the evolution of the average temperature of the gas at mid-height, the average sub-channel velocity and the average clad temperature in each rank obtained with filtering grids with different numbers of divisions in the axial direction, while Figures 6.53, 6.54 and 6.55 show the effect of an azimuthal refinement. As was observed for the computational mesh, the influence of different grids on the solid temperature is limited, while bigger variations are observed for the fluid velocities. As can be observed in Table 6.9, which reports the spread in the variables normalized to their arithmetic mean, the maximum difference for the solid temperatures is of the order of $1\ \%$ of the average, with a seemingly stronger influence of the axial refinement, compared to the azimuthal.

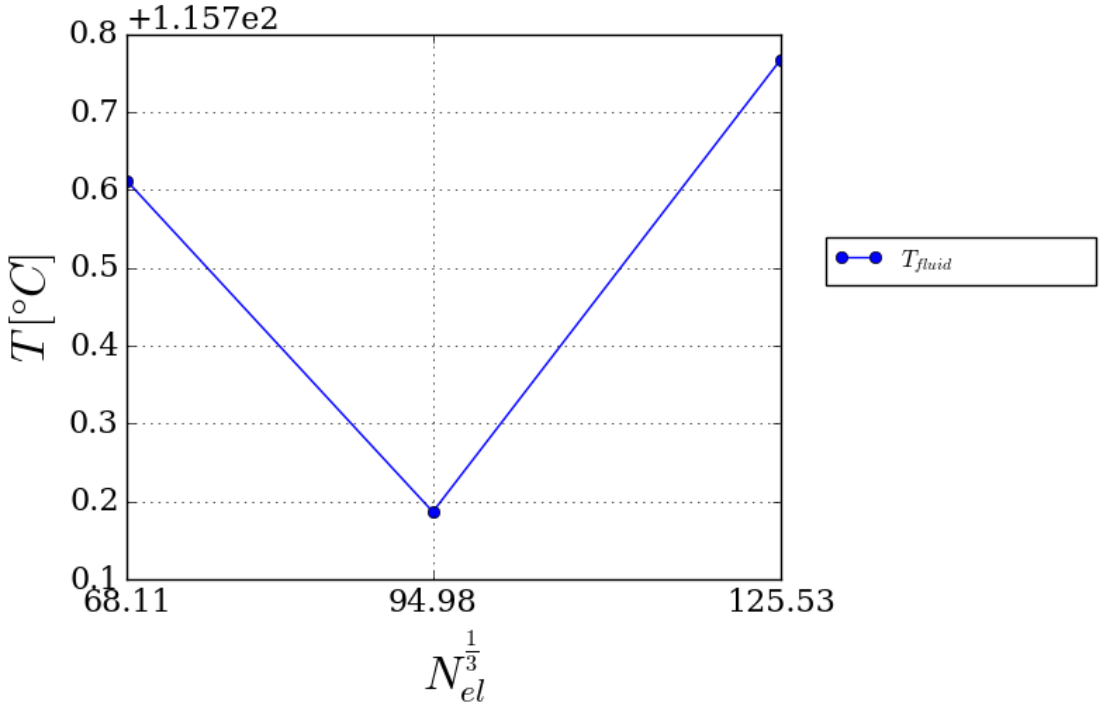

Figure 6.47: Predictions of the average temperature in a cross-section at $z = 0.5H$ for case T137, obtained through successive refinements of the solid mesh.

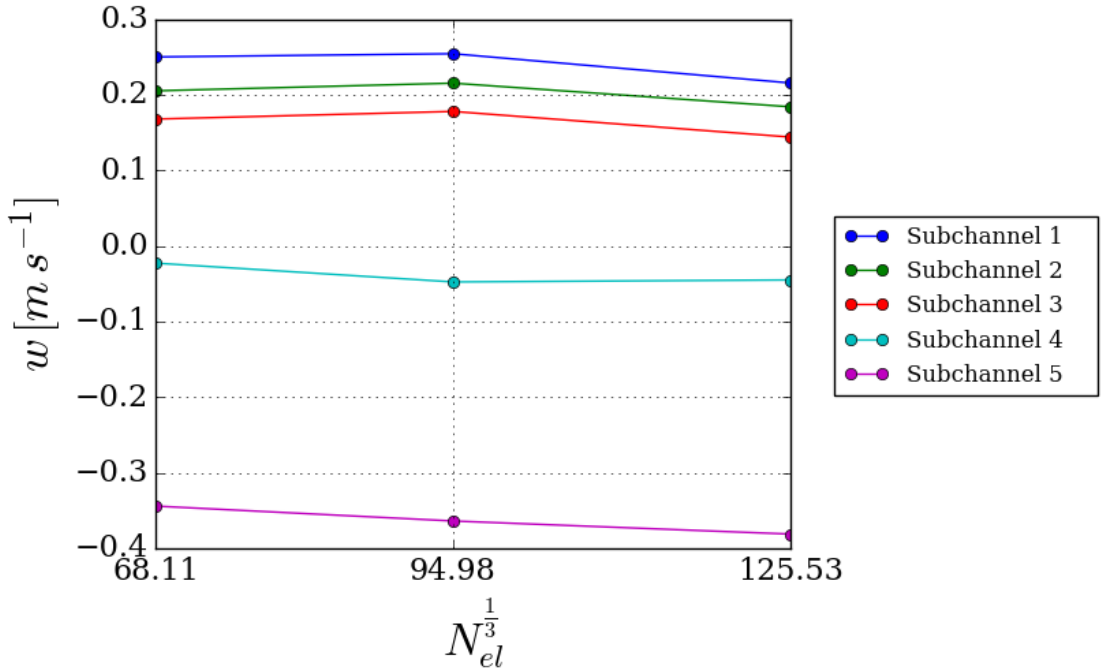

Figure 6.48: Predictions of the sub-channel velocities in a cross-section at $z = 0.5H$ for case T137, obtained through successive refinements of the solid mesh.

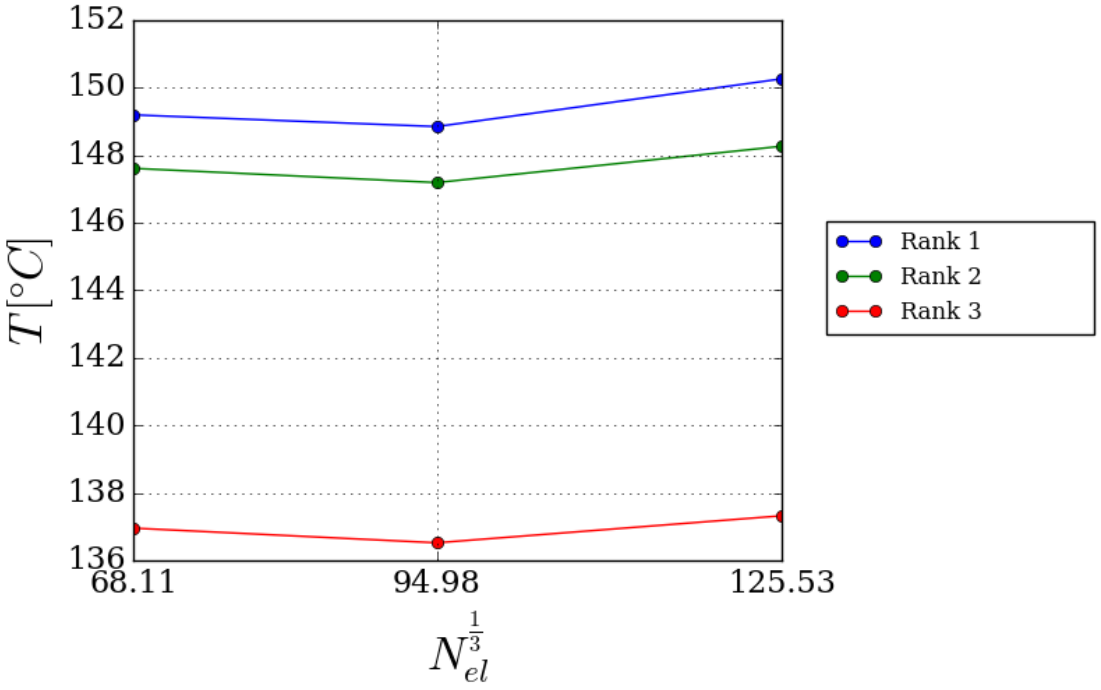

Figure 6.49: Predictions of the average solid temperature between $z = (0.5 \pm 0.05)H$ for case T137, obtained through successive refinements of the solid mesh.

Variable	Axial refinements [%]	Azimuthal refinements [%]
T_f	3.78	1.40
w_1	27.40*	12.85*
w_2	27.11*	10.89*
w_3	11.33*	8.50*
w_4	1.52*	6.87*
w_5	20.60*	22.83*
T_{w1}	1.14	0.18
T_{w2}	1.00	0.28
T_{w3}	1.05	0.26

Table 6.10: Relative spread $\frac{Y_{\max}-Y_{\min}}{Y_{\text{mean}}}$ in the values of a number of integral quantities at mid-height for the filtering meshes tested. The minimum, maximum and mean values were calculated between the values obtained at $z = 0.5H$ with different filtering meshes. Velocities marked with a star (*) were scaled against $w_{1,\text{finest}}$ to avoid amplifying the error in sub-channels with very low velocity.

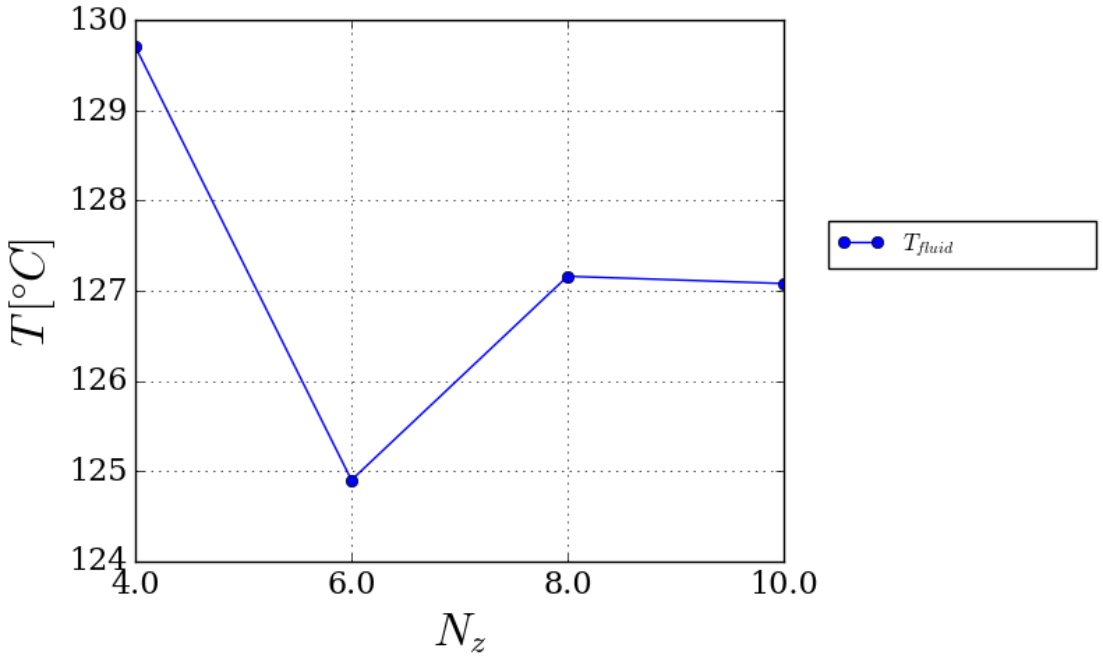

Figure 6.50: Predictions of the average temperature in a cross-section at $z = 0.5H$ for case T137, obtained through successive axial refinements of the filtering mesh.

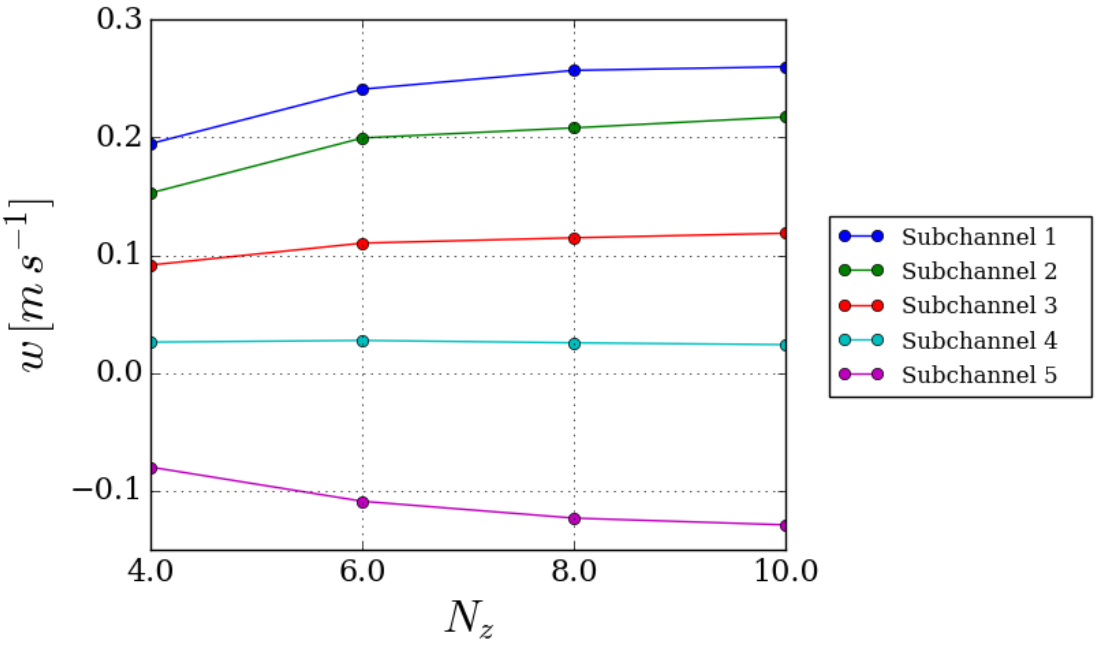

Figure 6.51: Predictions of the sub-channel velocities in a cross-section at $z = 0.5H$ for case T137, obtained through successive axial refinements of the filtering mesh.

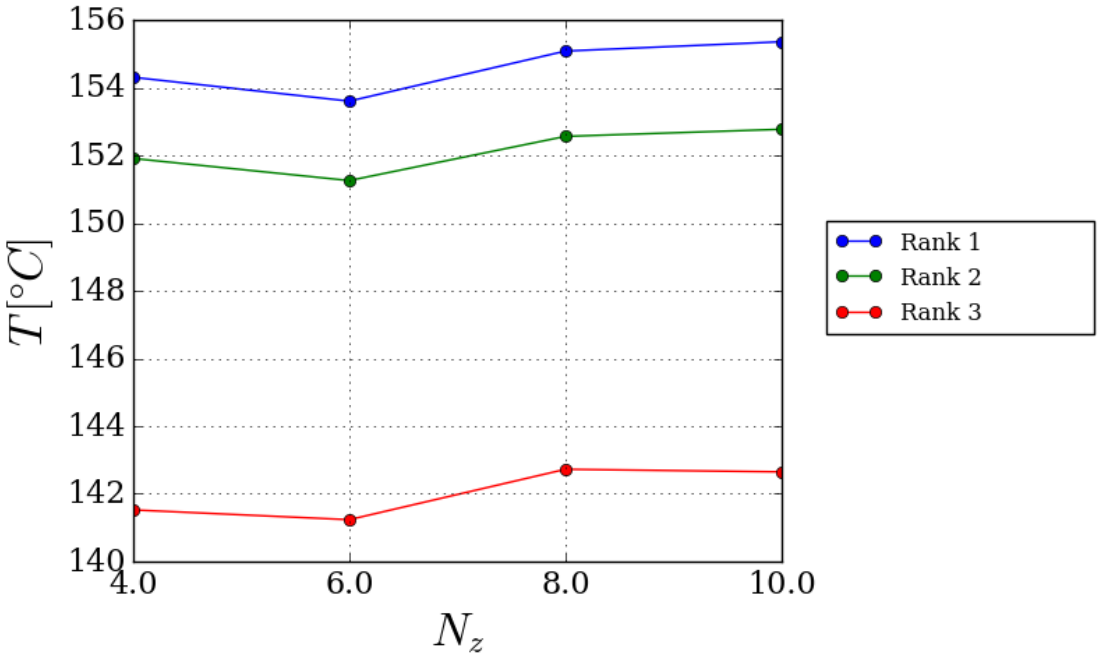

Figure 6.52: Predictions of the average solid temperature between $z = (0.5 \pm 0.05)H$ for case T137, obtained through successive axial refinements of the filtering mesh.

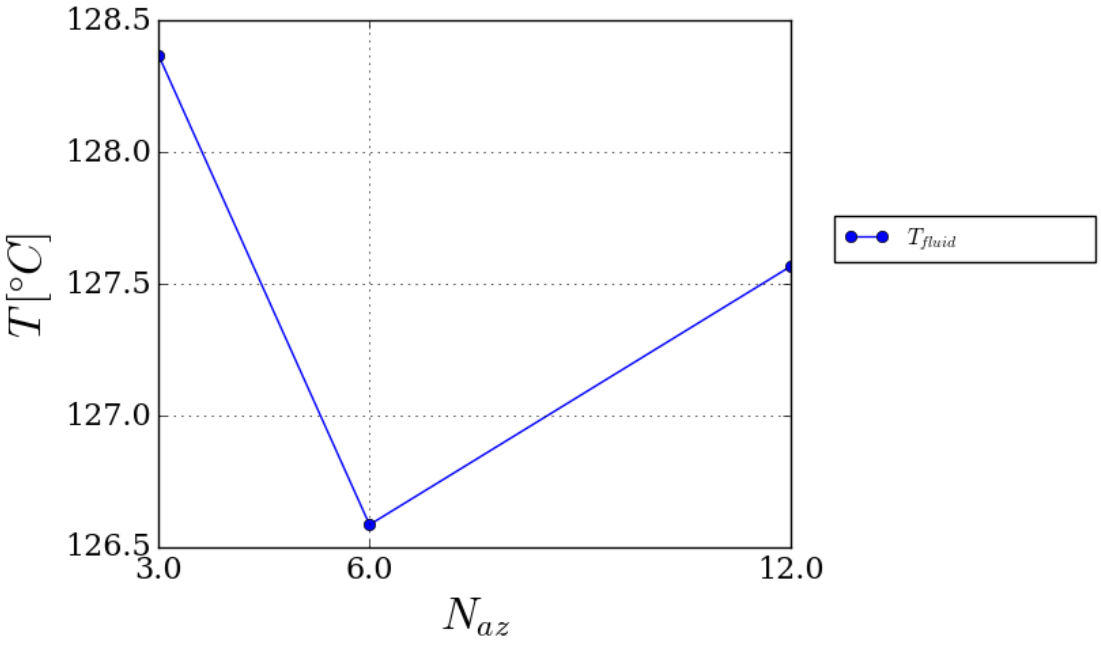

Figure 6.53: Predictions of the average temperature in a cross-section at $z = 0.5H$ for case T137, obtained through successive azimuthal refinements of the filtering mesh.

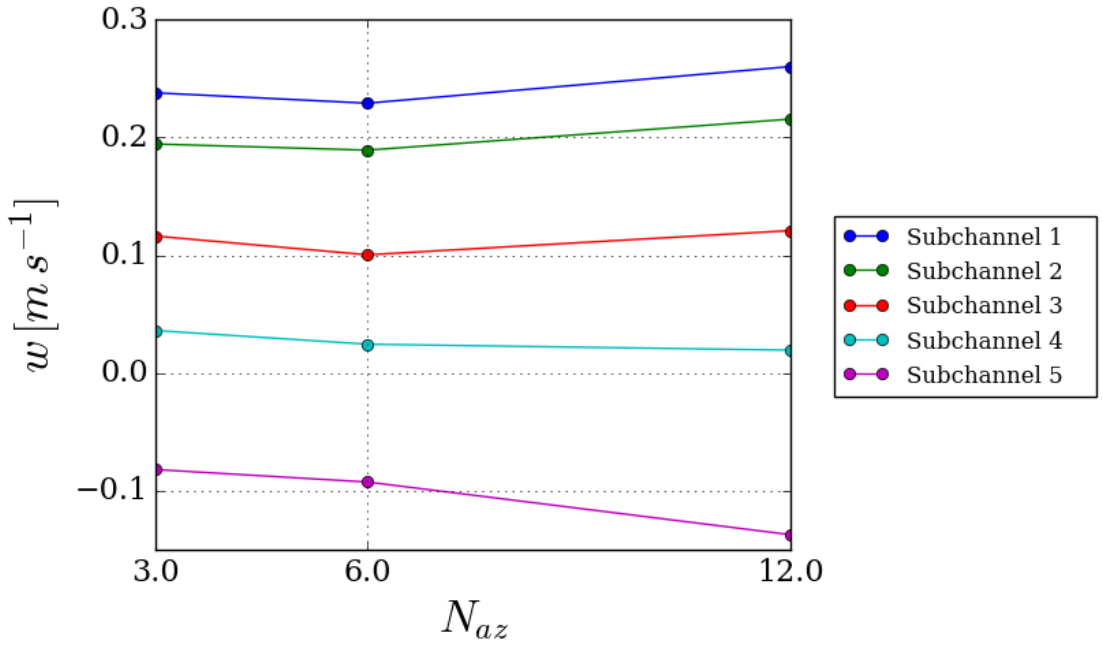

Figure 6.54: Predictions of the sub-channel velocities in a cross-section at $z = 0.5H$ for case T137, obtained through successive azimuthal refinements of the filtering mesh.

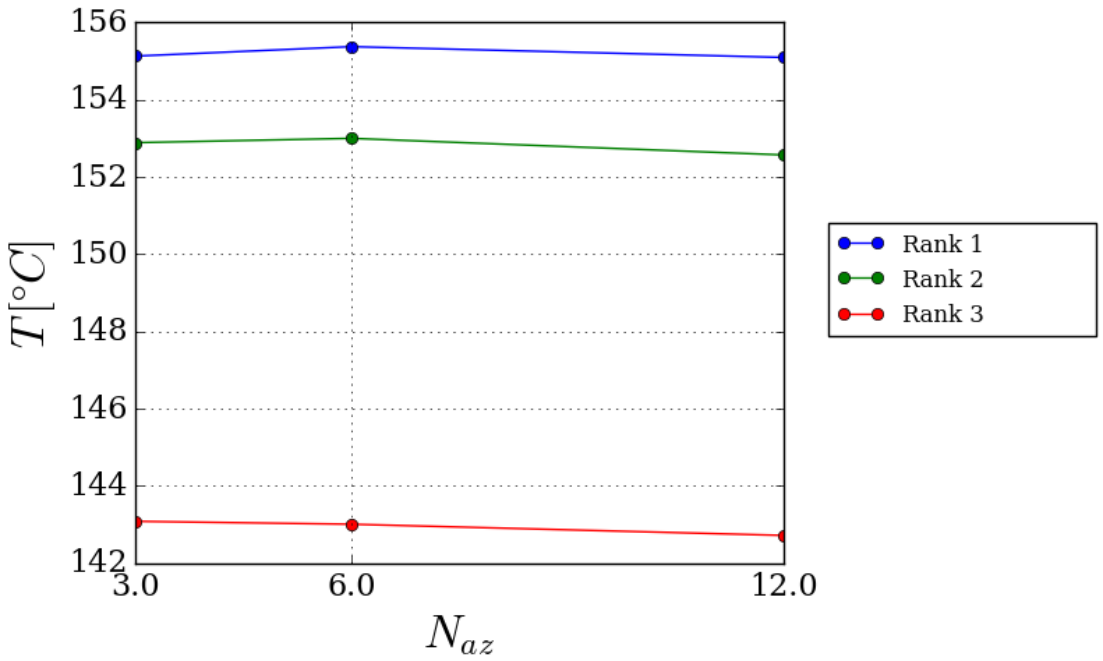

Figure 6.55: Predictions of the average solid temperature between $z = (0.5 \pm 0.05)H$ for case T137, obtained through successive azimuthal refinements of the filtering mesh.

6.3.4 Comparison with the experiment

In the following, the results obtained from the simulation of the experimental runs listed in Table 6.6 are presented. The calculations presented used Mesh B for the fluid domain and Mesh 1 for the solid domain. For each test, the following information will be provided:

- The convergence history of the stringer flow rate and the lower annulus temperature predicted by the one-dimensional solver.
- The profiles of the sub-channel axial velocity and temperature at a cross section located at $z = 0.5H$.
- The predictions of the clad temperatures at different heights for each rank of pins.

Experimental data are available for the stringer flow rate and the clad temperatures, which will allow a reliable evaluation of the accuracy of the predictions.

The following remarks should be recalled when interpreting the results presented below:

- The uncertainty of the temperature readings in the experiment was reported to be $\pm 3\,^{\circ}\mathrm{C}$, while for that for the flow through the stringer was $\pm 0.005\,\mathrm{kg\,s^{-1}}$.
- Since the filtering mesh used in these studies had 16 divisions in the axial direction, the profiles at mid-height were obtained by linear interpolation between the profiles calculated at the eight and ninth axial blocks, centred respectively at $z = 0.47H$ and $z = 0.53H$.
- The clad temperature reported for the experiment is the average between the readings of the thermocouples placed in the grooves on the pin claddings, close to the surface. The values reported for POSTR were therefore calculated as the average temperature at the boundary of the pins. The pins were divided in 16 axial blocks, and the temperatures plotted are the averages within the blocks, assigned at their centres.
- Whenever the difference between experimental data and the results of the computation is reported, the calculated temperature is linearly interpolated to the location of the thermocouples.

The reader may refer to Table 6.6 for information on the flow conditions during the tests. Unless it is mentioned otherwise, all calculations were run using the continuous mesh for the solid domain.

Test 60: strong net flow rate

Test 60 was selected by Moore[91] to prove the validity of the COOLFUEL-3D model to simulate the MEL experiment. The flow conditions imposed for this test run resulted in a net upward flow through the stringer, strong enough to make buoyancy effects negligible.

Figure 6.56 shows the stringer mass flow rate and the average gas temperature in the lower annulus output from the one-dimensional network solver at each time step. The stringer flow rate quickly converges to a value of $0.363\,\mathrm{kg\,s^{-1}}$, which matches well the measured value of $0.365\,\mathrm{kg\,s^{-1}} \pm 0.005\,\mathrm{kg\,s^{-1}}$. Figure 6.57, shows the proportion of the power generated in the pins which is removed by convection and thermal radiation, according to the energy balance calculated by SYRTHES. It is shown that cooling occurs essentially by convection in this scenario, with thermal radiation accounting for a mere $3.29\,\%$ of the total power. The fraction of the power generated which is removed through the sleeve in this scenario is $3.15\,\%$.

In Figure 6.58 the profiles of the sub-channel axial velocity and temperature are shown. They show the characteristic shape of forced flow along a rough pin bundle observed in Section 6.1 (see Figure 6.22), with the highest velocities observed along the smooth surface of the sleeve.

Figures 6.59 to 6.61 report the comparison between the prediction of the clad temperature by POSTR with the data from the MEL experiment, together with the results obtained by Moore[91] with COOLFUEL-3D. There is very good agreement between POSTR and the experiment, with the discrepancy between the results, $T_{\mathrm{MEL}} - T_{\mathrm{POSTR}}$, within $-1.84\,^{\circ}\mathrm{C}$ and $0.56\,^{\circ}\mathrm{C}$ for Rank 1, $-1.77\,^{\circ}\mathrm{C}$ and $5.98\,^{\circ}\mathrm{C}$ for Rank 2 and $-0.45\,^{\circ}\mathrm{C}$ and $4.68\,^{\circ}\mathrm{C}$ for Rank 3. The 'discontinuous' mesh for the pins was also tested, giving the results shown in Figures 6.62, 6.63 and 6.64. The results were similar with those obtained with the 'continuous' mesh, with the discrepancy between the experiment and the calculation being within $-3.58\,^{\circ}\mathrm{C}$ and $4.34\,^{\circ}\mathrm{C}$.

It is noted that the predictions given by COOLFUEL-3D for this test were not as close to the measurements as those by POSTR, with a maximum discrepancy of about $30\,^{\circ}\mathrm{C}$. The result was nonetheless considered successful in demonstrating the ability of the code to simulate the scenario under analysis.[91]

Test 123: weak net flow rate

Test 123 was carried out imposing weaker flow at the inlets than in Test 60, with larger flow from the FMCS than from the reactor. The net flow through the stringer was still directed upwards, but almost 15 times weaker, which increased the relative importance of buoyancy as a driving force. The case was selected by Moore[91] to validate COOLFUEL-3D for the simulation of weak flow conditions, and it was replicated with POSTR for the

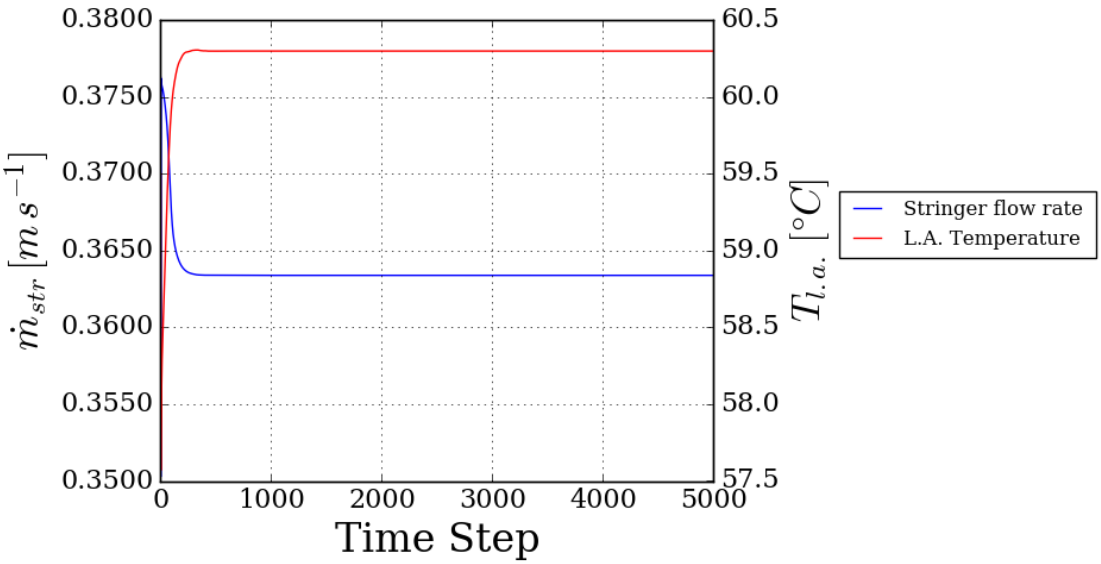

Figure 6.56: Convergence history of the stringer mass flow rate and the lower annulus temperature calculated by the one-dimensional solver for case T60.

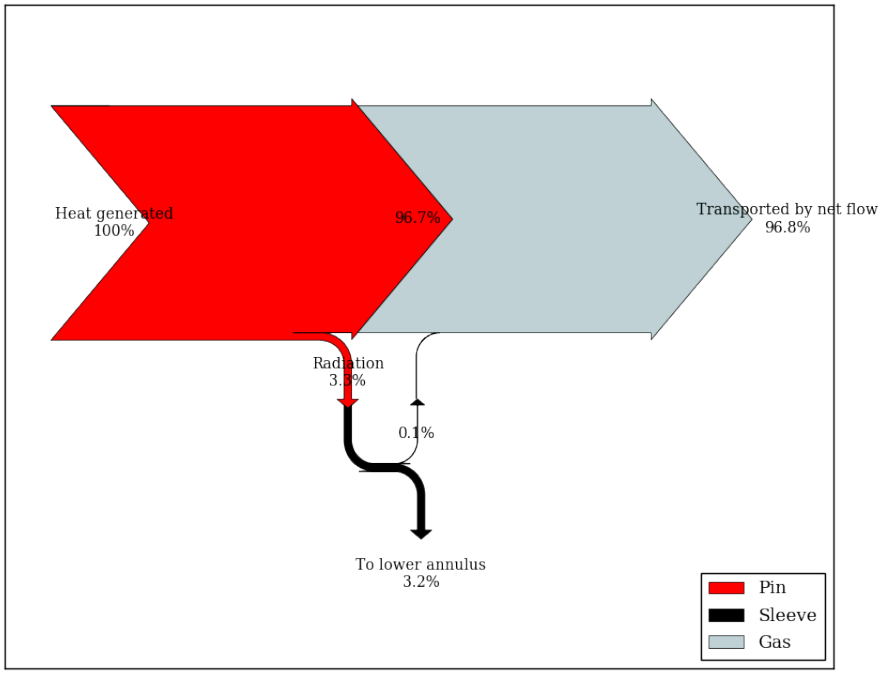

Figure 6.57: Heat removal paths for case T60 at steady state.

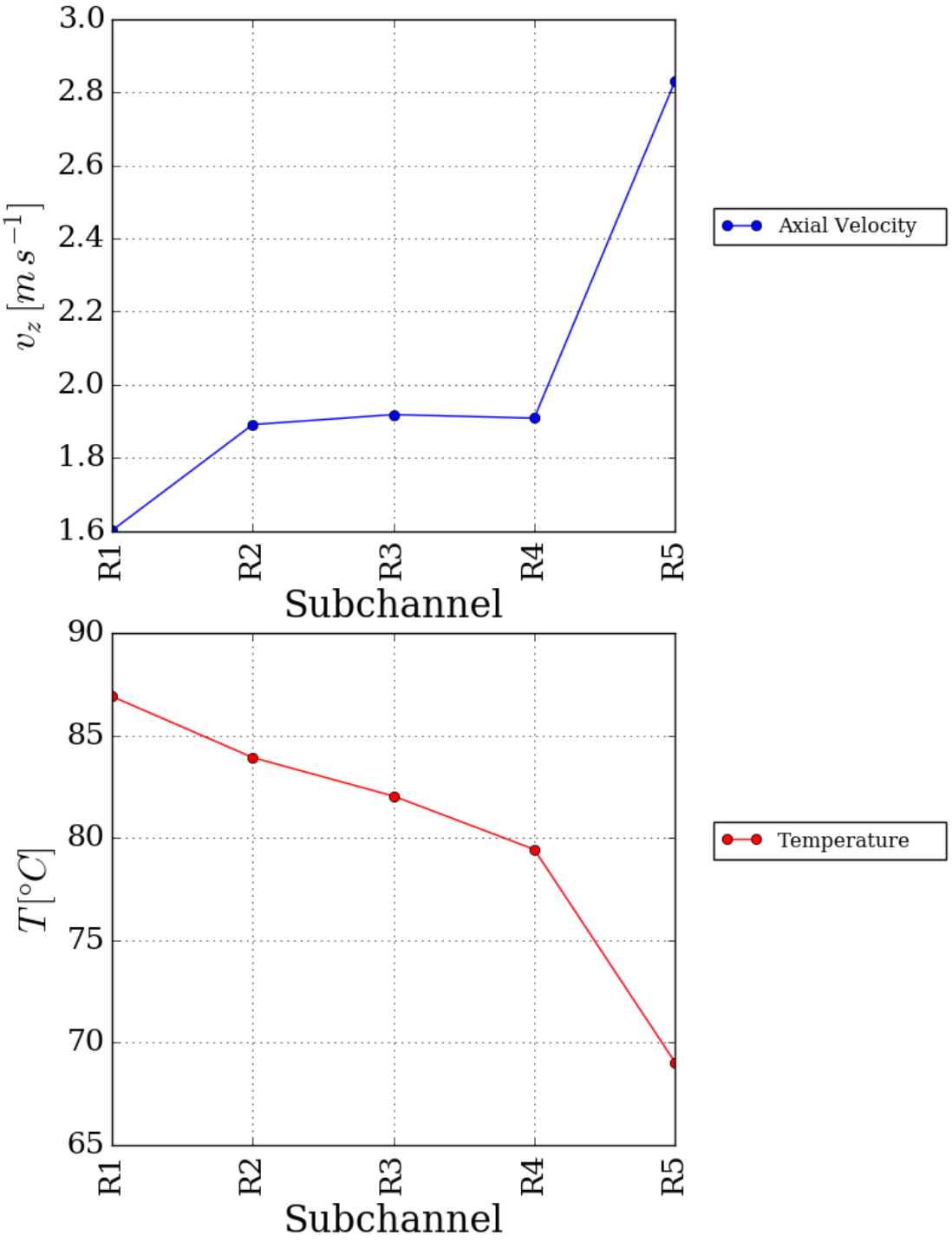

Figure 6.58: Predictions of sub-channel averages obtained with POSTR for case T60 at $z = 0.5H$.

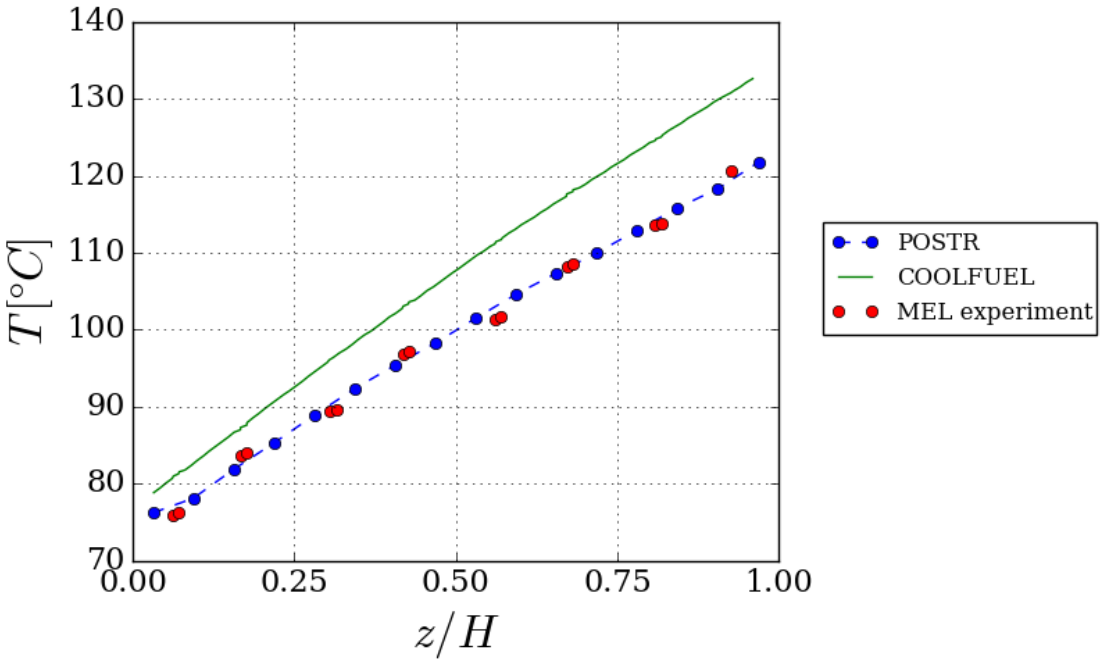

Figure 6.59: Predictions of maximum cladding temperature at different height in the first rank of pins, obtained with POSTR for case T60 using the 'continuous' mesh for the pins.

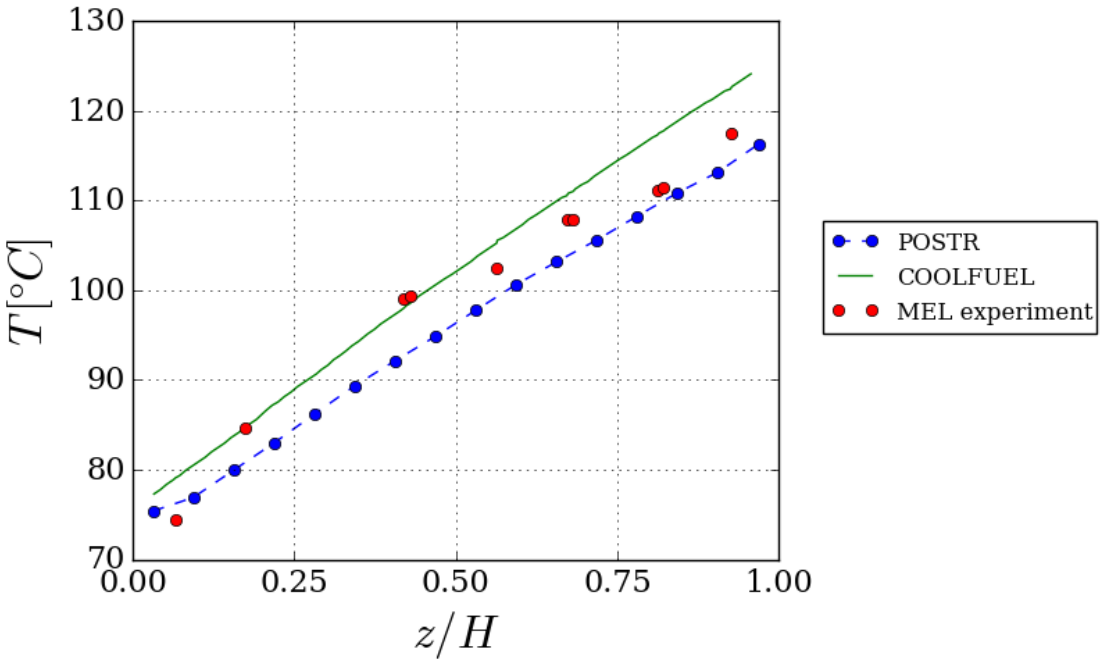

Figure 6.60: Predictions of maximum cladding temperature at different height in the second rank of pins, obtained with POSTR for case T60 using the 'continuous' mesh for the pins.

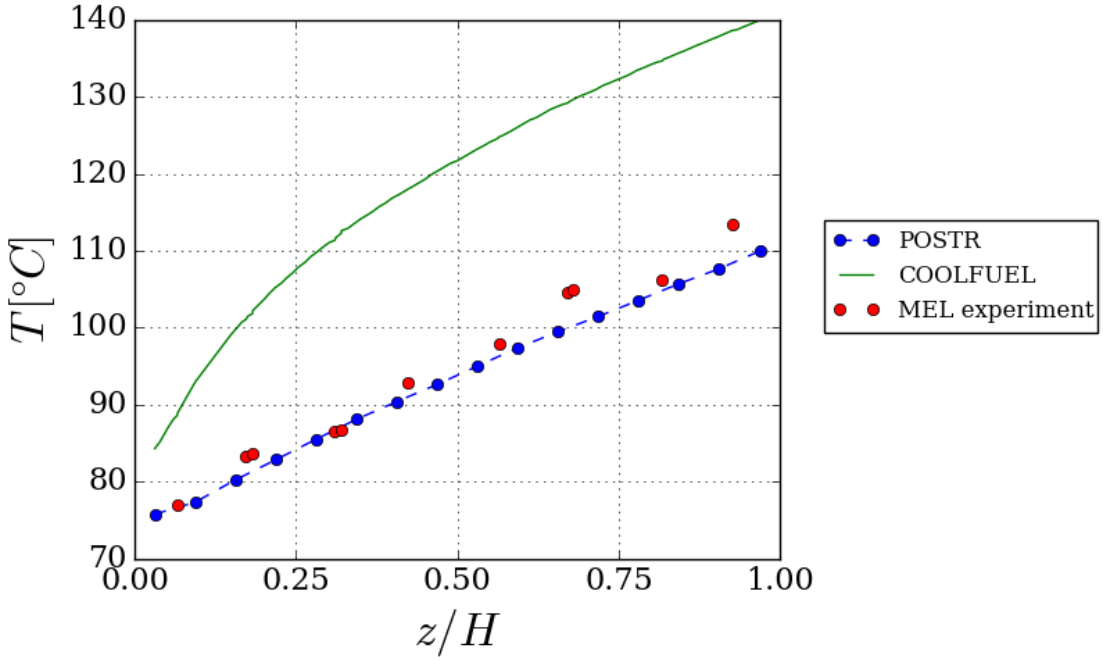

Figure 6.61: Predictions of maximum cladding temperature at different height in the third rank of pins, obtained with POSTR for case T60 using the 'continuous' mesh for the pins.

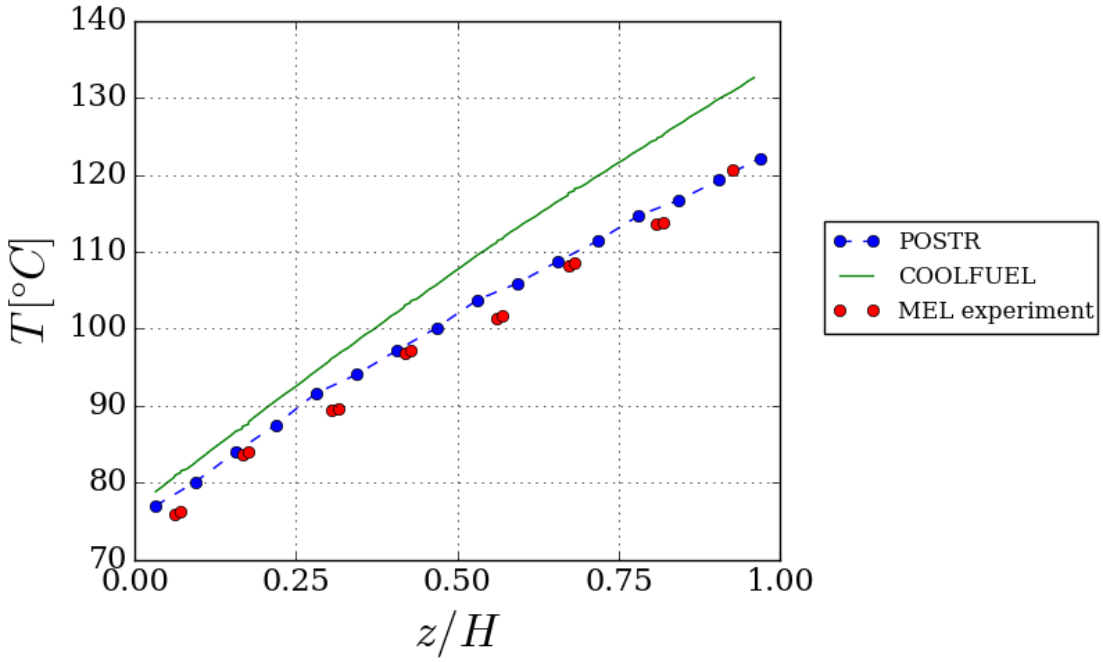

Figure 6.62: Predictions of maximum cladding temperature at different height in the first rank of pins, obtained with POSTR for case T60 using the 'discontinuous' mesh for the pins.

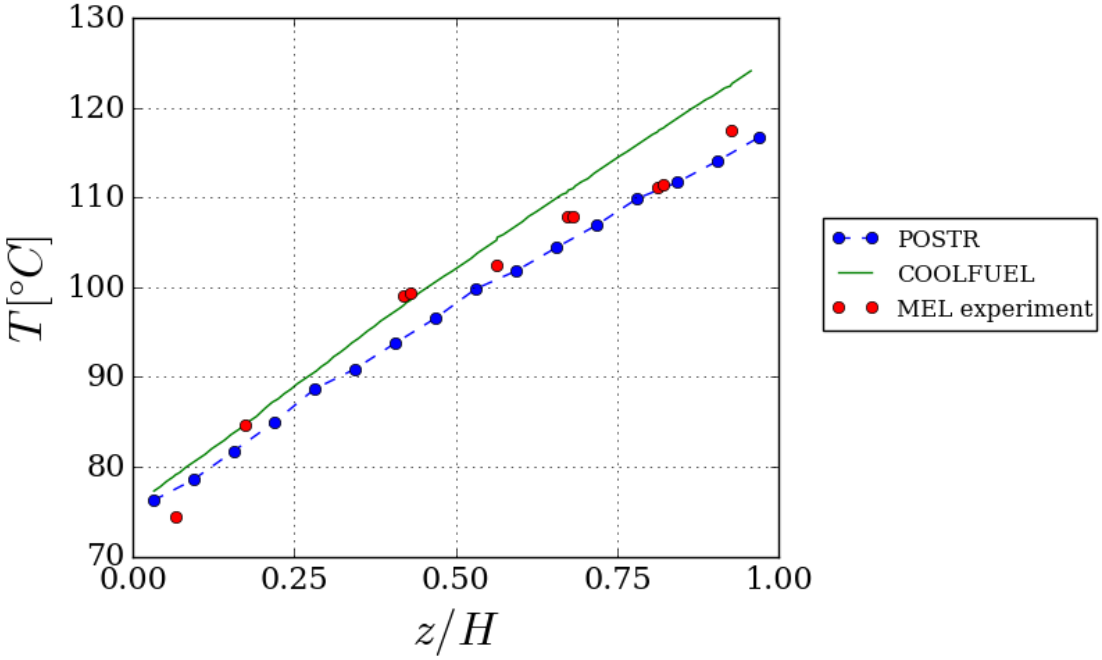

Figure 6.63: Predictions of maximum cladding temperature at different height in the second rank of pins, obtained with POSTR for case T60 using the 'discontinuous' mesh for the pins.

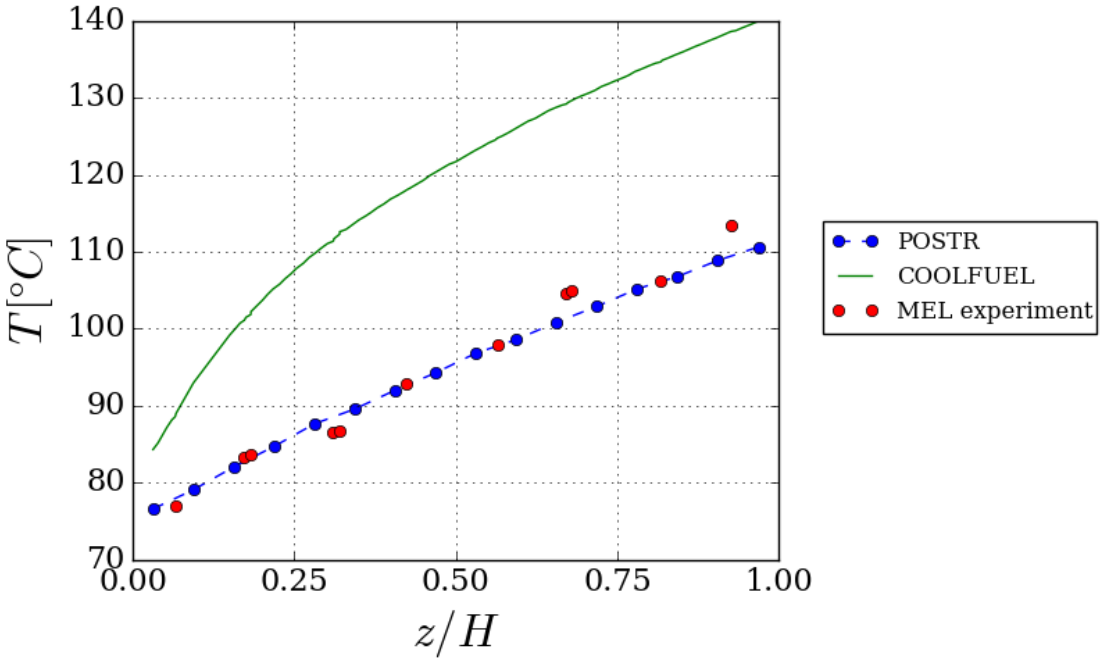

Figure 6.64: Predictions of maximum cladding temperature at different height in the third rank of pins, obtained with POSTR for case T60 using the 'discontinuous' mesh for the pins.

same purpose.

Figure 6.65 shows the stringer mass flow rate and the average gas temperature in the lower annulus output from the one-dimensional network solver at each time step. The calculated value of $0.027\,\mathrm{kg\,s^{-1}}$ is again in very good agreement with the measured value of $0.025\,\mathrm{kg\,s^{-1}} \pm 0.005\,\mathrm{kg\,s^{-1}}$. However, a first attempt to simulate the scenario uncovered instabilities in the lumped parameter model for the cooling of the graphite sleeve from the lower annulus, which caused the calculated temperature in the region to oscillate broadly from one time step to another. The cause of the problem was identified in the correlation used to calculate the contribution to the heat exchange due to buoyancy effects. The option of adding a relaxation coefficient in the calculation was therefore included, which allowed the calculation to converge smoothly to a prediction of $59.15\,^{\circ}\mathrm{C}$, as shown in Figure 6.65. As shown in Figure 6.66, at the lower flow rate encountered in this scenario compared to case T60 the relative importance of thermal radiation in the cooling of the pins increases significantly, with almost a quarter of the heat generated being removed by this mechanism through the sleeve.

The profiles for the sub-channel axial velocity and temperature (Figure 6.67) show significant differences with Test 60. In particular, the shape of velocity profile is visibly altered by the action of the buoyancy forces, which act to aid the flow in the heated central region, where the fuel bundle is located, and to oppose it in the region next to the sleeve, which is cooled from the lower annulus. The temperature profile is also altered, showing a small local peak in R4, This is possibly due to the lower flow velocity predicted in the region compared to the three innermost sub-channels.

The comparison between the clad temperatures reported for the experiment and those predicted by POSTR is presented in Figures 6.68, 6.69 and 6.70. Overall, the model underestimates the cladding temperatures, with discrepancies within $-3.89\,^{\circ}\mathrm{C}$ and $20.38\,^{\circ}\mathrm{C}$ for Rank 1, $-3.59\,^{\circ}\mathrm{C}$ and $16.60\,^{\circ}\mathrm{C}$ for Rank 2 and $-1.97\,^{\circ}\mathrm{C}$ and $15.63\,^{\circ}\mathrm{C}$ for Rank 3. Slightly more conservative predictions were given by COOLFUEL-3D, which shows better performance in this case than in the former.

Test 137: very weak net flow rate

Test 137 was carried out with a further reduction of the mass flow rates from the reactor and the fuelling machine compared to Test 123. Moreover, the stringer power was 2.77 times smaller, resulting in a reduction of the driving force due to buoyancy. The result was a drop in the net flow rate through the stringer by 10 times, with a reported value of $0.0025\,\mathrm{kg\,s^{-1}} \pm 0.0050\,\mathrm{kg\,s^{-1}}$. The flow measured was smaller than the associated uncertainty, which makes the case suitable to validate the model for conditions close to stagnation.

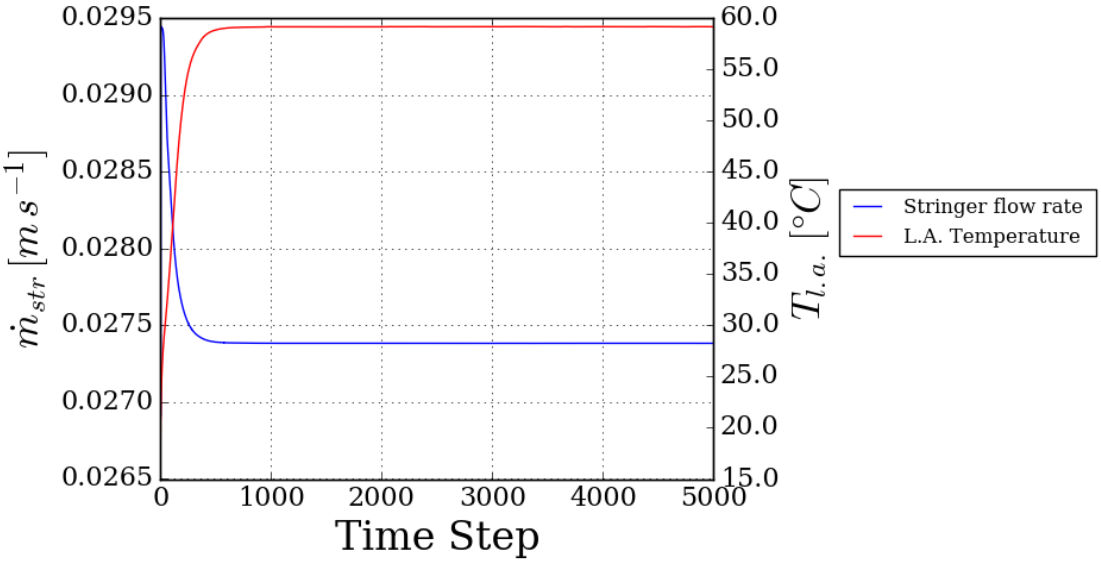

Figure 6.65: Convergence history of the stringer mass flow rate and the lower annulus temperature calculated by the one-dimensional solver for case T123.

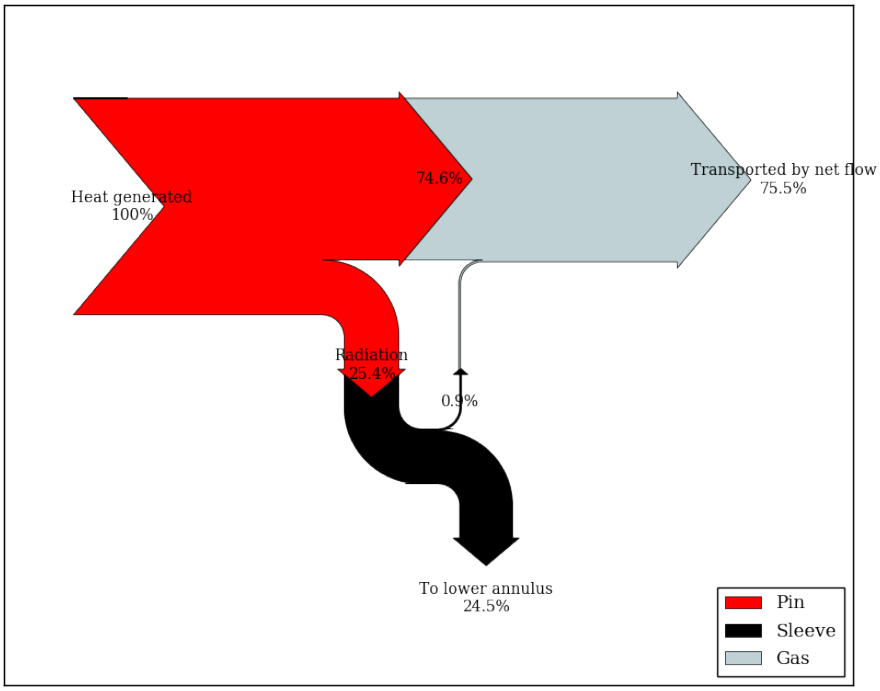

Figure 6.66: Heat removal paths for case T123 at steady state.

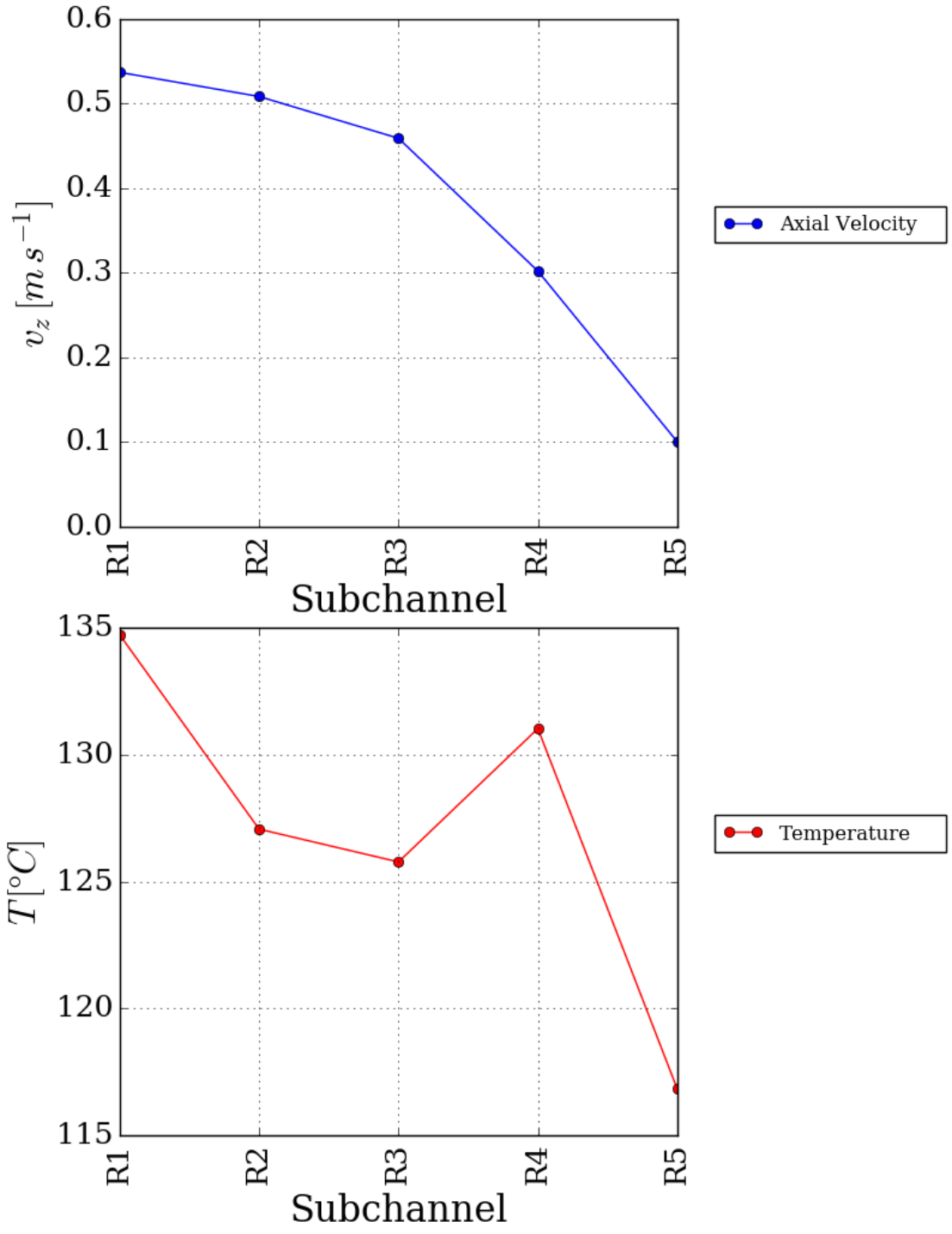

Figure 6.67: Predictions of sub-channel averages obtained with POSTR for case T123 at $z = 0.5H$.

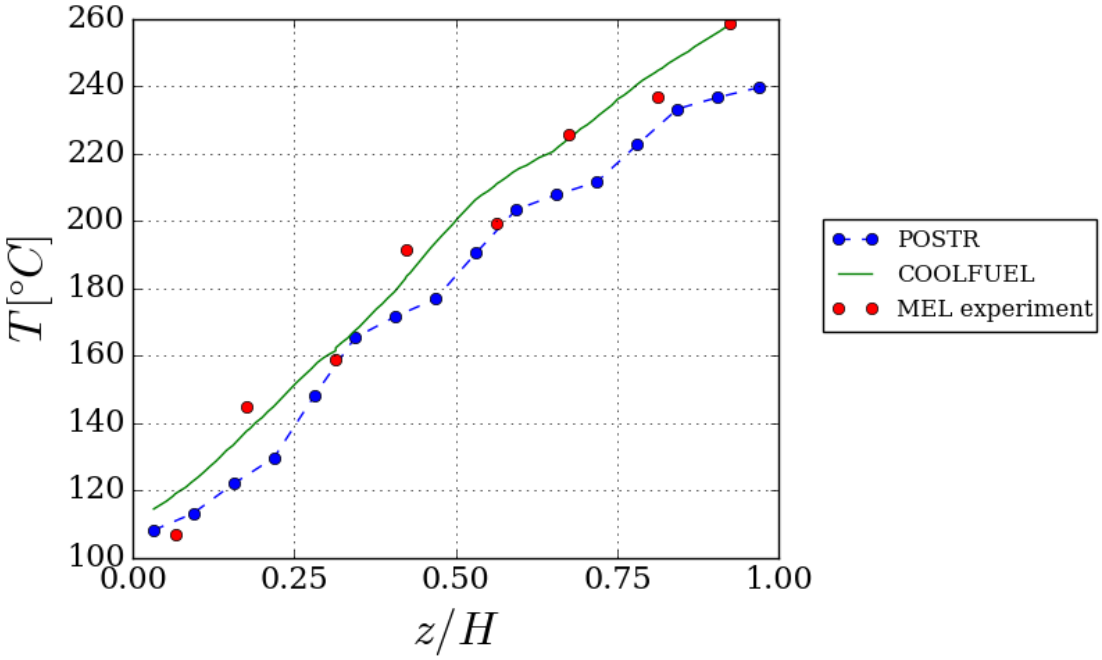

Figure 6.68: Predictions of maximum cladding temperature at different height in the first rank of pins, obtained with POSTR for case T123.

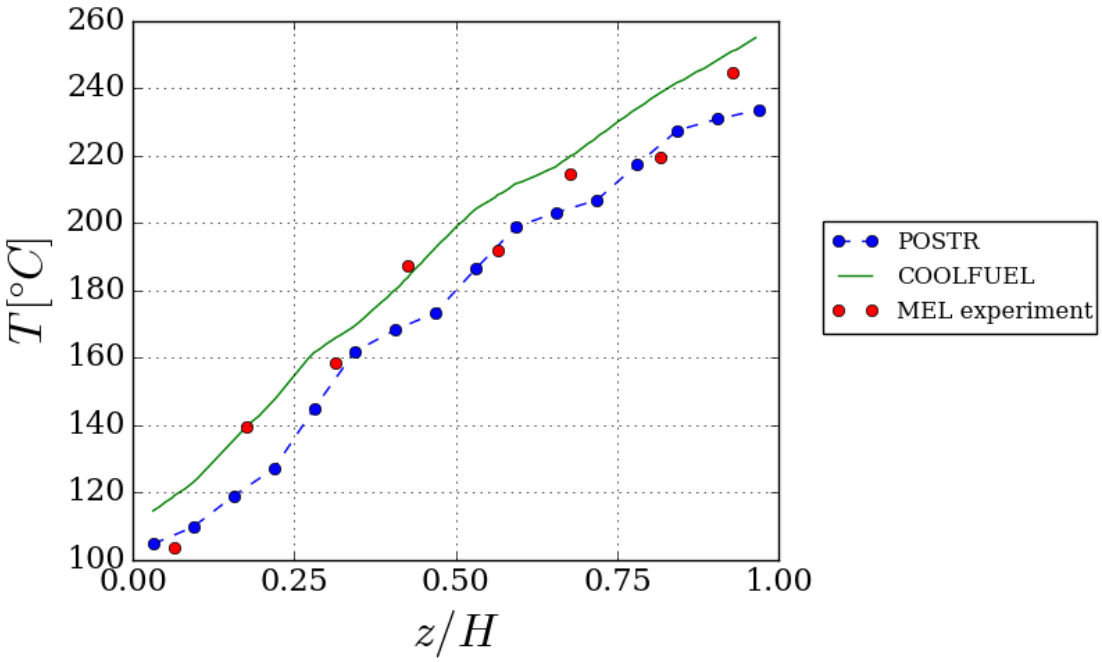

Figure 6.69: Predictions of maximum cladding temperature at different height in the second rank of pins, obtained with POSTR for case T123.

Figure 6.71 shows the stringer mass flow rate and the average gas temperature in the lower annulus predicted by the one-dimensional network solver at each time step. The value predicted for the mass flow rate is $0.006\,\mathrm{kg\,s^{-1}}$ which is higher than the measured value but within the uncertainty associated with it. As evident from Figure 6.72, thermal radiation remover as much as $44.37\,\%$ of the heat generated in the pins, a further increase from its contribution in case T123. Contrary to the other scenarios, this case benefits from the contribution of the internal circulation to the cooling of the stringer, with $15\,\%$ of the heat generated transferred from the gas to the sleeve and removed through it.

The profiles for the sub-channel axial velocity and temperature are shown in Figure 6.73. They show evident similarities in shape with those presented for Test 123, as an effect of the buoyancy forces acting on the flow. However, their increased relative influence is signalled by the negative velocities observed in the two outermost sub-channels, which signals the appearance of significant recirculation inside the stringer.

In Figures 6.74, 6.75 and 6.76 the clad temperatures predicted by POSTR are compared with the experimental data and the results obtained with COOLFUEL-3D. The three sets of data are in good agreement with each other, with the biggest difference occurring at the extremities of the bundle: the discrepancies are in the range $-17.17\,^{\circ}\mathrm{C}$ to $18.45\,^{\circ}\mathrm{C}$ for Rank 1, $-17.70\,^{\circ}\mathrm{C}$ to $7.09\,^{\circ}\mathrm{C}$ for Rank 2 and $-17.18\,^{\circ}\mathrm{C}$ to $8.92\,^{\circ}\mathrm{C}$ for Rank 3. Note that the maximum temperature is under-predicted by both POSTR and COOLFUEL-3D, a lack of conservativity that must be taken into account in any analysis that employs the codes.

6.3.5 Concluding remarks

In this section the validation of POSTR using data from a reliable experiment was described. The configuration studied in the experiment were relevant for the flow conditions encountered during the extraction of spent fuel from the reactor channel.

For this case, POSTR consisted of a one-dimensional solver for the simulation of the overall loop of the test rig, coupled with the three-dimensional model for the stringer. The system was proved capable of calculating with good approximation the flow rate through the stringer and the heat removal through the graphite sleeve.

The pin surface temperatures predicted by POSTR were in good agreement with the experimental data and with the output of COOLFUEL-3D, with the exception of the forced convection-dominated case where POSTR's results were much closer to the measurements than the older code.

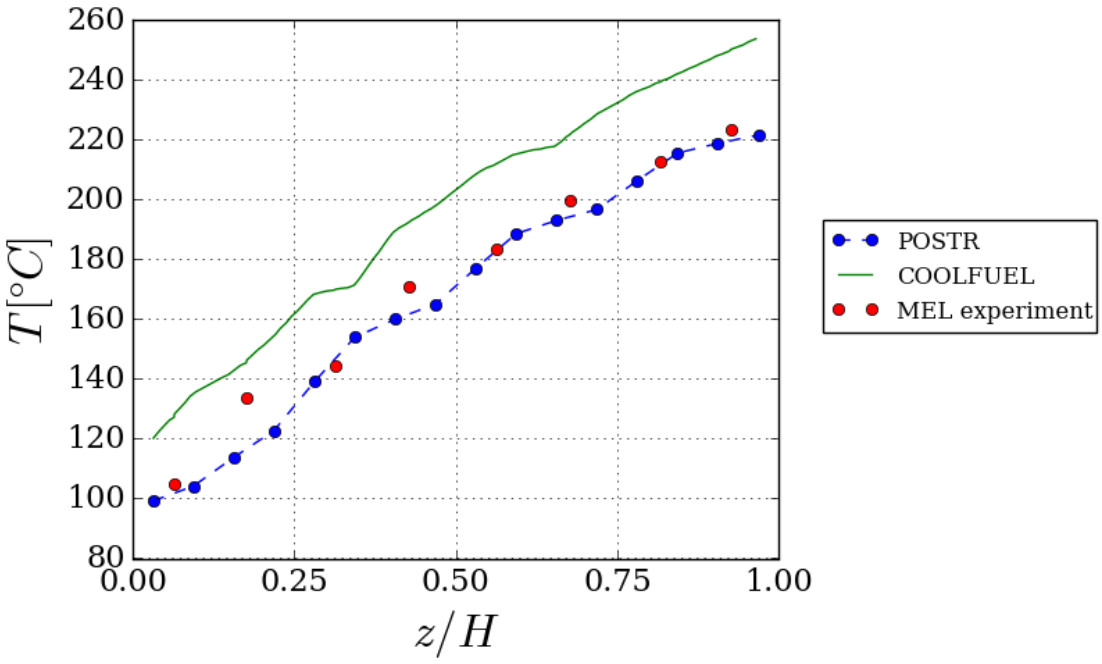

Figure 6.70: Predictions of maximum cladding temperature at different height in the third rank of pins, obtained with POSTR for case T123.

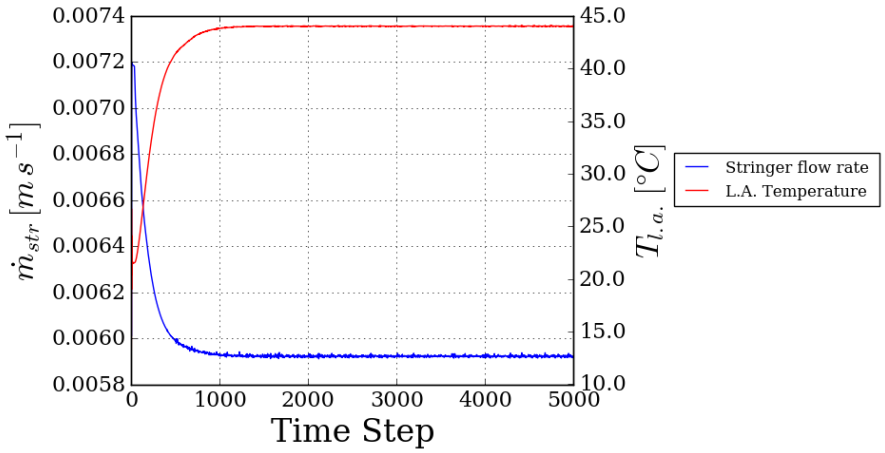

Figure 6.71: Convergence history of the stringer mass flow rate and the lower annulus temperature calculated by the one-dimensional solver for case T137.

6.4 Remarks on the usage of POSTR

In this chapter a series of usage cases for POSTR were presented. The results obtained were compared with the output of 'detailed' CFD simulations, the predictions of legacy software, and data from a large scale experiment. Satisfactory agreement was found in all scenarios, and the necessary caveats were pointed out for all the different cases.

An important problem highlighted in the discussion was the dependence of the calculation's results from the discretisation, in particular from the computational mesh used in the fluid domain. As a rule, when the scenario is dominated by forced convection, the results tend to converge to asymptotic values as the number of element increases. However, the simulations of buoyancy driven flows did not show a converging trend with increasingly fine meshes, which is not surprising given the nature of such flow. Natural convection calculations were also affected by oscillations of the computed variables in the fluid domain. Nevertheless, the model produced self-consistent results for the solid temperatures, which are ultimately the quantities of interest in refuelling cooling analyses.

Whenever reliable validation data are available it is recommended that a preliminary calibration study be performed on a selected mesh. Once the model is tuned for the application, the mesh should be kept fixed in all the studies simulated. An alternative approach could be based on a procedure similar to that followed in Section 6.2, with an analysis of the sensitivity of the results to the mesh employed.

In the calculations presented in this chapter, only the final fields were analysed, which made it possible to speed up the transients by defining a lower thermal capacity for the solid in the input for SYRTHES. This approach can be followed whenever only the steady state configuration of the system is of interest, since the thermal capacity will not affect the final temperature distribution. However, especially in buoyancy influenced scenarios, the analyst should verify that the temperature oscillations the fluid domain are not transmitted to the solid, in which case a higher thermal inertia should be imposed to dampen the fluctuations in the solid temperature.

On the whole, the results obtained built confidence in the capabilities of POSTR as a supporting tool for refuelling cooling analysis. It is the author's hope that the model will be successfully employed in the industrial practice, as a mean to estimate the degree of conservativity of the reliable and well-validated methodology currently followed.

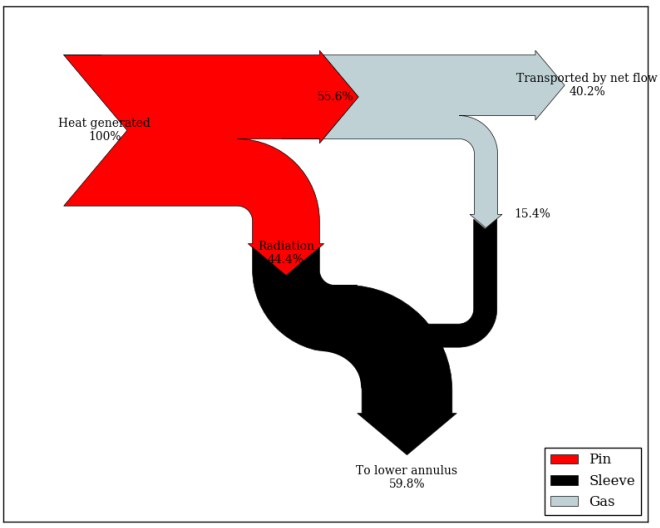

Figure 6.72: Heat removal paths for case T137 at steady state.

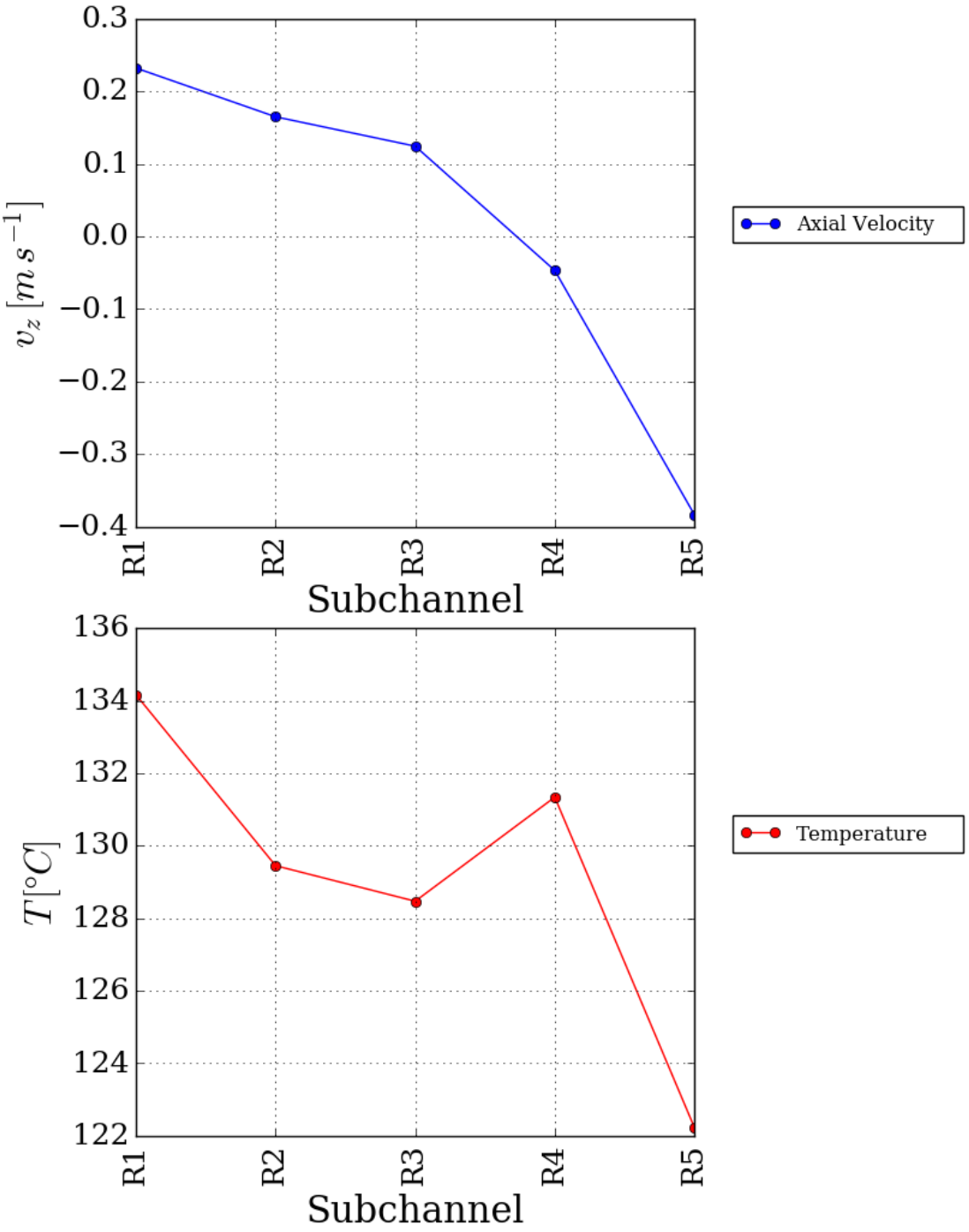

Figure 6.73: Predictions of sub-channel averages obtained with POSTR for case T137 at $z = 0.5H$.

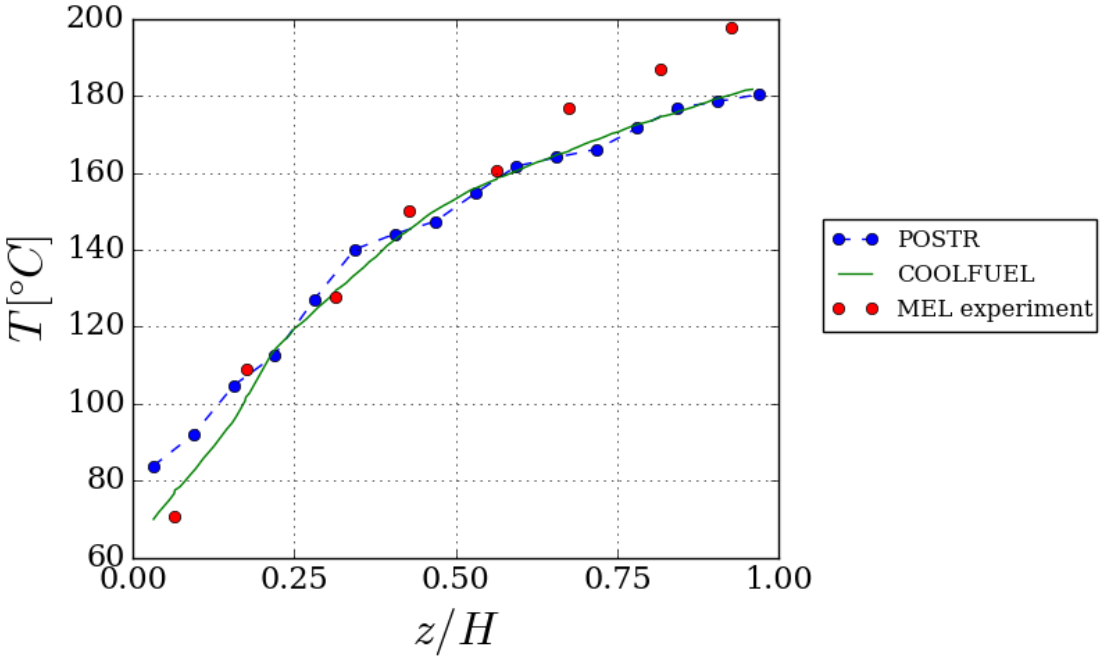

Figure 6.74: Predictions of maximum cladding temperature at different height in the first rank of pins, obtained with POSTR for case T137.

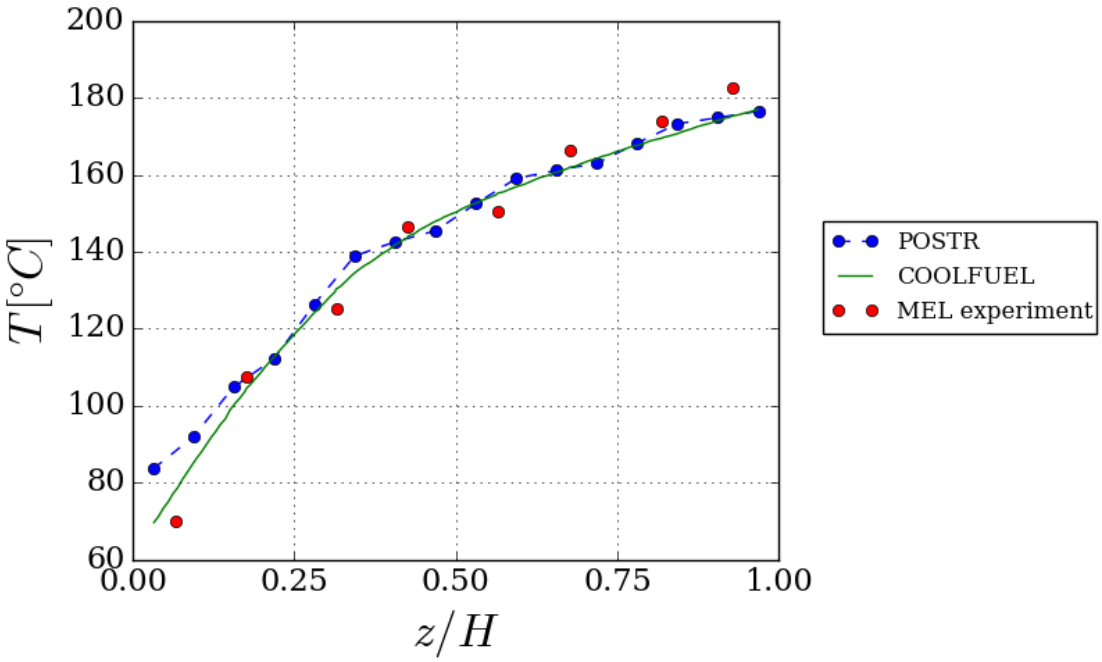

Figure 6.75: Predictions of maximum cladding temperature at different height in the second rank of pins, obtained with POSTR for case T137.

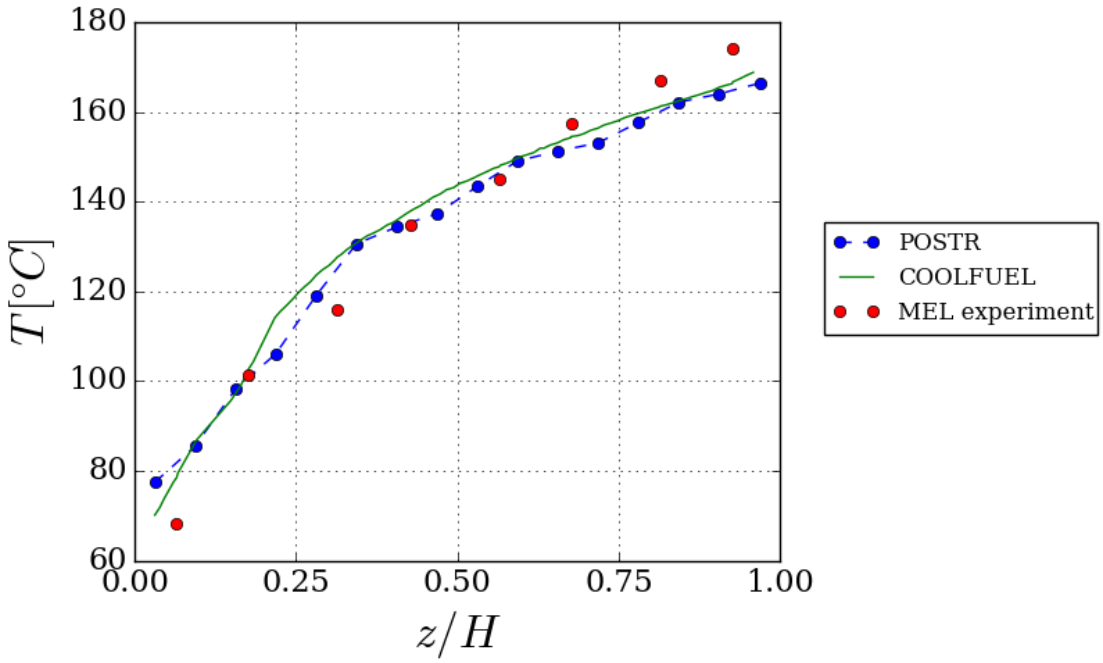

Figure 6.76: Predictions of maximum cladding temperature at different height in the third rank of pins, obtained with POSTR for case T137.

Conclusions and recommendations for future work

Summary

The work presented in this study was motivated by the lack of three-dimensional models for the simulation of the cooling of AGR fuel stringers during refuelling operations. Accurate knowledge of the temperatures of safety relevant components is of paramount importance for safety analysis, particularly in the stages of the fuel root encountered between the extraction of the stringer from the reactor and its dismantling in the Irradiated Fuel Disposal cell, when the heat generated by radioactive decay is significant.

The current industrial practice is based on well validated and reliable one-dimensional codes, which have been used successfully for decades. However, a known problem of this methodology is that it tends to predict excessively conservative temperatures in scenarios characterised by very low net flow rate through the stringer due to its inability to take into account three-dimensional phenomena such as buoyancy driven internal circulation. The project herein discussed aimed at contributing to the solution of this problem following two paths:

- By investigating natural convection in an enclosed fuel bundle, to gain an insight on the flow phenomena that may occur in scenarios relevant for refuelling cooling.

- By developing a numerical tool to support the analysis when three-dimensional effects contribute significantly decay heat removal.

The first approach was pursued using traditional CFD techniques, which used LES and RANS techniques on a body fitted mesh to resolve the details of the flow in a simplified geometry. The second methodology was based on the porous medium approximation, in order to reduce the computational size of the problem and make the tool developed suitable for routine calculations in industry. A summary of the outcomes of the two lines of work is given below.

Simulation of natural convection in an enclosed pin bundle

LES and RANS simulations of buoyancy driven flow in an enclosed fuel bundle were performed. The domain considered was modelled after the AGR fuel element for what concerned the disposition of the pins, although its height was reduced to $250\,\mathrm{mm}$, or about one fourth of the real-life fuel element, and no roughness was accounted for at the surface of the pins. The calculations and their results are described in Chapter 4.

The flow pattern observed in the Large Eddy Simulations was characterised by a Boundary Layer flow regime, with significant fluid motion close to the domain's boundary and a stagnant core region. Intense turbulence was found along the pins and the sleeve. Instabilities along the former were found took the form of upward travelling waves. Turbulent mixing was also observed at the bottom of the sleeve, where the descending flow impinges on the domain's floor.

The calculations showed that the profiles of axial velocity, temperature and turbulent kinetic energy do not change appreciably with the axial position, i.e. they become spatially fully developed except for the two regions at the bottom and the top of the domain, where they are formed or destroyed.

Correlations for the dependence of the Nusselt number on the Rayleigh number were obtained using two different formulations. In the first formulation the space between the pins were treated as tall rectangular enclosures, and the similarity between the correlations obtained for the two geometries was pointed out. The second formulation was based on a sub-channel approach, similar to that adopted in the development of the tool described in the next Section. This methodology was corroborated by the finding that the values of Nu in different sub-channels at different axial positions were accurately fitted by the same correlation.

Development of a numerical tool for refuelling cooling calculations

A numerical tool based on the porous medium approximation, named POSTR, was developed to support refuelling cooling calculations in scenarios where three-dimensional phenomena cannot be neglected. Its underlying model is described in Chapter 5, while its capabilities are demonstrated and validated in Chapter 6. The tool comprises of a set of subroutines for the CFD solver Code_Saturne, tasked with the simulation of the fluid domain, and a pre-compiled modified version of the finite element solver SYRTHES, for calculations of thermal conduction and radiation in the solid components.

The use of the porous medium approximations allows one to avoid resolving the real geometry of the space between the pins with a body fitted mesh, making it possible to use a much coarser mesh than would otherwise be necessary. The methodology adopted is based on a two-scale approach. The smallest scale is represented by the computational

mesh, used by Code_Saturne, for the solution of the governing equation. At the largest scale a filtering mesh, made coincident with the division of the bundle in sub-channels, is used to calculate the relevant geometric quantities, such as porosity and hydraulic diameter, and the source terms representing the interactions between the gas and the fuel. These source terms are computed using empirical correlations for the friction factor and the Nusselt number.

Conduction within the solid components, and radiative heat transfer between their surfaces is also included in the model. The fluid and solid domains are coupled to take into account their mutual interactions. For components such as the sleeve and the guide tube, this was carried out using the existing infrastructure provided by the solvers. For what concerns the pins, which are not resolved by the fluid mesh, an alternative methodology was implemented, which linked the thermal source term in the fluid domain to the boundary condition on the cladding surface in the solid domain.

The performances of the tool were first compared with those of traditional CFD simulations using body fitted meshes, referred to as the 'detailed' model (Section 6.1). Albeit small discrepancies were observed in the predictions of the solid temperatures, the overall agreement between the calculations was considered satisfactory.

A comparison between the predictions of POSTR and those of other software used in refuelling cooling calculations for a scenario of natural convection in an isolated fuel stringer is presented in Section 6.2. Despite the issues of stability and mesh dependence which were found to affect the model, the predictions compared well with those of the other codes.

Finally, a validation of the model using data from a large scale experiment is described in 6.3. The three-dimensional model for the fuel stringer, used to calculate the net flow rate cooling the fuel, was coupled with a one-dimensional network to model the rest of the test rig. The results were in good agreement with the measurements and with the predictions of a legacy code.

The test cases allowed to draw some recommendations on the usage of the tool, and demonstrated the potential of POSTR as a supporting tool for refuelling cooling analysis, to be used alongside the available tools to estimate the degree of conservativity which results from neglecting three-dimensional phenomena.

Recommendations for future research

Both lines of work summarised in the previous sections offer potential for additional work, to further the understanding of buoyancy driven flows along bundles of fuel pins and to perfect and extend the numerical tool developed. In this section, an attempt is

made to suggest potential extensions of the work described in this Thesis.

The 'detailed' calculations presented in Chapter 4 were limited to a single value for the heat flux from the pins, and were carried out in a domain which represented a small portion of the AGR fuel element. Also, the geometry of the pins was considerably simplified by neglecting the presence of the ribs on the cladding surface. Possible suggestions for further work can then be listed as follows:

- Extending the range of heat fluxes simulated. A hypothesis, based on the work of Elder[56] on simpler geometries, could be made to suggest that with increasing Rayleigh number the flow pattern observed, where instabilities are found in the form of travelling waves, would transition to a fully turbulent regime. Future research can be aimed at verifying or disproving this hypothesis.

- Investigating the effect of the height of the domain.

- Investigating the effect of the roughness of the pins. Since the actual geometry of the ribs would make the generation of the computational domain challenging, certain simplification may be adopted.

For what concerns POSTR, a number of possible extensions could be suggested:

- Extending the model to allow for the simulation of the cooling of damaged fuel, particularly following a handling incident resulting in a dropped stringer. This work has already been started within the Heat, Flow and Turbulence Research Group at the University of Sheffield.

- Coupling the three-dimensional model with a general purpose one-dimensional network solver, to make it possible to simulate more scenarios such as the one described in Section 6.3.

- Implement the capability to model spacers, braces and other obstructions to the flow through the stringer.

- Explicitly evaluate the tie bar temperature distribution, which is very important for refuelling cooling analysis. The effect of potential blockage of the tie bar and guide tube annulus should also be included in the investigation.

- Adopt advanced Coarse Mesh CFD methodologies to predict the details of the flow with a higher degree of accuracy.

Bibliography

[1] IEA. *World Energy Outlook 2018 Executive Summary*. 2018. URL: http://goo.gl/VYKGca.

[2] J. Worland. *What to Know About the Historic 'Paris Agreement' on Climate Change*. 2015. URL: http://goo.gl/dEZasP.

[3] H. M. Government. *The Clean Growth Strategy - Leading the way to a low carbon future*. 2017. URL: http://goo.gl/szuMKT.

[4] H. M. Government. *Industrial Strategy - Building a Britain fit for the future*. 2017. URL: http://goo.gl/LLEAZJ.

[5] H. M. Government. *Industrial Strategy - Nuclear Sector Deal*. 2018. URL: http://goo.gl/q8bmzh.

[6] J. W. Dawson and M. Phillips. "Gas-cooled Nuclear Reactor Designs, Operation and Fuel Cycle". In: I. Crossland. *Nuclear Fuel Cycle Science and Engineering*. 2012.

[7] E. Nonbøl. *Description of the Advanced Gas Cooled Type of Reactor (AGR)*. Tech. Report. NKS, 1996.

[8] M. Clark. *Fuel Route System Course*. Training Material. EDF Energy, 2012.

[9] A. Keshmiri. "Three-dimensional simulation of a simplified advanced gas-cooled reactor fuel element". In: *Nuclear Engineering and Design* 241.10 (2011), pp. 4122–4135.

[10] M. Yule. *Refuelling Cooling Safety Case Head Document*. Tech. Report. EDF Energy, 2014.

[11] M.-T. R. Fung. *CoolFuel 3-D V2 Modelling Report*. Tech. rep. NNC, 1995.

[12] C. Boyd. "Perspectives on CFD analysis in nuclear reactor regulation". In: *Nuclear Engineering and Design* (2015).

[13] T. Höhne, E. Krepper, and U. Rohde. *Application of CFD Codes in Nuclear Reactor Safety Analysis*. 2010.

[14] M. Scheuerer et al. *ECORA - Condensed Final Summary Report*. Tech. rep. ECORA, 2005.

[15] M. Scheuerer et al. "Evaluation of computational fluid dynamic methods for reactor safety analysis (ECORA)". In: *Nuclear Engineering and Design* 235.2 - 4 (2005), pp. 359–368.

[16] G. Zigh and J. Solis. *Computational Fluid Dynamics Best Practice Guidelines for Dry Cask Applications: Final Report*. Tech. rep. NRC, 2013.

[17] M. Reocreux. "Present Status and Prospective of CFD Code Use in Nuclear Safety Applications". In: *Technical Meeting on Use of Computational Fluid Dynamics (CFD Codes for Safety Analysis of Reactor Systems, including Containment)*. Ed. by IAEA. 2002.

[18] IAEA, ed. *Use of computational fluid dynamics codes for safety analysis of nuclear reactor systems*. International Atomic Energy Agency TECDOC-1379. Nov. 2003.

[19] F. Menter et al. *CFD Best Practice Guidelines for CFD Code Validation for Reactor Safety Applications*. Tech. rep. ECORA, 2002.

[20] U. Rohde et al. "Fluid mixing and flow distribution in a primary circuit of a nuclear pressurized water reactor - Validation of CFD codes". In: *Nuclear Engineering and Design* 237.15 - 17 (2007). NURETH-1111th International Topical Meeting on Nuclear Reactor Thermal Hydraulics, pp. 1639–1655.

[21] N. E. Todreas and M. S. Kazimi. *Nuclear Systems Volume I: Thermal Hydraulic Fundamentals, Second Edition*. CRC Press, 1990.

[22] C. Rapley and A. Gosman. "The prediction of fully developed axial turbulent flow in rod bundles". In: *Nuclear Engineering and Design* 97.3 (1986), pp. 313–325.

[23] E. Baglietto, H. Ninokata, and T. Misawa. "CFD and DNS methodologies development for fuel bundle simulations". In: *Nuclear Engineering and Design* 236.14-16 (2006). 13th International Conference on Nuclear Energy13th International Conference on Nuclear Energy, pp. 1503–1510.

[24] K. B. Lee and H. C. Jang. "A numerical prediction on the turbulent flow in closely spaced bare rod arrays by a nonlinear $k - \varepsilon$ model". In: *Nuclear Engineering and Design* 172.3 (1997), pp. 351–357.

[25] E. Baglietto and H. Ninokata. "A turbulence model study for simulating flow inside tight lattice rod bundles". In: *Nuclear Engineering and Design* 235.7 (2005), pp. 773–784.

[26] D. Chang and S. Tavoularis. "Numerical simulation of turbulent flow in a 37-rod bundle". In: *Nuclear Engineering and Design* 237.6 (2007), pp. 575–590.

[27] F. Abbasian, S. Yu, and J. Cao. “Experimental and numerical investigations of three-dimensional turbulent flow of water surrounding a CANDU simulation fuel bundle structure inside a channel”. In: *Nuclear Engineering and Design* 239.11 (Nov. 2009), pp. 2224–2235.

[28] S. Benhamadouche. “On the use of (U)RANS and LES approaches for turbulent incompressible single phase flows in nuclear engineering applications”. In: *Nuclear Engineering and Design* 312 (2017). 16th International Topical Meeting on Nuclear Reactor Thermal Hydraulics, pp. 2–11.

[29] E. Merzari et al. “Large-scale large eddy simulation of nuclear reactor flows: Issues and perspectives”. In: *Nuclear Engineering and Design* 312 (2017). 16th International Topical Meeting on Nuclear Reactor Thermal Hydraulics, pp. 86–98.

[30] X. Zhang and S. Yu. “Large eddy simulation of turbulent flow surrounding two simulated CANDU fuel bundles”. In: *Nuclear Engineering and Design* 241.9 (Sept. 2011), pp. 3553–3572.

[31] A. Bhattacharya, S. Yu, and G. Kawall. “Numerical simulation of turbulent flow through a 37-element CANDU fuel bundle”. In: *Annals of Nuclear Energy* 40.1 (Feb. 2012), pp. 87–105.

[32] D. Chang and S. Tavoularis. “Hybrid simulations of the near field of a split-vane spacer grid in a rod bundle”. In: *International Journal of Heat and Fluid Flow* 51.0 (2015). Theme special issue celebrating the 75th birthdays of Brian Launder and Kemo Hanjalic, pp. 151–165.

[33] S. He and J. Gotts. “A computational study of the effect of distortions of the moderator cooling channel of the Advanced Gas-cooled Reactor”. In: *Nuclear Engineering and Design* 235.9 (2005), pp. 965–982.

[34] A. Keshmiri et al. “Thermal-hydraulic analysis of flow in rib-roughened passages with application to gas-cooled nuclear reactors”. In: *Proceedings of the 6th International Symposium On Turbulence, Heat and Mass Transfer, ‘THMT’09’*. Sept. 2009.

[35] T. Masuoka and Y. Takatsu. “Turbulence model for flow through porous media”. In: *International Journal of Heat and Mass Transfer* 39.13 (Sept. 1996), pp. 2803–2809.

[36] D. Nield. “Comments on “turbulence model for flow through porous media”””. In: *International Journal of Heat and Mass Transfer* 40.10 (July 1997), p. 2499.

[37] A. Nakayama and F. Kuwahara. “A Macroscopic Turbulence Model for Flow in a Porous Medium”. In: *Journal of Fluids Engineering* 121.2 (1999), p. 427.

[38] M. H. Pedras and M. J. de Lemos. “Macroscopic turbulence modeling for incompressible flow through undeformable porous media”. In: *International Journal of Heat and Mass Transfer* 44.6 (2001), pp. 1081–1093.

[39] M. Chandesris, G. Serre, and P. Sagaut. “A macroscopic turbulence model for flow in porous media suited for channel, pipe and rod bundle flows”. In: *International Journal of Heat and Mass Transfer* 49.15–16 (2006), pp. 2739–2750.

[40] M. Drouin, O. Gregoire, and O. Simonin. “A consistent methodology for the derivation and calibration of a macroscopic turbulence model for flows in porous media”. In: *International Journal of Heat and Mass Transfer* 63 (2013), pp. 401–413.

[41] Y. Jin and A. V. Kuznetsov. “Turbulence modeling for flows in wall bounded porous media: An analysis based on direct numerical simulations”. In: *Physics of Fluid* 29 (2017).

[42] P. Chantelot. *Modelling of Dungeness B RHO D2 penetration*. Tech. rep. EDF Energy, 2014.

[43] D. Nield. “A note on the modeling of local thermal non-equilibrium in a structured porous medium”. In: *International Journal of Heat and Mass Transfer* 45.21 (2002), pp. 4367–4368.

[44] C. Fiorina et al. “GeN-Foam: a novel OpenFOAM® based multi-physics solver for 2D/3D transient analysis of nuclear reactors”. In: *Nuclear Engineering and Design* 294 (2015), pp. 24–37.

[45] L. Capone, S. Benhamadouche, and Y. A. Hassan. “Source terms modeling for spacer grids with mixing vanes for CFD simulations in nuclear reactors”. In: *Computers & Fluids* 126 (2016), pp. 141–152.

[46] K. T. Yang. “Natural Convection in Enclosures”. In: S. Kakaç, R. K. Shah, and W. Aung. *Handbook of Single-Phase Convective Heat Transfer*. 1987. Chap. 13.

[47] E. K. Glakpe, C. B. Watkins, and B. Kurien. “Solution of three-dimensional natural convection about a vertical square rod in a cylindrical enclosure”. In: *International Journal for Numerical Methods in Fluids* 7.2 (), pp. 155–173. eprint: `https://onlinelibrary.wiley.com/doi/pdf/10.1002/fld.1650070205`.

[48] D. Lu et al. “Experimental investigation on natural convection heat transfer characteristics of C-shape heating rods bundle used in PRHR HX”. In: *Annals of Nuclear Energy* 98 (2016), pp. 226–238.

[49] P. D. Weidman and G. Mehrdadtehranfar. “Instability of natural convection in a tall vertical annulus”. In: *The Physics of Fluids* 28.3 (1985), pp. 776–787. eprint: `https://aip.scitation.org/doi/pdf/10.1063/1.865045`.

[50] K. Hanjalić and S. Vasić. “Computation of turbulent natural convection in rectangular enclosures with an algebraic flux model”. In: *International Journal of Heat and Mass Transfer* 36.14 (1993), pp. 3603–3624.

[51] Z. Altaç and N. Uğurlubilek. “Assessment of turbulence models in natural convection from two- and three-dimensional rectangular enclosures”. In: *International Journal of Thermal Sciences* 107 (2016), pp. 237–246.

[52] P. Betts and I. Bokhari. “Experiments on turbulent natural convection in an enclosed tall cavity”. In: *International Journal of Heat and Fluid Flow* 21.6 (2000), pp. 675–683.

[53] A. Keshmiri, J. Uribe, and N. Shokri. “Benchmarking of Three Different CFD Codes in Simulating Natural, Forced, and Mixed Convection Flows”. In: 67 (June 2015).

[54] R. F. Bergholz. “Instability of steady natural convection in a vertical fluid layer”. In: *Journal of Fluid Mechanics* 84.4 (1978), pp. 743–768.

[55] M. Prud’homme and P. Le Quéré. “Stability of stratified natural convection in a tall vertical annular cavity”. In: *Physics of Fluids* 19.9 (2007), p. 094106. eprint: `https://doi.org/10.1063/1.2771260`.

[56] J. W. Elder. “Turbulent free convection in a vertical slot”. In: *Journal of Fluid Mechanics* 23.1 (1965), pp. 99–111.

[57] V. Lepiller et al. “Transition to turbulence in a tall annulus submitted to a radial temperature gradient”. In: *Physics of Fluids* 19.5 (2007), p. 054101. eprint: `https://doi.org/10.1063/1.2721756`.

[58] G. de Vahl Davis and R. W. Thomas. “Natural Convection between Concentric Vertical Cylinders”. In: *The Physics of Fluids* 12.12 (1969), pp. 198–207. eprint: `https://aip.scitation.org/doi/pdf/10.1063/1.1692437`.

[59] S. Wakitani. “Flow patterns of natural convection in an air-filled vertical cavity”. In: *Physics of Fluids* 10.8 (1998), pp. 1924–1928. eprint: `https://doi.org/10.1063/1.869708`.

[60] P. Venkata Reddy and G. Narasimham. “Natural convection in a vertical annulus driven by a central heat generating rod”. In: *International Journal of Heat and Mass Transfer* 51.19 (2008), pp. 5024–5032.

[61] P. Venkata Reddy et al. “Non-Boussinésq conjugate natural convection in a vertical annulus”. In: *International Communications in Heat and Mass Transfer* 37.9 (2010), pp. 1230–1237.

[62] J. R. Senapati, S. K. Dash, and S. Roy. “Numerical investigation of natural convection heat transfer from vertical cylinder with annular fins”. In: *International Journal of Thermal Sciences* 111 (2017), pp. 146–159.

[63] M. Hudina. “Heat Removal by Natural Circulation in Gas-Cooled Rod-Bundles”. In: *Specialists’ Meeting on Heat Exchanging Components of Gas-Cooled Reactors*. Ed. by S. F. I. for Reactor Research. 1984.

[64] M. Keyhani, F. Kulacki, and R. Christensen. “Experimental investigation of free convection in a vertical rod bundle—a general correlation for nusselt numbers”. In: *Journal of Heat Transfer* 107.3 (Jan. 1985), pp. 611–623.

[65] M. S. El-Genk, B. Su, and Z. Guo. “Experimental studies of forced, combined and natural convection of water in vertical nine-rod bundles with a square lattice”. In: *International Journal of Heat and Mass Transfer* 36.9 (1993), pp. 2359–2374.

[66] M. Arshad, M. H. Inayat, and I. R. Chughtai. “Experimental study of natural convection heat transfer from an enclosed assembly of thin vertical cylinders”. In: *Applied Thermal Engineering* 31.1 (2011), pp. 20–27.

[67] F. Shafiq et al. “CFD study of natural convection heat transfer from an enclosed assembly of vertical cylinders”. In: *2017 14th International Bhurban Conference on Applied Sciences and Technology (IBCAST)*. Jan. 2017, pp. 519–522.

[68] M. Abdul Basit et al. “Computer simulation of natural convection heat transfer from an assembly of vertical cylinders of PARR-2”. In: *Applied Thermal Engineering* 27.1 (2007), pp. 194–201.

[69] Y. Rao and E. Glakpe. “Three-Dimensional Natural Convection in a Rod Bundle – a Numerical Study in Boundary Fitted Coordinates”. In: *Numerical Methods in Thermal Problems* VII (1991), pp. 446–456.

[70] Y. Rao and E. Glakpe. “Three-dimensional natural convection in an enclosed vertical rod bundle with mixed boundary conditions”. In: *International Journal of Heat and Mass Transfer* 36.6 (1993), pp. 1517–1528.

[71] K. Hata, K. Fukuda, and T. Mizuuchi. “Natural convection heat transfer from vertical rod bundles in liquid sodium”. In: (Feb. 2016).

[72] J. H. Ferziger and M. Perić. *Computational Methods for Fluid Dynamics*. Springer, 1996.

[73] EDF. *Code Saturne 4.0.1 Theory Guide*. 2015.

[74] S. B. Pope. *Turbulent Flows*. Cambridge University Press, 2000.

[75] M. Ciofalo. “La turbolenza e i suoi modelli”. In Italian. In: G. Comini, G. Croce, and E. Nobile. *Fondamenti di termofluidodinamica computazionale*. 2008. Chap. 4.

[76] F. Ducros, F. Nicoud, and T. Poinsot. “Wall-Adapting Local Eddy-Viscosity Models for Simulations in Complex Geometries”. In: *Numerical Methods for Fluid Dynamics VI* (Jan. 1998).

[77] F. Nicoud and F. Ducros. “Subgrid-Scale Stress Modelling Based on the Square of the Velocity Gradient Tensor”. In: *Flow, Turbulence and Combustion* 62.3 (Sept. 1999), pp. 183–200.

[78] N. E. Todreas and M. S. Kazimi. *Nuclear Systems Volume II: Elements of Thermal Hydraulic Design, Second Edition*. CRC Press, 1990.

[79] M. H. Pedras and M. J. de Lemos. “On the definition of turbulent kinetic energy for flow in porous media”. In: *International Communications in Heat and Mass Transfer* 27.2 (2000), pp. 211–220.

[80] EDF. *Code Saturne Version 4.0.1 Practical User’s Guide*. 2015.

[81] EDF. *Code Saturne 5.0.0 Theory Guide*. 2017.

[82] C. Peniguel and I. Rupp. *SYRTHES 3.4 - Manuel Thèorique*. In French. 2012.

[83] I. Rupp and C. Peniguel. *SYRTHES 4.2 -User Manual*. 2014.

[84] EDF, CEA, and Open Cascade. *SALOME - The Open Source Integration Platform for Numerical Simulation*. 2005-2016. URL: `http://www.salome-platform.org`.

[85] F. P. Incropera and D. P. DeWitt. *Introduction to Heat Transfer*. Wiley, 1996.

[86] I. B. Celik, Z. N. Cehreli, and I. Yavuz. “Index of Resolution Quality for Large Eddy Simulations”. In: *Journal of Fluids Engineering* 127.5 (Sept. 2005), pp. 949–958.

[87] I. Celik, M. Klein, and J. Janicka. “Assessment Measures for Engineering LES Applications”. In: *Journal of Fluids Engineering* 131.3 (Feb. 2009).

[88] E. Romero. *Cooling of AGR Fuel Elements by Angled and Cross Flows - Correlations for Heat Transfer and Flow Losses*. Tech. rep. Nuclear Electric, 1994.

[89] A. A. Žukauskas. “Convective Heat Transfer in Cross Flow”. In: S. Kakaç, R. K. Shah, and W. Aung. *Handbook of Single-Phase Convective Heat Transfer*. 1987. Chap. 6.

[90] J. O. Hinze. *Turbulence*. 1975.

[91] D. Moore. *The Validation of CoolFuel-3D V2 for Low-Power Refuelling Using MEL Data*. Tech. rep. NNC, 1995.

[92] M. Nordlund et al. “Improved PISO algorithms for modeling density varying flow in conjugate fluid–porous domains”. In: *Journal of Computational Physics* 306 (2016), pp. 199–215.

[93] K. Chinembiri et al. “Numerical study of heat transfer in a distorted rod bundle”. In: *Nuclear Engineering and Design* (2018 - Under Review).

[94] R. Hornby and M.-T. R. F. Fung. *Torness/Heysham 2 low power refuelling* - COOLFUEL *modelling of stringer nosebrush in reactor standpipe faults.* Tech. rep. NNC, 1994.

[95] C. Trinca. POSTR*: guide to source code and simulation set-up*. 2018.

[96] E. Romero. *Cooling of Dropped AGR Fuel Element - Specification of Correlations for Buoyancy Free Heat Transfer and Flow Losses - Axial Flows*. Tech. rep. Nuclear Electric, 1994.

[97] G. A. Brown and J. Scriven. *Cross Flow Friction Factor Review*. Tech. rep. Nuclear Electric, 1992.

Appendix A

Implementation of POSTR

Foreword

This appendix is a condensed version of *POSTR: guide to source code and simulation set-up*,[95] an internal report for the use of EDF Energy and the Heat Flow and Turbulence Research Group of the University of Sheffield, which was meant as a guide for the analyst and the programmer who will use and extend the collection of scripts and patches for Code_Saturne and SYRTHES, collectively named POSTR. The following typographic conventions are used in the rest of the appendix:

- sans-serif fonts are used for the names of variables.
- `typewriter style` fonts are used for the names of subroutines.
- SMALL CAPITAL fonts are used for the names of modules and libraries.
- **bold face** fonts are used for the names of files.

A.1 Overview

POSTR is the working name given to the implementation of a computational model for the AGR fuel stringer using Code_Saturne and SYRTHES. The model is based on the assumption that the fuel pin bundle can be approximated as a porous matrix and its effect on the flow modelled by means of source terms for the momentum and energy equations. The simulations for the fluid and the solid domains are coupled to model their mutual interactions.

The source code of POSTR is contained in 16 files for Code_Saturne and in 7 files for SYRTHES, excluding from the count the modifications to header files and files specifically

modified for a specific scenario. The subroutine for Code_Saturne are written in Fortran and C, while those for SYRTHES are exclusively written in C.

The files for Code_Saturne are included in the case directory during the set-up of the study, and compiled before each calculation run. They contain parameters and flags that must be edited by the user according to the particular case under study.

The modifications made on SYRTHES, which required changes in some function definitions, made them incompatible with the main branch of the code and barred the possibility of compiling them before each run. A pre-compiled version of SYRTHES is therefore used in the code.

It is worth defining here some terms that will be used frequently in the following, in order to prevent ambiguities in the description:

Field indicates arrays in which the properties and variables are stored for each cell of the computational mesh. They can be accessed through pointers from every subroutine in Code_Saturne, except for the very early stage of the simulation, before their initialisation. They are the principal mean through which information is made available in Code_Saturne.

Sub-channel is used as a synonym of 'filtering block', that is a control volume within which the governing equations are filtered. In each simulation, the fluid domain is divided radially, azimuthally and axially by a grid of filtering blocks. Each of them encloses several cells of the computational mesh. All the modelled quantities are calculated on this scale and distributed among the cells contained in each block. Each sub-channel is identified by an identification number, used to associate each computational cell to a filtering block. This information is contained in a 'field': cells belonging to the same sub-channel will be associated with the same identification number. Note that the use of fields to store information implies that all data are associated with the cells of the computational mesh. Nonetheless, in the following, variables and properties having the same value in all cells belonging to the same sub-channel will be referred to as 'sub-channel values', whilst the phrase 'local values' will be used for quantities that can vary within the block.

Region refers to a portion of the domain, encompassing one or more sub-channels, which represent a particular component or section of the circuit. For many calculations only the fuel region is defined.

A.2 Code_Saturne subroutines

The part of the source code of POSTR concerning is distributed in sixteen files. Of these, eleven contain 'user subroutines', specifically designed to house custom code:

- **cs_user_modules.f90** contains a set of subroutines and variables used by the other subroutines, which carry out the bulk of the calculations required by the model.
- **cs_user_parameters.f90**, where the porous treatment and other solver options are activated.
- **cs_user_parameters.c**, where additional fields for the properties which are specific to the model are defined.
- **cs_user_extra_operations.f90**, which is called at the end of every time step and contains calls to subroutines that update the model specific fields.
- **cs_user_porosity.f90**, where the porosity field is defined.
- **cs_user_source_terms.f90**, where the flow resistance due to the solid components is imposed.
- **cs_user_physical_properties.f90**, where the turbulence model is implemented and the properties variations are taken into account.
- **cs_user_coupling.c** where the coupling with SYRTHES is established.
- **cs_user_boundary_conditions.f90**, which is used to impose thermal boundary conditions on the no-shear walls and for coupling with the one-dimensional solver.
- **usvosy.f90**, where the heat transfer coefficient between the coolant and the pins is defined.
- **cs_user_postprocess_var.f90**, which instruct the code to write useful information in the output files.

The remaining five are parts of Code_Saturne's main source code related to the coupling with SYRTHES, although they are compiled in the same way as the previous group. They are edited to implement the new volume coupling method or for minor modifications to the surface coupling:

- **cptssy.f90** calculates the source terms originated by the volume coupling. It is modified to use sub-channel quantities instead of local values.

- **cpvosy.f90** initiates the communication with SYRTHES for the volume coupling. It is modified to use sub-channel quantities instead of local values.

- **cs_syr4_coupling.c** contains the functions used to communicate with SYRTHES. The principal modifications to the coupling methodology are implemented in this file.

- **coupbi.f90** receives information from SYRTHES in the surface coupling. It is modified to store the wall temperature for use in the near-wall turbulence treatment.

- **coupbo.f90** sends information to SYRTHES in the surface coupling. It is modified to correct the heat transfer coefficient used in the surface coupling by multiplying it by the porosity in the near-wall cells.

In the following, a description of the subroutines that form the source code is given. For the sake of clarity, the subroutines will be divided in seven groups, according to the role they play in the model.

A.2.1 Geometric definition of the domain

This group comprises the subroutines involved in the definition of the distribution of the sub-channel porosity and hydraulic diameter. One can assign to this category the subroutines `compute_porosity` and `compute_hydr_diameter` in **cs_user_modules.f90**, and `usporo` in **cs_user_porosity.f90**.

The subroutine `compute_porosity` takes its name from the tasks it had in an early version of the code, where the porosity field was calculated at the beginning of the simulation using a numerical method. In the current version, the porosity field is computed using an external script and stored in an input file whose name is defined by the parameter solid_volume_filename. The file contains a table of six columns and one row for each cell of the computational mesh. Each row stores:

- The coordinates of the cells, in the first three columns.

- The porosity in the cells, in the fourth column.

- An identification number indicating the block of the filtering mesh that contains the cell, in the fifth column.

- An identification number indicating the domain region that contains the cell, in the sixth column.

Note that, although the porosity is indicated for every cell, it can only vary between different filtering blocks: cells having the same value on the fifth column will have the same porosity. After reading the file, the subroutine sums the volumes of all the cells associated to a filtering block. The block volumes are then stored into a field and used at other stages in the calculation.

The subroutine `compute_porosity` is invoked rather early in the execution of the solver, before the initialization of the arrays ('fields') that store and make available the properties values in Code_Saturne. For this reason, the values read from the input file are stored in a temporary array, and are then copied in the field by `usporo`.

The calculation of the sub-channel hydraulic diameter is carried out in subroutine `compute_hydr_diameter`. The calculation is based on the observation that, when the cross-section is axially uniform, one can write the hydraulic diameter as:

$$D_h = \frac{4A_f}{P_w} \cdot \frac{\Delta z}{\Delta z} = \frac{4V_f}{A_w} \tag{A.1}$$

where the subscript f refers to the area or volume occupied by the fluid, and the subscript w indicates the wet perimeter or surface. A similar expression can be given for the equivalent diameter for heat transfer, replacing the wet area with that of the heated surfaces.

By definition, the volume occupied by the fluid in the sub-channel is the volume of the filter block multiplied by the porosity. For what concerns the wet area, one should distinguish between the boundaries of the domain (sleeve and guide tube walls) and the pin walls. The former are calculated as sums of the areas of the boundary facelet wet by a given sub-channel, which are accessible internally. The latter must be provided externally: depending from the value of the flag areas_from_syrthes, the values communicated by SYRTHES can be employed, or they can be read from an input file similar to the one used for the porosity. The latter option is not recommended, save for debugging purposes.

At the end of the subroutine, the values calculated for the hydraulic and equivalent diameter and for the boundary and pins wall areas are stored in separate fields to be accessed in the following calculations.

A.2.2 Characterisation of the sub-channel flow

This group includes the subroutines for the calculation of the sub-channel averages of the flow variables and physical properties, as well as the non-dimensional numbers used in the correlations. They are all included in **cs_user_modules.f90**:

- `compute_reynolds_number`.

- `compute_reynolds_number_magnitude`.
- `compute_grashof_number`.
- `compute_grashof_number_boundary`.
- `average_velocity_in_filter`.
- `average_temperature_in_filter`.
- `average_wall_temperature_in_filter`.
- `average_properties_in_filter`.

The names of the subroutines are self explanatory, and their algorithms are relatively straight-forward. Nevertheless, a few comments may be useful:

- Since all the quantities calculated here are based on the sub-channels, the values calculated will be the same for all the cells belonging to the same filtering block.
- `compute_reynolds_number` uses the axial velocity to calculate the Reynolds number, while `compute_reynolds_number_magnitude` uses the magnitude of the velocity vector. The latter is always used unless the influence of the cross-flow on the Nusselt number is explicitly suppressed by setting the value of the flag `crossflow_nusselt_calculation` as false. Both subroutines calculate two different fields for the Reynolds number, one based on the hydraulic diameter and one on the pins diameter.
- `compute_grashof_number` evaluate Gr based on the pins temperature, whilst its counterpart `compute_grashof_number_boundary` uses the boundary temperature.
- All the averaging subroutines calculate intrinsic averages, except for the wall temperature which is averaged on the wall area. The use of bulk averages would be more rigorous, but it would be more challenging to implement.

A.2.3 Calculation of flow resistance

This group contains the subroutines tasked with calculating the flow resistance due to the presence of the solid components and with distributing it throughout the fluid domain. It is formed by subroutine `ustsnv`, in file **cs_user_source_terms.f90**, and by a number of subroutines in module POSTR_KERNEL which implement the correlations for the friction factor.

The procedure followed in subroutine `ustsnv` aims at calculating the force exerted by the solid on the gas in each cell of the computational mesh. The force exerted by the pins, F_pins, and the force exerted by the boundary surfaces, F_boundary, are calculated using sub-channel averaged values of the flow variables and properties, and are distributed in the computational mesh according to the volume of the cells.

The force due to the pins, F_pins, is calculated as:

$$F_{pins} = \frac{1}{2} Eu_c \cdot \rho |\vec{v}|^2 V_{cell} \tag{A.2}$$

where $|\vec{v}|$ is the magnitude of the average sub-channel velocity, V_{cell} is the volume of the computational cell and the coefficient Eu_c, which has the dimensions of a loss coefficient per unit length, is obtained by blending the axial and cross-flow friction factors. It is calculated as:

$$Eu_c = \sqrt{\left(\frac{4 f_{ax}}{D_h} \cos^{14} \phi\right)^2 + \left(\Omega \frac{Eu_{cf}}{\text{Pitch}} \sin^{1.32} \phi\right)^2} \tag{A.3}$$

where f_{ax} is the axial friction factor, Eu_{cf} is the cross flow loss coefficient (or Euler number), $\phi = \arccos(v_z/|\vec{v}|)$ is the angle of the flow velocity with the axial direction, and Ω is a tuning coefficient introduced to make the expression a good approximation for both in-line and staggered arrays of pins.[88] The cross-flow loss coefficient is calculated using correlations for forced flow, under the assumption that, for undamaged fuel, buoyancy will affect exclusively the axial flow. The axial friction factor, on the other hand. It is calculated as:

$$f_{ax} = \frac{\tau_{ax,pins}}{\frac{1}{2}\rho |\vec{v}|} \tag{A.4}$$

In turn, $\tau_{ax,pins}$, i.e. the axial shear stress along the pins, is calculated by blending the contribution due to forced flow and that due to buoyancy:

$$\begin{aligned} \tau_{ax} &= \sqrt[3]{\tau_{ax,forced}^3 + \tau_{ax,buoy}^3} \\ \tau_{ax,forced} &= \frac{1}{2} C_{f,forced} \cdot \rho v_z |v_z| \\ \tau_{ax,buoy} &= \frac{1}{2} C_{f,buoy} \cdot \rho U_n |U_n| \end{aligned} \tag{A.5}$$

where v_z is the axial velocity, C_f is the Fanning friction factor and $U_n = \sqrt[3]{g\beta(T_w - T_f)\nu}$ is a reference buoyancy velocity.

The value calculated for F_pins must be projected on the three Cartesian directions. The value assigned to the i-th direction is given as:

$$F_{pins,i} = F_{pins} \cos \phi_i = \frac{1}{2} Eu_c \cdot \rho |\vec{v}| v_i V_{cell} \tag{A.6}$$

where $v_i = |\vec{v}| \cos \phi_i$ is the i-th component of the average sub-channel velocity.

The resistance exerted by the boundary is calculated as the product of the shear stress along the boundary walls and the area of the wall surface adjoining the sub-channel. The force is distributed in the computational mesh according to the volume of the cells:

$$F_{boundary} = \tau_{ax,boundary} \cdot A_{w,boundary} \cdot \frac{V_{cell}}{V_{filter}} \tag{A.7}$$

Where $\tau_{ax,boundary}$ is a blending of the shear stress due to the forced and buoyant contributions, as shown for the pins in Equation A.5.

The sub-channel friction factors and loss coefficients used in Equations A.3 and A.5 are calculated by a set of subroutines, housed in **cs_user_modules.f90**. These subroutines select the appropriate correlation, based on whether the pins are assumed to be smooth or rough, and store the computed values in 'fields' which are then retrieved in `ustsnv`.

At the end of the subroutine, the resistance calculated is stored in a 'field' for post-processing purposes.

A.2.4 Heat transfer and coupling with SYRTHES

The subroutines in this group are tasked with the calculation of source terms and the modification of boundary conditions for the energy equation. Due to the nature of the model, the majority of them is related to the coupling with SYRTHES, to implement the new volume coupling or to adjust the existing surface coupling to the requirements of the model. It is possible to sub-divide the group, according to the scope of the subroutines involved, as done in the following.

Volume coupling and source terms

These subroutines contain the implementation of the new volume coupling methodology, carried out as an adaptation of the pre-existing infrastructure. For this reason, the files modified belong to Code_Saturne's base code, an endeavour made possible by its open source nature.

The operations in this sub-group can be further divided in two steps: the exchange of information with SYRTHES and the calculation of the source terms for the energy equation. The first task required modifications to subroutine `cpvosy`, housed in a file of the same name, and, on a lower level, by subroutine `cs_syr4_coupling_recv_tsolid`, in **cs_syr4_coupling.c**. The modification on `cpvosy` where aimed at the use of sub-channel values, instead of local values. The subroutine initiates both the inbound and outbound communication by invoking the subroutines `varsyi` and `varsyo`.

The first is in fact a Fortran wrapper for `cs_syr4_coupling_recv_tsolid`, which was modified with a twofold purpose:

- To receive from SYRTHES an array containing the areas of the surface elements of the solid mesh (on SYRTHESthis required the modifications described in Section A.3).

- To average the temperature received on each sub-channel, as:

$$ {}^{i}\langle T\rangle_{subch} = \frac{\sum_{i\in subch} T_i A_i}{\sum_{i\in subch} A_i} \tag{A.8} $$

Locating each solid element in the fluid mesh is made possible by the use of the PLE library distributed with Code_Saturne. The library associates each solid facelet with a cell in the computational mesh, which brings its contribution to the calculation of the sub-channel value. Note that it is possible, in some configurations, the presence of filtering blocks enclosing no solid. To avoid confusion with legitimate values, the unphysical value of $-300\,^{\circ}\mathrm{C}$ is assigned to those blocks.

The outbound communication was subject to a relatively minor modification, limited to passing the average values of the fluid temperature in place of the local ones as an argument to subroutine `varsyo`. The heat transfer coefficient is also communicated here: its calculation is discussed later in this section.

The calculation of the source terms required the modification of subroutines `cptssy`, housed in a file of the same name, and `cs_syr4_coupling_ts_contrib`, housed in file **cs_syr4_coupling.c**. As for the communication, the intervention was aimed at the use of sub-channel values instead of local ones. The heat source terms in a computational cell is then distributed in the computational grid as follows:

$$ \dot{Q}_{cell} = hA_w\left({}^{i}\langle T_w\rangle - {}^{i}\langle T_f\rangle\right)\cdot\frac{V_{cell}}{\gamma V_{filter}} \tag{A.9} $$

where ${}^{i}\langle T_w\rangle$ and ${}^{i}\langle T_f\rangle$ are the average wall and fluid temperature and γ is the porosity in the sub-channel.

Surface coupling

The coupling between Code_Saturne and SYRTHES through a shared boundary is carried out by the solvers by exchanging informations on the temperatures next to the surface and on a heat transfer coefficient. This mode of coupling was used in the model without substantial modifications to the infrastructure provided to the model, except for a correction

to the calculation of turbulent viscosity discussed in next Section. Nevertheless, some minor modifications were applied to subroutines `coupbi` and `coupbo`:

- In `coupbi`, where data from SYRTHES are received, the wall temperature is stored to be used in the correction to the turbulent viscosity.

- In `coupbo`, which sends out data to SYRTHES, the heat transfer coefficient is multiplied by the porosity in the near wall cell before being sent to SYRTHES. This was required to prevent an energy conservation issue in the communication.

Calculation of the heat transfer coefficient

Correlations for heat transfer are necessary to model the cooling of the fluid using the new volume coupling methodology and to provide a correction for the near wall turbulent conductivity, as required for the accuracy of the surface coupling.

Correlations for the Nusselt number are implemented in **cs_user_modules.f90**. As for the calculation of the friction factor, these correlations include the contributions of forced flow and buoyancy, as well as, for the pins, the contribution due to cross-flow. Correlations for smooth and rough pins were implemented. The overall sub-channel Nu for the fuel and the boundaries is calculated in subroutine `blend_nusselt_number` which performs two blending operations. The first one, between the forced and buoyant axial contributions, use a cubic expression similar to Equation A.5 and it is carried out for both the pins and the boundaries:

$$\mathrm{Nu}_{ax} = \sqrt[3]{\mathrm{Nu}^3_{ax,forced} + \mathrm{Nu}^3_{ax,buoy}} \tag{A.10}$$

The second blending concerns only the Nusselt number along the pins and blends together the contributions from axial and transversal flow:

$$\mathrm{Nu} = \sqrt{\mathrm{Nu}^2_{ax}\cos\phi_z + \left(\mathrm{Nu}_{cf}\frac{D_h}{D_p}\right)^2 \sin\phi_z} \tag{A.11}$$

where ϕ_z is the angle between the axial direction and the velocity vector and D_p is the diameter of the pins. The correction D_h/D_p on the second therm is required since Nu_{cf}, as obtained from the correlations, is defined using the pin diameter as the reference length.

A.2.5 Turbulence and physical properties

The subroutines for the treatment of variable properties and those involved in the modelling of turbulence are here grouped together. This is justified by the use of an algebraic

treatment for turbulence, which takes the form of an additional expression for the viscosity and thermal conductivity. The core subroutine of this group is `usphyv`, contained in **cs_user_physical_properties.f90**. In turn, `usphyv` relies on the operations carried out by a number of subroutines in **cs_user_modules.f90**: the correlations in module PROPERTIES and the subroutines `initialize_viscosity` and `mixing_length_turbulence`.

Subroutine `usphyv` has the task of filling the physical properties fields at every iterations. In addition to the built-in fields for the dynamic viscosity, thermal conductivity, density and specific heat, it makes use of four additional fields, storing the molecular and turbulent contributions to viscosity and conductivity. The subroutine begins with a call to `initialize_viscosity`. This is done once in the calculation and has the purpose of copying the values originally present in the built-in viscosity and conductivity fields, which will be later overwritten, in those created to house the molecular values.

The procedure continues with a call to the correlations to calculate the molecular values of the properties. In the current implementation, the average sub-channel values of the temperature are used in the computation. After that, the calculation of the turbulent viscosity and thermal conductivity is carried out. This is done using separate expressions for the fuel region and the surroundings. In the former, the formula used in POSTR's predecessor, COOLFUEL-3D, is used:[11,90]

$$\mu_t = \alpha_1 \sqrt{\frac{C_f}{2}} \rho |w| D_h \tag{A.12}$$

where α_1 is a coefficient equal to 0.035, C_f is the Fanning friction factor, ρ is the fluid density, and D_h is the hydraulic diameter. The Fanning friction factor used is an area average between the one calculated for the pins and that calculated for the boundary walls. An additional coefficient, turbulent_viscosity_tuning_factor, is multiplied to the expression and can be used for sensitivity studies.

The turbulent thermal conductivity is obtained by dividing μ_t by a turbulent Prandtl number, Turb_Prandtl , usually set equal to 1. To counteract the lack of damping close to the wall provided by the model, which would result in an over-estimation of the heat exchange, the conductivity in the near wall cells is replaced according to the formula:

$$\begin{aligned} \lambda_t &= h_{sc} \frac{T_w - {}^i\langle T_f \rangle}{T_w - T_I} Y - \lambda \\ &= h_{sc} K_T Y - \lambda \end{aligned} \tag{A.13}$$

where T_I is the temperature in the cell, T_w is the boundary temperature in the facelet adjoining the cell, ${}^i\langle T_f \rangle$ is the average temperature in the sub-channel and h_{sc} is a heat transfer coefficient calculated by correlation. This allows the heat transfer calculated in

the simulation to match the prediction of the correlation. Note that the coefficient K_T can assume negative values, especially at the beginning of the calculation. When this occurs, the value is clipped to zero, in which case one would have $\lambda_t = -\lambda$ making the effective conductivity at the wall equal to zero.

A.2.6 Boundary conditions

The definition of the boundary conditions is carried out mainly through Code_Saturne's Graphical User Interface (GUI). Nevertheless, a group of subroutines tasked with the treatment of the boundaries is included in POSTR, for two reasons:

- The domain walls are treated as no-shear surfaces, with the actual friction imposed as an additional source term: this is implemented considering them as symmetry surfaces in the GUI and specifying the correct thermal boundary condition through the subroutines.
- Some scenarios require coupling of the fluid domain with another solver for the external circuit, considered as a network of flow resistances.

These tasks are carried out by the subroutine `cs_user_boundary_conditions`, included in a file with the same name. For the second point, the current implementation requires that it should invoke a solver designed on a case-by-case basis. An example of such a solver was implemented in module LOOP1D, described in Section A.4.

A.2.7 Supporting subroutines

This group contains subroutines that play supporting roles which cannot be associated with a specific aspect of the model. They are listed below, together with a short description of their purpose:

- `copy_filter_field` in **cs_user_modules.f90** is called once Code_Saturne's fields are initialised, to copy the information stored in temporary arrays in the appropriate fields.
- `cubic_blend` in **cs_user_modules.f90** performs the blending of shear stresses and Nusselt numbers due to forced convection and buoyancy as $X = \sqrt[3]{X_{forced}^3 + X_{free}^3}$.
- `cs_user_model` in **cs_user_parameters.c** defines the property fields used in the model.
- `usipsu` in **cs_user_parameters.f90** activates solver features such as variable properties, porosity treatments and others.

- `cs_f_user_extra_operations` in **cs_user_extra_operations.f90** is called at the end of each time step and it calls all the subroutines responsible for the calculation of the modelled fields.

- `usvpst` in **cs_user_postprocess_var.f90** writes the modelled field in the output files, for post-processing purposes.

A.3 Modifications to SYRTHES

While in the fluid domain the geometric details are sacrificed in order to make the calculation of the global features of the flow faster, in the solid domain these details are maintained for all the components included in the model. Thus, the governing equations for conduction and radiation are solved without additional modelling. However, appropriate boundary conditions are required at every external surface of the domain. This poses a problem when the outer surface of the pins is considered: as discussed above, a sub-channel approach is followed to calculate an average fluid temperature and an appropriate heat transfer coefficient to impose a convective boundary condition in this location. This mode of coupling was not implemented in Code_Saturne and SYRTHES: in the original formulation, the volume coupling provided volumetric source terms for both the fluid an the solid domains. It was thus necessary to adapt the volume coupling infrastructure to force the solvers to communicate the information needed.

While, as discussed above, in Code_Saturne the modified files can be included in the case directory and an additional installation is not required, this is not possible in SYRTHES, and the modification had to be included in a pre-compiled version of the code, which is thus required for the use of POSTR. The reason behind this asymmetry lies mainly in the different ways through which data is communicated within the two solvers: whilst in Code_Saturne this is done principally by means of pointers, which can be obtained in every subroutine, in SYRTHES this is done exclusively through the arguments of the functions. Therefore, any function modified to handle new data must be redefined, which requires a modification of the header files: when the case is set up, this would cause conflicts during the compilation unless the same headers are used in the main installation.

Seven files of the kernel of SYRTHES were subject to modifications which are relevant to this discussion. The approach taken was to maintain as much as possible of the pre-existing volume coupling infrastructure, and to adapt and re-use code from the surface coupling implementation whenever feasible. In five of the files, the modifications were relatively minor and are here summarized:

- **syrthes.c** contains the main routine of the solver. It is modified to invoke the subroutines modified using their new definitions.

- **limite.c** is modified in the subroutine `decode_clim_all` to read the reference number of the coupled surfaces and to mark them to use a convective boundary condition of the type $q'' = h(T_{solid} - T_{fluid})$.

- **calmatbord.c** and **ressol.c** are modified to use the information from the new volume coupling method as boundary conditions for the coupled surfaces, when the solution matrix is assembled. The two subroutines modified, `mafcli` and `smfflu`, account respectively for the implicit term hT_{solid} and the explicit term hT_{fluid}.

- **bilan.c** is modified to account for the new volume coupling when calculating the energy balance on a surface, for post-processing purposes.

The remaining two files contain the functions that implement the communication with Code_Saturne and were the object of more extensive modifications. The objective was to re-purpose the subroutines tasked with the volume coupling, which were designed to handle information concerning volume elements, to exchange data regarding boundary facelets. The files modified were:

- **cfd_couplage.c**, in the subroutines `cfd_vol_init` and `cfd_trans_vol`, which, respectively, perform the initialization of the data structure scouvf and initiate the communication with Code_Saturne. The main purpose of the interventions was to convert scouvf, which was designed to store information on the volume elements belonging to the regions where the coupling was imposed, to house data refering to the boundary elements composing the coupled surfaces, similarly to the structure scoupf used in surface coupling.

- **syr_cfd_coupling.c**, for what concerns lower-level aspects of the coupling, namely the communication with Code_Saturne through invocation of the PLE libraries. As in **cfd_couplage.c**, the modifications were aimed at communicating information about boundary faces, rather than volume elements, avoiding at the same time conflicts with the surface coupling. Moreover, the communication was adapted to pass information on the area of the surfaces, beside the temperature. This feature, implemented in a new function called `_send_elt_var_hybrid`, was originally required only to calculate the average solid temperature in each sub-channel, but was then used for all the calculations in Code_Saturne involving the area of the solid in the sub-channel, including the evaluation of flow resistances.

A.4 Module LOOP1D

It is often necessary, in a simulation involving the cooling of the AGR stringer, to model the flow and heat transfer in its surrounding, which can vary significantly from one scenario to another. While possible in theory, including the regions in the fluid model and imposing an additional flow resistance according to the data available poses challenges to the stability of the calculation which are difficult to overcome. For this reason, an alternative methodology was conceived to simulate these kind of complex scenarios: to reserve the three-dimensional model to the interior of the stringer and to model the external region as a one-dimensional network, coupled with the former.

A solver flexible enough to model the broad range of scenarios encountered along the fuel route would be necessarily very complex, and it would probably be desirable to adapt an existing code to the purpose. However, for the test cases studied during the validation, it was decided to use a simpler, *ad-hoc* network solver, which was fast and easy to develop while still able to provide useful proof-of-concept results. The solver is housed in module LOOP1D contained in **cs_user_modules.f90**, whose first part is occupied by parameters which must be set-up at the beginning of the calculation.

Due to the case-specific nature of the approach, to simulate a different scenario would require the implementation of a new module. Nonetheless, it is reckoned that the structure of the current module would provide useful guidance to the programmer, should this need arise. Therefore, a description of the parameters and subroutines constituting the solver is presented below. The description refers to the simulation of the MEL experiment[91] carried out during the model validation. A schematic representation of the scenario is reproduced in Figure A.1 for the reader's convenience.

A.4.1 Parameters

The parameters which allow to set up the solver for a particular test run are listed below:

- tolerance sets the target value for the iterative solver.
- maxiter is the maximum number of iterations assigned to the Newton - Raphson solver. If this value is hit, it is a symptom of a convergence problem.
- maxgsiter is the set number of iterations for the 'inner' Gauss - Seidel solver.
- initial_ratio_stringer_flow is the fraction of the reactor flow assigned to the stringer at the beginning of the calculation. It acts as an 'initial guess', and may play a role in the stability of the algorithm.

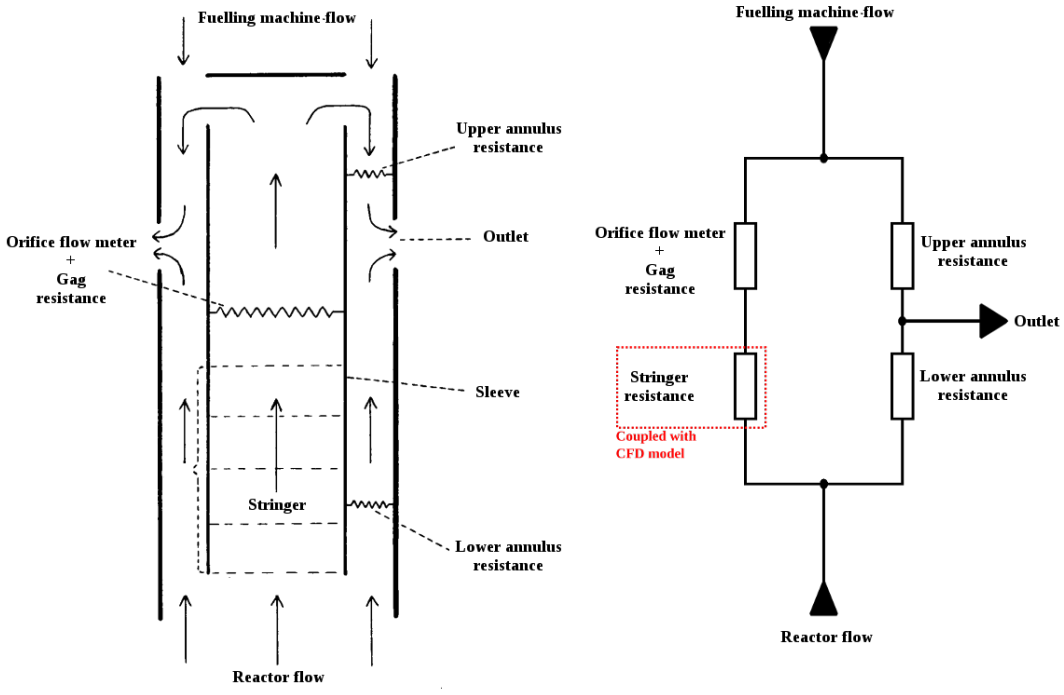

(b)

Figure A.1: Schematics of the model implemented in module LOOP1D.

- *component*_resistance are the flow resistances of the branches of the network, expressed as $R = \rho\Delta p/\dot{m}^2$.

- reactor_flow and fuelling_machine_flow are the flow rates coming in the network from the reactor and the fuelling machine, in $\mathrm{kg\,s^{-1}}$.

- reactor_flow_temperature and fuelling_machine_flow_temperature are the temperatures of the gas coming in the network from the reactor and the fuelling machine, in $^{\circ}\mathrm{C}$.

- lower_annulus_inner_diameter and lower_annulus_inner_diameter are used to calculate the hydraulic diameter of the outer annulus, required in the lumped parameter model of the heat transfer from the sleeve.

- inletname and outletname are the labels given to the inlet and outlet boundaries in the CFD model.

A.4.2 Subroutines

The module houses six subroutines, one of which, `solve_loop` implements the network solver and invokes the others, which carry out supporting tasks for the main calculation. There are two main phases in the solver execution: the solution of the flow network, to calculate the mass flow rates in each branch, and the lumped parameter calculation for the heat transfer from the sleeve to the lower annulus. The latter involves an exchange of information with SYRTHES, which is carried out through two auxiliary files:

- syrthes_com_file_out where Code_Saturne writes the average gas temperature and the heat transfer coefficient in the lower annulus, to be read by SYRTHES.

- syrthes_com_file_in where SYRTHES writes the average sleeve wall temperature and the thermal power coming to the lower annulus, to be read by Code_Saturne.

The subroutine `solve_loop` is called in `cs_user_boundary_conditions`, were the calculated stringer flow rate is imposed as an inlet condition for the CFD solver. The interactions between the subroutines, as well as the quantities involved, are depicted schematically in Figure A.2, whilst a more detailed description of the subroutines is given below.

Subroutine init1Dloop

This subroutine is called at the first execution of the solver. It performs two main tasks:

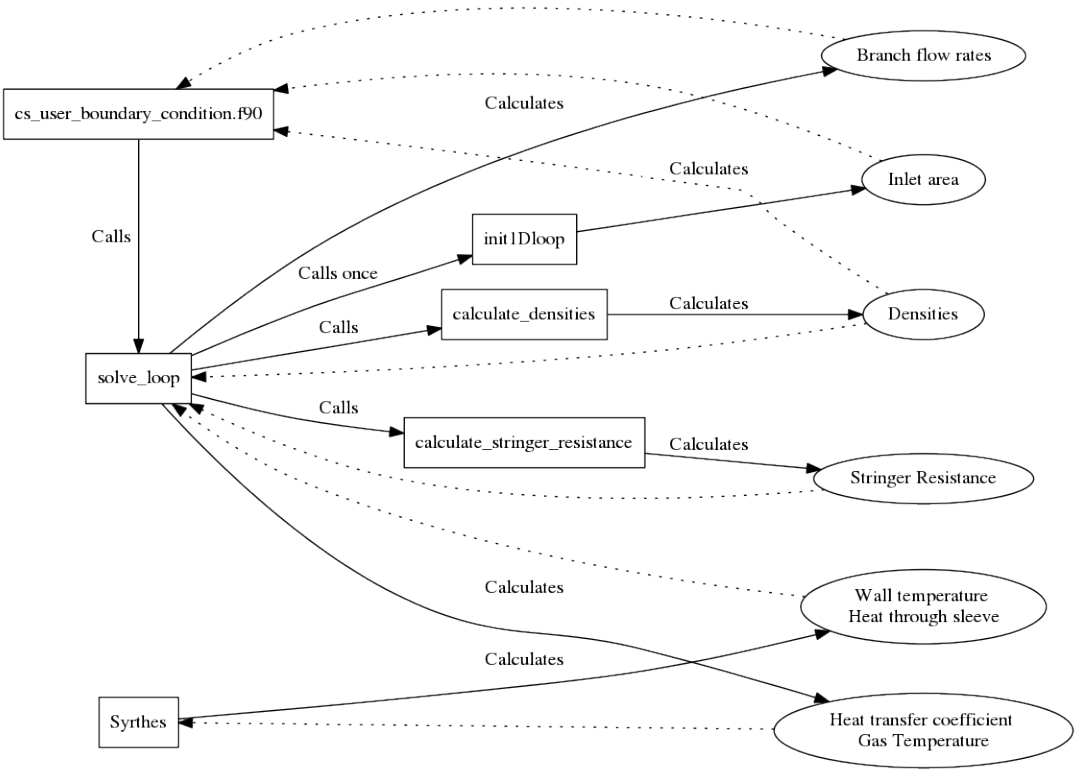

Figure A.2: Block diagram of the one-dimensional network solver.

- Calculates the inlet area, necessary to convert the flow rate computed by the solver into a uniform inlet velocity. This is done by adding together the areas of the facelets belonging to the inlet surface.

- Prevents a deadlock in the communication with SYRTHES by writing initial values for the wall temperature and thermal power from the sleeve in syrthes_com_file_in. The wall temperature is taken equal to the reactor gas temperature, while the power is imposed to zero.

Subroutine lower_annulus_thermal_properties

In this subroutine the physical properties of the gas in the lower annulus, save the density, are evaluated using the correlations in module PROPERTIES. They are used in the lumped parameter heat transfer calculation.

Subroutine read_heat_from_syrthes

In this subroutine the temperature on the outer wall of the sleeve and the thermal power crossing it, calculated by SYRTHES, is read from syrthes_com_file_in.

Subroutine calculate_densities

In this subroutine the gas densities in each of the branches of the network are calculated. For each branch, a different expression is used:

- The density of the incoming flows are calculated from the correlations in module PROPERTIES as the values corresponding to the respective temperatures.

- The density in the stringer is defined as the volume average of the density in the CFD domain.

- The density in the orifice-plug unit region assumed equal to the average density at the outlet of the CFD domain.

- The density in the upper annulus is calculated as the mixing average of the density of the fuelling machine flow and that of the orifice-plug unit region.

- For the density in the lower annulus, the value corresponding to the temperature in the region is taken.

Subroutine calculate_stringer_resistance

In this subroutine, the resistance in the stringer is calculated from the pressure field given by the CFD calculation at the previous time step. The resistance is calculated as:

$$R = \frac{\rho_{str}(p_{in} - p_{out})}{\dot{m}_{str}^2} \tag{A.14}$$

where p_{in} and p_{out} are the average pressure at the inlet and outlet surfaces. Since in Code_Saturne the pressure is available at the centres of the cells, the subroutine calculates the averages within the layers of cells adjoining the surfaces, p_{in}^* and p_{out}^*. The distance between the barycentres of these two layers, Δz^*, differs from the actual height of the domain, Δz, by the axial thickness of a cell of the computational mesh(Figure A.3). The pressure difference between the inlet and the outlet is thus extrapolated as:

$$(p_{in} - p_{out}) = (p_{in}^* - p_{out}^*)\frac{\Delta z}{\Delta z^*} \tag{A.15}$$

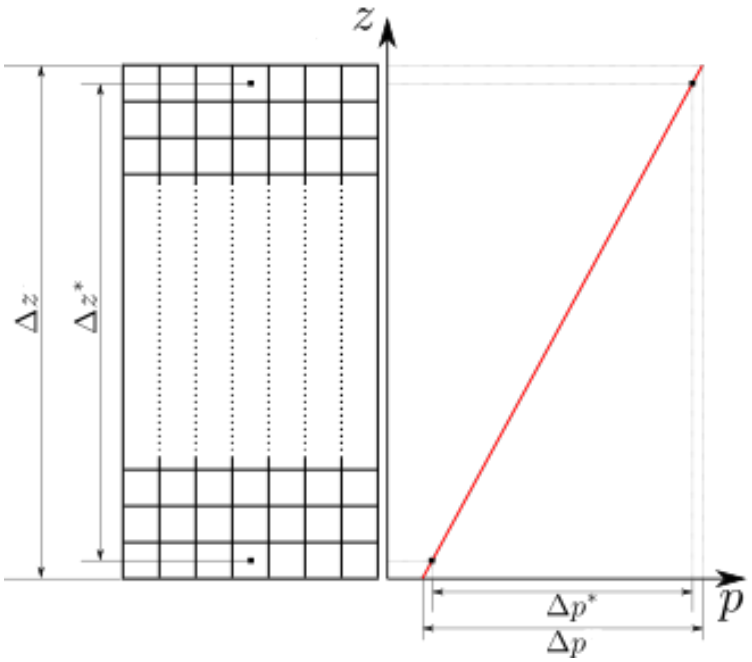

Figure A.3: Extrapolation of the pressure drop to calculate the stringer resistance.

Subroutine solve_loop

The first part of the subroutine calculates the flow rates in each of the branches of the network illustrated in Figure A.1b by solving the system:

$$\begin{cases} \dot{m}_{ua} = \dot{m}_{str} + \dot{m}_{fm} & \text{Continuity - Upper plenum} \\ \dot{m}_{ua} + \dot{m}_{la} = \dot{m}_{out} = \dot{m}_{re} + \dot{m}_{fm} & \text{Continuity - Outlet} \\ \left(\frac{R_{str}}{\rho_{str}} + \frac{R_{gag}}{\rho_{gag}}\right)\dot{m}_{str}^2 + \frac{R_{ua}}{\rho_{ua}}\dot{m}_{ua}^2 + \frac{R_{la}}{\rho_{la}}\dot{m}_{la}^2 = 0 & \text{Pressure balance} \end{cases} \tag{A.16}$$

The equation for the pressure balance required linearisation, which was carried out with the Newton-Raphson method. At iteration $k+1$ of the solver, the equation takes the form:

$$\begin{aligned} 2\left[\left(\frac{R_{str}}{\rho_{str}} + \frac{R_{gag}}{\rho_{gag}}\right)\dot{m}_{str,k}\right]\dot{m}_{str,k+1} + 2\left[\frac{R_{ua}}{\rho_{ua}}\dot{m}_{ua,k}\right]\dot{m}_{ua,k+1} + 2\left[\frac{R_{la}}{\rho_{la}}\dot{m}_{la,k}\right]\dot{m}_{la,k+1} = \\ \left[\left(\frac{R_{str}}{\rho_{str}} + \frac{R_{gag}}{\rho_{gag}}\right)\dot{m}_{str,k}\right]\dot{m}_{str,k} + \left[\frac{R_{ua}}{\rho_{ua}}\dot{m}_{ua,k}\right]\dot{m}_{ua,k} + \left[\frac{R_{la}}{\rho_{la}}\dot{m}_{la,k}\right]\dot{m}_{la,k} \end{aligned} \tag{A.17}$$

where the subscript k indicates quantities obtained at the previous iterations of the solver. The resulting system then undergoes a fixed number of iterations of the Gauss-Seidel solution method, after which the residuals are checked against a set tolerance. If convergence is not reached the coefficients are updated and another iteration begins.

The second part of the subroutine contains a lumped parameter model for the heat transfer from the graphite sleeve to the lower annulus. The calculation starts by reading the values calculated by SYRTHES for the outer sleeve temperature and the thermal power transferred to the fluid from syrthes_com_file_in. The latter is used to calculate the temperature increase of the gas in the lower annulus, which is used to estimate the average gas temperature, under the assumptions that the temperature increases linearly and the temperature at the inlet is the same as the reactor flow:

$$\overline{T}_{la} = T_{re} + \frac{\dot{Q}_{sleeve}}{2c_p\dot{m}_{la}} \tag{A.18}$$

The heat transfer coefficient is then calculated using correlations that account for both forced convection and buoyancy, as was described in Section A.2 for the flow through the fuel bundle. The temperature and the heat transfer coefficient are then written on syrthes_com_file_out, which will be read by SYRTHES to provide a boundary condition for the solid calculation.

Implementation on SYRTHES side

The thermal model for the lower annulus requires information on the outer sleeve temperature and on the thermal power supplied to the gas in the annulus, quantities calculated by SYRTHES, providing in turn boundary conditions for conduction in the graphite. For ease of implementation, this information is passed to and from Code_Saturne by means of auxiliary files, as mentioned above. The operations carried out by SYRTHES have the purpose of reading and writing these files.

The fluid temperature and heat transfer coefficient are read from syrthes_com_file_out and imposed as boundary conditions on the outer sleeve wall in subroutine `user_limfso`, one of the user subroutines provided by the solver, housed in file **user_cond.c**. The surface is identified by its 'reference number', which must be specified at the beginning of the file as the variable nrbalance. The file is the deleted to signal to Code_Saturne the completion of the operation.

To write the thermal power and wall temperature on syrthes_com_file_in, a subroutine executed at the end of each time step, was desired. As SYRTHES does not provide such a function to the user, it was included for the purpose and named `user_extra_operations`, after the equivalent function provided by Code_Saturne, and housed in **user_cond.c**. The wall temperature is calculated as an area average of the temperature in the facelets on the outer sleeve surface, while the total power is calculated as the integral of the heat flux, estimated using Newton's law of cooling. Similarly to the communication in the opposite

way, Code_Saturne signals the reception of the data by deleting the file: a check on its existence is thus carried out before the information is written.

Appendix B

Correlations for C_f and Nu used in COOLFUEL-3D

This appendix presents the correlations used in POSTR for the calculation of the source terms used in the model and described in Appendix A. The correlations for AGR fuel are the same used in COOLFUEL-3D[11], whilst those used in calculations involving smooth pins were taken from Todreas and Kazimi[21] and Todreas and Kazimi[78].

B.1 Flow resistance

Axial flow resistance

As shown in Equation A.5, the axial shear stress due to the pins and the boundary surfaces is calculated from a combination of a contribution from forced convection and one from natural convection. The friction factor from forced convection, $C_{f,forced}$ in Equation A.5, is calculated as:

$$C_{f,forced} = C\mathrm{Re}^{a} \tag{B.1}$$

The parameters C and a are given in Table B.1 for rough and smooth pins and for the boundary surfaces (sleeve and guide tube).

The friction factor from natural convection, $C_{f,buoy}$ in Equation A.5, is calculated as:

$$C_{f,buoy} = D\mathrm{Gr}^{b} \tag{B.2}$$

The parameters D and b are given in Table B.2 for rough pins and for the boundary surfaces.

Cross flow resistance

The loss coefficient for cross flow, Eu_{cf} in Equation A.3, is calculated as:

$$\log_{10} Eu_{cf} = \sum_{i=0}^{3} E_i \log_{10}^{i} \mathrm{Re}_D \tag{B.3}$$

for rough pins and as:

$$Eu_{cf} = \frac{1}{\Omega}\Big(\frac{P}{D_h}\Big)^{0.6}\Big(\frac{\mu}{\mu_w}\Big)^{-0.14} \cdot F\Big(\mathrm{Re}_{D_{pin}}\frac{D_h}{D_{pin}}\Big)^{g} \tag{B.4}$$

The parameters E_i are provided in Table B.3, while F and g are given in Table B.4.

B.2 Heat transfer

Heat transfer due to axial flow

As the axial shear stress, the Nusselt number is calculated by blending the values obtained from correlations for forced flow and and natural convection, as shown in Equation A.10.

Correlations for $\mathrm{Nu}_{ax,forced}$ along rough pins (Equation A.10) are given by Romero[96] in terms of the Stanton number $\mathrm{St} = \mathrm{Nu}/\mathrm{RePr}$ in the form:

$$\mathrm{St}_{ax,forced} = H\left(\frac{T_b}{T_w}\right)\mathrm{Re}^{j} \tag{B.5}$$

The parameters H and j are provided in Table B.5.

For smooth pins the correlation used is derived from the Dittus-Boelter correlation:[21]

$$\mathrm{Nu}_{ax,forced} = \psi \cdot 0.023\mathrm{Re}^{0.8}\mathrm{Pr}^{0.4} \tag{B.6}$$

where ψ accounts for the shape of the sub-channel and is calculated as:

$$\psi = 1 + 0.9120\big(1 - 2.0043e^{-D_h/D_{pin}}\big)\mathrm{Pr}^{0.4}\mathrm{Re}^{-0.1} \tag{B.7}$$

For the boundary surfaces, the forced convection contribution to the Nusselt number is given by the following correlation:[11]

$$\mathrm{Nu}_{ax,forced} = K\mathrm{Re}^{l}\mathrm{Pr}^{1/3} \tag{B.8}$$

The parameters K and l are given in Table B.6.

The contribution from natural convection $\mathrm{Nu}_{ax,buoy}$ is calculated for both rough pins and boundary surfaces as:

$$\mathrm{Nu}_{ax,buoy} = 0.068\mathrm{Ra}^{0.37} \tag{B.9}$$

Heat transfer due to axial flow

The Nusselt number due to cross flow, Nu_{cf} in Equation A.11, is calculated as:

$$\log_{10} \frac{\mathrm{Nu}_{cf}}{\mathrm{Pr}^{0.36}\left(\frac{\mathrm{Pr}}{\mathrm{Pr}_w}\right)^{0.25}} = \sum_{i=0}^{4} M_i \log_{10} \mathrm{Re}^i \tag{B.10}$$

The coefficients M_i are provided in Table B.7.

Re	C	a
Rough pins		
$< 2 \times 10^3$	35.6	-1
$2 \times 10^3 - 3 \times 10^3$	0.44035	-0.4221
$3 \times 10^3 - 5 \times 10^3$	0.146626	-0.28475
$5 \times 10^3 - 2 \times 10^4$	0.000181	0.50156
$2 \times 10^4 - 5 \times 10^4$	0.004937	0.16797
$> 5 \times 10^4$	0.027498	0.009246
Smooth pins	Inner channel	
$0 - +\infty$	0.038906875	-0.18
	Edge channel	
$0 - +\infty$	0.03823125	-0.18
Boundary surfaces		
$< 3 \times 10^3$	16	-1
$3 \times 10^3 - 2 \times 10^4$	0.079	-0.25
$> 2 \times 10^4$	0.046	-0.20

Table B.1: Parameters for the $C_{f,forced}$ correlation.[96]

Gr	D	b
Rough pins		
$< 3.36 \times 10^4$	2.38	1/12
$3.6 \times 10^4 - 8.39 \times 10^4$	86	-0.261
$> 8.39 \times 10^4$	1.74	1/12
Boundary surfaces		
$< 1.54 \times 10^6$	1.73	1/12
$1.54 \times 10^6 - 3.86 \times 10^6$	233	-0.261
$> 3.86 \times 10^6$	1.26	1/12

Table B.2: Parameters for the $C_{f,buoy}$ correlation.[11]

i	E_i
0	2.27859
1	-1.65333
2	0.31706
3	-0.02049

Table B.3: Parameters for the Eu correlation for rough pins.[97]

$\mathrm{Re}_{D_{pin}}$	F	g
$< 2 \times 10^2$	90	-1
$> 2 \times 10^2$	0.96	-0.145

Table B.4: Parameters for the Eu correlation for smooth pins. Obtained from manipulation of data taken from ref. [78]

Re	H	j
$< 2 \times 10^3$	17.6	-1
$2 \times 10^3 - 5 \times 10^3$	0.02664	-0.14573
$5 \times 10^3 - 10^4$	0.01064	-0.03797
$10^4 - 2 \times 10^4$	0.001281	0.19188
$2 \times 10^4 - 5 \times 10^4$	0.0101	-0.01662
$> 5 \times 10^4$	0.0834	-0.21179

Table B.5: Parameters for the $\mathrm{Nu}_{ax,for}$ correlation.[96]

Re	K	l
$< 2 \times 10^3$		$\mathrm{Nu} = 4$
$2 \times 10^3 - 10^4$	0.00038	1.233
$10^4 - 3 \times 10^4$	0.057	0.690
$> 3 \times 10^4$	0.0164	0.810

Table B.6: Parameters for the $\mathrm{Nu}_{ax,forced}$ correlation for boundary surfaces.[11]

i	M_i
0	0.2915
1	-0.131
2	0.278
3	-0.0524
4	0.00394

Table B.7: Parameters for the Nu_{cf} correlation.[88]

Appendix C

Analytical calculation of the porosity

As pointed out in Section 5.2, for intact fuel the calculation of the porosity in a given sub-channel reduces to the calculation of the fraction of the cross-sectional area of the pins which overlaps with the cross-sectional area of the sub-channel. Geometrically, the problem is equivalent to the calculation of the area of the intersection between two circles, one of which has the centre on the circumference of the other.[a] Figure C.1 shows the schematic representation of the scenario and presents the notation used in the following.

The objective is to find the area of the 'lens' $DCO'C'$. This is equal to twice the area of the 'half lens' $DCO'C'$, which in turn can be expressed as the sum of areas of the circular sectors OCO' and $O'CD$ minus the areas of the triangles OCB and $O'CB$:

$$\begin{aligned} A_{DCO'C'} &= 2(A_{OCO'} - A_{OCB} + A_{O'CD} - A_{O'CB}) \\ &= 2A_{OCO'} + 2A_{O'CD} - 2(A_{OCB} + A_{O'CB}) \end{aligned} \tag{C.1}$$

Let R_{ext} be the radius of the circle connecting the centres of the pins belonging to the rank considered, and let R_p be the external radius of the fuel pin. Let $x = \overline{OB}$, $R_{ext} - x = \overline{BO'}$ and $y = \overline{BC}$. Since OO' and CC' are the diagonals of the 'kite' $OCO'C'$, they are perpendicular to each other. Therefore, one can apply Pythagoras' theorem to the triangles OCB and $O'CB$ to find:

$$y^2 = R_{ext}^2 - x^2 = R_p^2 - (R_{ext} - x)^2 \Rightarrow x = \frac{2R_{ext}^2 - R_p^2}{2R_{ext}} \tag{C.2}$$

[a] For the general case of the intersection between two circles without constrains on the centres see `http://mathworld.wolfram.com/Circle-CircleIntersection.html`.

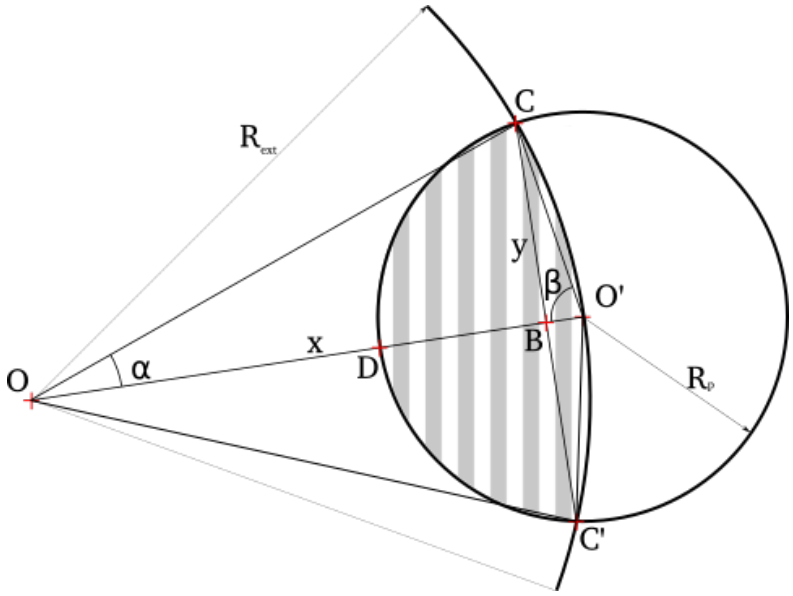

Figure C.1: Schematics of proof for Equation C.3.

which in turn allows one to find $R_{ext} - x$, y, α and β.

$$R_{ext} - x = \frac{R_p^2}{2R_{ext}}$$

$$y = \sqrt{R_p^2 - (R_{ext} - x)^2} = \frac{R_p}{2R_{ext}}\sqrt{4R_{ext}^2 - R_p^2}$$

$$\alpha = \arccos\frac{x}{R_{ext}} = \arccos\frac{2R_{ext}^2 - R_p^2}{2R_{ext}^2}$$

$$\beta = \arccos\frac{R_{ext} - x}{R_p} = \arccos\frac{R_p}{2R_{ext}}$$

The areas can then be calculated as follows:

$$A_{OCO'} = R_{ext}^2\frac{\alpha}{2} = \frac{R_{ext}^2}{2}\arccos\frac{2R_{ext}^2 - R_p^2}{2R_{ext}^2}$$

$$A_{O'CD} = R_p^2\frac{\beta}{2} = \frac{R_p^2}{2}\arccos\frac{R_p}{2R_{ext}}$$

$$A_{OCB} + A_{O'CB} = \frac{1}{2}xy + \frac{1}{2}(R_{ext} - x)y = \frac{1}{2}R_{ext}y = \frac{R_p}{4}\sqrt{4R_{ext}^2 - R_p^2}$$

which can be inserted in Equation C.1 to give:

$$A_{DCO'C'} = R_p^2\arccos\frac{R_p}{2R_{ext}} + R_{ext}^2\arccos\frac{2R_{ext}^2 - R_p^2}{2R_{ext}^2} - \frac{R_p}{2}\sqrt{4R_{ext}^2 - R_p^2} \quad \text{(C.3)}$$